Newtonian and Viscoelastic Fluid Flows in Extensional Microfluidic Devices with Multiple Fluid Streams

PhD Thesis

by

Gemma Catherine Houston

James Weir Fluid Laboratory

Department of Mechanical & Aerospace Engineering

University of Strathclyde, Glasgow

19th March 2023

This thesis is the result of the author's original research. It has been composed by the author and has not been previously submitted for examination which has led to the award of a degree.

Signed: Gemma Houston
Date: March 2023

ABSTRACT

Cross-shaped devices at the microscale are used widely to produce extensional-dominated flows in the context of different applications, for example, in microfluidic mixing, cell analysis and extensional rheometry measurements. For applications with non-Newtonian viscoelastic fluids, the small length scales characteristic of microfluidics, generate flows in which high deformation and high shear rates can be achieved, enhancing elastic effects while, at the same time, keeping inertia low. This characteristic makes these devices very attractive for investigating elastic driven phenomena, in particular, to study the well-known purely elastic instabilities that occur in the absence of inertia due to high streamline curvature and large normal stress differences. Past investigations of these instabilities in extensional flow devices have identified different transitions: including one in which the flow becomes asymmetric but remains steady; and others which involve the onset of time-dependent flow, eventually leading to elastic turbulence. Most previous studies however, have been limited to single fluid flows.

Using either a single or multiple fluid system involving Newtonian and/or viscoelastic (polymeric) fluids, the main objective of this thesis is to provide new insight on the effects of geometrical and operational parameters as well as fluid properties on fluid flow behaviour, and specifically, on the onset conditions of the flow induced elastic instabilities in extensional flow devices. Here, two different geometrical configurations are used: a) a microfluidic cross-slot device and b) a microfluidic flow focusing device, where extensional-dominated flows can be obtained in the presence and absence of a stagnation point, respectively. The hope is that this new knowledge can ultimately be utilised to control these instabilities, either to enhance or prevent them depending on a particular application.

In the cross-slot configuration, this study focuses on the stabilisation of purely elastic instabilities making use of systems involving multiple fluids. The impact of the Capillary number (i.e., the ratio of viscous to interfacial forces) and the ratio between the

viscosity of the two inlet fluids (both miscible and immiscible) flowing simultaneously is analysed to better understand the effects of these parameters on the interface between the two fluids, and on the onset of elastic instabilities. The microfluidic cross-slot is widely used in microfluidics and consists of bisecting channels with opposing inlets and outlets. This set-up produces a free stagnation point at the centre of the geometry resulting in an elongational flow in this region. For both Newtonian and viscoelastic cases, results show that an increase in the viscosity ratio alters the location of the interface between the two fluids, yielding a larger passage for the more viscous fluid in the outlet channels. A lower channel aspect ratio was shown to enhance these effects and to have a large impact on the shape of the interface at the centre of the cross-slot, with a 'dimple' appearing in the central region of the geometry. Increasing interfacial tension (i.e., reducing the Capillary number) resulted in a decreasing curvature of the interface and streamlines in this region. For the viscoelastic case, the results suggest that interfacial tension has a stabilising effect delaying the onset of the steady symmetry-breaking instability.

In the microfluidic flow focusing devices, flows of miscible Newtonian fluids act as a baseline to understand the fundamentals involved in flows within this geometry before progressing onto investigations using complex viscoelastic fluids. This device operates by having two opposing lateral streams that shape a third central inlet stream, producing a strong extensional flow near the centre of the geometry. Using pairs of Newtonian fluids, the shape and size of the produced central focused stream was found to depend on both the ratio of the inlet fluid velocities and the ratio of inlet viscosities. Results also show that the interfacial curvature along the depth of the cross-section of the microchannel, that is known to be present for high viscosity contrasts, is highly dependent on the ratio of inlet fluid viscosities and the microchannel aspect ratio (defined as the ratio between the height and width of the channel). Subsequently, the elastic instabilities that arise when using viscoelastic solutions are investigated, in both single and multiple fluid flow systems. For single fluid systems, results suggest that decreasing the channel aspect ratio from 0.84 to 0.22 causes an increase in the critical Weissenberg number (Wi) for the first flow transition (to steady asymmetric flow) from $Wi = 1.59$ to $Wi = 3.13$ respectively, and the size of the flow asymmetries, but a decrease in the range of Weissenberg number for which steady asymmetric flow is visible. To study the impact of elasticity jumps and

critical regions of extensional flow, two additional fluid configurations were compared to the result of the single fluid case: one where the central fluid stream is Newtonian (N) and the fluid in the lateral streams is viscoelastic (VE), and vice versa. The observed flow instabilities in both cases were of a similar nature to that of the single-fluid case. Interestingly, no significant change in the critical Weissenberg number for the transition to steady asymmetric flow was observed for the various configurations. However, placing the Newtonian fluid in the lateral streams delayed the transition to time-dependent flow significantly from $Wi = 4.69$ (single fluid case) to $Wi = 18.39$. These results suggest that these elastic instabilities cannot be solely related to the extensional flow within this set up and the shear region where there high streamline curvature is important.

ACKNOWLEDGEMENTS

First of all I would like to thank my PhD supervisor Dr Mónica Oliveira who has fully supported me from day one of my journey. Mónica has provided encouragement and guidance both academically and beyond and was always available for a chat when required – especially during the Covid-19 lockdown when things were difficult. Like all PhDs, my journey has had its ups and downs but Monica has been by my side through it all and I cannot thank her enough.

I would also like to thank Ewan Rycroft. We started our PhD journey together and I can't think of someone I would rather have shared this journey with. Ewan was always there to support me during laboratory work when I needed to brainstorm ideas and also managed to deal with my conversations when I was needing a break. Our trip to the Rheology course in Belgium is definitely a memory I will cherish and look forward to hopefully working together again in the future. I would also like to thank Jyoti Joshi for making long experimental days in the laboratory enjoyable – offering casual conversation during break times and being there to bounce ideas off of.

I would also like to extend my appreciation to all those who helped me at the start of my research journey: Joana Fidaglo for sharing her expertise on the microfabrication techniques, Andreia Silva for sharing expertise on the KRUSS drop shape analyser, Jose Ruiz-Lopez for sharing expertise on the DHR-2 rotational rheometer and also Pretheepan Radhakrishnan for always being a friendly face in the laboratory on long experimental working days. Without these lovely people my transition and laboratory training experience would have been completely different and would have taken significantly longer.

To those that have supported and contributed towards my published work: Professor Robert Poole, Dr Mahdi Davoodi, Dr Paolo Capobianchi and Jenna Downie. Without their assistance the work would not have been strengthened by the contribution of numerical simulations. In particular I would like to thank Paolo further for his patience

over the years, helping me understand various concepts and for introducing me to OpenFoam.

To my mum, dad and fiancé Fraser who have fully supported me throughout even when times were difficult and the PhD felt like it was never going to come to an end. They have motivated me to complete work when I was anxious and didn't think it was possible. I really want to thank them from the bottom of my heart.

Last but not least, I would like to thank the funding bodies who, without their support, this PhD would not have been possible: The University of Strathclyde, EPSRC (Project reference 1960606) and the Ronald Miller Foundation.

TABLE OF CONTENTS

LIST OF FIGURES ..... **I**

LIST OF TABLES ..... **XIII**

ACRONYMS ..... **XIV**

LIST OF SYMBOLS ..... **XVI**

CHAPTER 1: Introduction **1**

1.1 MICROFLUIDICS OVERVIEW & CHALLENGES 2

1.2 VISCOELASTIC FLOW INSTABILITIES IN MICROFLUIDICS 6

1.3 THESIS AIM AND OBJECTIVES 7

1.4 THESIS OUTLINE 10

1.5 REFERENCES 13

CHAPTER 2: Literature Review **20**

2.1 DIMENSIONLESS PARAMETER SPACE 21

2.1.1 The Reynolds Number *22*

2.1.2 The Weissenberg Number *24*

2.1.3 The Deborah Number *24*

2.1.4 The Capillary Number *25*

2.1.5 The Peclet Number *26*

2.2 NEWTONIAN FLUID FLOW INSTABILITIES 27

2.3 PURELY ELASTIC FLOW INSTABILITIES 32

2.4 PURELY ELASTIC INSTABILITIES IN MICROFLUIDIC DEVICES 37

2.4.1 Mixed Kinematic Flow Systems *39*

2.4.2 Shear Dominated Flow Systems *43*

2.4.3 Extension Dominated Flow Systems *45*

2.5 SUMMARY 52

2.6 REFERENCES 54

CHAPTER 3: Experimental Methods.....67

3.1 FABRICATION OF MICROFLUIDIC DEVICES.....68
3.2 FLUID PREPARATION & CHARACTERISATION 72
3.2.1 Rheological Behaviour 73
3.2.1.1 Newtonian Fluids.....73
3.2.1.2 Non-Newtonian Fluids.....74
3.2.2 Working Fluid Preparation.....75
3.2.3 Intrinsic Viscosity.....77
3.2.4 Critical Overlap Concentration 77
3.2.5 Solvent Quality 78
3.2.6 Shear Rheology.....78
3.2.7 Extensional Rheology.....81
3.2.8 Surface and Interfacial Tension Measurements.....87
3.2.9 Pycnometery.....94
3.3 FLOW CHARACTERISATION 95
3.3.1 Microfluidic Set-Up 95
3.3.2 Flow Visualisation.....96
3.4 EXPERIMENTAL UNCERTAINTIES.....99
3.4.1 Experimental Average Velocity Uncertainties 101
3.4.1 Experimental Velocity Ratio Uncertainties 102
3.5 REFERENCES.....104

CHAPTER 4: Stabilisation of purely elastic instabilities in cross-slot geometries 109

4.1 INTRODUCTION.....111
4.2 GEOMETRIC AND PROBLEM SET-UP CONFIGURATION.....114
4.3 GOVERNING EQUATIONS AND NUMERICAL METHOD 116
4.4 NON-DIMENSIONALISATION.....120
4.5 EXPERIMENTAL 121
4.6 ANALYTICAL SOLUTIONS FOR TWO-PHASE FLOW OF FULLY DEVELOPED NEWTONIAN FLUIDS IN A CHANNEL AND RECTANGULAR DUCTS.....123
4.7 RESULTS AND DISCUSSION 127

4.7.1 Newtonian fluids 128
4.7.2 Effect of elasticity on the symmetry-breaking instability 136
4.7.3 Effect of interfacial tension on the symmetry-breaking instability 142
4.8 CONCLUSIONS 150
4.9 REFERENCES 152

CHAPTER 5: Flow focusing with miscible fluids in microfluidic devices 158

5.1 INTRODUCTION 160
5.2 EXPERIMENTAL METHODOLOGY 167
5.3 DIMENSIONLESS PARAMETERS 171
5.4 NUMERICAL METHOD 172
5.5 ANALYTICAL SOLUTION FOR THE ONE-DIMENSIONAL PROBLEM 174
5.6 ANALYTICAL SOLUTION AND NUMERICAL RESULTS FOR THE 2D PROBLEM 177
5.7 RESULTS AND DISCUSSION 179
5.7.1 Effect of Velocity Ratio 180
5.7.2 Effect of Viscosity Ratio 184
5.8 CONCLUSIONS 192
5.9 REFERENCES 194

CHAPTER 6: Flow Focusing Device with Viscoelastic Fluids 199

6.1 INTRODUCTION 201
6.2 MATERIALS AND METHODS 205
6.2.1 Fluid Preparation and Characterisation 205
6.2.2 Microfluidic Geometry and Experimental Set-Up 207
6.2.3 Relevant Dimensionless Numbers 207
6.2.4 Image Analysis Techniques 208
6.3 RESULTS AND DISCUSSIONS 210
6.3.1 Part 1: Viscoelastic Instabilities in Single-Fluid Systems 210
6.3.1.1 Effect of Velocity Ratio and Weissenberg Number 211
6.3.1.2 Effect of Channel Aspect Ratio 217
6.3.2 Viscoelastic Instabilities – Multiple Fluid Systems 223
6.4 CONCLUSIONS 231

6.5 REFERENCES....234

CHAPTER 7: Conclusions & Future Work....238

7.1 MICROFLUIDIC CROSS-SLOT DEVICE....239
7.2 MICROFLUIDIC FLOW FOCUSING DEVICE....240
7.3 FINAL REMARKS & FUTURE WORK....242
7.4 REFERENCES....245

APPENDICES....247

8.1 APPENDIX A- ADDITIONAL INFORMATION FOR CHAPTER 4....248
8.2 APPENDIX B – ADDITIONAL INFORMATION FOR CHAPTER 5....249
8.3 APPENDIX C- EFFECT OF SHEAR THINNING....250
8.3.1 Introduction....250
8.3.2 Materials and Methods....251
8.3.2.1 Fluid Preparation and Characterisation....251
8.3.2.2 Microfluidic Geometry and Experimental Set-Up....253
8.3.3 Effect of Shear Thinning....254
8.4 APPENDIX REFERENCES....258

LIST OF FIGURES

Figure 1.1: Cover page of Issue 5424 of SCIENCE exemplifying different fluids (represented by the various coloured streams) flowing side-by-side in a system (1999). 5
Figure 1.2: Simple schematic of microfluidic cross-slot device showing fluid inlets and outlets. 8
Figure 1.3: Simple schematic of microfluidic flow focusing device showing fluid inlets and outlet. 9
Figure 2.1: Schematic of the three-dimensional parameter space adapted from the work of McKinley (2005) to characterise fluid flows, highlighting important dimensionless numbers. 21
Figure 2.2: Sketches from Osborne Reynolds' experimental investigation (1883) showing laminar and unsteady flow regimes as the fluid velocity (and thus the Reynolds number) is increased. Stage 1: Laminar regime, Stage 2a: Turbulent regime, Stage 2b: Turbulent Regime with "eddies" (Reynolds 1883). 23
Figure 2.3: Experimental image from the work of Saffman and Taylor (1958) showing air penetrating glycerine. 28
Figure 2.4: Simulation results from the work of Capobianchi and Lappa (2021) demonstrating the Marangoni Effect when a temperature gradient (shown by the contour: red indicating regions of high temperature) is present. 29
Figure 2.5: Different flow regimes encountered in the work of Cubaud and Mason (2008) illustrating the effects of a reducing Capillary number from a) the stable filament, to b) the jetting regime and then c) the dripping regime. 30
Figure 2.6: Experimental image from the work of Cubaud and Mason (2006) showing the transition from (a)-(b) swirling fluid instabilities to the (c)-(d) folding instabilities as the distance between the two flowing viscous threads is reduced. 32
Figure 2.7: Schematic of polymer/dumbbell stretching along a curved streamline for the Pakdel McKinley criterion (adapted from (Pakdel and McKinley 1996)). 34

Figure 2.8: Elastic instabilities observed in the experimental work of Bonhomme et al (2011) in the form of a) stable straight jet, b) wavy jets and c) advected wavy jets. 36
Figure 2.9: Overview of Microfluidic Geometries (Microfluidic Flows of Viscoelastic Fluids. Oliveira et al (2012)). Red boxes highlight the extensional cross-slot and flow focusing configuration that will be used in this work. 38
Figure 2.10: Purely Elastic Flow Instability Map (PEFIM) by Poole (2019) illustrating the 'relationships' between the different geometries. 39
Figure 2.11: 2D Schematic of an optimised smooth Contraction - Expansion Device, with a converging region followed by a diverging region, from the work of Liu et al (2020) highlighting areas of high extension / positive strain rate (orange) and compression / negative strain rate (blue). 41
Figure 2.12: Example of flow patterns that occur in both the forward and backward flow directions within a microfluidic triangular shaped rectifier. These observations were made in the work of Sousa et al (2010) highlighting the elastic instabilities that arise in the forward flow direction for increasing values of the Deborah number. 43
Figure 2.13: Schematic of 2D serpentine geometry. 44
Figure 2.14: Experimental results, using a singular Boger fluid, conducted to visualise elastic instabilities in a 3D microfluidic serpentine geometry for increasing values of Wi (a) steady flow, (b) and (c) visible instabilities with crossing streamlines shown to become more chaotic with increasing value of Wi. For visualisation purposes, fluorescent particles were added to one of the two inlet streams. 45
Figure 2.15: Schematic of a 3D microfluidic cross-slot device showing relevant variables and coordinate system. 46
Figure 2.16: Results showing elastic instabilities in the cross-slot device from past research a) Arratia et al. (2006) b) Poole et al. (2007). 49
Figure 2.17: Schematic of a 3D microfluidic flow focusing device showing relevant variables and coordinate system. 50
Figure 2.18: Experimental fluid patterns of a dilute Boger fluid (PEO) in a 3D microfluidic flow focusing device for increasing values of Wi (a) steady symmetric flow (b) steady asymmetric flow (c) time-dependent flow. 51

Figure 3.1: Schematic of PDMS microfluidic device fabrication procedure. 69
Figure 3.2: Spin coating program used to coat the glass slides with PDMS for microchannel fabrication - 3 Stage Cycle with a maximum rotational velocity of 6000 rpm and a hold time of 50 s. 71
Figure 3.3: Schematic of steady simple shear flow showing a fluid between two parallel plates. 73
Figure 3.4: Schematic of cone and plate geometry used to characterise fluid samples under shear. 79
Figure 3.5: Shear rheology data (DHR-2 Rotational Rheometer) for a dilute polymer solution of PEO (M_w 8x10^6) at a concentration of 280ppm in a 60/40 solution of water and glycerol highlighting applicable rheometer limits outlined in equations (3.13) (Lower Viscosity Limit) and (3.14) (Fluid Inertia Limit). 81
Figure 3.6: Schematic of Capillary Breakup Extensional Rheometer (CaBER, Thermo Scientific) operation process, a) initial configuration b) after the applied step-strain – during the capillary thinning. 82
Figure 3.7: Extensional rheology data (CaBER) for a dilute polymer solution of PEO (M_w 8x10^6) at a concentration of 280ppm in a 60/40 solution of water and glycerol. The red line is an exponential fit within the elasto-capillary range (refer to equation (3.25)). The figure shows measurement of the fluid filament for different samples from a single fluid batch. 85
Figure 3.8: Operability diagram for CaBer from research conducted by Rodd et al (2005). 87
Figure 3.9: Image of KRUSS Drop Shape Analyser (model DSA25) set up highlighting the fluid droplet suspended from a metal needle in air. 88
Figure 3.10: Schematic of extracted drop shape image showing Young-Laplace variables where ρ_d is the drop phase density, ρ is the density of the outer continuous phase φ is the tangent angle between the drop axis and the surface of an arbitrary reference plane with pressure Δp_0. 89
Figure 3.11: Schematic of iterative process involved using drop shape analyser from Berry (2015). 91
Figure 3.12: Experimental schematic from KRUSS Drop Shape Analyser (model DSA25) highlighting calibration lines (blue) and the final droplet profile from which measurements can be taken (red). 92

Figure 3.13: Experimental Data of interfacial tension obtained from the KRUSS Drop Shape Analyser (DSA25) for a polymeric fluid of PEO (M_w 4x10^6) at a concentration of 280ppm in a 50/50 solution of water and glycerol. 93
Figure 3.14: Schematic of pycnometer (enlarged for visualisation purposes) used to measure the density of fluids. 94
Figure 3.15: Image of microfluidic set up used for experiments. 95
Figure 3.16: Schematic of Epi-Fluorescence Microscopy light path. 97
Figure 3.17: Spectrum of excitation and emission wavelengths for ≈ 1 μm fluorescent tracer particles (FluoSpheres carboxylate- modified, 1.0 μm, Nile Red). 98
Figure 3.18: Spectrum of Transmittance vs Wavelength for the OLYMPUS U-MWIGA3 filter cube and DM570 OLYMPUS dichroic mirror (OLYMPUS). 98
Figure 4.1: a) Schematic of the cross-slot geometry with insets highlighting the notation used in 3D (top right) and a typical 2D computational mesh (bottom left). Here, $\tilde{h}$ indicates the passage width of Fluid-1 in the outlet arms. b) Schematic illustrating the experimental microfluidic cross-slot apparatus allowing for direct observation of the (x, y) plane. Not to scale. 115
Figure 4.2: Schematic of a) the 1D channel geometry (flow is left to right) and b) the 1D rectangular duct geometry (flow is into page) and the employed coordinate system. Not to scale. Note choice of coordinate system to match that of 'outlet' arms in cross-slot. 124
Figure 4.3: Variation of the height of the interface between two fluids with viscosity ratio for Newtonian fluids. The values of the numerical simulations presented in the ranges 0 < K^* < 0.5 and 0.5 < K^* < 1 are taken in the outlet arms for $y^* = 5W$ with Ca = 0.005 and Ca = ∞, respectively.....130
Figure 4.4: Visualisation of the interface between two Newtonian fluids in the fully developed region of the outlet arm with $Ca \rightarrow \infty$ and viscosity ratios a) K = 1, b) K = 0.16, c) K = 0.03 (where the fluid shown in dark grey is the most viscous one) using AR = 0.83 i) in the experiment and (ii–iii) in numerical simulations. Figures i) and ii) are presented in (x, y) plane centred at z^* = 0 for 1.5 < y^* < 2 while (iii) show a cross-sectional view of the channel ((x, z) plane) at y^* = 1...130

Figure 4.5: Effect of viscosity ratio with Ca = ∞ and a) K = 1, b) K = 0.03 for AR = 0.83 in i) the experiment and ii) in numerical simulations, where the most viscous fluid (Fluid-1) is on the left-hand side. 132

Figure 4.6: Effect of interfacial tension for K = 44.78 with (a) Ca = 5.90 × 10^{-1}, (b) Ca = 7.08 × 10^{-4} for i) AR = 0.83 in the experiment and ii) 2D numerical simulations. In the experiments, the oil is injected through inlet-1 and the aqueous solution through inlet-2. 134

Figure 4.7: Effect of aspect ratio for K = 0.03 with (a) AR = 0.83, (b) AR = 0.22 including definition of dimple size $\mathrm{d_h}$. The most viscous fluid (Fluid-1) is on the left-hand side. 135

Figure 4.8: Variation of the normalised dimple size (normalised by the channel width) with the viscosity ratio for different aspect ratios. Dimple size $\mathrm{d_h}$ is defined in Figure 4.7. 135

Figure 4.9: Streamlines obtained using i) numerical method superimposed on the magnitude of the non-dimensional velocity gradient with AR = 0.83 and $\mathrm{Ca} = \infty$ and ii) experimental results with AR = 0.83 for a) K = 1, b) K = 0.16, c) K = 0.03, where the most viscous fluid enters through inlet-1 (on the left-hand side). 136

Figure 4.10: Effect of viscoelasticity on the 2D steady symmetry-breaking instability of two fluids with K = 1, Ca = ∞ for a) $\mathrm{Wi_i}$ = 0.4, b) $\mathrm{Wi_i}$ = 0.515, c) $\mathrm{Wi_i}$ = 0.55, d) $\mathrm{Wi_i}$ = 1,and $i = \{1, 2\}$ 138

Figure 4.11: a) The stability diagram for symmetry-breaking instability and b) the variation of critical Weissenberg number with the ratio of Weissenberg numbers for two-phase flow problems with $\mathrm{Ca} = \infty$ and K = 1. 139

Figure 4.12: The local distribution of the M parameter before the onset of the instability at a) $\mathrm{Wi_1}$ = 0.51, b) $\mathrm{Wi_1}$ = 0.58, c) $\mathrm{Wi_1}$ = 0.735 and d) $\mathrm{Wi_1}$ = 1.18 for a) $\mathrm{Wi_2/Wi_1}$= 1, b) $\mathrm{Wi_2/Wi_1}$= 0.75, c) $\mathrm{Wi_2/Wi_1}$= 0.5 and d) $\mathrm{Wi_2/Wi_1}$ = 0.25 with $\mathrm{Ca} = \infty$ and K = 1. The white circles indicate the location where M reaches a critical value of ≈ 1 in Fluid-2. 141

Figure 4.13: Effect of interfacial tension on the symmetry-breaking instability of two fluids for a) Ca = ∞, b) Ca = 1, c) Ca = 0.1, (d) Ca = 0.05, with $\mathrm{Wi_i}$ = 0.6, $i = \{1, 2\}$ and K = 1. 143

Figure 4.14: Effect of Wii with $i = \{1, 2\}$ on the steady symmetry-breaking instability for K = 1 and different Capillary numbers. 144

Figure 4.15: Variation of critical values of Weissenberg number against Capillary number for K = 1. Analytical fit $1/\mathrm{Wi_i, cr} = (0.0185\mathrm{Ca}) + 1.938$ shown by solid line for $i = \{1, 2\}$. 146

Figure 4.16: Effect of the viscosity ratio parameter on the symmetry-breaking instability of two fluids for a) K = 1, b) K = 0.25, c) K = 0.5, d) K = 0.1, with $\mathrm{Wi_i}$= 1, $i = \{1, 2\}$and Ca = 0.005. 147

Figure 4.17: Onset of the new time-dependent symmetry-breaking instability in two different time instances for K = 0.001, $\mathrm{Wi_i}$ = 1, $i = \{1, 2\}$and Ca = 0.005. 149

Figure 4.18: The variation of $\mathrm{r.m.s.}$ of the asymmetry parameter for the time-dependent symmetry-breaking instability with K = 0.001 and Ca = 0.005 using an increasing $\mathrm{Wi_i}$ramp (open) and decreasing ramp (closed symbols) for $i = \{1, 2\}$. 149

Figure 5.1: Examples of various flow focusing configurations used for bringing fluid streams into contact: a) where an orifice at the centre of the geometry is used to aid control of the shape of the outlet central focused stream; b) with angled lateral inlet streams, and c) with perpendicular lateral inlet streams. The latter configuration is used in this work and important variables are identified in the schematic, where $\mu_i, \mathrm{Q_i}$ and $\mathrm{U_i}$ indicate the viscosity, flow rate and velocity of each of the fluid streams, respectively. The subscripts $\mathrm{i} = 1$ and $\mathrm{i} = 2$ refer to the fluid in the central and lateral inlets, respectively, and $\mathrm{i} = 3$ refers to the outlet. 161

Figure 5.2: Example of the cross-sectional shape of the central focused stream in the outlet channel obtained in numerical simulations of this work for viscosity ratio $\mathrm{K} > 1$ ($\mathrm{VR} = 1, \mathrm{K} = 9.56$) and $\mathrm{AR} = 0.84$, where Fluid 1 is shown in grey and Fluid 2 is shown in black. 163

Figure 5.3: Schematic of a) 3D microfluidic flow focusing device used in this work showing relevant variables and coordinate system, and b) experimental flow visualisation set up. 168

Figure 5.4: Example of a microscope image obtained with the central fluid stream dyed with Rhodamine-B and undyed lateral streams, highlighting the region over which the measurement of the outlet central focused stream width was performed (the reported value of $\mathrm{W_f}$ being an average across the highlighted region). 170

Figure 5.5: Normalised grayscale profile along the width of the outlet channel at location $x/W = 2.5$ (within the experimental measurement region) for $AR = 0.84$, $K = 1$ and $VR = 1$. The profile highlights the variation of grayscale intensity in the regions of the interface between the undyed outer fluid and the central focused fluid stream dyed with Rhodamine-B. 171

Figure 5.6: Schematic of a) the full 1D geometry used to replicate the outlet channel of the flow focusing device highlighting the region of symmetry and the employed coordinate system, b) the 1D geometry used to derive the 1D analytical expression considering the symmetry of the flow. 175

Figure 5.7: Comparison of analytical solution and 2D numerical simulations (at $x/W = 2.5$) showing a) Impact of velocity ratio for $K = 1$ b) Impact of viscosity ratio for $VR = 1$, $VR = 2$ and $VR = 5$. 177

Figure 5.8: Comparison of analytical solution and 2D numerical simulations (at $x/W = 2.5$) showing the impact of viscosity ratio when $VR = 1$ on the normalised velocity profile (normalised using the maximum velocity at the centreline ($y/W = 0.5$) for each case) in the y-direction for a) $K = 1$ b) $K = 1.76$ c) $K = 3.74$ and d) $K = 5.64$. 179

Figure 5.9: Flow patterns observed in the flow focusing geometry with $AR = 0.84$ and $Q_1 = 0.02$ ml/h, with matching fluid in all inlets ($K = 1$) and different velocity ratios a) $VR = 1$, b) $VR = 5$. i-ii) Experimental images obtained by adding i) fluorescent tracer particles to all inlet streams to show the pathlines and ii) Rhodamine-B dye to the central fluid inlet only. iii) 3D numerical simulations, where Fluid 1 is shown in gray and Fluid 2 is shown in black. 181

Figure 5.10: Outline of the separating streamlines observed from numerical simulations at the centre plane with increasing velocity ratio within the flow focusing geometry of $AR = 0.84$, for $K = 1$. 182

Figure 5.11: Experimental measurements and 3D numerical simulation results of the normalised width of the central focused outlet stream at the centre plane of the flow focusing geometries of $AR = 0.84$ and $AR = 0.22$ with increasing velocity ratio for $K = 1$. Comparison of the results with the derived 2D analytical solution (Equation (5.13)) and Hele-Shaw solution $W_f/W = 1 + 2\,(VR)K\text{-}1$ (Wu and Nguyen 2005) are also shown. 183

Figure 5.12: Qualitative flow patterns observed in the flow focusing geometry with $AR = 0.84$, for $VR = 1$ and three viscosity ratios a) $K = 1$, b) $K = 3.74$, and c) $K = 9.56$: i) comparison of experimental (top half) and 3D numerical simulation (bottom half) at the $z = D/2$ centre plane, showing the focusing of the central stream ; ii) 3D numerical simulations showing the filament cross-section in the y-z plane at $x/W = 2.5$, where Fluid 1 is shown in grey and Fluid 2 is shown in black. 185

Figure 5.13: Impact of viscosity ratio on the normalised width of the central focused outlet stream at the $z = D/2$ centre plane for $VR = 1$. Comparison of experimental and 3D numerical simulations for $AR = 0.84$. 186

Figure 5.14: Variation of the cross-sectional shape of the central focused stream with viscosity ratio for $VR = 1$. Comparison of the profile of the interface along the channel depth with increasing K obtained using 3D numerical simulations with a) $AR = 0.84$, and b) $AR = 0.22$. 187

Figure 5.15: Comparison of the normalised width of the central focused outlet stream along the z-direction obtained in the 3D numerical simulations and in the experiments with $AR = 0.84$ for a) $K = 3.74$, and b) $K = 9.56$. $W_{f,z}$ represents the central focused stream width at a particular z position $(0 < z/D < 1)$ and horizontal error bars indicate the experimental depth of field estimated for the optical set-up used in this work. 188

Figure 5.16: a) Contours of the magnitude of the rate-of-strain tensor, S, and its shear component, S_{xy}, observed in the y-z plane in the flow focusing geometry with $AR = 0.84$ and $VR = 1$ and three viscosity ratios $K = 1, 3.74, 9.56$ for full channel depth $(0 < z/D < 1)$ at location $x/W = 2.5$. b) Contours for the S_{xy} component for the case $AR = 0.22$ (only half of the domain is shown) for the same conditions in (a). Solid white lines showing the location of the interface are superimposed in each image. 190

Figure 5.17: Impact of viscosity ratio on the central focused outlet stream in flow focusing geometries at the centre plane $z = D/2$ for $VR = 1$. Comparison of the normalised width of the focused stream for increasing values of K obtained from 3D numerical simulations for $AR = 0.84$ and $AR = 0.22$. 191

Figure 5.18: Impact of viscosity ratio on the central focused outlet stream for $VR = 1$ comparing the normalised width obtained via the 2D analytical solution with the

normalised width averaged along the cross-section obtained in the simulations for $\mathrm{AR} = 0.84$ and $\mathrm{AR} = 0.22$. 192
Figure 6.1: Shear rheology flow curves (DHR-2 Rotational Rheometer) for the solution of PEO (M_w 8x10^6) at a concentration of 280ppm in a 60/40 solution of water and glycerol (cf. Table 6.1). Measurement limits outlined in equations (3.13) and (3.14) are shown as dashed lines. 206
Figure 6.2: An experimental image exemplifying asymmetric flow within the flow focusing microfluidic device highlighting the variables used to determine the asymmetry parameter. The measurements were carried out at $\mathrm{x} = 0$ with additional checks carried out at $\mathrm{x} = 0.5\mathrm{W}$ (green line). 209
Figure 6.3: Flow patterns in the flow focusing device (at $\mathrm{z} = \mathrm{D}/2$ using a single Newtonian fluid (deionised water) at $\mathrm{VR} = 25$ for different inlet flow conditions a) Re_3= 7.69x10^{-1} b) Re_3= 4.92 to highlight the symmetric flow obtained for Newtonian fluid flows over the range of Re covered in this chapter. 210
Figure 6.4: Flow patterns for $\mathrm{VR} = 25$ with increasing values of Wi in the flow focusing device ($\mathrm{AR} = 0.84$) using the same viscoelastic solution (PEO 280ppm in 60:40 water/glycerol solution) in all inlet streams a) $\mathrm{Wi} = 1.32$ b) $\mathrm{Wi} = 2.64$ c) $\mathrm{Wi} = 3.31$ d) $\mathrm{Wi} = 5.29$. For all cases $\mathrm{Re} < 0.2$. 212
Figure 6.5: Flow classification map in the Wi-VR domain for single-phase Boger fluid (PEO 280ppm in 60:40 water/glycerol solution) flow within the flow focusing device of $\mathrm{AR} = 0.84$. Blue circles indicate the symmetric flow regime, orange crosses indicate the asymmetric flow regime and red triangles indicate the time-dependent flow regime. 213
Figure 6.6: Supercritical bifurcation diagram for asymmetric flow patterns within the flow focusing device using single-phase viscoelastic fluid flow (PEO 280ppm in 60:40 water/glycerol solution) showing the effect of Wi on the degree of asymmetry for high and low VR. Solid lines represent the fit (equation (6.5)). Low velocity ratio ($\mathrm{VR} = 10$) data is shown in green and high velocity ratios ($\mathrm{VR} \geq 20$) are shown in black, in particular, black squares indicate $\mathrm{VR} = 20$, black diamonds indicate $\mathrm{VR} = 25$ and black circles indicate $\mathrm{VR} = 30$. Solid symbols represent $|\chi|$ and hollow symbols represent $-|\chi|$ highlighting the bistable nature of this instability. 215

Figure 6.7: Flow patterns for $\mathrm{Wi} = 2.65$ with increasing values of VR in the flow focusing device using single-phase viscoelastic solution (PEO 280ppm in 60:40 water/glycerol solution) a) $\mathrm{VR} = 10$ b) $\mathrm{VR} = 20$ c) $\mathrm{VR} = 25$ d) $\mathrm{VR} = 30$ showing that for high velocity ratios the size of the asymmetry is shown to remain approximately constant while for the $\mathrm{VR} = 10$ case the asymmetry is visibly smaller. For all cases $\mathrm{Re} < 0.2$. 217

Figure 6.8: Experimental images showing the impact of Wi on the flow patterns observed for single-phase flow of PEO $(\mathrm{M_w}8\ \mathrm{x}10^6)$, ...218

Figure 6.9: Flow map in H-Wi parameter space at $\mathrm{VR} = 20$ for single-phase viscoelastic fluid flow in the flow focusing devices of varying channel aspect ratios and Weissenberg number. Blue symbols indicate the symmetric flow regime, orange symbols indicate the asymmetric flow regime and red symbols indicate the time-dependent flow regime. 220

Figure 6.10: Effect of Wi on the degree of asymmetry for asymmetric flow patterns within the flow focusing device using single-phase viscoelastic fluid flow (PEO 280ppm in 60:40 water/glycerol solution): for $\mathrm{AR} = 0.84$ at $\mathrm{VR} \geq 20$, and $\mathrm{AR} = 0.28$ and $\mathrm{AR} = 0.22$ at $\mathrm{VR} = 20$. Solid lines represent the fit to the supercritical bifurcation equation (equation (6.5)). Black data represents the case of $\mathrm{AR} = 0.84$, green data represents the case of $\mathrm{AR} = 0.28$ and red data represents the case of $\mathrm{AR} = 0.22$. Solid symbols represent $|\chi|$ and hollow symbols represent $-|\chi|$ highlighting the bistable nature of this instability. 222

Figure 6.11: Experimental flow configurations for flows of multiple fluids in the flow focusing device. CASE A – The reference single-phase flow system where polymer solution occupied all inlet streams. CASE B - Newtonian fluid is inserted through the central inlet channel and the polymeric fluid through two lateral/ side channels CASE C - Newtonian fluid is inserted into the two lateral inlet channels and the polymeric fluid flows in through the central channel.....224

Figure 6.12: Experimental images showing the impact of Wi on the flow patterns observed for the three fluid configurations at $\mathrm{VR} = 25$ using viscoelastic solution (VE) of PEO $(\mathrm{M_w}8\ \mathrm{x}10^6)$, 280ppm $(\mathrm{w/w})$, in Water/ Glycerol (60/40) and Newtonian solution (N) of Water/ Glycerol (48.4/51.6). The first transition from steady symmetric flow to steady asymmetric flow is indicated by the orange

highlighted images and the second transition to time-dependent flow is indicated by the red highlighted images. 226

Figure 6.13: Flow classification maps in the Wi-VR domain in the flow focusing device of $\mathrm{AR} = 0.84$ for multiple fluid flow configurations; CASE A, CASE B and CASE C. Fluids used are a viscoelastic solution (VE) of PEO ($\mathrm{M_w}$8 x10^6), 280ppm ($\mathrm{w/w}$), in Water/ Glycerol (60/40) and a Newtonian solution (N) of similar shear viscosity. Blue circles indicate the symmetric flow regime, orange crosses indicate the asymmetric flow regime and red triangles indicate the time-dependent flow regime. 228

Figure 6.14: Bifurcation diagram for asymmetric flow patterns within the flow focusing device using multiple fluids. Effect of Wi-Wic on the degree of asymmetry for $\mathrm{AR} = 0.84$ at $\mathrm{VR} \geq 20$. Solid lines represent the data fit (equation (6.5)). Black data represents the case of single-phase flow, orange data represents the case with the Newtonian fluid in the central stream and viscoelastic fluid in the lateral side streams and blue data represents the case with the Newtonian fluid in the lateral side streams and the viscoelastic fluid in the central stream. Solid symbols represent $|\chi|$ and hollow symbols represent $-|\chi|$ highlighting the bistable nature of this instability. 230

Figure B.1: Comparison of the normalised width of the central focused outlet stream along the z-direction obtained in the 3D numerical simulations and in the experiments with $\mathrm{AR} = 0.84$ for $\mathrm{K} = 5.64$ 249

Figure B.2: Comparison of the normalised width of the central focused outlet stream along the z-direction obtained in the 3D numerical simulations and in the experiments with $\mathrm{AR} = 0.84$ for $\mathrm{K} = 15.07$ 249

Figure C.1: Steady shear rheology data (DHR-2 Rotational Rheometer) for the viscoelastic fluids described in Table C.1. Rheometer limits outlined in equations (3.13) and (3.14) are shown. Black squares represent data for 1000ppm fluid, red circles represent data for 2000ppm fluid and grey triangles represent data for 3000ppm fluid 253

Figure C.2: Flow classification map in the $Wi - VR$ domain for single-phase viscoelastic fluid flow within the flow focusing device of $AR = 0.84$ for three shear thinning solutions (PEO1000, PEO2000 and PEO3000). Blue circles indicate symmetric flow regime, orange crosses indicate steady asymmetric flow

regime, red triangles indicate the time-dependent flow regime, akin to that seen with Boger fluids and green stars represent the extra flow regime 255

LIST OF TABLES

Table 3.1: Quantitative data obtained from the exponential fit displayed in Figure 3.7 (refer to equation (3.25)). using extensional rheology data (CaBer). Data is shown for different samples from a single fluid batch of a dilute polymer solution of PEO (Mw 8x10^6) at a concentration of 280ppm in a 60/40 solution of water and glycerol. 86

Table 3.2: Experimental Data of interfacial tension obtained from the KRUSS Drop Shape Analyser (DSA25) for a polymeric fluid of PEO (M_w 4x10^6) at a concentration of 280ppm in a 50/50 solution of water and glycerol. 93

Table 3.3: Uncertainty values for measured independent parameters. 101

Table 4.1: Characteristics of the computational meshes. NC is number of cells, W is channel width and D is channel depth. 119

Table 4.2: Mesh dependency study for 2D simulations using M21 with 13005 and mesh M22 with 51005 cells. 119

Table 4.3: Characterisation of different fluids used in the experiment. 122

Table 5.1: Summary of previous studies, proposed correlations for estimating the size of the Newtonian fluid focused stream, and conditions under which they apply. For variable definitions see Figure 5.1. 164

Table 5.2: Characteristics of the fluids used in the experimental work including fluid composition and physical properties (density and viscosity) at 20°C. 169

Table 5.3: Boundary conditions used in numerical simulations in the flow focusing device utilising numbered channel notation from Figure 5.3a. 173

Table 6.1: Characteristics of the fluids used in the experimental work including fluid composition and physical properties (density and viscosity) at 20 °C. 206

Table 6.2: Parameters of bifurcation data curves fitted to experimental measurements for multiple fluid flow configurations. 230

Table C.1: Characteristics of the fluids used in the experimental work including fluid composition and physical properties (density, CaBER relaxation time and zero-shear viscosity) at 20 °C. 252

ACRONYMS

1D	One-Dimensional
2D	Two-Dimensional
3D	Three-Dimensional
CaBER	Capillary Breakup Extensional Rheometer
CCD	Charged-Coupled Device
DHR	Discovery Hybrid Rheometer
DM	Dichroic Mirror
DSA	Drop Shape Analyser
Em	Emission
Ex	Excitation
Exp	Experimental
FENE	Finite Extensible Nonlinear Elastic
FENE-CR	Finite Extendable Non-linear Elastic – Chilcott and Rallison
HPF	High Purity Perfluorodecalin
μPIV	Micro-Particle Image Velocimetry
N	Newtonian
NA	Numerical Aperture
NC	Number of Cells
NMP	No-moving Parts
Num	Numerical
OSCER	Optimized Shape Cross-Slot Elongation Rheometry

PAA	Polyacrylic Acid
PB	Polybutene
PDMS	Polydimethylsiloxane
PEFIM	Purley Elastic Flow Instability Map
PEO	Polyethylene Oxide
PF	Phase-Field
PIB	Polyisobutylene
PVA	Polyvinyl Alcohol
r.m.s	Root Mean Square
sPTT	Simplified Phan-Thien Tanner
UCM	Upper Convected Maxwell
VE	Viscoelastic
VOF	Volume-of-Fluid
%wt	Percentage of total weight of fluid

LIST OF SYMBOLS

A	Area
$\boldsymbol{A}$	Arbitrary Matrix
a	Unknown constant that scales the reference length in Chapter 4
a_1	Magnitude of flow asymmetry in flow focusing device
a_i	Variable used to calculate parameter, P
a_P	Polymer constant used in Chapter 3 to calculate the intrinsic viscosity
AP	Asymmetry parameter of instability in cross-slot device
AP_n	Value of AP at time, t
$AP_{r.m.s}$	Root mean square of AP
$\langle AP \rangle$	Average of AP
AR	Aspect ratio
AR_0	Aspect ratio of initial sample loading in CaBER device
AR_f	Final aspect ratio of sample loading in CaBER device
$A_1 - A_4$	Unknown constants in 2D problems in Chapter 4
a', b'	Unknown constants in Chapter 4
$\bar{a}, \bar{b}$	Unknown constants in Chapter 4
a_c, b_c	Geometrical parameters in expression of Knight et al. (1998) in Chapter 5
$\overline{A}, \overline{B}, \overline{C}, \overline{D}$	Constants of integration in Chapter 5

B^*	Constant of order 1 dependent on channel geometry in Chapter 5 from work of Knight et al. (1998)
$\tilde{b}$	Jump of normal stress at interface of two fluids in cross-slot device
$b_{\overline{X}}$	Total systematic standard uncertainty
$C_1 - C_4$	Unknown constants in 1D problems in Chapter 4
c	Polymer concentration
c^*	Critical overlap concentration for polymer solutions
Ca	Capillary number
d	Distance
d_h	Size of the dimple at the interface between two fluids in cross-slot device
D	Depth of channel
D_0	Initial diameter of fluid filament in CaBER device at time t=0
D_c	Diffusion coefficient
D_F	Observed diameter of filament in CaBER device
D_{PLATE}	Diameter of plate for CaBER device
De	Deborah number
$D(A)/Dt$	Material derivative of arbitrary matrix A
Ec	Elasto-capillary number
El	Elasticity number
$\in$	Total error/ uncertainty
$\in_P$	Total error/ uncertainty associated with parameter, P

$\in_{a_i}$	Total error/ uncertainty associated with variable used to parameter, P
F	Driving force in Chapter 3 – Newton's Law
$\boldsymbol{F}$	Capillary force applied at the interface of two fluids due to the existence of an interfacial tension
f_i	Function for the linear-sPTT model for a particular fluid phase
F_{sb}	Supercritical bifurcation data function
g	Gravitational force
G	Applied constant pressure gradient
G^*	Dimensionless pressure gradient
G_E	Elastic modulus of viscoelastic fluid
$\mathcal{H}$	Parameter used to assess effect of channel aspect ratio (AR) on instabilities within flow focusing device defined as $AR/(AR+1)$
h	Half height of central focused stream i.e., $W_f/2$ in flow focusing device
$\tilde{h}$	Passage width of Fluid-1 in the outlet arms of the cross-slot device
h^*	Dimensionless $\tilde{h}$
H	Vertical extension of semi-portion of the domain i.e., $W/2$ in Chapter 5
h_0	Initial plate separation of CaBER device
h_f	Final plate separation of CaBER device

k	Error source
K	Viscosity ratio
K^*	Modified form of the viscosity ratio parameter
K_P	Polymer constant used in Chapter 3 to calculate intrinsic viscosity
L	Length of the domain in the x-direction
$\tilde{L}$	Characteristic Length Scale
l_{cap}	Caillary length
m	Mass
m_1	Mass before fluid inserted for pycnometry density measurements
m_2	Mass of container and fluid for pycnometry density measurements
M	Pakdell – McKinley criterion
M_c	Unknown constant relating to critical onset for intstability in cross-slot device
M_{crit}	Critical value of M for onset of instability
M_w	Molecular weight
N	Total number of measurements
$\boldsymbol{n}$	Unit vector normal to the interface
P	Parameter of interest
p	Pressure
p^*	Dimensionless pressure
Δp	Pressure difference

Δp_0	Pressure difference at reference plane (drop shape analyser measurements)
Pe	Peclet number
Q	Volumetric flow rate
Q_i	Volumetric flow rate of particular inlet fluid
Q_{ij}	Volumetric flow rate of fluid in outlet channel of cross-slot device
$\mathfrak{R}$	Characteristic radii of curvature
R	Radius
R_1, R_2	Principal radii of curvature of droplet (drop shape analyser measurements)
R_c	Radius of cone for shear viscosity measurements
Re	Reynolds number
s	Arc length
s_X	Standard deviation
$s_{\overline{X}}$	Random error within the system
S	Magnitude of the rate-of-strain tensor
$\boldsymbol{S}$	Rate-of-strain tensor
S_n	Projection of the traction in the direction of motion tangent to the interface which has a normal, n
S_{xy}	Shear component of the rate-of-strain tensor
t	Time
t_f	Characteristic timescale of the flow

t_b	Critical breakup time for the breaking of the Newtonian filament
T	Torque
T_{MIN}	Minimum measurable torque of the rheometer
U	Average Velocity of fluid
U_f	Average velocity in focused stream of flow focusing device from work of Lee et al. (2006)
U_*	Ratio of average velocity in focused stream of the flow focusing device to the average velocity in the outlet channel from work of Lee et al. (2006)
$\mathbf{u}$	Velocity vector
u^*	Dimensionless velocity vector
U_B	Bulk velocity
U_i	Average inlet velocity of particular fluid phase
$U_i{}^*$	Dimensionless velocity in the y-direction with respect to the bulk velocity U_B of particular fluid phase
$\tilde{U}_b$	Reference scale of velocity field
$\tilde{U}$	Characteristic flow velocity
u_r	Radial velocity component
u_x	x-direction velocity component
$u_{i,x}$	x-direction velocity component of particular fluid stream
u_y	y-direction velocity component
V	Volume
VR	Velocity ratio used in flow focusin device

w	Weight
W	Channel width
W_{2L}, W_{2R}	Width that each of the lateral fluid streams occupy within central channel of flow focusing device at x=0
W_f	Width of central focused stream at the centre plane
W_f^*	Dimensional central focused stream width
$\overline{W}_f$	Average width of the central focused stream along channel depth
$W_{f,z}$	Central focused stream width at a particular z position
Wi	Weissenberg number
Wi_i	Weissenberg number of particular fluid stream
Wi_c	Critical Weissenberg number of first steady asymmetric instability in flow focusing device
Wi_{cr}	Critical Weissenberg number for symmetry breaking instability in cross-slot device
$\overline{X}$	Population mean
X_j	Value of each individual measurement
x, y, z	Cartesian coordinates
x^*, y^*, z^*	Dimensionless cartesian coordinates
$\Delta x, \Delta y, \Delta z$	Mesh spacing in cartesian coordinate system

Greek Letters

α	Scalar phase indicator/ volume fraction
β	Solvent viscosity ratio

β_i	Solvent-to-total viscosity ratio of a particular fluid phase
$\beta_{\overline{X}}$	Singular systematic error estimate
$\beta_{\overline{X}k}$	Systematic error associated with error source
δ_i	δ -function at interface (cross-slot device)
$\boldsymbol{\nabla}$	Nabla operator
$\dot{\gamma}$	Rate of deformation/ shear rate
ε	Extensibility parameter
ε_i	Extensibility parameter of a particular fluid phase
$\dot{\varepsilon}$	Extension rate
$\dot{\varepsilon}_{FF}$	Strain rate for flow focusing device
ε_H	Hencky strain
$\varepsilon_{H_{FF}}$	Hencky strain for flow focusing device
$[\eta]$	Intrinsic viscosity
θ	Cone angle for shear viscosity measurements
κ	Interface curvature in cross-slot device
λ	Relaxation time of viscoelastic fluid
λ_i	Relaxation time of particular viscoelastic fluid phase
μ	Viscosity of fluid
μ_0	Zero-shear rate viscosity of fluid
μ_{MIN}	Lower limit for the measurable shear viscosity
μ_{MAX}	Upper limit for the measurable shear viscosity
μ_p	Viscosity contribution of polymer
μ_s	Viscosity of Newtonian solvent
ρ	Density

ρ_i	Density of particular fluid phase
ρ_d	Drop phase density
σ	Surface tension/ Interfacial tension
$\boldsymbol{\tau}$	Viscoelastic contribution of the stress tensor
τ^*	Dimensionless τ
$\boldsymbol{\tau_i}$	Viscoelastic contribution of the stress tensor of a particular fluid phase
τ_{11}	Normal elastic stress in streamwise direction
τ_{xy}	Shear stress
$\overset{\nabla}{\boldsymbol{\tau}}_{\mathbf{i}}$	Upper-convective derivative of the extra-stress tensor
υ	Solvent quality
φ	Tangent angle between drop axis and the surface of an arbitrary reference plane (drop shape analyser measurements)
ψ	Ratio of inlet pressures
χ	Asymmetry parameter of steady asymmetric instability in flow focusing device
Ω	Angular velocity

Subscripts	
i	Represents particular fluid stream (1 or 2)
j	Represents particular outlet channel in cross-slot device (1 or 2)

Superscripts	
T	Transpose

CHAPTER 1

Introduction

This thesis starts with an introductory chapter which will set the context for this work introducing each of the main aspects involved in this work in turn. This chapter is not a literature review but instead gives an overview of the research field, the motivations of this work and the overall outline of the thesis.

The focus of this thesis is to investigate extensionally dominated flows within microfluidic devices where single or multiple fluid systems are involved. Characterising the flow within these devices when a combination of Newtonian and non-Newtonian fluids with viscoelastic properties are used, provides new insight into the development of flow induced elastic instabilities that arise in these multiple fluid systems.

1.1 MICROFLUIDICS OVERVIEW & CHALLENGES

Over the past few decades microfluidics has been an area that has captivated researchers worldwide encouraging engineers to work closely with a range of other disciplines including Biology to study cell culture (Shah et al. 2011, Jaccard et al. 2014, van Duinen et al. 2015, Coluccio et al. 2019, Ortseifen et al. 2020), Cosmetics (Lee et al. 2001, Park et al. 2021) and Food (Muschiolik 2007, Comunian et al. 2014) for emulsions and formulations, and Medicine in relation to drug delivery (Damiati et al. 2018, Hassan and Zhang 2019) and personalised diagnosis (Weigl et al. 2008, Rivet et al. 2011). Microfluidics studies fluid transportation, mixing, separation, manipulation and control at small length scales, typically in the range of tens or hundreds of microns (Stone and Kim 2001, Whitesides 2006). These small length scales and the unique characteristics of these microdevices offer a novel approach with a variety of benefits and challenges over typical conventional methods. The small dimensions are very attractive to researchers allowing complex flow patterns to be studied in a defined and controllable manner while reducing the required sample volume, sample waste, experimental time and thus leading to overall cost reductions (Whitesides 2006, Hassan and Zhang 2019). Traditionally, microfluidic devices were fabricated using silicon or glass however, more recently elastomeric materials such as polydimethylsiloxane (PDMS) have become very popular due to their significantly simpler and less expensive fabrication procedures. These devices are adaptable for specific purposes, portable and have low power requirements (Stone and Kim 2001).

Additionally, due to the high surface-to-volume ratios typical of microfluidics, surface forces effects are enhanced relative to their macroscale counterparts and are therefore important to consider (Stone and Kim 2001, Oliveira et al. 2012, Ortseifen et

al. 2020). High surface-to-volume ratios can be advantageous for particular applications (Pennathur et al. 2008), where untraditional surface forces have more influence in comparison to volume forces (i.e., inertia and body forces (gravity)) (Pennathur et al. 2008, Oliveira et al. 2012).

Research as well as applications using microfluidics often involve multiple fluids (Whitesides 2006), which can be either miscible or immiscible depending on the application. Previous researchers have used microfluidics to generate monodisperse bubbles and droplets of a dispersed phase in a continuous fluid stream to find innovative ways of creating foams or emulsions (Garstecki et al. 2005, Garstecki et al. 2006, Christopher and Anna 2007, Nie et al. 2008, Seemann et al. 2012); to promote chemical reactions (Jensen 2001, deMello 2006); and for Lab on a Chip diagnostic applications where additional fluid streams can be used to dilute samples or to probe a reaction for detection purposes (Weigl et al. 2008, Rivet et al. 2011).

Many microfluidic applications require fluid mixing, which can be difficult to achieve at small length scales (Stone and Kim 2001, Green et al. 2007). At the macroscale, fluid mixing can be achieved efficiently by convection, like mixing milk into a warm tea or coffee, or by fluid turbulence (Knight et al. 1998, Whitesides 2006). These mixing processes are strongly dominated by inertia.
An important dimensionless number in this context is the Reynolds Number which defines the ratio of inertial to viscous stresses in a fluid system and is commonly used to determine the flow regime, namely laminar or turbulent flow:

$$Re = \frac{\rho U \tilde{L}}{\mu} \qquad (1.1)$$

where ρ (kg/m^3) and μ (Pa s) are the density and viscosity of the fluid respectively, $\tilde{L}$ (m) is a characteristic length scale of the geometry used and U (m/s) is the average flow velocity. Typically, at the macroscale, in order to maintain a laminar flow, a highly viscous fluid or a low velocity flow needs to be used. Reducing the characteristic length scale to the microscale (e.g., from 1m to 100μm) would result in a decrease of the

Reynolds number by around four orders of magnitude, typically leading to laminar flows in which viscous stresses dominate over inertial stresses (Green et al. 2007).

At the microscale, flows of Newtonian fluids, even those with low viscosities like water tend to remain laminar, meaning that for example, two streams of different fluids tend to flow together side-by-side in microfluidic devices (as exemplified in the 'iconic' cover page of SCIENCE as shown in Figure 1.1 (1999)). Depending on the desired application, these laminar flows using low viscosity fluids can be considered an advantage e.g., for separation purposes (Kersaudy-Kerhoas et al. 2009, Sajeesh and Sen 2014) or a challenge, for example when mixing is required (Oliveira et al. 2012, Ward and Fan 2015). Mixing in these cases is dominated by diffusion and occurs as a result of the molecular interactions at the interface between the two fluids. Even at these small length scales, diffusion usually involves prohibitively long timescales. For practical applications, additional measures using active or passive methods are usually adopted if mixing is required (Green et al. 2007, Ward and Fan 2015).

Active methods rely on the use of external power sources such as pumps or actuators for forcing the fluid to behave in a particular desired manner (Nguyen 2012). Passive mixing methods are advantageous in terms of simplicity and operational flexibility, and arise as a result of natural flow behaviour of the fluids or due to geometrical configurations (deMello 2006, Green et al. 2007). These methods do not require the use of external expensive equipment and therefore maintain the advantage of portability and low power requirements that microfluidic devices possess.

For applications with non-Newtonian viscoelastic fluids, the small length scales characteristic of microfluidics, generate flows in which high deformation and high shear rates can be achieved, enhancing elastic effects while, at the same time, keeping inertia low (Rodd et al. 2005, Oliveira et al. 2007, Sousa et al. 2015). This characteristic makes these devices very attractive for investigating elastic driven phenomena which are the focus of this thesis.

Due to these enhanced elastic effects when working with non-Newtonian viscoelastic fluids, there is a chance of developing elastic instabilities which people have

associated with the development of elastic turbulence (Groisman and Steinberg 2000). Using this elastic turbulence for mixing purposes is currently a topic of debate and of high interest to this research field (Steinberg 2021). In the next section some of these elastic instabilities and their underlying mechanisms will be discussed, in particular those that arise when using microfluidics, as this is the platform chosen for this work.

Figure 1.1: Cover page of Issue 5424 of SCIENCE exemplifying different fluids (represented by the various coloured streams) flowing side-by-side in a system (1999).

1.2 VISCOELASTIC FLOW INSTABILITIES IN MICROFLUIDICS

When a small amount of high molecular weight polymer is added to a Newtonian aqueous solution, creating a viscoelastic solution, the non-linear viscoelastic behaviour breaks down the flow reversibility of low Reynolds number flows. As a consequence, viscoelastic fluid flows have been shown to exhibit a cascade of flow transitions, eventually leading to turbulent-like flow (Shaqfeh 1996). Different transitions have been identified: including one in which the flow becomes asymmetric but remains steady; and others which involve the onset of time-dependent flow (Arratia et al. 2006, Oliveira et al. 2009). These flow instabilities escalate to random fluctuations in the flow system with some similarities to those of inertial turbulence, although they are clearly distinct phenomena (Groisman and Steinberg 2000, Qin and Arratia 2017, Varchanis et al. 2020). This remarkably complex flow behaviour has been termed “elastic turbulence” by Groisman and Steinberg in the year 2000 and arises from the interaction between the polymer’s molecular structure and the flow (Groisman and Steinberg 2000). These instabilities and "turbulent-like" characteristics can be desirable e.g., to promote mixing enhancement under adverse conditions, like in the case of very viscous systems or flows at small scales, as turbulent flows are known to mix things much more efficiently (Groisman and Steinberg 2001, Lam et al. 2009, Oliveira et al. 2009, Sousa et al. 2009, Galindo-Rosales et al. 2014) or, can be a hinderance, e.g., in rheometric devices where viscometric flows are required (Guillot et al. 2006, Haward et al. 2012, Ober et al. 2013, Zografos et al. 2019).

A number of researchers have studied the onset of these elastic instabilities, however, these have mainly focussed on flows involving a single fluid. Following initial investigations of instabilities in (shear-dominated) viscometric flows, such as Taylor-Couette and the cone-and-plate (Shaqfeh 1996), microfluidic devices have arguably become the preferred platform for studying elastic instabilities and elastic turbulence in shear-dominated (e.g., in serpentine channels, (Zilz et al. 2012, Galindo-Rosales et al. 2014, Casanellas et al. 2016)), extension dominated (e.g., in cross-slots and flow focusing devices, (Arratia et al. 2006, Oliveira et al. 2009)) and under conditions of mixed kinematics (e.g., contraction flows, (Sousa et al. 2009) or flows past a cylinder,

(Davoodi et al. 2019, Haward et al. 2020, Varchanis et al. 2020)). It has been shown that small length-scales, in which surface effects are enhanced, accentuate the role of elasticity to levels that allow elastic-driven instabilities and turbulence to develop and be studied in the absence of inertial effects, which is in stark contrast with the high Reynolds number conditions required for classical hydrodynamic turbulence. However, studies of elastic flow instabilities and turbulence in microfluidic systems involving multiple fluids are less common (Datta et al. 2022). There has already been some interest shown in this area especially in research involving e.g., emulsions (Poole et al. 2012) and oil ganglia displacement for enhanced oil recovery applications (Clarke et al. 2015, Browne et al. 2020, Kumar et al. 2021), however, the understanding at the fundamental level is still limited. Studying these simple single and multiple-fluid flows using microfluidic devices will help us further understand these complex flows, adding to the research field by exploring ways to control flow induced elastic instabilities (Datta et al. 2022).

1.3 THESIS AIM AND OBJECTIVES

The main purpose of this work is to gain fundamental new knowledge and provide new insight on elastic instabilities within more complex flows where multiple fluids are involved, with a view of ultimately controlling these instabilities (enhancing or preventing/delaying them, depending on the application). In particular, this work focuses on extension dominated microfluidic flows involving Newtonian and/or viscoelastic (polymeric) fluids, and investigates the effects of geometrical and operational parameters as well as fluid properties on flow behaviour and specifically on the onset of elastic instabilities. The work carried out by the author in this context is mostly experimental, complemented by numerical and analytical methodologies. Two different microfluidic configurations were used in this work: cross-slot and flow focusing microfluidic devices.

The microfluidic cross slot consists of bisecting channels with opposing inlets and outlets (cf. Figure 1.2). This set-up produces flows with a free stagnation point at the centre of the geometry resulting in an elongational flow in this region. At the stagnation

point, a fluid element can be “trapped” for an indefinite time thus experiencing significant strain.

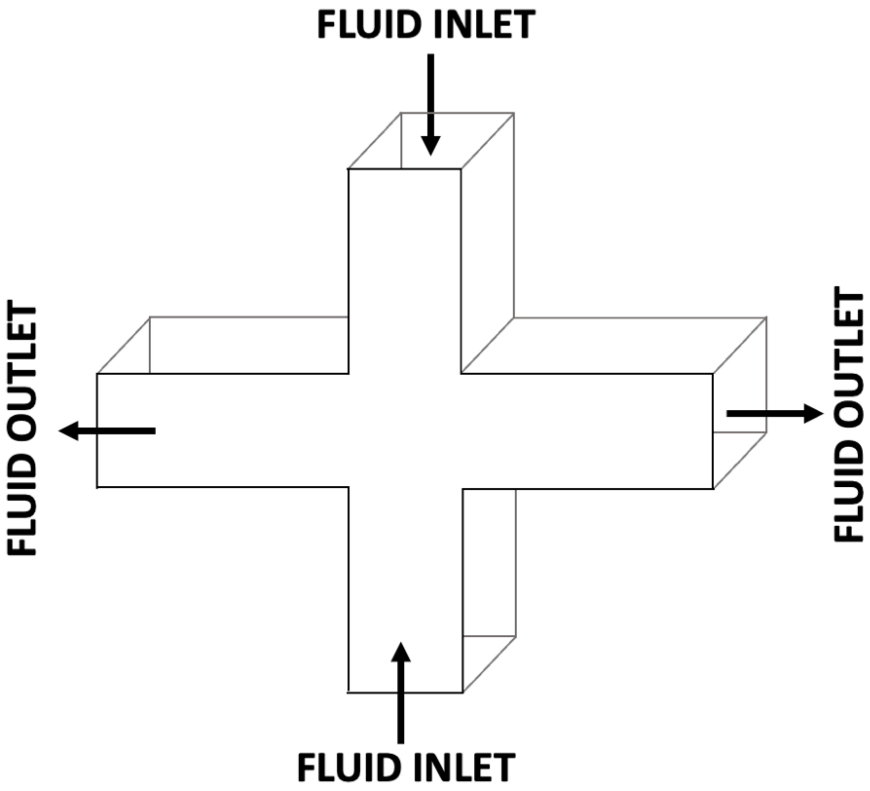

Figure 1.2: Simple schematic of microfluidic cross-slot device showing fluid inlets and outlets.

In this configuration, flows of Newtonian and viscoelastic fluids are analysed experimentally, analytically and using numerical simulations with the aim to better understand the effects of various parameters on the interface that exists when two different fluids are used, and on the onset of elastic instabilities. This part of the work focuses on the study of the effects of the ratio between the viscosity of the two inlet fluids (referred to as the ‘viscosity ratio’ throughout this work), the effects of Capillary number (i.e., the ratio of viscous to interfacial forces) as well as the effect of geometrical parameters on the flow behaviour when multiple fluids are present. In particular, the thesis focuses on the impact of these parameters on the position and shape of the interface between the two fluids and on the onset conditions for purely elastic instabilities that arise within this geometry.

The flow focusing device operates with three fluid inlets and one fluid outlet as shown in Figure 1.3: two opposing lateral side streams that shape a third central inlet stream producing a focused stream along the centre of the outlet channel. This configuration creates a stagnation-point-free extensional flow near the centre of the geometry.

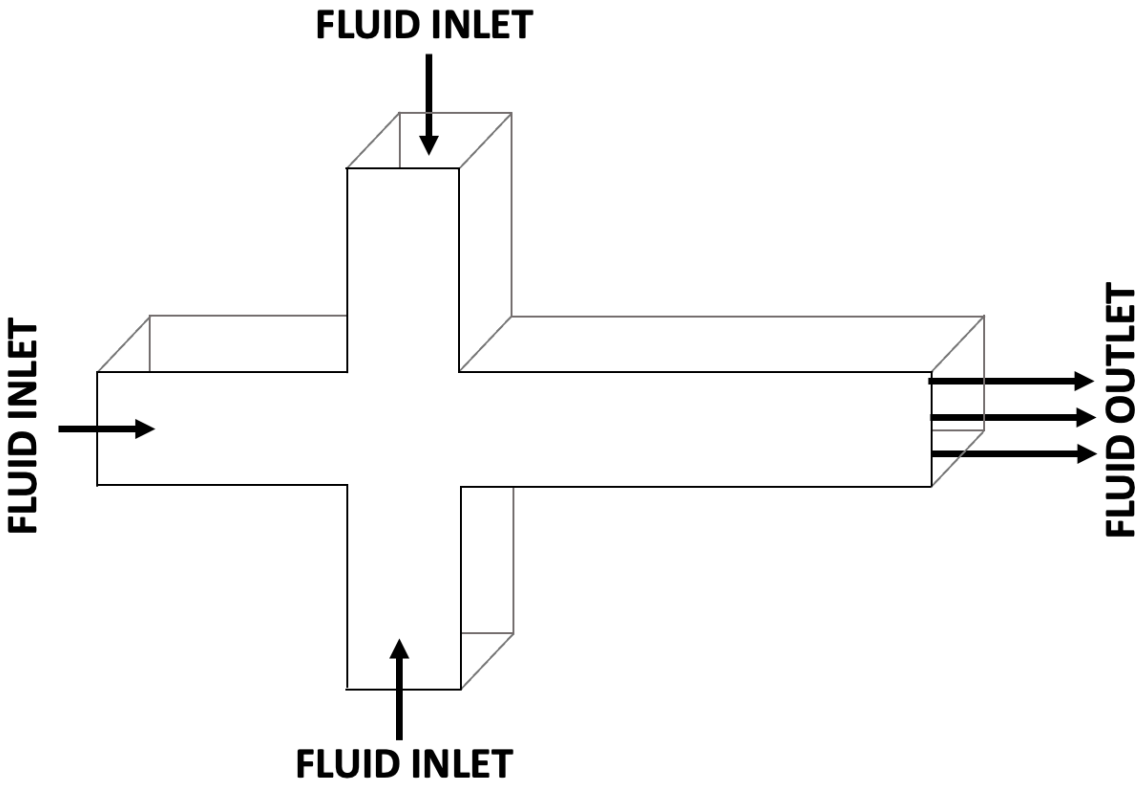

Figure 1.3: Simple schematic of microfluidic flow focusing device showing fluid inlets and outlet.

This part of the work focuses on the flow behaviour when geometric parameters are altered or when multiple fluids (where property jumps exist across the interface between the fluid streams) are involved. Past research has suggested that the elastic instabilities that arise within this flow configuration are due to the strong extensional flows that occur at the centre of the geometry (Oliveira et al. 2009, Ballesta and Alves 2017). This work experimentally investigates the onset conditions of the purely elastic instabilities that arise in this geometry, to provide further insight to the underlying mechanisms.

Before using complex fluids in this geometry, Newtonian fluids give a baseline understanding of the fundamentals involved in these flows. The effects of various parameters on the characteristics (i.e., the shape and size) of the produced central focused stream in the outlet channel was investigated. The parameters of interest are those which have a large impact on the development of this outlet stream, in particular an intermediate range of viscosity ratios (defined in this geometry as the ratio between the viscosity of the fluid in the lateral streams to the viscosity of the fluid in the central inlet stream) is used, while simultaneously considering the effect of the ratio of inlet velocities and microchannel aspect ratio (defined as the ratio between the height and width of the microchannel). This work also provides further insight into the curved interface along the depth of the cross-section that has been observed in previous research when high viscosity contrasts are present in parallel flow systems (Knight et al. 1998, Cubaud and Mason 2008, Cubaud et al. 2012, Cubaud and Mason 2012). This fundamental understanding aids progression onto investigations where complex viscoelastic fluids are used.

1.4 THESIS OUTLINE

This thesis is organised by chapters and the results and discussion are structured into two parts according to the microfluidic geometry under investigation, namely the cross-slot (Chapter 4) and the flow focusing device (Chapters 5 and 6). Each results chapter (Chapters 4 - 6) begins with a literature review and key findings of previous studies that are related to the work. It is important to note that in this thesis when a system is referred to as “multi-phase”, although this is not strictly accurate it refers broadly to any system that involves multiple fluids (including those with miscible and immiscible fluids).

The present work has so far led to two publications in international journals, presented in Chapter 4 (Davoodi et al. 2021) and Chapter 5 (Houston et al. 2023). In addition, various parts of this research have been presented at different conferences both UK and International in the form of 3 oral presentations and 3 poster presentations.Following this introductory chapter that gives a brief background and motivation to this research, the remaining chapters are organised as follows:

Chapter 2 presents a literature review, providing a brief overview of isothermal, incompressible flows of both Newtonian and non-Newtonian fluids along with a discussion on important parameters used to characterise these flows. This chapter then moves on to discuss various types of instabilities that can arise in these flow systems, with a particular focus on purely elastic instabilities. A general overview of the geometrical configurations in which these purely elastic instabilities have been observed in past research is given alongside a discussion on the important features associated with these instabilities.

Chapter 3 details the various experimental procedures involved within this project from the fabrication of the microfluidic devices to the methods involved in the preparation and characterisation of the working fluids. The chapter will then proceed to present the experimental flow visualisation techniques and laboratory set-up used for flow characterisation. Fluid compositions and characterisation results along with other experimental particularities for each set of experiments will be detailed in the relevant results' chapters.

Chapter 4 focuses on the stabilisation of purely elastic instabilities in cross-slot geometries. It makes use of multiple fluids to study the effects of the ratio between the viscosity of the two inlet fluids (referred to throughout this work as the 'viscosity ratio') and the effects of Capillary number (i.e., the ratio of viscous to interfacial forces) on the position and shape of the interface between two fluids in the microfluidic cross-slot device. In this work, experimental results are compared with analytical solutions and numerical simulations. Further numerical simulations investigate the impact of the viscosity ratio, interfacial tension and elasticity jumps on the flow induced elastic instabilities within this flow configuration. This research was conducted in collaboration with colleagues at the University of Liverpool and has been published in the *Journal of Fluid Mechanics* under the title "Stabilization of purely elastic instabilities in cross-slot geometries" (Davoodi et al. 2021).

Chapter 5 focuses on flows of miscible Newtonian fluids through microfluidic flow focusing geometries and will act as a baseline to understand the fundamentals involved in flows within this geometry before progressing onto investigations using

complex viscoelastic fluids. The combined effect of the ratio between the viscosities and velocities of the lateral and central inlet streams on the characteristics (i.e., shape and size) of the central focused outlet stream is studied. This work involves experiments and supporting 3D numerical simulations. An analytical expression for the two-dimensional case, relating the width of the central focused stream in the outlet channel with the velocity ratio and the viscosity ratio, is also derived from first principles. This chapter will also analyse the interfacial curvature along the depth of the cross-section of the microchannel that is known to be present for high viscosity contrasts. This work was conducted in collaboration with colleagues at the University of Strathclyde and has been published in *Physics of Fluids* under the title “Flow focusing with miscible fluids in microfluidic devices” (Houston et al. 2023)

Chapter 6 focuses on elastic instabilities that arise when using viscoelastic solutions, in both single and multiple fluid flow systems, within a microfluidic flow focusing device. Using single-phase flows, this chapter studies how the onset of these instabilities can be affected by geometrical and other operational parameters. More interestingly, this chapter also studies the effects of introducing a Newtonian fluid alongside a non-Newtonian fluid with viscoelastic properties, investigating how elasticity jumps and regions of extensional flow influence the onset conditions, and the development of the flow induced elastic instabilities that arise in this geometry.

Chapter 7 summarises the main findings reported in this thesis and provides suggestions for associated future work.

1.5 REFERENCES

(1999). SCIENCE 285(5424).

Arratia, P. E., Thomas, C. C., Diorio, J. D. and Gollub, J. P. (2006). "Elastic Instabilities of Polymer Solutions in Extensional Flows ".

Browne, C. A., Shih, A. and Datta, S. S. (2020). "Pore-Scale Flow Characterization of Polymer Solutions in Microfluidic Porous Media." Small 16(9): e1903944.

Casanellas, L., Alves, M. A., Poole, R. J., Lerouge, S. and Lindner, A. (2016). "The stabilizing effect of shear thinning on the onset of purely elastic instabilities in serpentine microflows." Soft Matter 12(29): 6167-6175.

Christopher, G. F. and Anna, S. L. (2007). "Microfluidic methods for generating continuous droplet streams." Journal of Physics D: Applied Physics 40(19): R319-R336.

Clarke, A., Howe, A. M., Mitchell, J., Staniland, J., Hawkes, L. and Leeper, K. (2015). "Mechanism of anomalously increased oil displacement with aqueous viscoelastic polymer solutions." Soft Matter 11(18): 3536-3541.

Coluccio, M. L., Perozziello, G., Malara, N., Parrotta, E., Zhang, P., Gentile, F., Limongi, T., Raj, P. M., Cuda, G., Candeloro, P. and Di Fabrizio, E. (2019). "Microfluidic platforms for cell cultures and investigations." Microelectronic Engineering 208: 14-28.

Comunian, T. A., Abbaspourrad, A., Favaro-Trindade, C. S. and Weitz, D. A. (2014). "Fabrication of solid lipid microcapsules containing ascorbic acid using a microfluidic technique." Food Chem 152: 271-275.

Cubaud, T., Jose, B. M., Darvishi, S. and Sun, R. (2012). "Droplet breakup and viscosity-stratified flows in microchannels." International Journal of Multiphase Flow 39: 29-36.

Cubaud, T. and Mason, T. G. (2008). "Formation of miscible fluid microstructures by hydrodynamic focusing in plane geometries." Phys Rev E Stat Nonlin Soft Matter Phys 78(5): 056308.

Cubaud, T. and Mason, T. G. (2012). "Interacting viscous instabilities in microfluidic systems." Soft Matter 8(41): 10573–10582.

Damiati, S., Kompella, U. B., Damiati, S. A. and Kodzius, R. (2018). "Microfluidic Devices for Drug Delivery Systems and Drug Screening." Genes (Basel) 9(2): 103.

Datta, S. S., Ardekani, A. M., Arratia, P. E., Beris, A. N., Bischofberger, I., McKinley, G. H., Eggers, J. G., López-Aguilar, J. E., Fielding, S. M., Frishman, A., Graham, M. D., Guasto, J. S., Haward, S. J., Shen, A. Q., Hormozi, S., Morozov, A., Poole, R. J., Shankar, V., Shaqfeh, E. S. G., Stark, H., Steinberg, V., Subramanian, G. and Stone, H. A. (2022). "Perspectives on viscoelastic flow instabilities and elastic turbulence." Physics of Fluids 7(8): Online.

Davoodi, M., Domingues, A. F. and Poole, R. J. (2019). "Control of a purely elastic symmetry-breaking flow instability in cross-slot geometries." Journal of Fluid Mechanics 881: 1123-1157.

Davoodi, M., Houston, G., Downie, J., Oliveira, M. S. N. and Poole, R. J. (2021). "Stabilization of purely elastic instabilities in cross-slot geometries." Journal of Fluid Mechanics 922: A12.

deMello, A. J. (2006). "Control and detection of chemical reactions in microlfuidic systems." Nature 442: 394-402.

Galindo-Rosales, F. J., Campo-Deaño, L., Sousa, P. C., Ribeiro, V. M., Oliveira, M. S. N., Alves, M. A. and Pinho, F. T. (2014). "Viscoelastic instabilities in micro-scale flows." Experimental Thermal and Fluid Science 59: 128-139.

Garstecki, P., Fuerstman, M. J., Stone, H. A. and Whitesides, G. M. (2006). "Formation of droplets and bubbles in a microfluidic T-junction-scaling and mechanism of break-up." Lab Chip 6(3): 437-446.

Garstecki, P., Ganan-Calvo, A. M. and Whitesides, G. M. (2005). "Formation of bubbles and droplets in microfluidic systems." Bulletin of the Polish Academy of Sciences Technical Sciences 53(4).

Green, J., Holdø, A. E. and Khan, A. (2007). "A review of passive and active mixing systems in microfluidic devices." The International Journal of Multiphysics 1(1): 1-32.

Groisman, A. and Steinberg, V. (2000). "Elastic turbulence in a polymer solution flow." Nature 405: 53-55.

Groisman, A. and Steinberg, V. (2001). "Effcient mixing at low Reynolds numbers using polymer additives." Nature 410: 905-908.

Guillot, P., Panizza, P., Salmon, J.-B., Joanicot, M. and Colin, A. (2006). "Viscosimeter on a Microfluidic Chip." Langmuir 22: 6438-6445.

Hassan, S. and Zhang, Y. S. (2019). Microfluidic technologies for local drug delivery. Microfluidics for Pharmaceutical Applications: 281-305.

Haward, S. J., Hopkins, C. C. and Shen, A. Q. (2020). "Asymmetric flow of polymer solutions around microfluidic cylinders: Interaction between shear-thinning and viscoelasticity." Journal of Non-Newtonian Fluid Mechanics 278: 104250.

Haward, S. J., Oliveira, M. S., Alves, M. A. and McKinley, G. H. (2012). "Optimized cross-slot flow geometry for microfluidic extensional rheometry." Phys Rev Lett 109(12): 128301.

Houston, G., Capobianchi, P. and Oliveira, M. S. N. (2023). "Flow focusing with miscible fluids in microfluidic devices." Physics of Fluids 1 35 (5): 052015.

Jaccard, N., Macown, R. J., Super, A., Griffin, L. D., Veraitch, F. S. and Szita, N. (2014). "Automated and online characterization of adherent cell culture growth in a microfabricated bioreactor." J Lab Autom 19(5): 437-443.

Jensen, K. F. (2001). "Microreaction engineering - is small better?" Chemical Engineering Science 56: 293-303.

Kersaudy-Kerhoas, M., Dhariwal, R., Desmulliez, M. P. Y. and Jouvet, L. (2009). "Hydrodynamic blood plasma separation in microfluidic channels." Microfluidics and Nanofluidics 8(1): 105-114.

Knight, J. B., Vishwanath, A., Brody, J. P. and Austin, R. H. (1998). "Hydrodynamic Focusing on a Silicon Chip: Mixing Nanoliters in Microseconds." Physical Review Letters 80(17): 3863-3866.

Kumar, M., Aramideh, S., Browne, C. A., Datta, S. S. and Ardekani, A. M. (2021). "Numerical investigation of multistability in the unstable flow of a polymer solution through porous media." Physical Review Fluids 6(3): 033304.

Lam, Y. C., Gan, H. Y., Nguyen, N. T. and Lie, H. (2009). "Micromixer based on viscoelastic flow instability at low Reynolds number." Biomicrofluidics 3(1): 14106.

Lee, M. H., Oh, S. G., Moon, S. K. and Bae, S. Y. (2001). "Preparation of Silica Particles Encapsulating Retinol Using O/W/O Multiple Emulsions." J Colloid Interface Sci 240(1): 83-89.

Muschiolik, G. (2007). "Multiple emulsions for food use." Current Opinion in Colloid & Interface Science 12(4-5): 213-220.

Nguyen, N.-T. (2012). Chapter 7 - Active micromixers. Micromixers: Fundamentals, Design and Fabrication, William Andrew Publishing: 239-294.

Nie, Z., Seo, M., Xu, S., Lewis, P. C., Mok, M., Kumacheva, E., Whitesides, G. M., Garstecki, P. and Stone, H. A. (2008). "Emulsification in a microfluidic flow-focusing device: effect of the viscosities of the liquids." Microfluidics and Nanofluidics 5(5): 585-594.

Ober, T. J., Haward, S. J., Pipe, C. J., Soulages, J. and McKinley, G. H. (2013). "Microfluidic Extensional Rheometry using a Hyperbolic Contraction Geometry." Rheologica Acta 52: 529–546.

Oliveira, M. S. N., Alves, M. A. and Pinho, F. T. (2012). Microfluidic Flows of Viscoelastic Fluids. Transport and Mixing in Laminar Flows: From Microfluidics to Oceanic Currents. R. Grigoriev, Wiley-VCH Verlag GmbH & Co. KGaA.: 131 - 174.

Oliveira, M. S. N., Alves, M. A., Pinho, F. T. and McKinley, G. H. (2007). "Viscous flow through microfabricated hyperbolic contractions." Experiments in Fluids 43(2-3): 437-451.

Oliveira, M. S. N., Pinho, F. T., Poole, R. J., Oliveira, P. J. and Alves, M. A. (2009). "Purely elastic flow asymmetries in flow-focusing devices." Journal of Non-Newtonian Fluid Mechanics 160(1): 31-39.

Ortseifen, V., Viefhues, M., Wobbe, L. and Grunberger, A. (2020). "Microfluidics for Biotechnology: Bridging Gaps to Foster Microfluidic Applications." Front Bioeng Biotechnol 8: 589074.

Park, D., Kim, H. and Kim, J. W. (2021). "Microfluidic production of monodisperse emulsions for cosmetics." Biomicrofluidics 15(5): 051302.

Pennathur, S., Meinhart, C. D. and Soh, H. T. (2008). "How to exploit the features of microfluidics technology." Lab Chip 8(1): 20-22.

Poole, R. J., Budhiraja, B., Cain, A. R. and Scott, P. A. (2012). "Emulsification using elastic turbulence." Journal of Non-Newtonian Fluid Mechanics 177-178: 15-18.

Qin, B. and Arratia, P. E. (2017). "Characterizing elastic turbulence in channel flows at low Reynolds number." Physical Review Fluids 2(8) : 083302.
Rivet, C., Lee, H., Hirsch, A., Hamilton, S. and Lu, H. (2011). "Microfluidics for medical diagnostics and biosensors." Chemical Engineering Science 66: 1490-1507.

Rodd, L. E., Scott, T. P., Boger, D. V., Cooper-White, J. J. and McKinley, G. H. (2005). "The inertio-elastic planar entry flow of low-viscosity elastic fluids in micro-fabricated geometries." Journal of Non-Newtonian Fluid Mechanics 129(1): 1-22.

Sajeesh, P. and Sen, A. K. (2014). "Particle separation and sorting in microfluidic devices: a review." Microfluidics and Nanofluidics 17(1): 1-52.

Seemann, R., Brinkmann, M., Pfohl, T. and Herminghaus, S. (2012). "Droplet based microfluidics." Rep Prog Phys 75(1): 016601.

Shah, P., Vedarethinam, I., Kwasny, D., Andresen, L., Dimaki, M., Skov, S. and Svendsen, W. E. (2011). "Microfluidic bioreactors for culture of non-adherent cells." Sensors and Actuators B: Chemical 156(2): 1002-1008.

Shaqfeh, E. S. G. (1996). "Purely elastic instabilities in viscometric flows." Annual Reviews Fluid Mechanics 160: 122-139.

Sousa, P. C., Coelho, P. M., Oliveira, M. S. N. and Alves, M. A. (2009). "Three-dimensional flow of Newtonian and Boger fluids in square–square contractions." Journal of Non-Newtonian Fluid Mechanics 160(2-3): 122-139.

Sousa, P. C., Pinho, F. T., Oliveira, M. S. and Alves, M. A. (2015). "Purely elastic flow instabilities in microscale cross-slot devices." Soft Matter 11(45): 8856-8862.

Steinberg, V. (2021). "Elastic Turbulence: An Experimental View on Inertialess Random Flow." Annual Review of Fluid Mechanics 53(1): 27-58.

Stone, H. A. and Kim, S. (2001). "Microfluidics: Basic Issues, Applications, and Challenges." AIChE Journal 47(6): 1250 - 1254.

van Duinen, V., Trietsch, S. J., Joore, J., Vulto, P. and Hankemeier, T. (2015). "Microfluidic 3D cell culture: from tools to tissue models." Curr Opin Biotechnol 35: 118-126.

Varchanis, S., Hopkins, C. C., Shen, A. G., Tsamopoulos, J. and Haward, S. J. (2020). "Asymmetric flows of complex fluids past confined cylinders: A comprehensive numerical study with experimental validation." Phys Fluids (1994) 32(5): 053103.

Ward, K. and Fan, Z. H. (2015). "Mixing in microfluidic devices and enhancement methods." J Micromech Microeng 25(9): 94001-17.

Weigl, B., Domingo, G., LaBarre, P. and Gerlach, J. (2008). "Towards non- and minimally instrumented, microfluidics-based diagnostic devices." The Royal Society of Chemistry 8: 1999-2014.

Whitesides, G. M. (2006). "The origins and the future of microfluidics." Nature 442(no. 7101): 368-373.

Zilz, J., Poole, R. J., Alves, M. A., Bartolo, D., Levaché, B. and Lindner, A. (2012). "Geometric scaling of a purely elastic flow instability in serpentine channels." Journal of Fluid Mechanics 712: 203-218.

Zografos, K., Haward, S. J. and Oliveira, M. S. N. (2019). "Optimised multi-stream microfluidic designs for controlled extensional deformation." Microfluidics and Nanofluidics 23(12): 1-21.

CHAPTER 2

Literature Review

Fluids are everywhere in the world around us, in all parts of our everyday lives, from the blood running through our veins to the water we drink and the air we breathe. The research area of interest to this thesis, fluid mechanics, considers both fluids at rest (fluid statics) and fluids in motion (fluid dynamics) and has been of interest to researchers for a number of years and continues to be a challenge to this day. In particular, the main research interest here lies in complex fluid systems both single-phase or those involving multiple fluid streams.

In this thesis we are concerned with isothermal, incompressible flows of both Newtonian and non-Newtonian fluids. This chapter will provide a general insight into these flows and a number of important parameters that accompany them. We will then progress to introduce various types of flow instabilities that can arise within each of these flows including the complex purely elastic instabilities known to occur when non-Newtonian viscoelastic fluids are used.

2.1 DIMENSIONLESS PARAMETER SPACE

These fluid flow problems are generally characterised in a non-dimensional way, often referred to as dimensional analysis (Bridgman 1963). The work of McKinley (2005) provides a visual representation of the three-dimensional space of dimensionless numbers to characterise the fluid flows relevant to this work (shown in Figure 2.1).

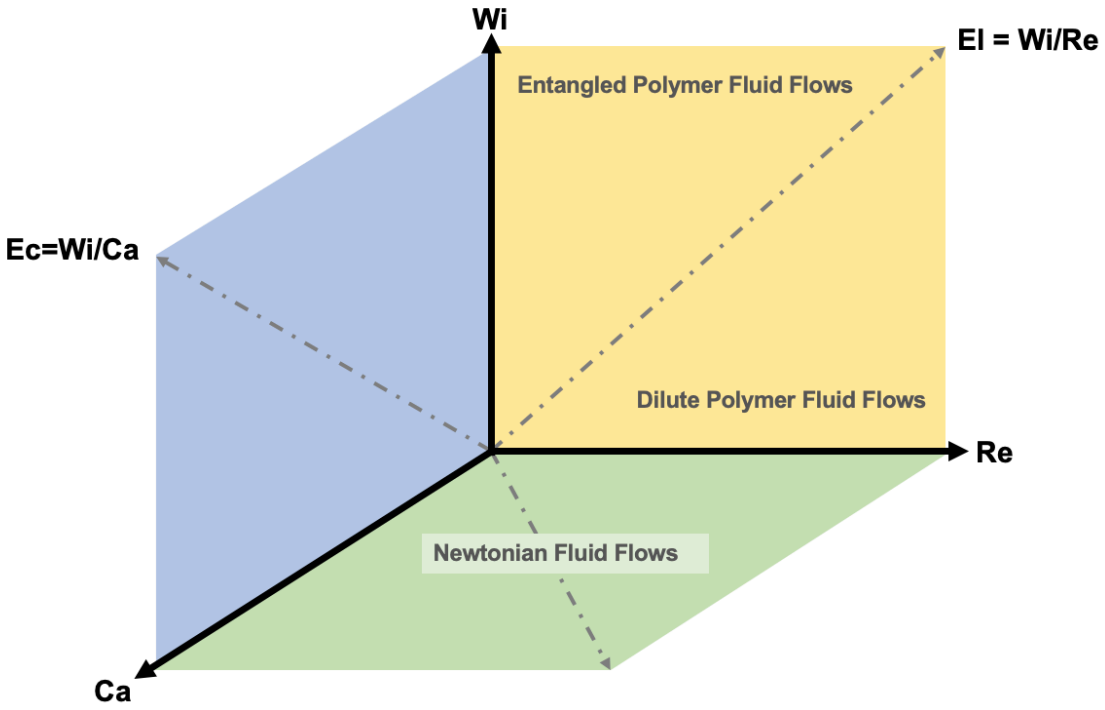

Figure 2.1: Schematic of the three-dimensional parameter space adapted from the work of McKinley (2005) to characterise fluid flows, highlighting important dimensionless numbers.

The content of this thesis will cover flows of Newtonian Fluids (both miscible and immiscible) and those of viscoelastic polymeric solutions. The three main axes in Figure 2.1 represent the Reynolds number (Re, the ratio of inertial to viscous stresses, cf. Section 2.1.1), the Capillary number (Ca, the ratio of the viscous stresses to surface tension forces, cf. Section 2.1.4) and the Weissenberg number (Wi, the ratio of elastic to viscous stresses, cf. Section 2.1.2). The relevant region of the parameter space depends on the fluid flow system under consideration. For example, multiphase flows of Newtonian fluids are characterised in the Reynolds number and Capillary number

parameter space (the region highlighted in green in Figure 2.1), while single-phase complex fluid flows are characterised in the Reynolds number-Weissenberg number parameter space (the region highlighted in yellow in Figure 2.1). The ratio between these parameters is defined as the ratio between the elastic and inertial forces and is known as the Elasticity number:

$$El = \frac{Wi}{Re} = \frac{\lambda \mu}{\rho \tilde{L}^2} \qquad (2.1)$$

where λ (s) represents the relaxation time of a viscoelastic fluid, μ (Pa s), the viscosity of the fluid, ρ (kg/m^3), the fluid density and $\tilde{L}$ (m), a characteristic length scale.

2.1.1 The Reynolds Number

The Reynolds Number is one of the most commonly used dimensionless numbers in fluid mechanics and is used to determine the flow regime of the system. This number is named after Osborne Reynolds (1883) who carried out a well-known experimental investigation characterising the flow transition, from the laminar to the turbulent regime, of water in a straight pipe. To visualise the flow patterns a dye was injected to the central stream of water flowing through the pipe. Experimental observations demonstrated two clear stages and a singular flow transition for increasing flow velocities as shown in Figure 2.2.

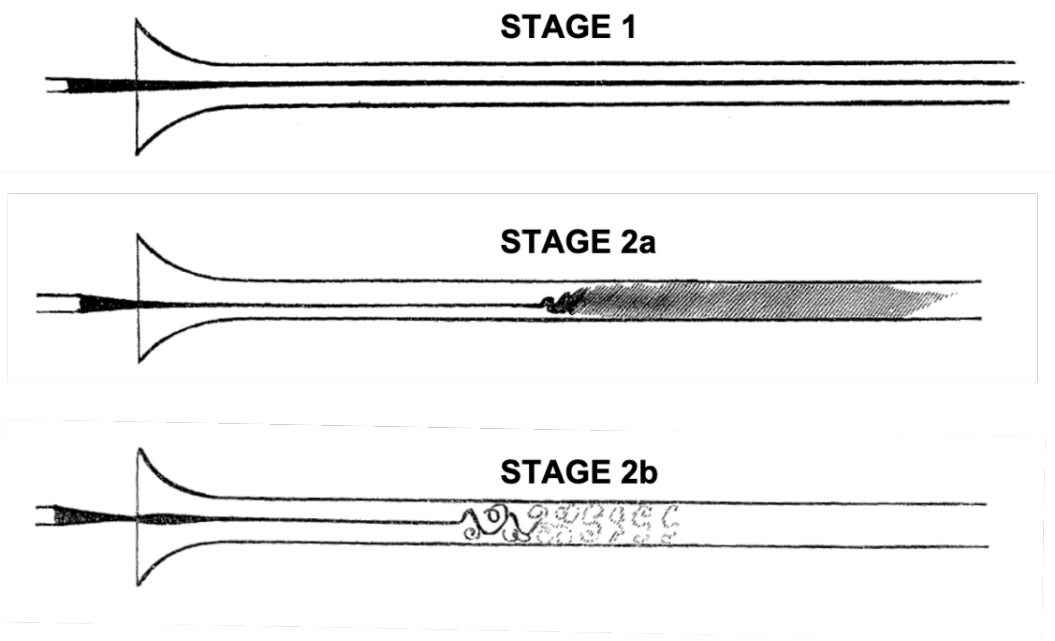

Figure 2.2: Sketches from Osborne Reynolds' experimental investigation (1883) showing laminar and unsteady flow regimes as the fluid velocity (and thus the Reynolds number) is increased. Stage 1: Laminar regime, Stage 2a: Turbulent regime, Stage 2b: Turbulent Regime with "eddies" (Reynolds 1883).

Stage 1 demonstrates that when velocities are sufficiently low, the flow is stable and the dyed fluid stream is shown to be "a beautiful straight line" along the centre of the pipe. This flow can be defined as Laminar Flow. As the velocity is increased incrementally into Stage 2a, the flow was found to become unstable. This can be shown in the fully developed region of the pipe, at a considerable distance from the inlet, where both streams are shown to mix thus filling the entire pipe with dyed fluid. This flow can be defined as Turbulent. As the flow velocity was increased further, this transition was found to gradually move closer to the pipe inlet. Osborne Reynolds looked closer at the findings and observed the flow patterns of this turbulent regime under light from an electric spark (cf. Stage 2b in Figure 2.2). This showed the dyed fluid to form noticeable "curls" known as "eddies" (Reynolds 1883).

The Reynolds number is formally defined as the ratio of inertial stresses to viscous stresses in a fluid system (Deshpande et al. 2010). For low values of the Reynolds Number so that $Re << 1$, the inertial forces in the system become negligible and the

flow is dominated by viscous effects (Kundu and Cohen 2002). The Reynolds Number can be expressed as:

$$Re = \frac{Inertial\ Stresses}{Viscous\ Stresses} = \frac{\rho U \tilde{L}}{\mu} \qquad (2.2)$$

where ρ (kg/m^3) and μ (Pa s) are the density and viscosity of the fluid respectively, $\tilde{L}$ (m) is a characteristic length scale of the geometry used and U (m/s) is the average flow velocity.

2.1.2 The Weissenberg Number

In 1964 James Lindsay White introduced the Weissenberg Number which represents the elastic stresses to the viscous stresses in a fluid system (White 1964). Originally White referred to this as the "Viscoelastic Ratio" representing the recoverable strain of a fluid. White quotes previous research conducted by Karl Weissenberg at the First International Rheological Congress and consequently changes the name of this term to the "Weissenberg number" (White 1964). The Weissenberg Number can be expressed as:

$$Wi = \frac{Elastic\ Stresses}{Viscous\ Stresses} = \lambda \dot{\gamma} \qquad (2.3)$$

where λ (s) and $\dot{\gamma}$ (1/s) denote the relaxation time of the fluid and the characteristic rate of deformation / shear respectively. Physically this dimensionless quantity represents the 'recoverable strain' in a fluid (White 1964, Poole 2012).

2.1.3 The Deborah Number

Whenever the flow dynamics of a system can be determined using one length scale the Weissenberg number is equivalent to that of the Deborah number (Dealy 2010, Poole 2012). The Deborah number is a ratio of time scales of the flow system. This is formally defined as the ratio between the relaxation time of the fluid, λ (s), i.e., the time it takes a fluid to adjust to an applied stress or deformation, and the characteristic time

scale of the flow, t_f (s) (Barnes 2000). This parameter has often been used to determine the "fluidity" of a material where the expected response will be "fluid-like" if the characteristic time of the flow is long, or the relaxation time of the fluid is short. Alternatively, the material response would be characterised as being "solid-like" (Barnes 2000, Poole 2012).

$$De = \frac{Time\ scale\ of\ f luid}{Time\ scale\ of\ f low} = \frac{\lambda}{t_f} \qquad (2.4)$$

If the flow system geometry can be characterised using only one length scale, t_f can be estimated using the average velocity of the flow, U, and a characteristic length scale, $\tilde{L}$ thus making the Deborah number and the Weissenberg number equivalent (Poole 2012). In this thesis, the Weissenberg number will be the utilised notation as the Deborah number may not be sufficient to characterise the effects of viscoelasticity within a flow system (Poole 2012). In past research, the Weissenberg number and the Deborah number are regularly interchanged which is why it was thought important to introduce this parameter at this stage.

2.1.4 The Capillary Number

When immiscible fluids are involved in a fluid system a dimensionless number known as the Capillary number is important. This number is defined as the ratio of the viscous stresses and the surface tension stresses that act at the interface between two fluids (Rapp 2017). The Capillary number can be expressed as:

$$Ca = \frac{Viscous\ Stresses}{Surf ace\ Tension\ Stresses} = \frac{\mu U}{\sigma} \qquad (2.5)$$

where U (m/s) is the average flow velocity of the fluid, μ (Pa s) is the viscosity of the fluid and σ (kg/s^2) is the surface tension or interfacial tension due to the capillary forces that act at the interface between fluids.

2.1.5 The Peclet Number

Another important variable when multiple fluids are involved within a flow system is known as the Peclet number. This is not illustrated in the schematic of Figure 2.1 however, as it is important to the work of this thesis it was thought essential to introduce at this stage. This dimensionless correlation relates the convective and diffusive transport effects within a fluid flow so that when $Pe << 1$ diffusive effects dominate and when $Pe >> 1$ convective effects dominate (White 1991, Rapp 2017). When the Peclet number is large ($Pe > 1000$), miscible fluids have been found to be capable of flowing together without mixing in a system, exhibiting a “sharp” interface (d'Olce et al. 2009, Bonhomme et al. 2011). The Peclet number can be expressed as:

$$Pe = \frac{Convective\ Transport}{Diffusive\ Transport} = \frac{U\tilde{L}}{D_c} \qquad (2.6)$$

where U (m/s) is the average flow velocity of the fluid, $\tilde{L}$ (m) is a characteristic length scale and D_c (m/s^2) is the diffusion coefficient between the fluid streams.

2.2 NEWTONIAN FLUID FLOW INSTABILITIES

In fluid flow systems dynamic instabilities are known to arise due to a number of different physical mechanisms, in particular the properties of the fluids involved, the flow geometries and the driving stresses of the flow (Cubaud and Mason 2008). For the purpose of this thesis, this literature review will now go on to provide a background of research surrounding fluid flow instabilities in various geometries. However, it is imperative to note that although we will highlight important examples the list is not exhaustive.

Earlier work conducted by G. I. Taylor (Taylor 1923) introduced one of today's most well-known and thus most documented Newtonian flow instability – the Taylor-Couette instability (Pakdel and McKinley 1996). This Taylor-Couette geometry is now looked upon as a benchmark flow in fluid mechanics and is achieved by placing a liquid between two coaxial rotating cylinders, a set-up which has not only been used to visualise instabilities, but also widely used to measure fluid viscosities (Mallock 1888). As the angular velocity of the inner cylinder is increased beyond a critical value, the flow becomes unstable with the generation of a secondary flow in the axial direction. This can be visualised as a series of vortices formed within individual square compartments, known as Taylor cells, that counter rotate, in pairs, in a "gear-like" fashion (Taylor 1923). A number of other flow regimes have been visualised (Andereck et al. 2006) as the velocities of the inner and outer cylinders are altered, including spiral regimes, which can be observed when the cylinders are changed to a counter rotating motion. When the outer cylinder rotates around a stationary inner cylinder, a sharp transition to turbulence has also been observed (Taylor 1923, Barnes 2000, Andereck et al. 2006). The inertial origin of this Taylor-Couette instability, for both the secondary flows and the turbulence, leads to limited conditions under which this geometry can be used to measure the rheological properties of low-viscosity fluids (Barnes 2000).

Another classical form of dynamic instability using Newtonian fluids is the Taylor-Saffman instability, often referred to as the viscous fingering instability (Saffman and Taylor 1958, Taylor 1960, Saffman 1986). This occurs when a less viscous fluid is

inserted into a tube containing a more viscous fluid at rest. The displacing less viscous fluid takes the form of a central column that pushes a portion of the viscous fluid out of the tube outlet, whilst some of the viscous fluid remains as a layer along the channel walls. This effect can be visualised in Figure 2.3 (Taylor 1960, Petitjeans and Maxworthy 1996). However, when the inverse fluid configuration is used (i.e., the more viscous fluid is inserted into a fluid of lower viscosity) these instabilities are not observed (Saffman and Taylor 1958). Gravitational effects have a large effect on these instabilities, in particular on the shape of the produced “finger” and the size of the layer of displaced fluid that remains on the channel walls (Petitjeans and Maxworthy 1996).

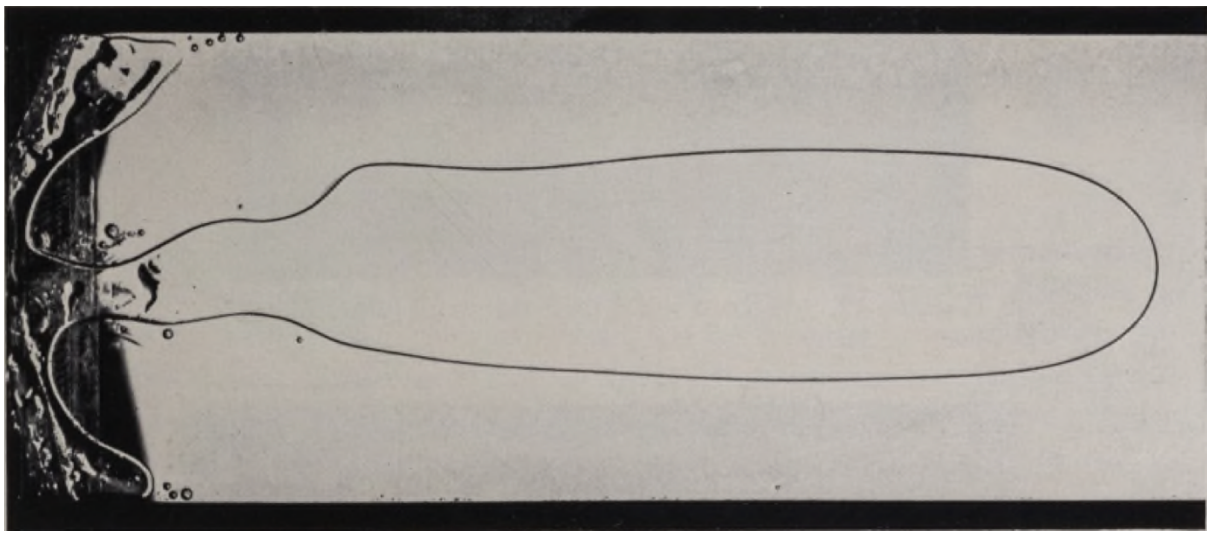

Figure 2.3: Experimental image from the work of Saffman and Taylor (1958) showing air penetrating glycerine.

When large gradients in surface tension or temperature are present at the interface between two fluids within a flow system, the fluids may be subjected to the Marangoni Effect (Levich and Krylov 1969). An example of the effect of a temperature distribution is shown in the work of Capobianchi and Lappa (2021) and illustrated in Figure 2.4, where particles of numerical simulations are shown to accumulate in regions where the temperature contour is at its highest (red). A common practical example demonstrating this would be when a fluid of lower surface tension (for example a soapy water solution) is added to a system where a bulk fluid of higher surface tension is present (for example water with particles for visualisation). Adding a lower surface

tension fluid to a higher surface tension fluid containing suspended particles, will cause the fluid, and thus the particles, to move to the regions of high surface tension (Levich and Krylov 1969, Roché et al. 2014). This effect has been utilised in a number of engineering applications including in the stability and formation of emulsions (Ivanov and Kralchevsky 1997) and droplets (Rallison 1984, Seemann et al. 2012).

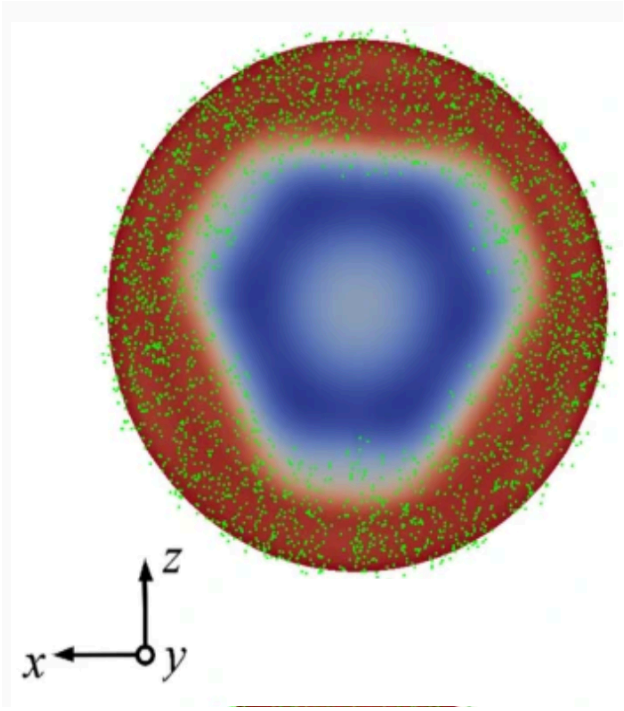

Figure 2.4: Simulation results from the work of Capobianchi and Lappa (2021) demonstrating the Marangoni Effect when a temperature gradient (shown by the contour: red indicating regions of high temperature) is present.

For co-flowing systems of multiple fluids, capillary instabilities (or Rayleigh Instabilities) have been extensively studied in a range of microfluidic geometries (Utada et al. 2007), for example the flow focusing device (Christopher and Anna 2007, Nie et al. 2008, Seemann et al. 2012) and the T-channel (Garstecki et al. 2006) with specific interest placed on the generation of emulsions, a system where one fluid is suspended within another in the form of a small stream of droplets. This type of instability is driven by surface tension forces and is known to occur when fluid viscosities and interfacial tension values are altered within a flow system. This type of

instability can lead to a variety of formations, from long thin threads at high Capillary numbers as shown in Figure 2.5a (Cubaud and Mason 2008, Wang et al. 2020), to the formation of small monodisperse droplets below a critical transitional Capillary number (Cubaud and Mason 2008). The most commonly observed mechanisms for the formation of droplets are the dripping and jetting regimes (Utada et al. 2007). The dripping regime can be observed when low flow rates, or low inertial conditions, are imposed on the system. This can be observed as a stream of droplets in Figure 2.5c. When the flow rates are increased and thus the inertial forces exceed the capillary forces, the flow transitions to the jetting regime (cf. Figure 2.5b) where a thin thread will form before droplet breakup is observed (Christopher and Anna 2007, Utada et al. 2007).

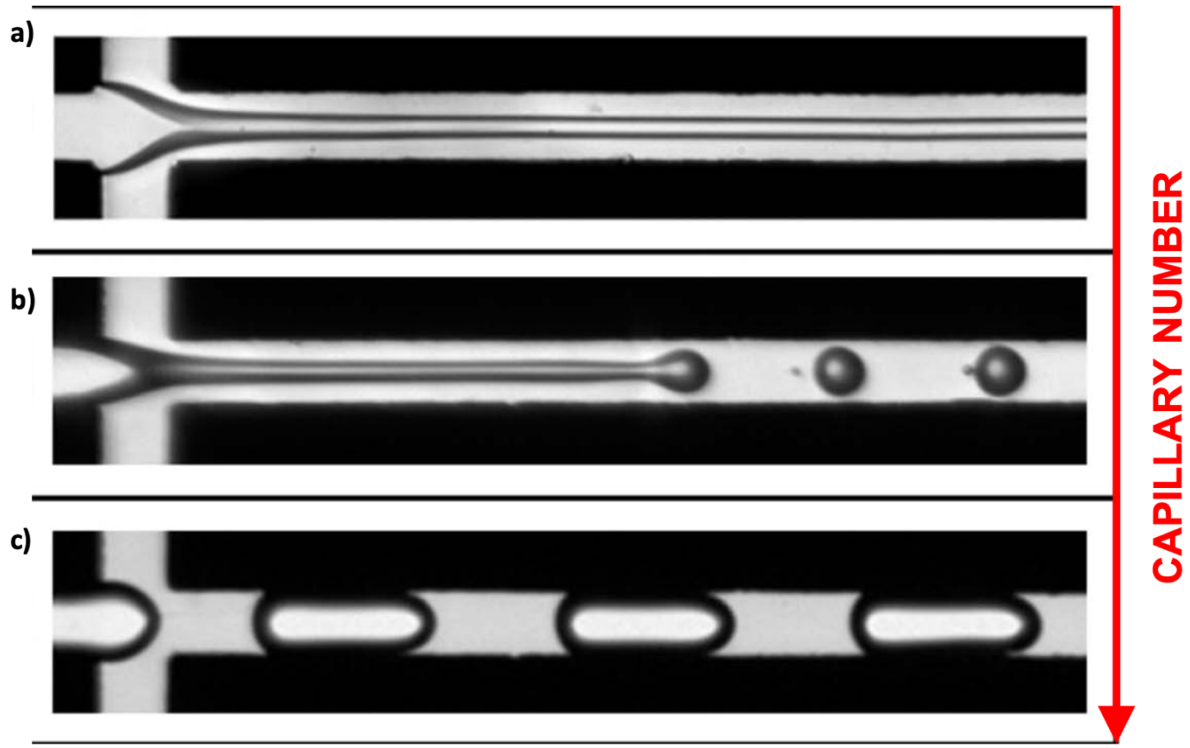

Figure 2.5: Different flow regimes encountered in the work of Cubaud and Mason (2008) illustrating the effects of a reducing Capillary number from a) the stable filament, to b) the jetting regime and then c) the dripping regime.

When inertial effects are negligible ($Re < 1$), dynamic instabilities are still known to occur in Newtonian flows. Folding instabilities have been found to arise when miscible

fluid systems are used in diverging channels, in particular, where a viscous fluid is surrounded by a fluid that is at least 15 times less viscous. (Cubaud and Mason 2006). Under these conditions the central focused stream takes the form of a cylindrical “viscous thread” and has been found to bend and fold as it moves through a diverging channel (i.e., a flow system that increases in cross-sectional area thus causing a deceleration of the flow). This effect can be compared to the way in which honey behaves when squeezed from a tube and is caused by the combination of compressive stresses and deceleration of the flow (Cubaud and Mason 2006, Cubaud and Mason 2012). Swirling instabilities are known to occur when the viscous thread is located near to the channel walls, i.e., in the region of high shear (Cubaud and Mason 2007). This instability is formed as a result of the differences in velocities at either side of the thread filament (Cubaud and Mason 2012). Figure 2.6 illustrates both the swirling and folding instabilities for two parallel flowing viscous thread streams within a diverging slit microchannel. As the distance between the two viscous threads reduces, moving the streams closer together and further from the walls of the microchannel, a transition from the swirling to the folding instability occurs (Cubaud and Mason 2006).

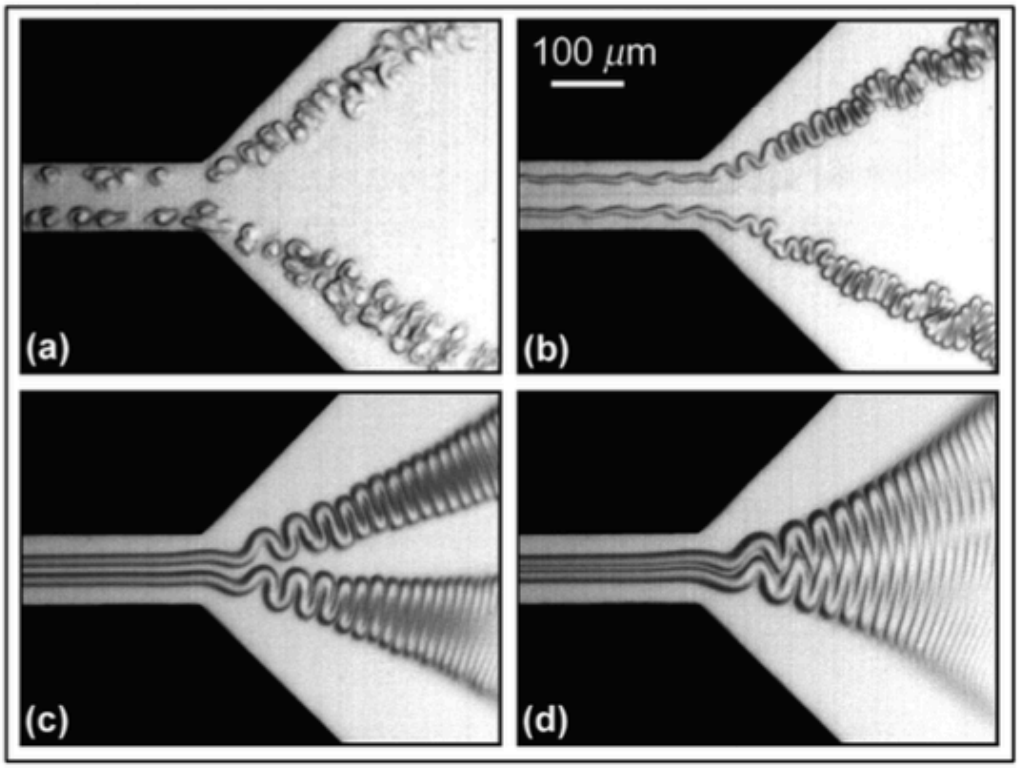

Figure 2.6: Experimental image from the work of Cubaud and Mason (2006) showing the transition from (a)-(b) swirling fluid instabilities to the (c)-(d) folding instabilities as the distance between the two flowing viscous threads is reduced.

2.3 PURELY ELASTIC FLOW INSTABILITIES

In this thesis, the focus is on the so-called “purely elastic” instabilities, which are observed for viscoelastic fluid flows at arbitrary small values of Reynolds number. The instabilities arise solely because of the viscoelastic properties of the fluid, are not observed in a Newtonian equivalent system and have critical onset conditions reported in terms of the Weissenberg number. The properties of these instabilities have proven to enable efficient mixing at the microscale, which would otherwise be difficult to achieve (Groisman and Steinberg 2001). There are also situations where these instabilities are deemed undesirable for example, in microfluidic rheometer applications these instabilities alter the desired flow field hindering the correct measurement of the fluid characteristics (Oliveira et al. 2007, Haward et al. 2012, Zografos et al. 2019).

To allow the role of elasticity to be investigated experimentally, Boger fluids are greatly used in the creeping flow range, for which $Re << 1$, to isolate elastic effects from inertial effects and effects of variable shear rate-dependent viscosity. Boger fluids, were formally introduced by David Boger (1977/1978) and are viscoelastic fluids that are highly elastic but effectively have approximately constant shear viscosity for varying shear rates. They are created by adding small concentrations of high-molecular weight polymers to a viscous Newtonian solvent. These solvents are often chosen to have large viscosities to increase the characteristic relaxation time of the fluid, reduce the inertial effects and therefore highlight elasticity effects (Boger 1977/1978, James 2009). As these solutions are sufficiently dilute, the viscosity contributed by the polymer is only a fraction of the total viscosity, and under steady shear these solutions exhibit an approximately constant viscosity (Boger 1977/1978). Common Boger fluids include, but are not limited to, solutions with small amounts of Polyethylene oxide (PEO) or Polyacrylamide (PAA) added to water/glycerol mixtures, or Polybutene (PB) solutions with a small amount of Polyisobutylene (PIB). These fluids are often modelled using the Upper Convected Maxwell (UCM) or Oldroyd-B rheological equations (Maxwell 1867, Oldroyd 1950).

In the review by Steinberg (2021), some of the earliest observations of elastic instabilities are mentioned, including the work of Giesekus (1968), where turbulence is first mentioned alongside viscoelasticity, and the work of Groisman and Steinberg (2000) where a comparison of elastic turbulence to turbulence in high Reynolds number flows is given. Very important research that aids our fundamental understanding of these instabilities was produced in the late 1980s and early 1990s, through the series of work conducted by Muller, Larson and Shaqfeh within the Taylor-Couette flow device (Muller et al. 1989, Larson et al. 1990, Shaqfeh et al. 1992). Using a highly elastic Polyisobutylene Boger fluid, under creeping flow conditions, the flow was found to transition, at a critical value of Weissenberg number, from a two-dimensional steady flow to a time-dependent three-dimensional oscillatory flow, with a wavelength that decreased over time (Shaqfeh 1996). Unlike the steady Taylor instability visualised when using Newtonian fluids (Taylor 1923) these instabilities were not of inertial origin, they were in fact observed at a Reynolds number of around 10^{-3} . The source of these instabilities was instead found to be driven by the fluid

elasticity (Shaqfeh 1996). This sparked high research interests, with viscometric flows now being one of the most studied flows for visualising elastic instabilities. This category of viscometric flows includes other rheometric devices such as the cone and plate geometry and the parallel plate geometry (McKinley et al. 1991) where swirling instabilities have been observed above critical values of the Weissenberg number. Pakdel and McKinley (McKinley et al. 1996, Pakdel and McKinley 1996) approached this shear flow problem by looking at polymer molecules as “dumbbells”. In these shear flows, the molecules are stretched as shown in Figure 2.7, which amplifies the stress along the streamlines, namely, the hoop stress. These molecules then relax in a characteristic time scale, λ, known as the relaxation time of the fluid, and interact with the velocity fluctuations of the system ultimately giving rise to secondary flows (Shaqfeh 1996). All of the above examples involve some degree of streamline curvature and the underlying mechanism for the instabilities that arise are argued to be the streamline curvature and large hoop stress along streamlines. In contrast, there have been a number of studies demonstrating the features of purely elastic turbulence in straight channels, where no curvature is present (Morozov and van Saarloos 2007, Pan et al. 2013, Lellep et al. 2021). Instead, these instabilities, at low Reynolds numbers, have been found to occur beyond a critical level of inlet flow perturbations, generally created by cylinders within the fluid inlets (Pan et al. 2013, Qin and Arratia 2017). However, as mentioned previously, the focus of this thesis will be on the curvature induced instabilities and therefore this section will now go on to discuss this in more detail.

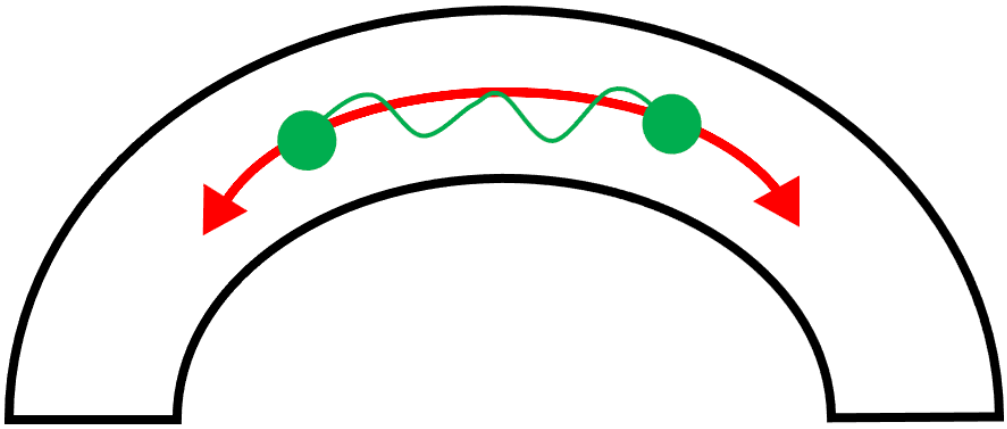

Figure 2.7: Schematic of polymer/dumbbell stretching along a curved streamline for the Pakdel McKinley criterion (adapted from (Pakdel and McKinley 1996)).

McKinley et al. (1996) introduced a well-known dimensionless parameter that combines the aforementioned stress difference, viscosity, shear rate, a stress relaxation timescale and a velocity gradient. The Pakdel-Mckinley criterion, M, provides a critical condition that must be exceeded for the onset of purely elastic instabilities (McKinley et al. 1996):

$$\sqrt{\frac{\lambda \tilde{U}}{\Re}\frac{\tau_{11}}{\left(\mu_0 \dot{\gamma}\right)}} \geq M \qquad (2.7)$$

where λ and μ_0 are the relaxation time and zero-shear rate viscosity of the polymeric fluid respectively, $\tilde{U}$ and τ_{11} are the characteristic fluid velocity and normal elastic stress in the streamwise direction respectively, $\Re$ is the characteristic radii of curvature of the streamlines and $\dot{\gamma}$ is the magnitude of the shear rate. The ratio at the left-hand side of this equation $\left(\lambda \tilde{U}/_{\Re}\right)$ corresponds to a dimensionless measure that compares the characteristic length scale over which the disturbance is advected $(\lambda \tilde{U})$ to the streamline curvature of the system. The other ratio $(\tau_{11}/(\mu_0 \dot{\gamma}))$ introduces the relative effect of the elastic stresses in the streamwise direction. This criterion has been widely applied in shear dominated rotational flows with a typical magnitude in the range of $4 \leq M \leq 6$. The critical conditions for the onset of these purely elastic instabilities have been found to depend very much on the geometry itself, for example, a value of $M_{crit} = 5.9$ was determined within the Taylor-Couette device and a value of $M_{crit} = 4.6$ for the cone and plate rheometric device (McKinley et al. 1996).

Other elastic instabilities have been observed in past research which are not related to the tensions along these curved streamlines but instead occur as result of fluid property differences at the interface (Chen 1991, Chen 1991, Hinch et al. 1992, Bonhomme et al. 2011). An example of this work is in the experiments of Bonhomme et al (2011) within a co-flowing system using water and Polyvinyl alcohol (PVA)

solutions, where no streamline curvature was present. Elastic instabilities that were strongly dependent on flow rate were observed identifying three different flow regimes as shown in Figure 2.8. The first at low flow rates where a stable straight jet remained along the channel outlet (cf. Figure 2.8a) before progressing onto the two unstable regimes at higher flow rates in the form of “advected wavy jets” that began a distance downstream (cf. Figure 2.8c), and “wavy jets” that spanned the full geometry outlet (cf. Figure 2.8b) (Bonhomme et al. 2011).

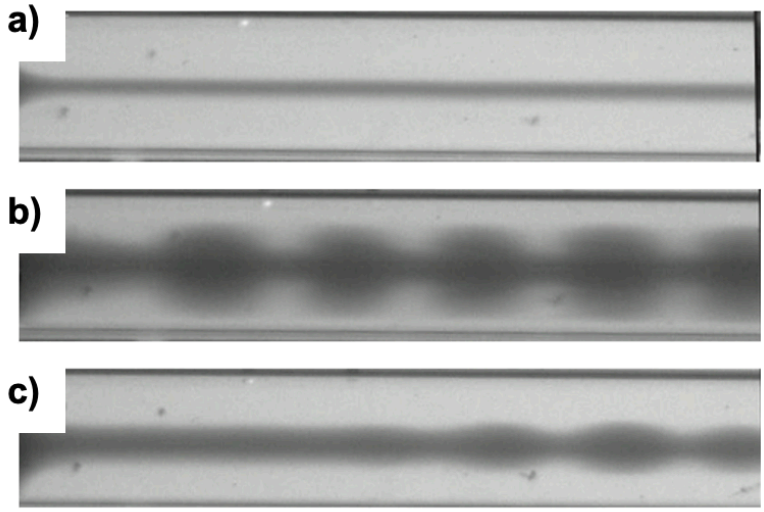

Figure 2.8: Elastic instabilities observed in the experimental work of Bonhomme et al (2011) in the form of a) stable straight jet, b) wavy jets and c) advected wavy jets.

As a result of the flow conditions inertial effects, molecular diffusion and viscosity stratification were ruled out as the origin for these instabilities and instead they were proven to be driven by differences in the normal stress across the interface (Hinch et al. 1992). These instabilities are described as being similar to the viscosity stratification instability observed using Newtonian fluids by Yih et al (Yih 1967) with large waves shown to develop at higher value of the Reynolds number.

The focus of this thesis are the so called elastic instabilities with “curved streamlines” that arise when inertial effects are negligible and thus the instabilities are deemed purely elastic in nature. This literature review will now go on to provide a background of these purely elastic instabilities, detailing various geometries and observations from past research.

2.4 PURELY ELASTIC INSTABILITIES IN MICROFLUIDIC DEVICES

Initial investigations of the purely elastic instabilities, as discussed above, were carried out in simple shear flows that previously had been used universally to measure rheological properties (Shaqfeh 1996). These devices only require a small amount of sample and the relevantly small characteristic length associated with these geometries allowed these studies to be carried out under near inertial less flow conditions (Oliveira et al. 2012).

Much of the later research into elastic instabilities took advantage of the development of microfluidic devices in the late 20th century (Whitesides 2006, Convery and Gadegaard 2019). These miniature devices opened new opportunities to explore these elastic instabilities in various complex flow configurations including shear dominated, extension dominated and those of mixed kinematics, whilst reducing the required sample volume, sample waste, experimental time and thus leading to overall cost reductions (Oliveira et al. 2012). As the elasticity number (equation (2.1)) scales with a characteristic length scale of the geometry (i.e., $\widetilde{L}^{-2}$), the small length scales associated with microfluidics enhance elastic effects whilst keeping inertia low (Oliveira et al. 2007, Sousa et al. 2015). For detailed reviews of single-phase flows in microfluidics the reader is referred to e.g., (Oliveira et al. 2012, Galindo-Rosales et al. 2014, Haward 2016, Datta et al. 2022).

Elastic instabilities in microfluidic devices have been observed in a wide range of microfluidic geometries, exhibiting flows as varied as shear dominated, extensional dominated and flows with mixed kinematics (cf. examples in Figure 2.9). These instabilities are associated with high streamline curvature and large normal stress differences (McKinley et al. 1996, Pakdel and McKinley 1996). This streamline curvature can be produced and adjusted by simply changing the geometry itself, like in the case of a serpentine channel (cf. Figure 2.9k) (Zilz et al. 2012) or by the flow conditions applied on the flow, like in the flow focusing device (cf. Figure 2.9h) (Oliveira

et al. 2009). A number of reviews have discussed these different geometries with the production of interesting graphics, like the one from the work of Oliveira et al (2012) (cf. Figure 2.9) and Poole (2019) (cf. Figure 2.10). Within this thesis the geometries that will be utilised are the flow focusing device and the cross-slot, indicated in red in Figure 2.9.

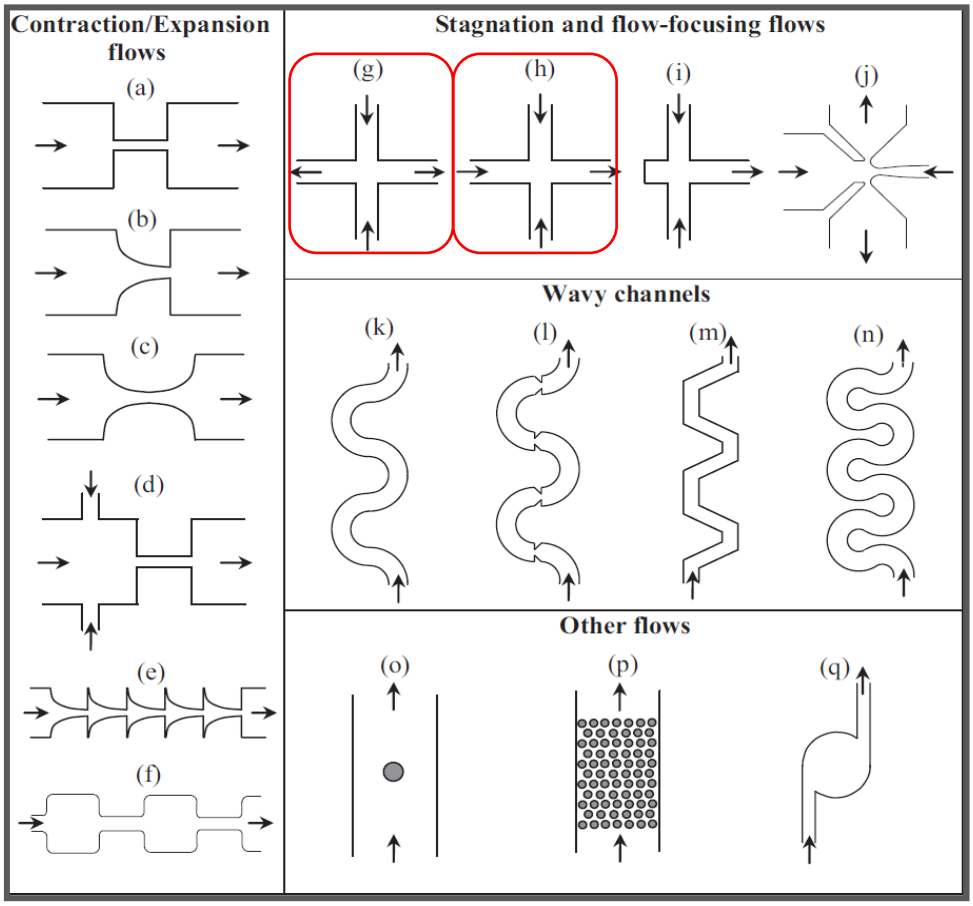

Figure 2.9: Overview of Microfluidic Geometries (Microfluidic Flows of Viscoelastic Fluids. Oliveira et al (2012)). Red boxes highlight the extensional cross-slot and flow focusing configuration that will be used in this work.

Poole (2019) illustrated the “relationships” between the different geometries (cf. Figure 2.10) highlighting that by simply making small adjustments to a particular geometry you can move from one flow type to another. For example, by smoothing out the ‘bumps’ of the microfluidic rectifier you can create a wavy serpentine channel moving from a flow of mixed kinematics to one dominated by shear flow effects.

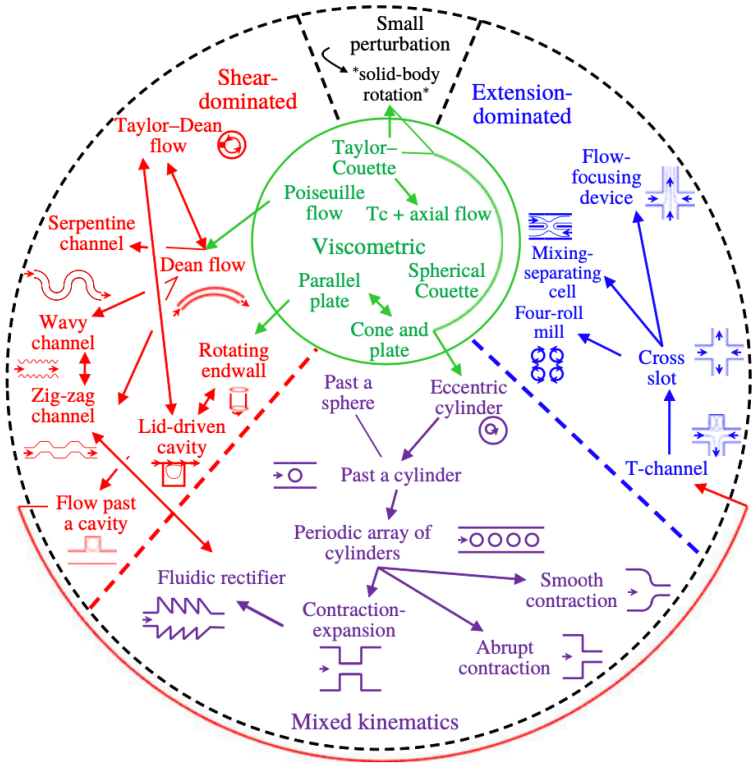

Figure 2.10: Purely Elastic Flow Instability Map (PEFIM) by Poole (2019) illustrating the 'relationships' between the different geometries.

A variety of different geometries from Figure 2.9 and Figure 2.10 will now be introduced briefly to give a background of past research findings in different types of flow / flow configurations, i.e. shear dominated, extension dominated or mixed flow kinematics.

2.4.1 Mixed Kinematic Flow Systems

Moving on from the work of Muller, Larson and Shaqfeh that was previously introduced within the Taylor-Couette flow device (Muller et al. 1989, Larson et al. 1990, Shaqfeh et al. 1992), adjusting the positioning of the cylinders creates an eccentric cylinder geometry. This adjustment would result in a gap reduction on one side of the cylinder which introduces an area where the flow will also experience some extensional, squeezing, effects alongside the geometry shear effects, and thus takes us nicely into the mixed kinematics flow geometries.

Dris and Shaqfeh (1998) studied elastic instabilities in this flow set up in their research using Polyisobutylene – Polybutene Boger fluids and a local linear stability theoretical analysis for the flow of an Oldroyd-B fluid. They concluded that beyond a critical Weissenberg number secondary vortex structures form. These structures evolve into finer structures (i.e., flows of a higher wavelength) with time and as the eccentricity (i.e., the distance between the axes of the cylinders) is increased (Dris and Shaqfeh 1998). This macroscale eccentric flow is very similar to that of the flow around a cylinder (or cylinders) which has been studied extensively by several researchers both at the macro and at the micro-scale (McKinley et al. 1993, Shiang et al. 2000, Haward et al. 2020, Varchanis et al. 2020) due to its close relation to polymer processing applications.

When fluid flows around a cylinder located in a flow channel, stagnation points exist both upstream and downstream of the cylinder. In these areas, the fluid reaches a zero velocity and is subject to strong extensional effects. As the fluid then passes above and below the cylinder, the narrow gap between the cylinder and the channel walls will cause the fluid to experience a velocity increase and shear dominated flow (McKinley et al. 1993). McKinley et al (1993) presented the first macroscale experimental observations of elastic instabilities within this geometry using a highly elastic Boger fluid. At a critical value of the Deborah number, they visualised an initial bifurcation from a two-dimensional steady extensional flow in the downstream wake of the cylinder to a three-dimensional steady flow along the length of the cylinder. Progressing to higher values of the Deborah number transitioned this flow to a time-dependent three-dimensional flow (McKinley et al. 1993). More recent experimental findings within this flow configuration using microfluidics have observed the development of an asymmetric flow around the cylinder (i.e., where more fluid passes either above or below the cylinder instead of remaining symmetric and even on both sides). This asymmetry has been found to develop as a result of the combined effect of high elasticity and shear thinning fluid properties (Haward et al. 2020, Varchanis et al. 2020, Haward et al. 2021, Hopkins et al. 2021).

The contraction geometry which can be in the form of either a smooth or abrupt reduction of the channel characteristic dimension (cf. Figure 2.9 and Figure 2.11), falls

into place following the above discussion as an alternative flow set up to aid in the understanding of engineering polymer processes such as extrusion and injection moulding (Barnes 2000).

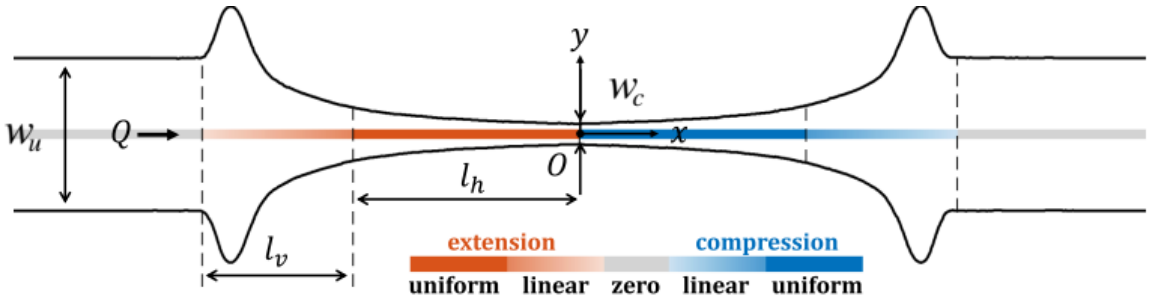

Figure 2.11: 2D Schematic of an optimised smooth Contraction - Expansion Device, with a converging region followed by a diverging region, from the work of Liu et al (2020) highlighting areas of high extension / positive strain rate (orange) and compression / negative strain rate (blue).

Typically, in this contraction – expansion device, the fluid flows from a section of large cross-sectional area into a confined space of smaller cross-sectional area, where a fluid element is subjected to extensional flow a finite position along the contraction before emerging into another larger flow area where the fluid element experiences a compression flow (cf. Figure 2.11). The flow in this geometry experiences a region of controlled strong extension through the contraction, and regions of shear flow near the channel walls. This configuration can be 2D, axisymmetric where the flow travels through circular capillaries (Oliveira et al. 2007), 2D, planar where channels of square/rectangular cross-section are used and the contraction/expansion occurs only in one direction (Alves et al. 2004, Khalkhal and Muller 2022) or 3D with square or rectangular channels where the contraction/expansion occurs in two directions simultaneously (Alves et al. 2005, Sousa et al. 2009, Raihan et al. 2021). The flow patterns within the abrupt geometry are well characterised with the knowledge of the development of vortex structures upstream of the abrupt contraction for all configurations, even for Newtonian fluid flows (Boger 1987, Alves et al. 2004, Alves et al. 2005, Oliveira et al. 2007, Sousa et al. 2009). When using a viscoelastic fluid, these vortex structures, in high contraction ratio geometries have been shown to increase in

size as the velocity, thus the Deborah number of the flow increases until a critical point (Boger 1987). Beyond this critical point a number of other flow behaviours are observed for 3D configurations including asymmetric vortex growth, before proceeding on to an unstable periodic flow (Alves et al. 2005, Sousa et al. 2009). Asymmetric structures are typically bistable which means that although a vortex grows larger on one side it can also be visible on the other side. High elasticity Boger fluids have been shown to develop lip vortices (Alves et al. 2005, Sousa et al. 2009) and, at high flow rates, flow reversal in the recirculation areas has been observed (Sousa et al. 2009). When hyperbolic/smooth contraction inlets are used, as shown in Figure 2.11, instead of the abrupt inlet, shown in Figure 2.9a, vortex formation upstream of the contraction is supressed and therefore this flow set up has been proposed as a method of measuring the extensional rheology of complex fluids (Oliveira et al. 2007, Ober et al. 2013). For the case of the hyperbolic contraction-expansion geometry, elastic instabilities have been observed downstream of the contraction which break down this ideal flow field. These conditions therefore have to be avoided for rheological measurements and highlight an application where having an understanding of how to control these instabilities is of interest (Oliveira et al. 2007).

By combining a series of contraction-expansion geometries a microfluidic rectifier can be created (Groisman and Quake 2004). Microfluidic rectifiers are devices that can have flow in both the forward and backward directions however, for the same pressure drop, the flow rate in each direction can differ. (Sousa et al. 2010, Kawale et al. 2019, Tao et al. 2020). In microfluidics, these devices can be found within pumps, namely valveless micropumps which are also known as no-moving parts (NMP) micropumps (Nabavi 2009).

In the work of Sousa et al (2010), when a triangular shaped rectifier was used (cf. Figure 2.12.), elastic instabilities were found to arise in the forward flow direction only for increasing values of the Deborah number. In this geometry the flow was found to transition from steady symmetric flow to unsteady asymmetric flow as the Deborah number was increased. The flow then returned to steady symmetric flow in both flow directions at yet higher values of the Deborah number as can be observed in Figure 2.12.

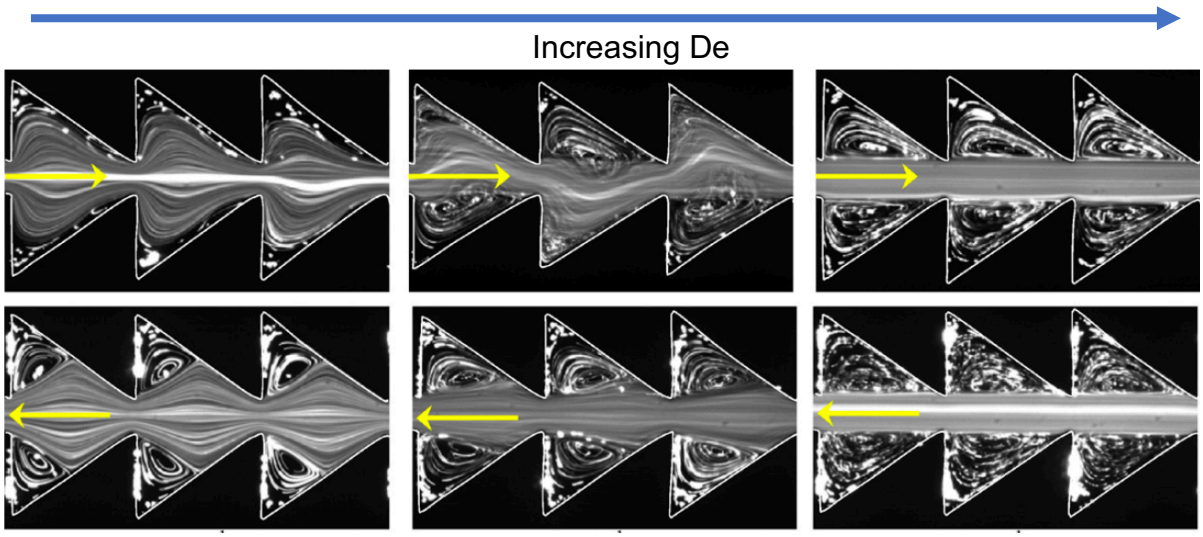

Figure 2.12: Example of flow patterns that occur in both the forward and backward flow directions within a microfluidic triangular shaped rectifier. These observations were made in the work of Sousa et al (2010) highlighting the elastic instabilities that arise in the forward flow direction for increasing values of the Deborah number.

Similar patterns were observed when a viscoelastic fluid was used within a hyperbolic shaped microfluidic rectifier (Sousa et al. 2010, Sousa et al. 2012) however, in this case elastic instabilities were found to arise in both directions. The critical onset conditions for these elastic instabilities were found to be higher (i.e., occur at a higher Deborah number) in the backward flow direction than in the forward direction.

2.4.2 Shear Dominated Flow Systems

The serpentine geometry, also referred to as a curvilinear channel produces shear dominated flow and has been investigated by a number of researchers using single-phase viscoelastic fluids (Zilz et al. 2012, Poole et al. 2013, Casanellas et al. 2016). In general, this geometry is composed of an inlet (or inlets) followed by a series of 'half loops' as shown in the schematic of Figure 2.13. An advantage of this flow set up is that the curvature of the flow is directly related to the geometry and can therefore be easily adjusted for specific needs/investigations (Lindner 2014). Instabilities have been found to arise as a result of the curvature of the system, the stream wise first normal–stress differences generated in the flowing fluid and the centrifugal forces that act on the curved channel in accordance with the Pakdel and McKinley criterion (Pakdel and McKinley 1996, Poole et al. 2013).

Figure 2.13: Schematic of 2D serpentine geometry.

Figure 2.14 shows an example of elastic instabilities that arise when using a Boger fluid within a 3D microfluidic serpentine geometry obtained in preliminary experiments for this PhD work. The same Boger fluid was used in both inlet streams and for visualisation purposes, fluorescent particles were added to one of the two streams. The results, shown in Figure 2.14, are in qualitative agreement with those of Zilz et al. (2012) demonstrating that at low values of the Weissenberg number the two streams travel in parallel along the channel (cf. Figure 2.14a). Increasing the velocity, and thus the flow beyond a critical Weissenberg number, resulted in visible flow instabilities with crossing streamlines (cf. Figure 2.14b). As the velocity was further increased the flow became more chaotic (cf. Figure 2.14c). The critical onset conditions of this instability have been found to be strongly dependent on the radius of curvature of the geometry (Zilz et al. 2012) and of the characteristics of the working fluid (i.e., the degree of shear thinning (Casanellas et al. 2016)).

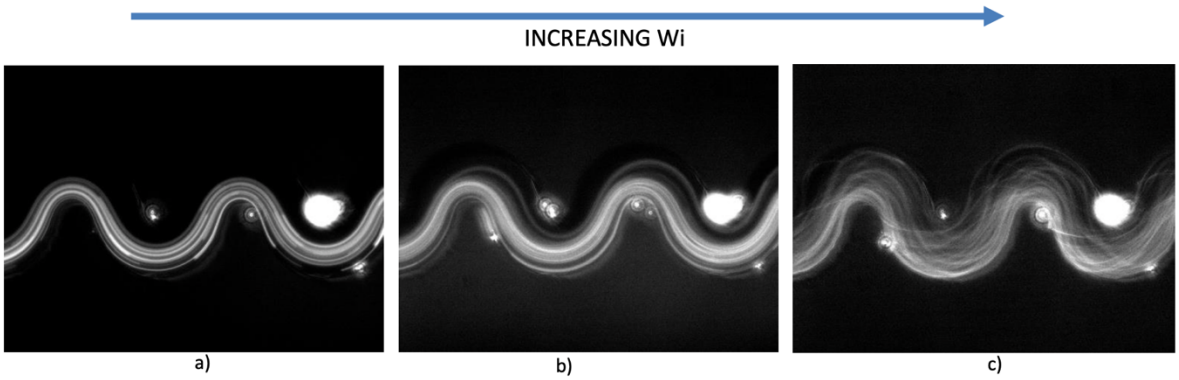

Figure 2.14: Experimental results, using a singular Boger fluid, conducted to visualise elastic instabilities in a 3D microfluidic serpentine geometry for increasing values of Wi (a) steady flow, (b) and (c) visible instabilities with crossing streamlines shown to become more chaotic with increasing value of Wi. For visualisation purposes, fluorescent particles were added to one of the two inlet streams.

The serpentine geometry has been used for various applications including demonstrations of effective mixing using both elastic fluid instabilities (Groisman and Steinberg 2001) and Newtonian fluid droplet mechanics (Wang et al. 2015), and has also been utilised as a rheological measuring device (Lindner 2014).

2.4.3 Extension Dominated Flow Systems

It is clear that an advanced understanding of these instabilities under shear-dominated flow conditions exists from the early viscometric flows (McKinley et al. 1996, Shaqfeh 1996) to those within geometries such as the serpentine channel (Zilz et al. 2012), however, most work in extensional dominated flows is more recent (Haward et al. 2016). It is therefore important to enhance the knowledge of the conditions under which these purely elastic instabilities arise in extensional flow configurations in order to improve and ultimately benefit various industrial applications including inkjet printing, fibre-spinning, extrusion and more (Haward et al. 2016). This is where the work of this thesis lies with specific literature review information provided in each of the results chapters (Chapters 4 - 6).

Extensionally-dominated cross-shaped devices have been used in past research to study the onset of various instabilities, in either a cross-slot (Arratia et al. 2006, Poole

et al. 2007), T-channel (Soulages et al. 2009) or flow focusing arrangement, which are able to produce elongational flows (Oliveira et al. 2009, Ballesta and Alves 2017). As outlined in the introductory chapter, both the microfluidic cross-slot device and the flow focusing device will be the focus of the results chapters of this thesis.

The cross-slot is arguably the classic configuration used to study the effects of elongational flow. The geometry consists of perpendicular, bisecting rectangular channels with two sets of opposing inlets and outlets, as shown in Figure 2.15. This configuration results in a flow field with a stagnation point located at the centre of symmetry, where the velocity is zero, generating an elongational flow in the central region. At the stagnation point, a fluid element can be “trapped” for an indefinite amount of time thus experiencing significant strain, potentially enabling “steady-state” conditions to be achieved. An optimised version of this geometry has been proposed as an extensional rheometer by Alves (2008) and Haward et al (2012) namely, the Optimized Shape Cross-Slot Elongation Rheometry (OSCER) geometry.

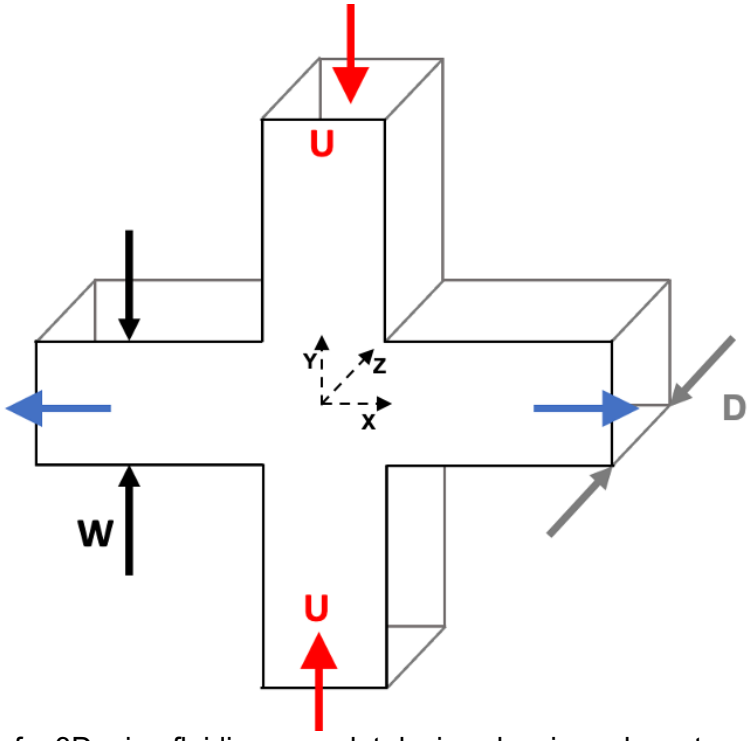

Figure 2.15: Schematic of a 3D microfluidic cross-slot device showing relevant variables and coordinate system.

The earliest experimental report of elastic instabilities within this cross-slot device was in the work of Arratia et al (2006). The flow patterns observed highlighted three distinct flow regimes with two transitions to instability (cf. Figure 2.16a): one in which the flow remains steady and symmetric before transitioning to a first instability where the flow remains steady but becomes asymmetric in nature, i.e., when unequal rates of fluid from each inlet flow through each of the outlets. As the Weissenberg number of the flow increases, or the flow rates of the inlet streams are increased (for the same fluid in the same geometry), the flow experiences a second transition to a time-dependent flow. These findings were first confirmed in numerical simulations conducted by Poole et al (2007) using the Upper Convected Maxwell (UCM) viscoelastic fluid model (cf. Figure 2.16b). Since then, this has been seen in simulations using a range of different constitutive models for example FENE-CR (Chilcott and Rallison 1988, Rocha et al. 2008) and the simplified Phan-Thien and Tanner (SPTT) model (PhanThien and I.Tanner 1977, Cruz et al. 2014, Davoodi et al. 2019). The nature and critical onset conditions for these instabilities in the cross-slot device have been shown to be strongly dependent on the channel aspect ratio (i.e., channel height/channel width) (Poole et al. 2007, Sousa et al. 2015) and also on the rheological properties of the fluids (Sousa et al. 2015). Both numerical and experimental investigations have shown that when the channel aspect ratio is equal to or greater than 1 (i.e., the channel width and height are the same or, the channel height is larger than the channel width) both transitions occur. However, as the aspect ratio is reduced below 1 (i.e., the channel width becomes larger than the channel height) the flow transitions directly from steady symmetric flow to the time-dependent flow regime, missing out the steady asymmetric flow regime completely. The bounding channel walls are thus said to have a stabilising effect on the instabilities that arise within the microfluidic cross-slot device (Poole et al. 2007, Sousa et al. 2015). The increased wall effects enhance the shear flow and reduce the extensional stretching effects on the polymer molecules, which were thought to be the driving source of these instabilities (Arratia et al. 2006, Sousa et al. 2015). However, recent work by Davoodi et al (2019) using the cross-slot device with a cylinder placed at the centre of the geometry, argues that the extensional flow cannot be solely responsible for these instabilities, but instead highlights that these could actually be classed as “curved streamline instabilities” produced as a result of the streamline curvature and the high deformation rates near the corners of the device (Davoodi et al. 2019). In addition, in the work of Sousa et al (2015), both flow

transitions within the cross-slot device were found to occur when the solvent viscosity ratio, defined as the viscosity of the solvent / zero shear rate viscosity of the viscoelastic solution, $\beta \lesssim 0.05$, however as the fluid tended towards a Boger fluid (i.e., low/dilute polymer concentrations where , $\beta \gtrsim 0.05$) the flow was found to transition directly from the steady symmetric flow to the time-dependent flow regime, missing out the asymmetric flow regime altogether.

All of the aforementioned studies within the cross-slot device have been limited to single fluid flows. In the present thesis, the work on flow induced elastic instabilities in the cross-slot device is expanded to consider flows involving multiple fluids, see Chapter 4 of this thesis, where results showing effects of fluid rheological properties and interfacial tension within the cross-slot device are discussed.

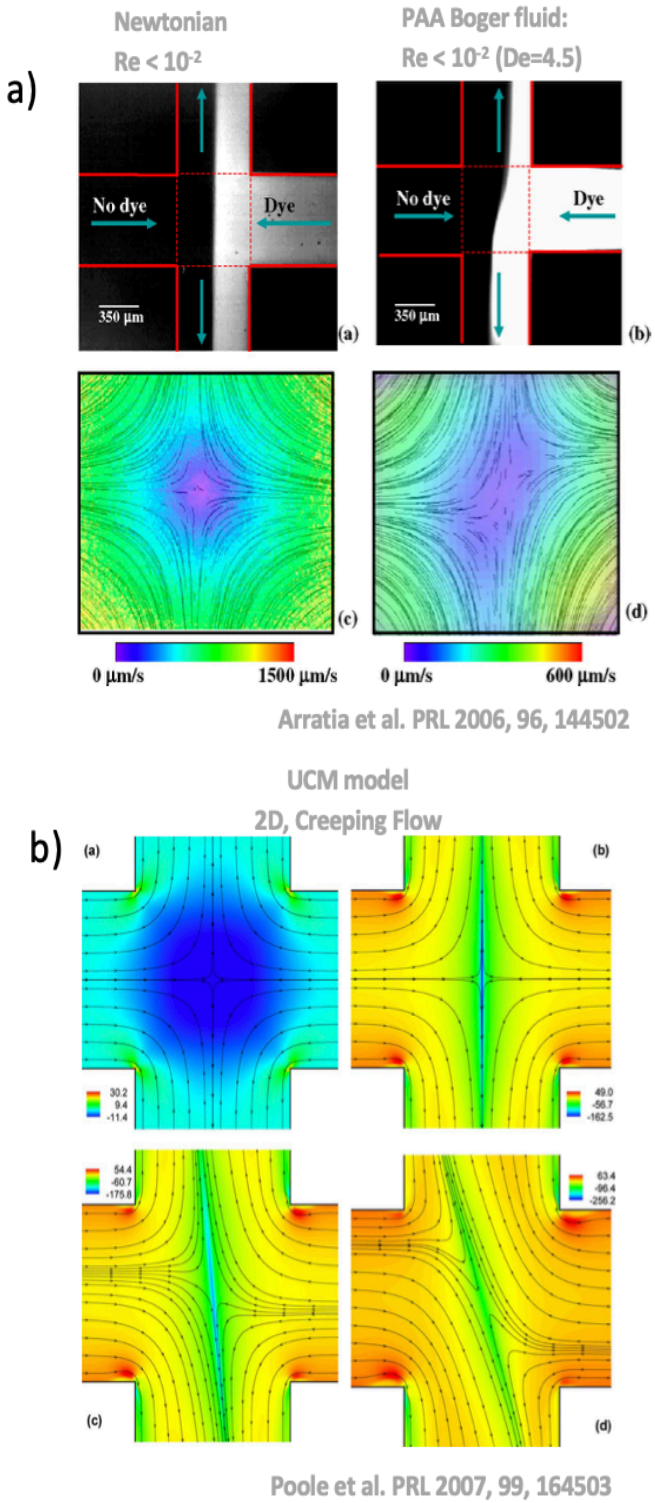

Figure 2.16: Results showing elastic instabilities in the cross-slot device from past research a) Arratia et al. (2006) b) Poole et al. (2007).

The flow focusing device operates by having two opposing lateral/side streams that shape a third central inlet stream (cf. Figure 2.17) producing a converging flow region. These flow devices are often used for bringing different streams into contact, to promote mixing (Nguyen and Huang 2005) or for droplet generation (Cubaud et al. 2005). One interesting characteristic of this geometry is that, unlike other converging flow microdevices, such as abrupt and smooth contractions, the Hencky strain can be adjusted, by varying the velocities of the lateral streams without changing the size or shape of the device (Ballesta and Alves 2017).

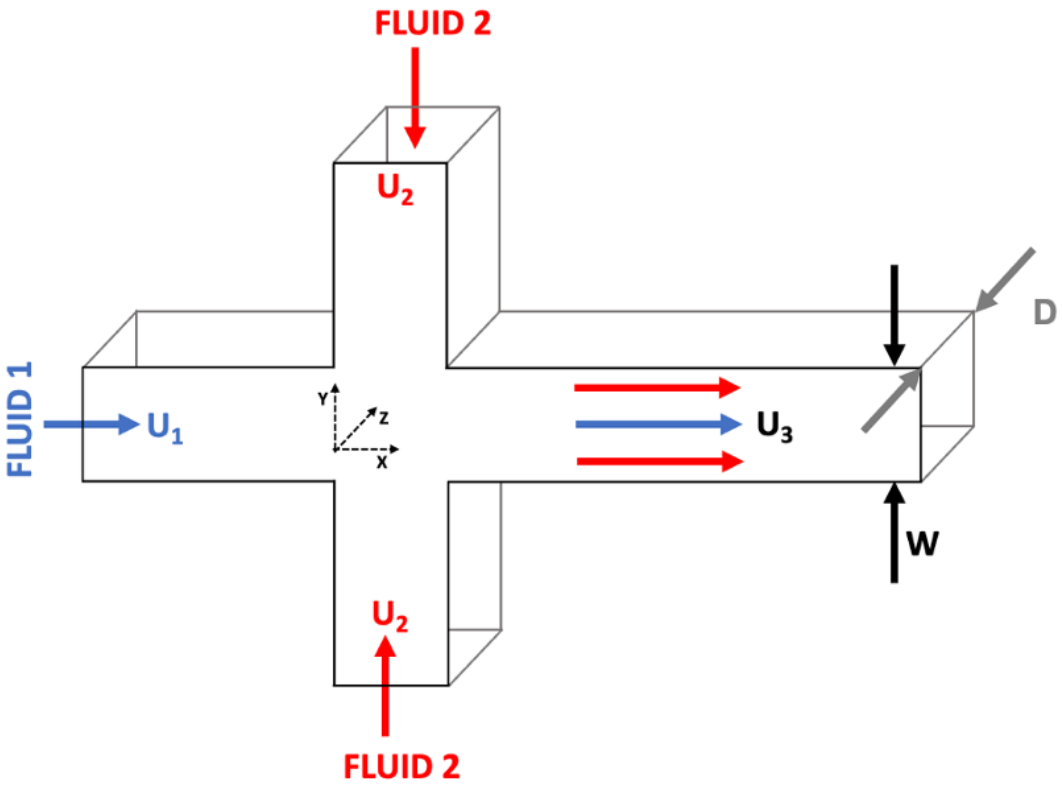

Figure 2.17: Schematic of a 3D microfluidic flow focusing device showing relevant variables and coordinate system.

Purely elastic flow instabilities have been observed within this flow device with three distinct flow regimes (Oliveira et al. 2009, Oliveira et al. 2011) (cf. Figure 2.18). At low values of the Weissenberg number the flow is symmetrical relative to the centreline (cf. Figure 2.18a). Flows within this device are generally investigated using a parameter known as the velocity ratio. Throughout this work, the velocity ratio is

defined as the ratio between the average velocity of the side inlet streams to that of the central inlet stream. For low velocity ratio flows, the flow transitions directly from a steady symmetric flow to a time-dependent flow above a critical value of the Weissenberg number. For moderate to high velocity ratios, two transitions have been observed for increasing Weissenberg number: a first transition to steady asymmetric flow (cf. Figure 2.18b) and a second transition at higher Wi where time-dependent flow is visible with crossing streamlines (cf. Figure 2.18c). In the work of Ballesta and Alves (2017), the time-dependent flow regime was further broken down; transitioning from periodic flow to semi-periodic and then chaotic flow states as the Weissenberg number increased. It is important to highlight once again that when using the same flow conditions with a Newtonian fluid no instabilities were observed (Oliveira et al. 2011, Oliveira et al. 2012). Similar findings have been observed both experimentally (Oliveira et al. 2011, Ballesta and Alves 2017) and in numerical simulations (Oliveira et al. 2009).

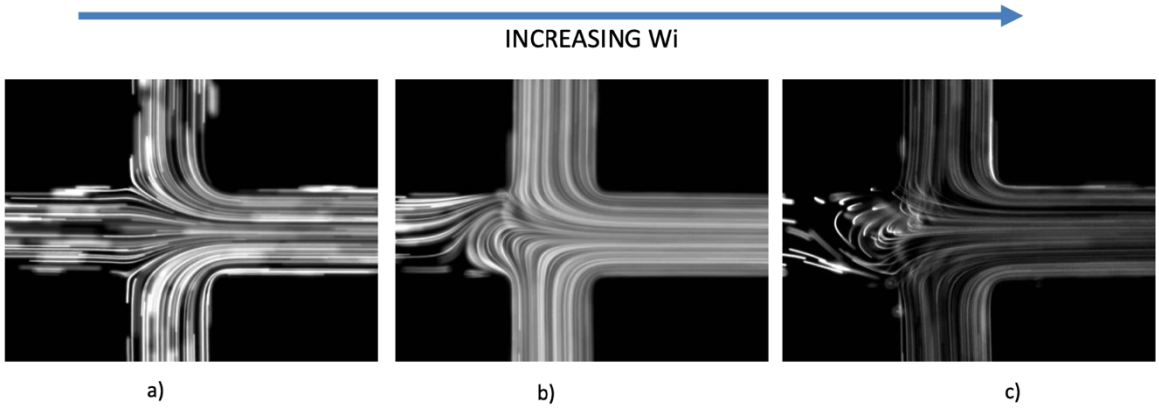

Figure 2.18: Experimental fluid patterns of a dilute Boger fluid (PEO) in a 3D microfluidic flow focusing device for increasing values of Wi (a) steady symmetric flow (b) steady asymmetric flow (c) time-dependent flow.

The critical onset conditions and the size of the asymmetries that form have been shown to depend on the ratio of the width of the lateral to central inlet arms (Oliveira et al. 2009) however, to the author's knowledge, no research studies have shown the effect of changing channel aspect ratio within this geometry, i.e., channel height to width ratio. Alongside this research gap, only single fluid flows have been used highlighting an opening for the work of this thesis where the effects of geometrical

parameters and multiple fluid streams on the onset of these purely elastic curved streamline instabilities are investigated (see Chapter 6). Past research has suggested that the important factor for the development of viscoelastic instabilities within the flow focusing device is the strong extensional flows that occur at the centre of the geometry (Oliveira et al. 2009, Ballesta and Alves 2017). However, the work of Chapter 6 shows, similar findings to that of Davoodi et al (2019) within the cross-slot device, that these instabilities may not be solely related to the extensional flow effects and instead could be related to streamline curvature and the high deformation rates near the re-entrant corners.

2.5 SUMMARY

This literature review highlighted the amount of work that has been conducted to understand the various forms of purely elastic flow instabilities known to occur in viscoelastic fluid flows. Beyond this, there has been a lot of work on inertial-elastic instabilities (Rodd et al. 2005, Haward and McKinley 2013, Burshtein et al. 2017) however, this is not the focus of this work.

Generally, in extensional flow devices, past researchers have identified different flow regimes: steady symmetric flow, steady asymmetric flow and time-dependent flow, which eventually lead on to elastic turbulence. However, most previous studies have been limited to single fluid flows. This work will utilise microfluidics in both the extensional flow focusing and the cross-slot configurations to understand these instabilities in more complex flows, where multiple fluids are involved, along with varying geometrical parameters and fluid properties. Experimental data produced in this thesis will also provide useful validation for future numerical work involving multiple complex fluids.

Ultimately, the work of this thesis aims to provide an enhanced understanding of purely elastic flow instabilities in extensional flow devices, to determine ways of controlling these instabilities. Microfluidic devices are being continually used and optimised in a wide range of applications and, as such, it is important an understanding of how to

control and manipulate fluids within these devices exists to allow the effects of elastic instabilities to be minimised or maximised for particular applications.

2.6 REFERENCES

Alves, M. A. (2008). Design of a Cross-Slot Flow Channel for Extensional Viscosity Measurements. AIP Conference Proceedings.

Alves, M. A., Oliveira, P. J. and Pinho, F. T. (2004). "On the effect of contraction ratio in viscoelastic flow through abrupt contractions." Journal of Non-Newtonian Fluid Mechanics 122(1-3): 117-130.

Alves, M. A., Pinho, F. T. and Oliveira, P. J. (2005). "Visualizations of Boger fluid flows in a 4:1 square-square contraction." AIChE Journal 51(11): 2908-2922.

Andereck, C. D., Liu, S. S. and Swinney, H. L. (2006). "Flow regimes in a circular Couette system with independently rotating cylinders." Journal of Fluid Mechanics 164: 155-183.

Arratia, P. E., Thomas, C. C., Diorio, J. D. and Gollub, J. P. (2006). "Elastic Instabilities of Polymer Solutions in Extensional Flows ".

Ballesta, P. and Alves, M. A. (2017). "Purely elastic instabilities in a microfluidic flow focusing device." Physical Review Fluids 2(5): 053301.

Barnes, H. A. (2000). A Handbook of Elementary Rheology, Institute of Non-Newtonian Fluid Mechanics.

Boger, D. V. (1977/1978). "A highly elastic constant viscosity fluid." Journal of Non-Newtonian Fluid Mechanics 3: 87-91.

Boger, D. V. (1987). "Viscoelastic flows through contractions." Annual Review of Fluid Mechanics 19: 157-182.

Bonhomme, O., Morozov, A., Leng, J. and Colin, A. (2011). "Elastic instability in stratified core annular flow." Phys Rev E Stat Nonlin Soft Matter Phys 83(6): 065301-065301.

Bridgman, P. W. (1963). "Dimensional analysis." Yale University Press.

Burshtein, N., Zografos, K., Shen, A. Q., Poole, R. J. and Haward, S. J. (2017). "Inertioelastic Flow Instability at a Stagnation Point." Physical Review X 7(4): 041039.

Capobianchi, P. and Lappa, M. (2021). "Particle Accumulation Structures in a 5 cSt Silicone Oil Liquid Bridge: New Data for the Preparation of the JEREMI Experiment." Microgravity Science and Technology 33(2): Online.

Casanellas, L., Alves, M. A., Poole, R. J., Lerouge, S. and Lindner, A. (2016). "The stabilizing effect of shear thinning on the onset of purely elastic instabilities in serpentine microflows." Soft Matter 12(29): 6167-6175.

Chen, K. (1991). "Elastic instability of the interface in Couette flow of viscoelastic liquids." Journal of Non-Newtonian Fluid Mechanics 40: 261-267.

Chen, K. (1991). "Interfacial instability due to elastic stratification in concentric coextmsion of two viscoelastic fluids." Journal of Non-Newtonian Fluid Mechanics 40: 155-175.

Chilcott, M. D. and Rallison, J. M. (1988). "Creeping flow of dilute polymer solutions past cylinders and spheres." Journal of Non-Newtonian Fluid Mechanics 29: 381-432.

Christopher, G. F. and Anna, S. L. (2007). "Microfluidic methods for generating continuous droplet streams." Journal of Physics D: Applied Physics 40(19): R319-R336.

Convery, N. and Gadegaard, N. (2019). "30 years of microfluidics." Micro and Nano Engineering 2: 76-91.

Cruz, F. A., Poole, R. J., Afonso, A. M., Pinho, F. T., Oliveira, P. J. and Alves, M. A. (2014). "A new viscoelastic benchmark flow: Stationary bifurcation in a cross-slot." Journal of Non-Newtonian Fluid Mechanics 214: 57-68.

Cubaud, T. and Mason, T. G. (2006). "Folding of viscous threads in diverging microchannels." Phys Rev Lett 96(11): 114501.

Cubaud, T. and Mason, T. G. (2007). "Swirling of viscous fluid threads in microchannels." Phys Rev Lett 98(26): 264501.

Cubaud, T. and Mason, T. G. (2008). "Capillary threads and viscous droplets in square microchannels." Physics of Fluids 20(5): 053302.

Cubaud, T. and Mason, T. G. (2012). "Interacting viscous instabilities in microfluidic systems." Soft Matter 8(41): 10573–10582.

Cubaud, T., Tatineni, M., Zhong, X. and Ho, C. M. (2005). "Bubble dispenser in microfluidic devices." Phys Rev E 72(3): 037302.

d'Olce, M., Martin, J., Rakotomalala, N., Salin, D. and Talon, L. (2009). "Convective/absolute instability in miscible core-annular flow. Part 1: Experiments." Journal of Fluid Mechanics 618: 305-322.

Datta, S. S., Ardekani, A. M., Arratia, P. E., Beris, A. N., Bischofberger, I., McKinley, G. H., Eggers, J. G., López-Aguilar, J. E., Fielding, S. M., Frishman, A., Graham, M. D., Guasto, J. S., Haward, S. J., Shen, A. Q., Hormozi, S., Morozov, A., Poole, R. J., Shankar, V., Shaqfeh, E. S. G., Stark, H., Steinberg, V., Subramanian, G. and Stone, H. A. (2022). "Perspectives on viscoelastic flow instabilities and elastic turbulence." Physics of Fluids 7(8): Online.

Davoodi, M., Domingues, A. F. and Poole, R. J. (2019). "Control of a purely elastic symmetry-breaking flow instability in cross-slot geometries." Journal of Fluid Mechanics 881: 1123-1157.

Dealy, J. M. (2010). "Weissenberg and Deborah Numbers – their definition and use." Rheol. Bull 79(2): 14-18.

Deshpande, A., Y. (Abhijit Yeshwa), Murali Krishnan, J. and Sunil Kumar, P. B. (2010). Rhelogy of complex fluids, New York ; London : Springer.

Dris, I. M. and Shaqfeh, E. S. G. (1998). "Experimental and theoretical observations of elastic instabilities in eccentric cylinder flows: local versus global instability." Journal of Non-Newtonian Fluid Mechanics 80: 1-58.

Galindo-Rosales, F. J., Campo-Deaño, L., Sousa, P. C., Ribeiro, V. M., Oliveira, M. S. N., Alves, M. A. and Pinho, F. T. (2014). "Viscoelastic instabilities in micro-scale flows." Experimental Thermal and Fluid Science 59: 128-139.

Garstecki, P., Fuerstman, M. J., Stone, H. A. and Whitesides, G. M. (2006). "Formation of droplets and bubbles in a microfluidic T-junction-scaling and mechanism of break-up." Lab Chip 6(3): 437-446.

Giesekus, H. (1968). "Nicht-lineare Effekte beim Strömen viskoelastischer Flussigkeiten durch Schlitz- und Lochdüsen." Rheol. Acta 7: 127-138.

Groisman, A. and Quake, S. R. (2004). "A microfluidic rectifier: anisotropic flow resistance at low Reynolds numbers." Phys Rev Lett 92(9): 094501.

Groisman, A. and Steinberg, V. (2000). "Elastic turbulence in a polymer solution flow." Nature 405: 53-55.

Groisman, A. and Steinberg, V. (2001). "Effcient mixing at low Reynolds numbers using polymer additives." Nature 410: 905-908.

Haward, S. J. (2016). "Microfluidic extensional rheometry using stagnation point flow." Biomicrofluidics 10(4): 043401.

Haward, S. J., Hopkins, C. C. and Shen, A. Q. (2020). "Asymmetric flow of polymer solutions around microfluidic cylinders: Interaction between shear-thinning and viscoelasticity." Journal of Non-Newtonian Fluid Mechanics 278: 104250.

Haward, S. J., Hopkins, C. C., Varchanis, S. and Shen, A. Q. (2021). "Bifurcations in flows of complex fluids around microfluidic cylinders." Lab Chip 21(21): 4041-4059.

Haward, S. J. and McKinley, G. H. (2013). "Instabilities in stagnation point flows of polymer solutions." Physics of Fluids 25(8): 83104.

Haward, S. J., McKinley, G. H. and Shen, A. Q. (2016). "Elastic instabilities in planar elongational flow of monodisperse polymer solutions." Sci Rep 6: 33029.

Haward, S. J., Ober, T. J., Oliveira, M. S. N., Alves, M. A. and McKinley, G. H. (2012). "Extensional rheology and elastic instabilities of a wormlike micellar solution in a microfluidic cross-slot device." Soft Matter 8(2): 536-555.

Haward, S. J., Oliveira, M. S., Alves, M. A. and McKinley, G. H. (2012). "Optimized cross-slot flow geometry for microfluidic extensional rheometry." Phys Rev Lett 109(12): 128301.

Hinch, E. J., Harris, O. J. and Rallison, J. M. (1992). "The instability mechanism for two elastic liquids being co-extruded." Journal of Non-Newtonian Fluid Mechanics 43: 311-324.

Hopkins, C. C., Haward, S. J. and Shen, A. Q. (2021). "Tristability in Viscoelastic Flow Past Side-by-Side Microcylinders." Phys Rev Lett 126(5): 054501.

Ivanov, I. B. and Kralchevsky, P. A. (1997). "Stability of emulsions under equilibrium and dynamic conditions." Colloids and Surfaces 128: 155-175.

James, D. F. (2009). "Boger Fluids." Annual Review of Fluid Mechanics 41(1): 129-142.

Kawale, D., Jayaraman, J. and Boukany, P. E. (2019). "Microfluidic rectifier for polymer solutions flowing through porous media." Biomicrofluidics 13(1): 014111.

Khalkhal, F. and Muller, S. (2022). "Analyzing flow behavior of shear-thinning fluids in a planar abrupt contraction/expansion microfluidic geometry." Physical Review Fluids 7(2): 023303.

Kundu, P. K. and Cohen, I. M. (2002). Fluid Mechanics, Second Edition, Academic Press.

Larson, R. G., Shaqfeh, E. S. G. and Muller, S. J. (1990). "A purely elastic instability in Taylor–Couette flow." Journal of Fluid Mechanics 218(-1): 573-600.

Lellep, M., Linkmann, M., Eckhardt, B. and Morozov, A. (2021). "Purely elastic linear instabilities in parallel shear flows with free-slip boundary conditions." Journal of Fluid Mechanics 928: R3.

Levich, V. G. and Krylov, V. S. (1969). "Surface Tension Driven Phenomena." Annual Review of Fluid Mechanics 1(1): 293-316.

Lindner, A. (2014). "Flow of complex suspensions." Physics of Fluids 26(10): 101307.

Mallock, A. (1888). "Determination of the viscosity of water." Proceedings of the Royal Society of London 45: 126-132.

Maxwell, J. C. (1867). "On the dynamical theory of gases." Philosophical Transactions of the Royal Society of London 157: 49-88.

McKinley, G. H. (2005). Dimensionless Groups For Understanding Free Surface Flows of Complex Fluids. SOR Rheology Bulletin. HML Report Number 05-P-05.

McKinley, G. H., Armstrong, R. C. and Brown, R. A. (1993). "The wake instability in viscoelastic flow past confined circular cylinders." Philos. Trans. Royal Society London 344(1671): 265–304.

McKinley, G. H., Byars, J. A., Brown, R. A. and Armstrong, R. C. (1991). "Observations on the elastic instability in cone-and-plate and parallel-plate flows of a polyisobutylene Boger fluid." Journal of Non-Newtonian Fluid Mechanics 40: 201-229.

McKinley, G. H., Pakdel, P. and Oztekin, A. (1996). "Rheological and geometric scaling of purely elastic flow instabilities." Journal of Non-Newtonian Fluid Mechanics 67: 19-47.

Morozov, A. N. and van Saarloos, W. (2007). "An introductory essay on subcritical instabilities and the transition to turbulence in visco-elastic parallel shear flows." Physics Reports 447(3-6): 112-143.

Muller, S. J., Larson, R. G. and Shaqfeh, E. S. G. (1989). "A purely elastic transition in Taylor-Couette flow." Rheologica Acta 28(6): 499-503.

Nabavi, M. (2009). "Steady and unsteady flow analysis in microdiffusers and micropumps: a critical review." Microfluidics and Nanofluidics 7(5): 599-619.

Nguyen, N. T. and Huang, X. (2005). "Mixing in microchannels based on hydrodynamic focusing and time-interleaved segmentation: modelling and experiment." Lab Chip 5(11): 1320-1326.

Nie, Z., Seo, M., Xu, S., Lewis, P. C., Mok, M., Kumacheva, E., Whitesides, G. M., Garstecki, P. and Stone, H. A. (2008). "Emulsification in a microfluidic flow-focusing device: effect of the viscosities of the liquids." Microfluidics and Nanofluidics 5(5): 585-594.

Ober, T. J., Haward, S. J., Pipe, C. J., Soulages, J. and McKinley, G. H. (2013). "Microfluidic Extensional Rheometry using a Hyperbolic Contraction Geometry." Rheologica Acta 52: 529–546.

Oldroyd, J. G. (1950). "On the formulation of rheological equations of state." Proceedings of the Royal Society of London. Series A. Mathematical and Physical Sciences 200(1063): 523–541.

Oliveira, M., Pinho, F. T. and Alves, M. A. (2011). Extensional Flow of Newtonian and Boger Fluids Through a Flow Focusing Microdevice. 3rd Micro and Nano Flows Conference. Thessaloniki, Greece: 1-6.

Oliveira, M. S. N., Alves, M. A. and Pinho, F. T. (2012). Microfluidic Flows of Viscoelastic Fluids. Transport and Mixing in Laminar Flows: From Microfluidics to Oceanic Currents. R. Grigoriev, Wiley-VCH Verlag GmbH & Co. KGaA.: 131-174.

Oliveira, M. S. N., Alves, M. A., Pinho, F. T. and McKinley, G. H. (2007). "Viscous flow through microfabricated hyperbolic contractions." Experiments in Fluids 43(2-3): 437-451.

Oliveira, M. S. N., Oliveira, P. J., Pinho, F. T. and Alves, M. A. (2007). "Effect of contraction ratio upon viscoelastic flow in contractions: The axisymmetric case." Journal of Non-Newtonian Fluid Mechanics 147(1-2): 92-108.

Oliveira, M. S. N., Pinho, F. T. and Alves, M. A. (2012). "Divergent streamlines and free vortices in Newtonian fluid flows in microfluidic flow-focusing devices." Journal of Fluid Mechanics 711: 171-191.

Oliveira, M. S. N., Pinho, F. T., Poole, R. J., Oliveira, P. J. and Alves, M. A. (2009). "Purely elastic flow asymmetries in flow-focusing devices." Journal of Non-Newtonian Fluid Mechanics 160(1): 31-39.

Pakdel, P. and McKinley, G. H. (1996). "Elastic Instability and Curved Streamlines." Physical Review Fluids 77(12): 2459-2462.

Pan, L., Morozov, A., Wagner, C. and Arratia, P. E. (2013). "Nonlinear elastic instability in channel flows at low Reynolds numbers." Phys Rev Lett 110(17): 174502.

Petitjeans, P. and Maxworthy, T. (1996). "Miscible displacements in capillary tubes. Part 1. Experiments." Journal of Fluid Mechanics 326: 37-56.

PhanThien, N. and I.Tanner, R. (1977). "A new constitutive equation derived from network theory." Journal of Non-Newtonian Fluid Mechanics 2(4): 353-365.

Poole, R. J. (2012). "The Deborah and Weissenberg numbers." The British Society of Rheology, Rheology Bulletin 53(2): 32-39.

Poole, R. J. (2019). "Three-dimensional viscoelastic instabilities in microchannels." Journal of Fluid Mechanics 870: 1-4.

Poole, R. J., Alves, M. A., Afonso, A. P., Pinho, F. T. and Oliveira, P. J. (2007). “Purely-elastic flow instabilities in a microfluidic cross-slot geometry.”

Poole, R. J., Alves, M. A. and Oliveira, P. J. (2007). "Purely elastic flow asymmetries." Phys Rev Lett 99(16): 164503.

Poole, R. J., Lindner, A. and Alves, M. A. (2013). "Viscoelastic secondary flows in serpentine channels." Journal of Non-Newtonian Fluid Mechanics 201: 10-16.

Qin, B. and Arratia, P. E. (2017). "Characterizing elastic turbulence in channel flows at low Reynolds number." Physical Review Fluids 2(8): 083302.

Raihan, M. K., Wu, S., Song, Y. and Xuan, X. (2021). "Constriction length dependent instabilities in the microfluidic entry flow of polymer solutions." Soft Matter 17(40): 9198-9209.

Rallison, J. M. (1984). "The deformation of small viscous drops and bubbles in shear flows." Annual Review of Fluid Mechanics 16(45): 45-66.

Rapp, B. E. (2017). Chapter 9- Fluids. Microfluidics: Modelling, Mechanics and Mathematics, Elesvier.

Rapp, B. E. (2017). Fluids. Microfluidics: Modelling, Mechanics and Mathematics: 243-263.

Reynolds, O. (1883). "An experimental investigation of the circumstances which determine whether the motion of water shall be direct or sinuous, and of the law of resistance in parallel channels." Phil. Trans. R. Soc. 174: 935-982.

Rocha, G. N., Poole, R. J., Alves, M. A. and Oliveira1, P. J. (2008). “Numerical study of the flow of FENE-CR viscoelastic fluids in a planar cross-slot geometry” II Conferencia Nacional de Métodos Numéricos em Mecânica de Fluidos e Termodinâmica ‘08, Ed. V.A.F. Costa et al, Univ. Aveiro, 8 e 9 Maio 2008 (e CD-ROM). Aveiro, Portugal.

Roché, M., Li, Z., Griffiths, I. M., Le Roux, S., Cantat, I., Saint-Jalmes, A. and Stone, H. A. (2014). "Marangoni Flow of Soluble Amphiphiles." Physical Review Letters 112(20): 208302.

Rodd, L. E., Scott, T. P., Boger, D. V., Cooper-White, J. J. and McKinley, G. H. (2005). "The inertio-elastic planar entry flow of low-viscosity elastic fluids in micro-fabricated geometries." Journal of Non-Newtonian Fluid Mechanics 129(1): 1-22.

Saffman, P. G. (1986). "Viscous fingering in Hele-Shaw cells." Journal of Fluid Mechanics 173: 73-94.

Saffman, P. G. and Taylor, G. I. (1958). "The penetration of a fluid into a porous medium or Hele-Shaw cell containing a more viscous liquid." Proc. Royal Society London 245(1242): 312-329.

Seemann, R., Brinkmann, M., Pfohl, T. and Herminghaus, S. (2012). "Droplet based microfluidics." Rep Prog Phys 75(1): 016601.

Shaqfeh, E. S. G. (1996). "Purely elastic instabilities in viscometric flows." Annual Reviews Fluid Mechanics 160: 122-139.

Shaqfeh, E. S. G., Muller, S. J. and Larson, R. G. (1992). "The effects of gap width and dilute solution properties on the viscoelastic Taylor-Couette instability." Journal of Fluid Mechanics 235(-1): 285-317.

Shiang, A. H., ztekin, A. O., Lin, J.-C. and Rockwell, D. (2000). "Hydroelastic instabilities in viscoelastic flow past a cylinder confined in a channel." Experiments in Fluids 28: 128—142.

Soulages, J., Oliveira, M. S. N., Sousa, P. C., Alves, M. A. and McKinley, G. H. (2009). "Investigating the stability of viscoelastic stagnation flows in T-shaped microchannels." Journal of Non-Newtonian Fluid Mechanics 163(1-3): 9-24.

Sousa, P. C., Coelho, P. M., Oliveira, M. S. N. and Alves, M. A. (2009). "Three-dimensional flow of Newtonian and Boger fluids in square–square contractions." Journal of Non-Newtonian Fluid Mechanics 160(2-3): 122-139.

Sousa, P. C., Pinho, F. T., Oliveira, M. S. and Alves, M. A. (2015). "Purely elastic flow instabilities in microscale cross-slot devices." Soft Matter 11(45): 8856-8862.

Sousa, P. C., Pinho, F. T., Oliveira, M. S. N. and Alves, M. A. (2010). "Efficient microfluidic rectifiers for viscoelastic fluid flow." Journal of Non-Newtonian Fluid Mechanics 165(11-12): 652-671.

Sousa, P. C., Pinho, F. T., Oliveira, M. S. N. and Alves, M. A. (2012). "High performance microfluidic rectifiers for viscoelastic fluid flow." RSC Adv. 2(3): 920-929.

Steinberg, V. (2021). "Elastic Turbulence: An Experimental View on Inertialess Random Flow." Annual Review of Fluid Mechanics 53(1): 27-58.

Tao, R., Ng, T., Su, Y. and Li1, Z. (2020). "A microfluidic rectifier for Newtonian fluids using asymmetric converging–diverging microchannels." Physics of Fluids 32(5): 52010.

Taylor, G. I. (1923). "VIII. Stability of a viscous liquid contained between two rotating cylinders." Philosophical Transactions of the Royal Society of London. Series A, Containing Papers of a Mathematical or Physical Character 223(605-615).

Taylor, G. I. (1960). "Deposition of a viscous fluid on the wall of a tube." Journal of Fluid Mechanics 10(02): 161-165.

Utada, A. S., Fernandez-Nieves, A., Stone, H. A. and Weitz, D. A. (2007). "Dripping to jetting transitions in coflowing liquid streams." Phys Rev Lett 99(9): 094502.

Varchanis, S., Hopkins, C. C., Shen, A. G., Tsamopoulos, J. and Haward, S. J. (2020). "Asymmetric flows of complex fluids past confined cylinders: A comprehensive numerical study with experimental validation." Phys Fluids (1994) 32(5): 053103.

Wang, J., Wang, J., Feng, L. and Lin, T. (2015). "Fluid mixing in droplet-based microfluidics with a serpentine microchannel." RSC Advances 5(126): 104138-104144.

Wang, N., Semprebon, C., Liu, H., Zhang, C. and Kusumaatmaja, H. (2020). "Modelling double emulsion formation in planar flow-focusing microchannels." Journal of Fluid Mechanics 895: A22.

White, F. M. (1991). Viscous FluidFlow. New York, McGraw-Hill Book Co.

White, J. L. (1964). "Dynamics of viscoelastic fluids, melt fracture, and the rheology of fiber spinning." Journal of applied polymer science 8(5): 2339-2357.

White, J. L. (1964). "Dynamics of viscoelastic fluids, melt fracture, and the rheology of fiber spinning." Applied Polymer Science 8: 2339-2357.

Whitesides, G. M. (2006). "The origins and the future of microfluidics." Nature 442(no. 7101): 368-373.

Yanan Liu, Konstantinos Zografos, Joana Fidalgo, Charles Duchêne, Clément Quintard, Thierry Darnige, Vasco Filipe, Sylvain Huille, Olivia du Roure, Monica S. N. Oliveira and Lindner, A. (2020). "Optimised hyperbolic microchannels for the mechanical characterisation of bio-particles." Soft Matter 16(43): 9844-9856.

Yih, C.-S. (1967). "Instability due to viscosity stratification." Journal of Fluid Mechanics 27(2): 337-352.

Zilz, J., Poole, R. J., Alves, M. A., Bartolo, D., Levaché, B. and Lindner, A. (2012). "Geometric scaling of a purely elastic flow instability in serpentine channels." Journal of Fluid Mechanics 712: 203-218.

Zografos, K., Haward, S. J. and Oliveira, M. S. N. (2019). "Optimised multi-stream microfluidic designs for controlled extensional deformation." Microfluidics and Nanofluidics 23(12): 1-21.

CHAPTER 3

Experimental Methods

This chapter details the various experimental procedures involved in this research. It begins by discussing how the microfluidic devices are fabricated before proceeding to a general overview of the fluids used, how they are prepared and finally how they are characterised. The final section of this chapter details the general experimental set up for flow visualisation. Further information on specific experimental techniques employed for each section of work will be provided in each individual results chapter (Chapters 4 - 6).

3.1 FABRICATION OF MICROFLUIDIC DEVICES

Early microfluidic devices were fabricated using glass or silicon materials however, it is now common to use polymer materials instead due to their low cost, small fabrication timescales and other advantages. PDMS (polydimethylsiloxane) is arguably one of the most common polymer materials used to fabricate microfluidic devices and presents several advantages (Tsao 2016). The advantages of using PDMS include: ease of use and low fabrication costs compared to other materials; high optical transmissivity allowing flow to be easily visualised inside the channels using a microscope; high gas permeability allowing air bubbles to be easily removed from experimentation; good thermal stability allowing the microfluidic devices to be easily cured thermally and PDMS is chemically inert to most fluids (Xia and Whitesides 1998). There are various fabrication techniques that can be adopted using PDMS (McDonald and Whitesides 2002). The microfluidic devices used in this work were fabricated using soft-lithography by casting polydimethylsiloxane (PDMS) onto pre-made silicon SU-8 moulds. Fabricating the microfluidic devices involves various steps that have to be carried out with precision to ensure microfluidic devices can be produced repeatedly and accurately. Ideally, this process should be performed in a clean room where the level of contaminants, such as dust and other particles are minimised, and temperature and humidity are well controlled. Figure 3.1 shows a schematic of the described process.

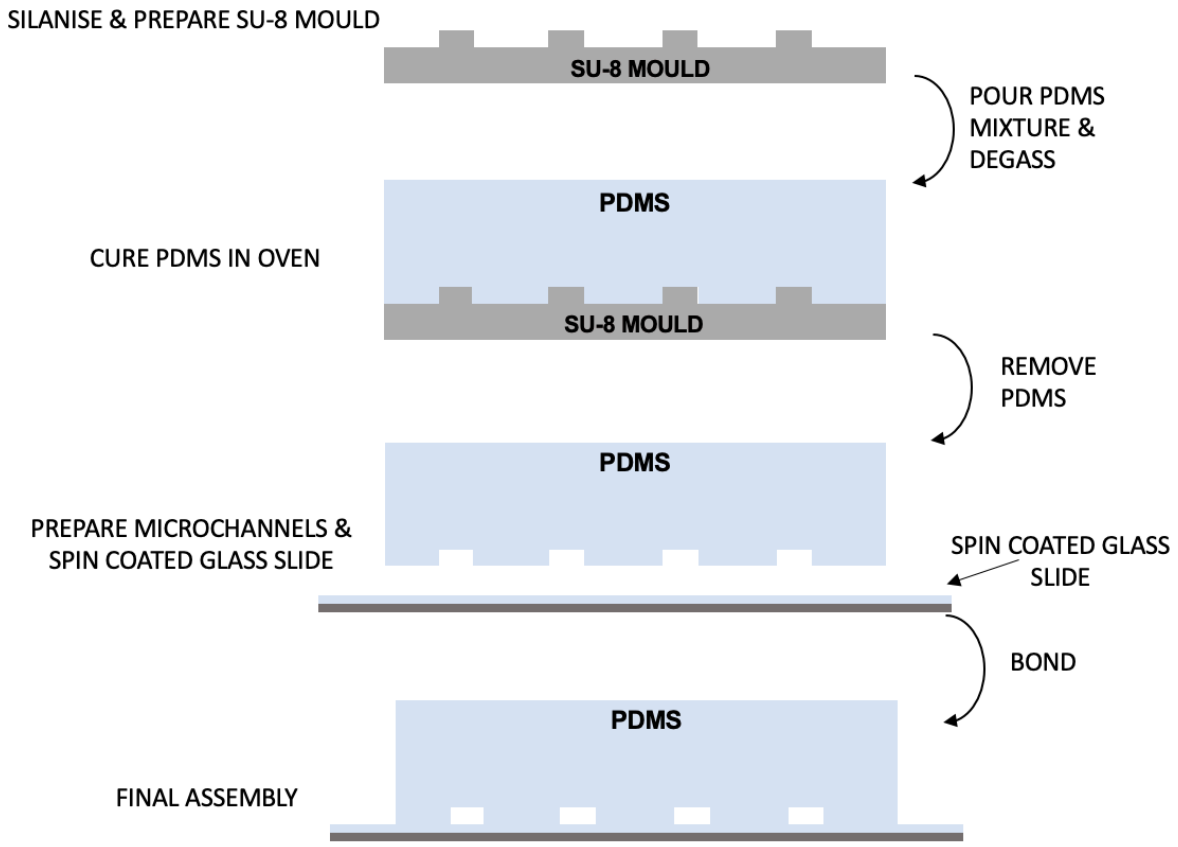

Figure 3.1: Schematic of PDMS microfluidic device fabrication procedure.

Step 1: Preparation and silanise the SU-8 Mould

In order to aid the release of PDMS from the SU-8 silicon mould, silanisation must first be carried out before the fabrication process and repeated when the PDMS becomes difficult to remove from the mould. This process is carried out in a fume hood and uses vapour deposition (Sousa 2010).

The SU-8 mould is initially washed using isopropanol and dried using compressed air inside a fit-for-purpose room. The mould is then placed in an uncovered petri dish inside the fume hood. Using a pipette, drops of Trichlorosilane ((TRICHLORO(1H,1H,2H,2H-PERFLUOROOCTYL)-SI), Sigma Aldrich) are placed on the petri dish to the side of the mould. This is left inside the fume hood for 25 minutes to allow the vapour to deposit onto the mould. The mould is then transferred into a clean petri dish and covered.

After silanisation, aluminium foil is placed around the mould to avoid spillage of PDMS during the next stage. It is important that the aluminium foil is flat across the base of the mould to ensure a flat microfluidic device is produced. The mould is then placed into a clean petri dish.

Step 2: Prepare the PDMS Mixtures

PDMS (Sylgard 184, Dow Corning) is mixed with the curing agent at a desired ratio (Curing Agent: PDMS). Increasing this ratio is known to increase the Young's Modulus of the material and thus the overall stiffness of the produced microfluidic device (Kim et al. 2015). Different ratios were tested for the two connecting PDMS layers in order to obtain a high-quality seal. For the microfluidic devices in this work a ratio of 1:9 was used and a ratio of 1:20 was used for the thin PDMS layer that covers the glass slide. A mixer (THINKY ARE-250 CE) was used to homogenise the PDMS mixtures.

The PDMS mixture, at a ratio of 1:9, is poured into the mould (cf. Figure 3.1b). The combined mould and PDMS is then placed in a desiccator connected to a vacuum pump to remove all air bubbles from the mixture.

Step 3: Prepare Glass Slides and Spin Coat

Trials were performed where the bonding conditions and cleaning procedures were varied. The optimum conditions found were then used for all microfluidic devices produced.

The glass slides are cleaned using isopropanol and dried using compressed air before being placed in the spin coater (Laurell Technologies, WS-650 Series) and secured using vacuum. A small quantity (1 ml) of the 1:20 PDMS mixture is deposited onto the stationary cleaned glass slide before the spin coater program is activated.

The spin coater program operates in a 3 stage cycle: In stage 1 the rotational velocity of the sample is increased quickly to a desired value; in stage 2 the sample is held at this constant rotational velocity where the PDMS is spread over the glass slide to create a uniform layer; in stage 3 the rotational velocity is reduced to zero, cf. Figure 3.2.

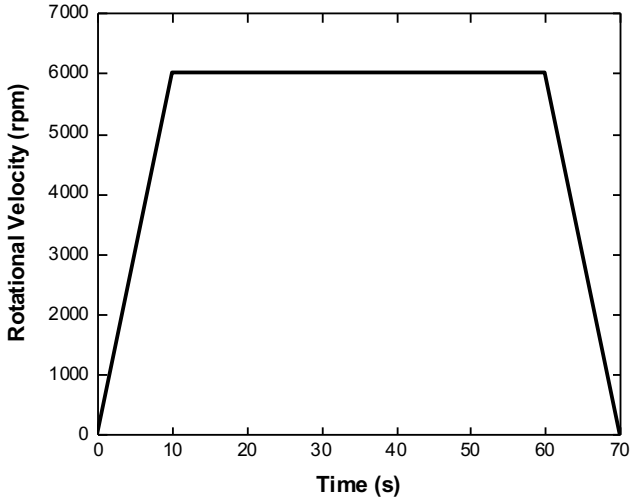

Figure 3.2: Spin coating program used to coat the glass slides with PDMS for microchannel fabrication - 3 Stage Cycle with a maximum rotational velocity of 6000 rpm and a hold time of 50 s.

The conditions used for this work were a rotational velocity of 6000 rpm and a hold time of 50 seconds. This produces a PDMS layer of approximately 45 μm, a reasonable thickness allowing it to be easily bonded whilst being thin enough for flow visualisation using the microscope. During the trials it was found that increasing the rotational velocity caused a reduction of the thickness of the PDMS layer in agreement with previous research (Scriven 1988).

Step 4: Curing PDMS

The PDMS coated glass slide and the combined mould with PDMS were placed into the oven to cure for 25 minutes at 80°C.

Step 5: Prepare the Microfluidic Devices

After the PDMS is cured and removed from the oven the mould is left to cool. The cured coated glass slides are placed into a covered petri dish to avoid contamination. To avoid causing damage to the silicon mould, thin layers are removed from the edges and base of the mould using a sharp scalpel blade, before carefully removing the PDMS from the silicon mould. Using the sharp scalpel blade the PDMS is cut into

smaller blocks around the microfluidic devices to a size suitable to fit onto a standard glass slide. The holes for inlets and outlets were punched perpendicularly using a hole punch. The PDMS surfaces are then cleaned using scotch tape to remove excess PDMS before washing with isopropanol and then dried using compressed air.

Step 6: Final Assembly

The PDMS microfluidic device is then placed face down onto the PDMS coated glass slide. In some cases, a small pressure is applied to ensure a high-quality seal. The final assembled device is then placed into the oven to cure for a further 12 hours at 80°C. When the devices are removed from the oven it is important to cover the inlet and outlet ports with scotch tape to avoid contamination. The final assemblies are then placed in a clean petri dish for safe storage.

For this work, microchannels of various geometric configurations were created using this procedure for a range of channel widths $(96\ \mu m < W < 126\ \mu m)$ and channel depths $(26\ \mu m < D < 92\ \mu m)$. Although the microchannels are designed to have sharp corners, due to the fabrication method adopted this is not the case. As such, the corners will always be slightly rounded in experimental work conducted in this thesis, an aspect that is not studied in the work presented. It is believed that the corners have no noticeable effect on the flow patterns/ findings of this work for all of the flow conditions studied.

3.2 FLUID PREPARATION & CHARACTERISATION

This section gives a brief introduction to the classification of fluids depending on their rheological behaviour before explaining how the fluids used in this work were prepared. A detailed description of how these fluids are characterised using various rheological measurements is then provided.

3.2.1 Rheological Behaviour

The term “Rheology” is defined as *the study of the deformation and flow of matter* with the term “Rheo” taken from the Greek word “Rhein” meaning flow. This definition was first proposed by Professor Bingham and then accepted when the American Society of Rheology was founded in 1929 (Barnes et al. 1989, Morrison 2001, Irgens 2014). Rheology plays a role in many aspects of our everyday lives from the blood that flows in our bodies to the fluids we consume, and in several industrial industries such as chemical engineering, material science and biology (Barnes 2000, Morrison 2001).

In general, fluids can be classed as being part of one of two main categories namely Newtonian Fluids or Non-Newtonian Fluids.

3.2.1.1 Newtonian Fluids

Newtonian Fluids follow Sir Isaac Newton’s law of viscosity where the shear stress (τ_{xy}) is linearly proportional to the shear rate ($\dot{\gamma}$):

$$\tau_{xy} = \mu\dot{\gamma} \qquad (3.1)$$

Consider the shear flow of a fluid of viscosity μ (Pa s) between two parallel plates, separated by a distance, d (m), with the upper plate moving at velocity, U (m/s), and the bottom plate remaining stationary as shown in Figure 3.3 (Barnes et al. 1989).

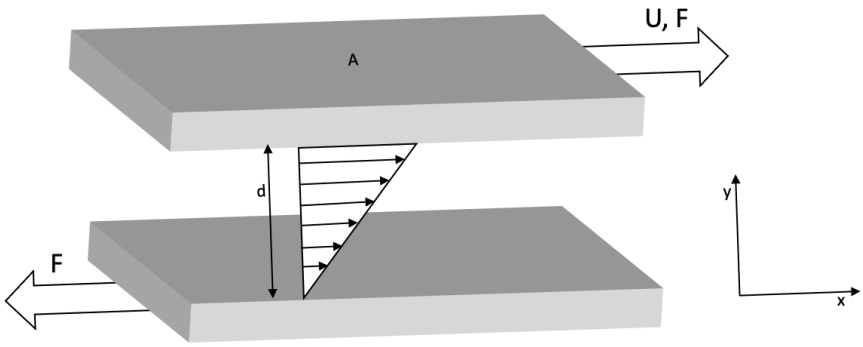

Figure 3.3: Schematic of steady simple shear flow showing a fluid between two parallel plates.

In order to move this top plate at a constant velocity a tangential driving force, F (N), is applied. The shear stress, τ_{xy}, that resists this motion is defined in terms of the material area, A (m^2), to which this force is applied:

$$\tau_{xy} = \frac{F}{A} \quad (3.2)$$

The shear stress between adjacent fluid layers is proportional to the velocity gradients between the two layers:

$$\dot{\gamma} = \frac{dU}{dy} = \frac{U}{d} \quad (3.3)$$

The constant of proportionality in this case is the coefficient of viscosity, μ (Pa s). The shear viscosity can be understood as a fluid's resistance to shear flow (Barnes et al. 1989). Newtonian fluids have a constant viscosity at all shear rates. Common fluids, such as water, honey and oil are classed as Newtonian fluids.

3.2.1.2 Non-Newtonian Fluids

Fluids that do not follow Newton's law of viscosity are called non-Newtonian fluids. Typically, the viscosity of a non-Newtonian fluid is shear rate dependent:

$$\tau_{xy} = \mu(\dot{\gamma})\,\dot{\gamma} \quad (3.4)$$

Non-Newtonian fluids can be divided into three main categories namely: time-dependent fluids, time-independent fluids and viscoelastic fluids (Irgens 2014).

Time-dependent fluids are said to be the more complex, where for a constant shear rate, the shear stress can change over time. This includes e.g., thixotropic fluids, where the shear stress of the fluid decreases over time, and rheopectic fluids, where the shear stress increases over time (Irgens 2014).

Time-independent fluids are often called “generalised Newtonian Fluids”. A common fluid in this category is the Bingham fluid. This fluid is said to have a yield-stress below which the fluid will not flow. Beyond this critical value the fluid flows can behave as a Newtonian fluid (Barnes et al. 1989). Other common generalised Newtonian fluids include shear thickening or shear thinning inelastic fluids. A shear thickening fluid has a viscosity that increases with increasing shear rate. A shear thinning fluid behaves in precisely the opposite way with the viscosity of the fluid decreasing as the shear rate increases (Irgens 2014).

Materials respond in different ways when subjected to a shear stress. When the applied shear stress is removed a material can instantly return to its original equilibrium state (elastic response) or permanently deform (viscous response). Viscoelastic fluids exhibit a combination of both elastic and viscous behaviour (Irgens 2014). A viscoelastic fluid can be created e.g., by adding small amounts of a high-molecular weight polymer to a viscous Newtonian solvent. These fluids are said to exhibit a memory, when the applied shear stress is removed the viscoelastic fluid will return back to its equilibrium state, not instantly, but in a timescale defined as the relaxation time of the fluid, $\lambda\,(\mathrm{s})$ (Morrison 2001).

It is often the case that non-Newtonian fluids fall under multiple categories for example it is common to have a viscoelastic fluid that exhibits shear thinning behaviour.

3.2.2 Working Fluid Preparation

In this thesis both Newtonian and non-Newtonian viscoelastic fluids were used. The Newtonian fluids were deionised water or water and glycerol solutions. The properties of these fluids have been studied extensively in past research (Association 1963). A variety of solutions were prepared with varying concentrations of glycerol to cover a range of viscosities. The fluid composition was often made to ensure the shear viscosity was comparable to a specific viscoelastic fluid. The prepared solutions were divided into two parts where Rhodamine-B dye (Sigma-Aldrich) at a concentration of around 0.016%, or 1 μm fluorescent tracer particles (FluoSpheres carboxylate-modified, 1.0 μm, Nile Red) at concentration of approximately 0.02%wt, were added

for flow visualisation. In the cross-slot experiments (Chapter 4) deionised water or Perfluorodecalin (HPF10, Sigma Aldrich) were used as reference fluids.

The non-Newtonian viscoelastic fluids used here are solutions of high molecular weight polymer in a viscous Newtonian solvent. The polymer used in this work is Polyethylene oxide (PEO) with a high molecular weight, M_w (4x10^6 or 8x10^6 g/mol). Polymers with a high molecular weight generally have long chains meaning the associated polymeric fluids find it more difficult to flow due to polymer entanglement (highly dependent on the polymer concentration of the solution). This results in the fluids having higher fluid viscosities and enhanced elastic properties than fluids that involve lower molecular weight polymers (Ebnesajjad 2016). PEO is a water-soluble polymer that is used in various branches of industry such as cosmetics, pharmacy and medicine (Hassouna et al. 2007).

The viscoelastic fluids were prepared by weighing the individual fluid components using a precision balance (OHAUS, Adventurer Pro AV264C) to achieve the desired composition. The PEO powder was added to deionised water and mixed gently using a magnetic stirrer at a low rotational speed to avoid degradation of the polymer. This fluid was left to mix for at least 24 hours, or until the polymer had completely dissolved, at ambient room temperature (20-22°C). When necessary, the desired amount of glycerol was then added to the PEO-water mixture and mixed gently again using the magnetic stirrer at a low rotational speed. This solution was left to mix for approximately 1 hour at ambient room temperature (20-22°C) until homogeneous. Hassouna et al studied the photodegradation of PEO and found that this could be more problematic in dilute solutions than in more concentrated solutions (Hassouna et al. 2007). As such, the solutions were prepared and stored in sealed glass containers covered with tin foil to avoid photodegradation of the polymer. These dark containers were stored in the fridge. The prepared solutions were seeded with ≈ 1 μm fluorescent tracer particles (FluoSpheres carboxylate- modified, 1.0 μm, Nile Red) at a concentration of approximately 0.02%wt, to be used in flow visualisation.

3.2.3 Intrinsic Viscosity

The intrinsic viscosity, $[\eta]$ (cm^3/g), is defined as the polymer's contribution to the total viscosity of the solution at zero shear rate (Bird et al. 1977). For dilute solutions this can be expressed as:

$$[\eta] = \lim_{\dot{\gamma}\to 0} \lim_{c\to 0} \frac{\mu - \mu_s}{\mu_s c} \qquad (3.5)$$

where μ_s (Pa s) is the viscosity of the Newtonian solvent into which the polymer is dissolved and c is the polymer concentration. The intrinsic viscosity is related to molecular weight using a power law expression, known as the Mark–Houwink relation:

$$[\eta] = K_P M_w^{\,a_P} \qquad (3.6)$$

where K_P and a_P are constants relating to the polymer, the Newtonian solvent, and the temperature. For the PEO solutions (PEO in aqueous solutions of water or water and glycerol) this relation can be expressed as (Tirtaatmadja et al. 2006):

$$[\eta] = 0.072 M_w^{\,0.65} \qquad (3.7)$$

3.2.4 Critical Overlap Concentration

The critical overlap concentration, c^*, is an important characteristic of a polymer solution and is used to categorise a polymeric fluid as either dilute, semi-dilute or concentrated. For a PEO solution this can be calculated as (Grassley 1980):

$$c^* = \frac{0.77}{[\eta]} \qquad (3.8)$$

The definition of the critical overlap concentration is the concentration for which the polymer coils within a polymeric solutions begin to overlap with each other (Tirtaatmadja et al. 2006). When the concentration of the polymeric solution, $c << c^*$,

the solution can be considered dilute. In these solutions there is little or no polymer interactions within the fluid (R. Larson et al. 1994). For most of these solutions the fluid viscosity appears constant for all values of shear rate. As the concentration of polymer is increased so that $c \sim c^*$, the solution is then considered "semi-dilute" where polymer interactions are known to occur within the fluid and shear thinning properties of the fluids can arise. Increasing the concentration further beyond c^*, where $c >> c^*$, the fluid is said to enter the "entangled" regime (Clasen et al. 2006).

3.2.5 Solvent Quality

Tirtaatmadja et al (2006) found that both water and mixtures of glycerol and water can be classed as "good solvents" for PEO. Using the Zimm theory for dilute solutions of polymer coils in a solvent incorporating hydrodynamic interactions, the solvent quality, υ, for the solvents used in this work was found to be 0.55 (Tirtaatmadja et al. 2006). This solvent quality can be utilised to form another expression to calculate the intrinsic viscosity:

$$[\eta] \sim M_w^{3\upsilon - 1} \qquad (3.9)$$

The limiting values of the solvent quality, υ, lie within 0.5 and 0.6, representing a theta solvent and good solvent, respectively (Doi and Edwards 1986).

3.2.6 Shear Rheology

Steady shear measurements were conducted for both Newtonian and viscoelastic fluids on a controlled stress DHR-2 Rotational Rheometer (TA Instruments) to measure shear viscosities.

In this thesis, all fluids were characterised using a cone and plate geometry which allows for a uniform shear-rate throughout the fluid sample. The geometry used has a diameter of 60 mm and a cone angle of 1°. The manufacturer's software TRIOS was utilised to collect the experimental data. This is a commonly used geometry for rheological measurements due to its good precision and accuracy alongside its ease of use (Strivens and Schoff 2010). This geometry operates in a similar way to the

parallel plate where the sample is placed on the bottom stationary plate. This plate is a Peltier plate and with the help of a thermostatic bath, controls the temperature imposed on the sample. The top geometry is lowered with the sample filling completely the space between both the geometry and the Peltier plate. Advantages for using this geometry is that only a small amount of sample is required to perform the tests and the shear rate is kept uniform throughout (Barnes 2000). The cone is truncated to ensure it does not come into contact with the bottom plate, avoiding friction and other mechanical errors occurring, as shown in Figure 3.4.

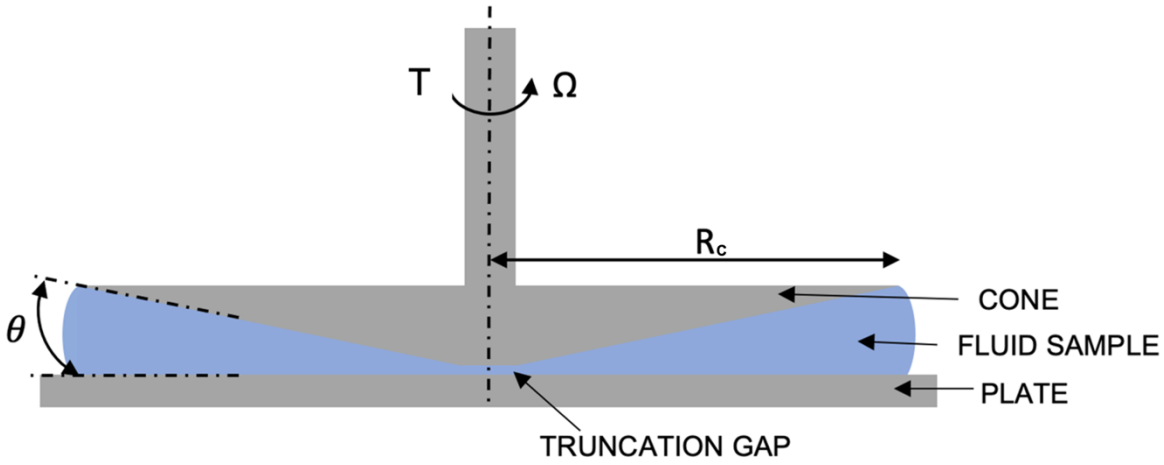

Figure 3.4: Schematic of cone and plate geometry used to characterise fluid samples under shear.

The angular velocity, Ω, increases linearly with distance from the centre of the geometry however, due to the small cone angle, θ, the gap height also increases allowing the shear rate to maintain a constant value. The shear rate can be expressed as:

$$\dot{\gamma} = \frac{\Omega}{\theta} \qquad (3.10)$$

The torque, T, applied on the cone for a certain angular velocity along with the radius of the cone, R_C, can be used to calculate the shear stress τ_{xy}:

$$\tau_{xy} = \frac{3T}{2\pi R_c^{\,3}} \qquad (3.11)$$

The viscosity can then be calculated as (Barnes 2000):

$$\mu(\dot{\gamma}) = \frac{\tau_{xy}}{\dot{\gamma}} = \frac{3T\theta}{2\Omega\pi R_c^{\,3}} \qquad (3.12)$$

Measured values of the viscosity were taken every 10 seconds and steady state conditions were satisfied when 3 consecutive measurements were within 3%. Research conducted by Sdougos et al (2006) iterates the importance of determining the upper and lower limits for which the viscosity can be measured for each geometry. For the cone and plate geometry the minimum limit was calculated using 20x the minimum measurable torque of the rheometer, (equation (3.13), where T_{MIN} = 10 nN m for the DHR-2 rheometer (TA Instruments (2013)) to be conservative:

$$\mu_{MIN}(\dot{\gamma}) = \frac{3\left(20T_{MIN}\right)}{2\pi R_c^{\,3}\dot{\gamma}} \qquad (3.13)$$

The maximum measurable torque of the DHR-2 rheometer is given as 200 mN m (TA Instruments (2013)).

Inertial instabilities are also known to occur in shear measurements and are more than likely to occur prior to reaching the maximum measurable torque limit of the rheometer. These instabilities are due to high angular velocities and resulting strong centrifugal forces (Strivens and Schoff 2010). An additional upper limit for the measurable shear viscosity is therefore calculated as (Sdougos et al. 2006):

$$\mu_{MAX}(\dot{\gamma}) = \frac{\Omega\theta^2\rho R_c^{\,2}}{6} \qquad (3.14)$$

Figure 3.5 exemplifies experimental data from the controlled stress DHR2- Rotational Rheometer (TA Instruments) at a temperature of 20℃ ± 1℃ highlighting all applicable limits of measurement as outlined above in equations (3.13) and (3.14).

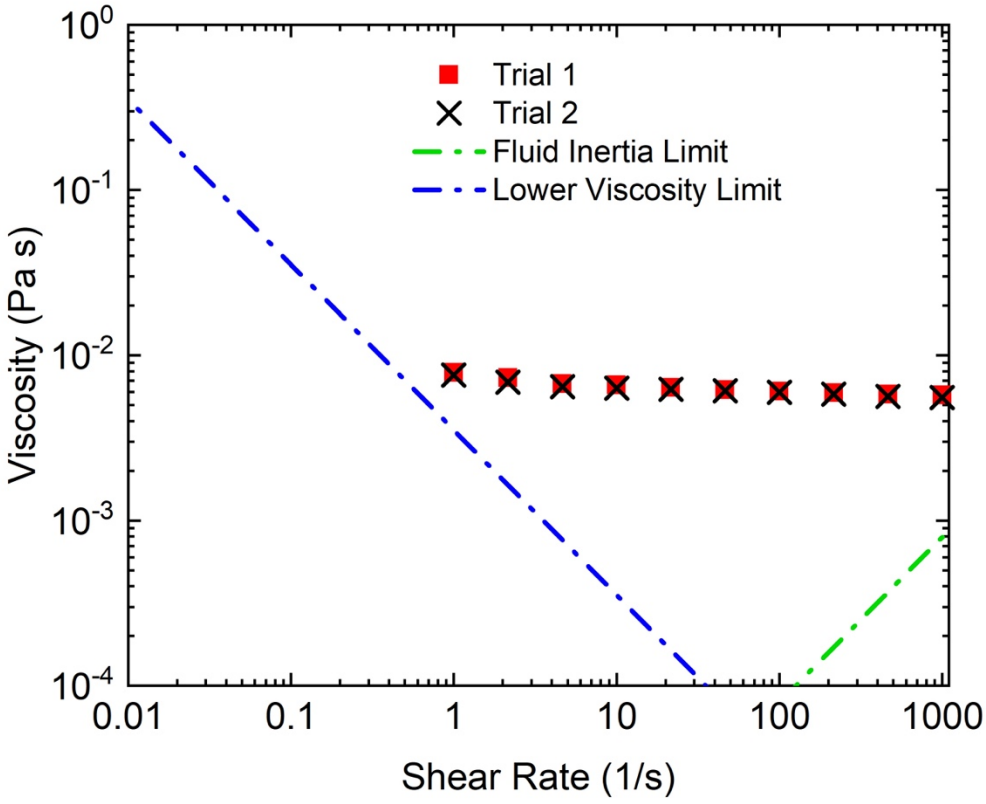

Figure 3.5: Shear rheology data (DHR-2 Rotational Rheometer) for a dilute polymer solution of PEO (M_w 8x10^6) at a concentration of 280ppm in a 60/40 solution of water and glycerol highlighting applicable rheometer limits outlined in equations (3.13) (Lower Viscosity Limit) and (3.14) (Fluid Inertia Limit).

3.2.7 Extensional Rheology

The rheological behaviour of fluids must also be understood in extensional flow however, this is known to be difficult for low-viscosity fluids (Sousa et al. 2016). For a Newtonian fluid a simple correlation exists where the viscosity measured using uniaxial extensional flow is three times that of the viscosity measured under shear (Barnes et al. 1989). For non-Newtonian fluids however, the ratio of extensional viscosity to the shear viscosity can vary and be orders of magnitude greater than for Newtonian fluids. Previous researchers have looked into various configurations to measure the properties of these fluids under extensional flow and this work uses the Capillary Breakup Extensional Rheometer (CaBER) device which is frequently used

to measure the relaxation times of viscoelastic fluids with low viscosities and low elasticities (Galindo-Rosales et al. 2012).

In this thesis, a HAAKE Capillary Breakup Extensional Rheometer (CaBER, Thermo Scientific) is used to measure the extensional properties and in particular the relaxation time of the complex fluids. The fluid is loaded between two cylindrical plates of diameter, D_{PLATE}, initially separated by height, h_0 as shown in Figure 3.6a. The fluid forms a liquid bridge. The plates are then separated rapidly by an applied axial step-strain to a final height, h_f causing the liquid bridge to become unstable and subsequently thin under capillary forces (cf. Figure 3.6b). The filament diameter, D_F, decreases as a function of time under these capillary forces and is strongly influenced by the viscous, elastic and inertial effects within the fluid. The filament diameter is measured at the mid-point to then determine the relaxation time of the fluid (McKinley et al. 2001). This process is illustrated in Figure 3.6.

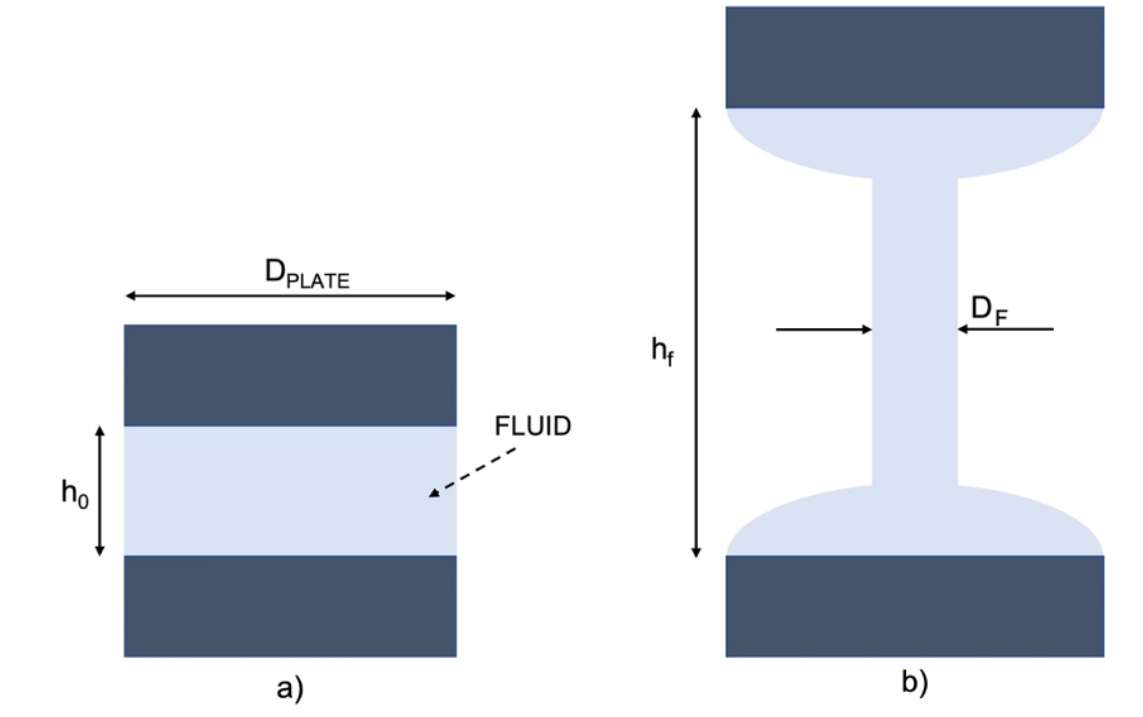

Figure 3.6: Schematic of Capillary Breakup Extensional Rheometer (CaBER, Thermo Scientific) operation process, a) initial configuration b) after the applied step-strain – during the capillary thinning.

The initial loading of the sample between the cylindrical plates can play an important role in obtaining reliable results. According to Rodd et al (2005) the optimal loading conditions correspond to an aspect ratio in the range $0.5 \leq AR_0 \leq 1$. The aspect ratio of the initial sample loading can be calculated as:

$$AR_0 = \frac{h_0}{D_{PLATE}} \quad (3.15)$$

Ideally this initial liquid bridge should maintain a cylindrical shape. To support this, the initial plate separation, h_0, must be smaller than or equivalent to the capillary length, l_{cap}, calculated using the surface tension of the fluid, σ, (Rodd et al. 2005) as:

$$h_0 \leq l_{cap} = \sqrt{\frac{\sigma}{\rho g}} \quad (3.16)$$

The total stretch imposed on the sample is controlled by the final aspect ratio, when the plates are fully separated:

$$AR_f = \frac{h_f}{D_{PLATE}} \quad (3.17)$$

In the present work, the diameter of the plates used in the CaBER was 6 mm. The initial sample height, h_0, imposed depended greatly on the fluid properties and was typically in the range of 2.50 - 3.01 mm ($AR_0 = 0.4 - 0.5$), and the final sample height, h_f was set to a value of around 9.22 mm ($AR_f = 1.53$). Both values lie within the recommended operating ranges. The applied step-strain duration was typically 50 ms and the fluid filament diameter at the mid-point was measured using a laser (resolution of 10 μm).

Following Macosko (1994), for a steady uniaxial extension of a fluid with a typically constant rate of extension, $\dot{\varepsilon}$, the velocity components can be expressed by:

$$u_x = \dot{\varepsilon} x \tag{3.18}$$

$$u_r = -\frac{1}{2}\dot{\varepsilon} r \tag{3.19}$$

At the final sample height the rate of extension can be expressed by (Macosko and Larson 1994):

$$\dot{\varepsilon} = \frac{1}{h_f}\frac{dh_f}{dt} \tag{3.20}$$

The rate of extension can also be expressed in terms of the observed filament diameter (McKinley et al. 2001):

$$\dot{\varepsilon} = -\frac{2}{D_F(t)}\frac{dD_F(t)}{dt} \tag{3.21}$$

The Hencky Strain conveys the total deformation experienced by the fluid and is obtained by integrating the above equations (McKinley et al. 2001) :

$$\varepsilon_H = \dot{\varepsilon} t = \ln\left(\frac{h_f}{h_0}\right) = 2\ln\left(\frac{D_0}{D_F(t)}\right) \tag{3.22}$$

where D_0 represents the initial diameter of the filament at time $t = 0$. The capillary thinning and breakup of Newtonian and viscoelastic fluids is substantially different. The filament diameter of a Newtonian fluid decreases linearly with time and can be described as (Entov and Hinch 1997):

$$\frac{D_F(t)}{D_0} = \frac{\sigma}{6\mu D_0}\left(t_b - t\right) \tag{3.23}$$

where t_b is the critical breakup time for the breaking of the Newtonian filament. On the other hand, the filament diameter for a viscoelastic fluid decreases exponentially over time. This can be expressed as (Rodd et al. 2005):

$$\frac{D_F(t)}{D_0} = \left(\frac{G_E D_0}{2\sigma}\right)^{\frac{1}{3}} e^{\left(-t/3\lambda\right)} \qquad (3.24)$$

where G_E is the elastic modulus of the viscoelastic fluid with relaxation time λ. Liang and Mackley (1994) simplify this equation to first approximations allowing the characteristic time constant to be measured using:

$$\frac{D_F(t)}{D_0} \propto e^{\left(-t/3\lambda\right)} \qquad (3.25)$$

The relaxation time of the viscoelastic fluid can then be calculated by fitting experimental data from the HAAKE CaBER to the linear region of the $\log\left(D_F(t)/D_0\right)$ as a function of time plot.

To ensure accuracy and repeatability for each fluid, three measurements were taken each time. Figure 3.7 exemplifies experimental data from the HAAKE CaBER at a temperature of 20℃ ± 1℃ highlighting the linear region (in red) from which the relaxation time was obtained.

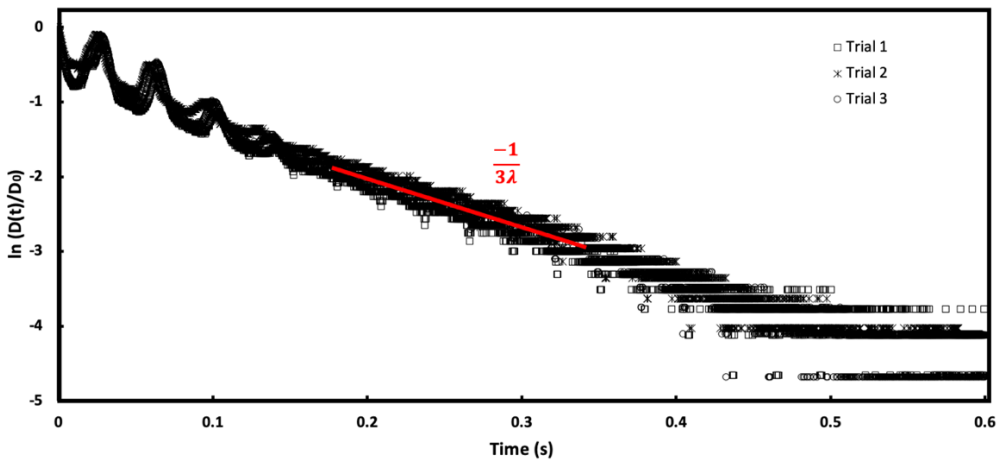

Figure 3.7: Extensional rheology data (CaBER) for a dilute polymer solution of PEO (M_w 8x10^6) at a concentration of 280ppm in a 60/40 solution of water and glycerol. The red line is an exponential fit within the elasto-capillary range (refer to equation (3.25)). The figure shows measurement of the fluid filament for different samples from a single fluid batch.

The data that lies before the linear region (0-0.15 ms) in Figure 3.7 highlights inertio-capillary oscillations that occur when the plates are initially separated which dampen due to the viscosity of the fluid (Oliveira et al. 2006). The data that falls after the linear region (0.35-0.6 ms) in Figure 3.7, represents the breakup of the fluid filament.

The quantitative results associated with Figure 3.7 can be found in Table 3.1 yielding a final average value of 51.58 ± 0.42 (where the error reported represents the standard deviation of the data).

Table 3.1: Quantitative data obtained from the exponential fit displayed in Figure 3.7 (refer to equation (3.25)). using extensional rheology data (CaBer). Data is shown for different samples from a single fluid batch of a dilute polymer solution of PEO (M_w 8x10^6) at a concentration of 280ppm in a 60/40 solution of water and glycerol.

Measurement	Relaxation Time (ms)
Trial 1	51.11
Trial 2	51.91
Trial 3	51.71

Research conducted by Rodd et al (2005) found that the minimum relaxation time measurable with the HAAKE CaBER is of the order 1 ms. Their work created an “operability diagram” as shown in Figure 3.8 and advises that multiple tests be performed for fluids near either of the boundaries (i.e., fluids with low relaxation time and/or low viscosity) to achieve the most reliable results.

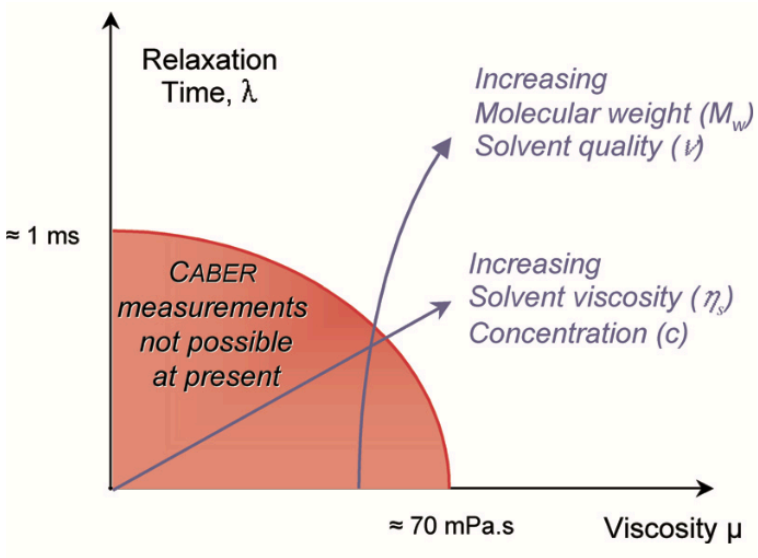

Figure 3.8: Operability diagram for CaBer from research conducted by Rodd et al (2005).

3.2.8 Surface and Interfacial Tension Measurements

Immiscible fluids that are brought together in a system remain separated by a thin fluid interface due to intermolecular forces (Israelachvili 1991, Berg 2010). These forces are a result of molecular interactions and stop molecules moving from one fluid to the other (diffusion) by forming an energy barrier. Van der Waals (1979) found that it was only above a critical temperature that the interface became ‘infinite’ thus lowering the energy barrier and allowing diffusion to take place. Otherwise, the interface between two immiscible fluids maintains a constant shape and the interfacial tension at this interface is deemed ‘static’.

To measure both the surface tension and interfacial tension between immiscible fluids in the present work, the pendant drop measuring technique was adopted. This method consists of a fluid droplet suspended from a metal needle in air or into another immiscible liquid using a cuvette. Gravitational forces deform the produced fluid droplet allowing an interfacial tension to be quantified from an extracted experimental image. Measurements were performed using a Kruss Drop Shape Analyser (model DSA25, (resolution of 0.01 mN/m)) with a needle of diameter 0.382 mm (cf. Figure 3.9).

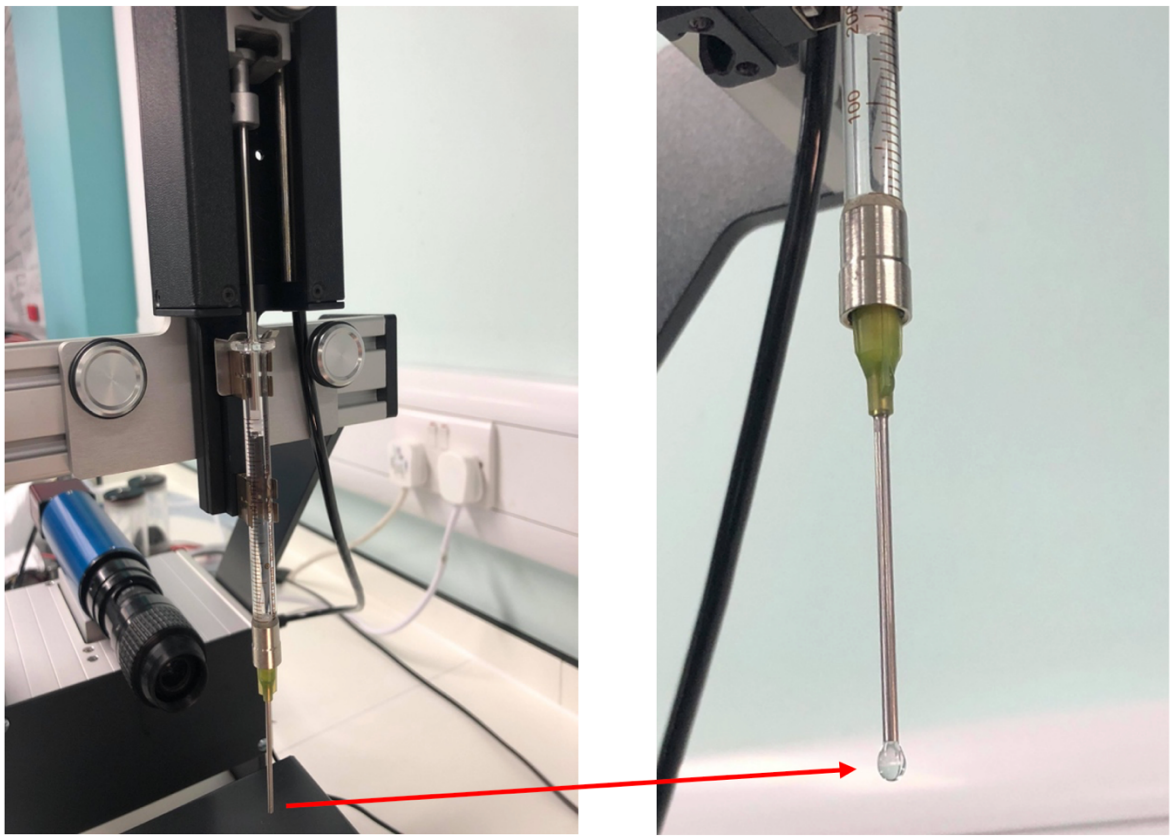

Figure 3.9: Image of KRUSS Drop Shape Analyser (model DSA25) set up highlighting the fluid droplet suspended from a metal needle in air.

To ensure the values obtained from this method are reliable and accurate there are a number of factors that must be adhered to.

- The experimentally observed droplet image must be as clear as possible to enable an accurate profile extraction to avoid irregularities from optical equipment and external light sources. In this work a diffused light source was used.
- The needle must be in a vertical position to ensure the z-direction of the droplet is parallel to gravitational forces.
- The fluid droplet must be as large as possible, without making the system unstable.

A static pendant drop obeys the Young-Laplace equation that was first numerically studied by Bashforth and Adams (1883). A schematic of the associated variables is shown in Figure 3.10.

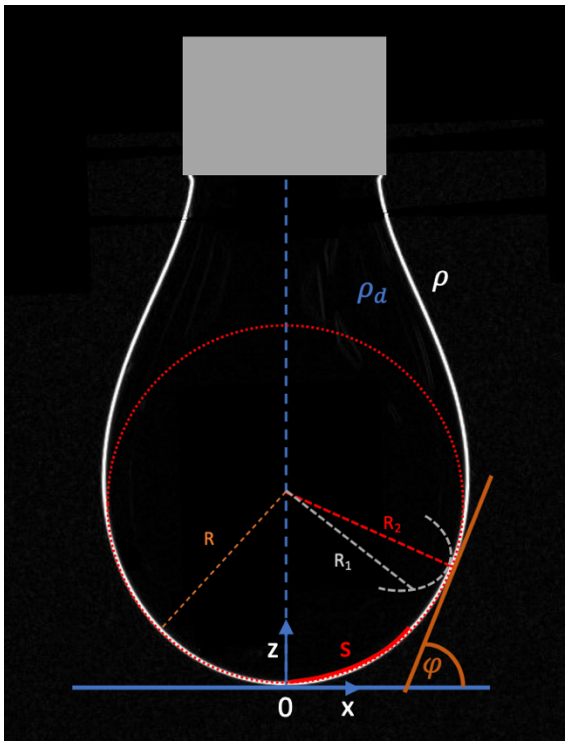

Figure 3.10: Schematic of extracted drop shape image showing Young-Laplace variables where ρ_d is the drop phase density, ρ is the density of the outer continuous phase φ is the tangent angle between the drop axis and the surface of an arbitrary reference plane with pressure Δp_0.

This relationship relates the surface tension/interfacial tension (σ), the pressure difference between the inside of the droplet and the surroundings (Δp) and the principal radii of curvature R_1 and R_2 of the droplet:

$$\sigma\left(\frac{1}{R_1}+\frac{1}{R_2}\right)=\Delta p \qquad (3.26)$$

The pressure difference (Δp) for the static system subject only to gravitational forces can be expressed as:

$$\Delta p=\Delta p_0-\Delta \rho g z=\Delta p_0-\left(\rho_d-\rho\right)gz \qquad (3.27)$$

where ρ_d is the drop phase density, ρ is the density of the outer continuous phase, z and x are distances from an arbitrary reference plane with pressure Δp_0 (Berg 2010).

At the lowest point of the droplet $R_1 = R_2 = R$ and $R_2 = {}^{x}/_{\sin\varphi}$, where φ is the tangent angle between the drop axis and the surface, giving:

$$\frac{1}{R_1} + \frac{\sin\varphi}{x} = \frac{2}{R} - \frac{\Delta\rho gz}{\sigma} \qquad (3.28)$$

Parameterisation using the arc length, s, allows the Young-Laplace equation to be expressed as a set of differential equations which are solved simultaneously to give the shape of the drop (Yakhshi-Tafti et al. 2011):

$$\begin{cases} \dfrac{d\varphi}{ds} = -\dfrac{\sin\varphi}{x} + \dfrac{2}{R} - \dfrac{\Delta\rho gz}{\sigma} \\ \dfrac{dx}{ds} = \cos\varphi \\ \dfrac{dz}{ds} = \sin\varphi \\ (x=0,\ s=0,\ z=0,\ \varphi=0) \end{cases} \qquad (3.29)$$

Numerically solving this set of differential equations gives a theoretically predicted interface (droplet) shape. Using an iterative solving method, the geometric droplet parameters that define the experimentally observed droplet profile can be determined, allowing the surface tension/interfacial tension value to be obtained. A schematic is shown in Figure 3.11 from research conducted by Berry (2015).

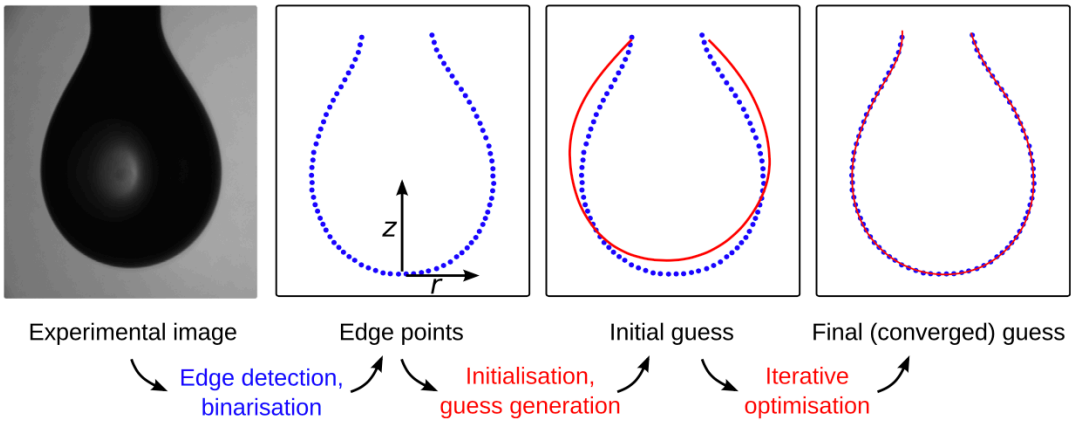

Figure 3.11: Schematic of iterative process involved using drop shape analyser from Berry (2015).

Figure 3.12 shows an experimental image obtained using the KRUSS Drop Shape Analyser (model DSA25). Two blue lines were positioned over the needle tip, for which an accurate width was known, allowing the image magnification factor to be calculated by the system. The third blue line was placed between the needle and the drop, below which the drop shape would be determined. The red line around the drop edge represents the final iterated droplet profile from which values of surface tension can be obtained.

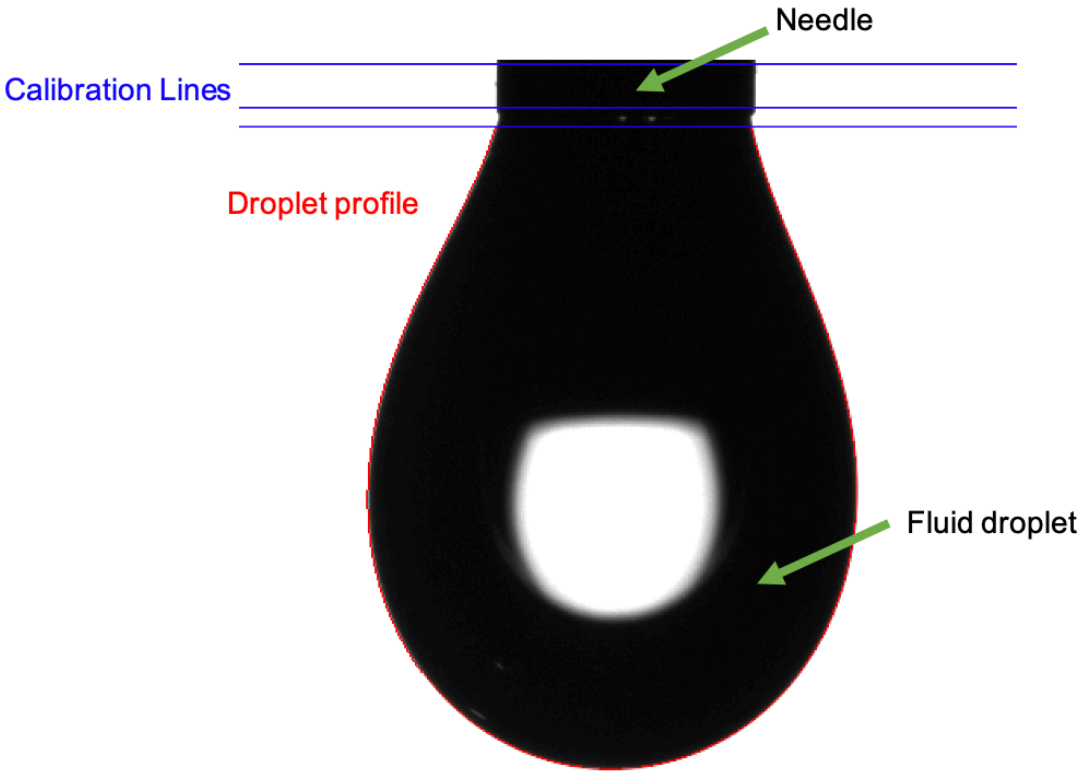

Figure 3.12: Experimental schematic from KRUSS Drop Shape Analyser (model DSA25) highlighting calibration lines (blue) and the final droplet profile from which measurements can be taken (red).

To ensure accuracy and repeatability, for each fluid five measurements were taken and the final average value is reported and used in this work. Each measurement was comprised of an average of 50 individual measurements over time. Figure 3.13 and Table 3.2 exemplify experimental data from the drop shape analyser at a temperature of 20℃ ± 1℃. The maximum associated random error for surface tension/interfacial tension measurements reported in this work is around ± 1%.

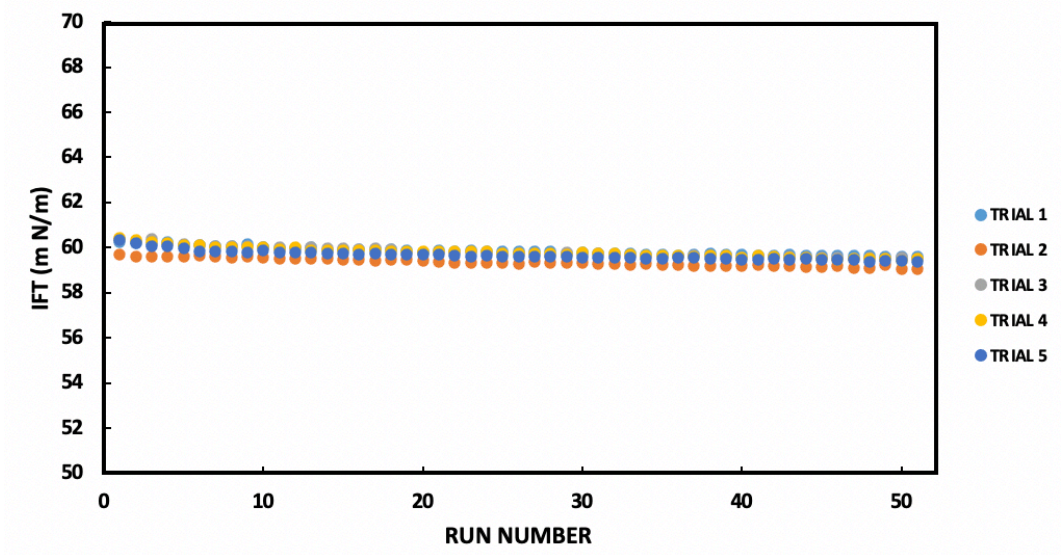

Figure 3.13: Experimental Data of interfacial tension obtained from the KRUSS Drop Shape Analyser (DSA25) for a polymeric fluid of PEO (M_w 4x10^6) at a concentration of 280ppm in a 50/50 solution of water and glycerol.

Table 3.2: Experimental Data of interfacial tension obtained from the KRUSS Drop Shape Analyser (DSA25) for a polymeric fluid of PEO (M_w 4x10^6) at a concentration of 280ppm in a 50/50 solution of water and glycerol.

Measurement	σ (mN/m)	Standard Deviation (mN/m)
Trial 1	59.84	0.18
Trial 2	59.35	0.17
Trial 3	59.81	0.23
Trial 4	59.79	0.23
Trial 5	59.66	0.21
FINAL	59.69	0.20

3.2.9 Pycnometery

In this work glass pycnometers were used to measure the fluid densities, ρ (kg/m^3). These devices are fixed volume vessels (V = 10 ml) with a long stopper containing a capillary hole as shown in Figure 3.14 (Dyer 2004).

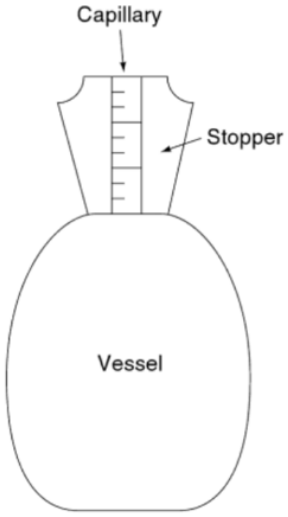

Figure 3.14: Schematic of pycnometer (enlarged for visualisation purposes) used to measure the density of fluids.

Initially the empty device is weighed using a precision balance, m_1, before the fluid sample is inserted. For precise density measurements it is important that the fluid be inserted correctly, where it is shown to be level with the capillary hole and the outside of the device must be cleaned to ensure an accurate sample volume (Dyer 2004). All measurements were conducted at a temperature of $20 \pm 1°\mathrm{C}$. The device with the fluid sample inside was then measured using the precision balance, m_2, and the density is calculated by:

$$\rho = \frac{\left(m_2 - m_1\right)}{V} \qquad (3.30)$$

3.3 FLOW CHARACTERISATION

3.3.1 Microfluidic Set-Up

All microfluidic experiments were carried out using a set up similar to that shown in Figure 3.15. The flow was visualised using an inverted microscope (Olympus IX71), equipped with an objective lens (usually 10X or 20X) and an adequate filter cube. The images were acquired using a CCD camera (Olympus XM10) and processed using an image processing program, ImageJ. The flow was illuminated using a 100 W metal halide lamp (PRIOR Scientific, Lumen 200 Fluorescence). The microfluidic device was placed on a moving platform that is controlled using a joystick. The microfluidic device is connected to SGE gastight syringes (with a displaced volume accuracy of ± 1%) using Tygon tubing and metal connectors. A high precision syringe pump with independent modules (neMESYS, Cetoni GmbH) was used for precise fluid control of the sample.

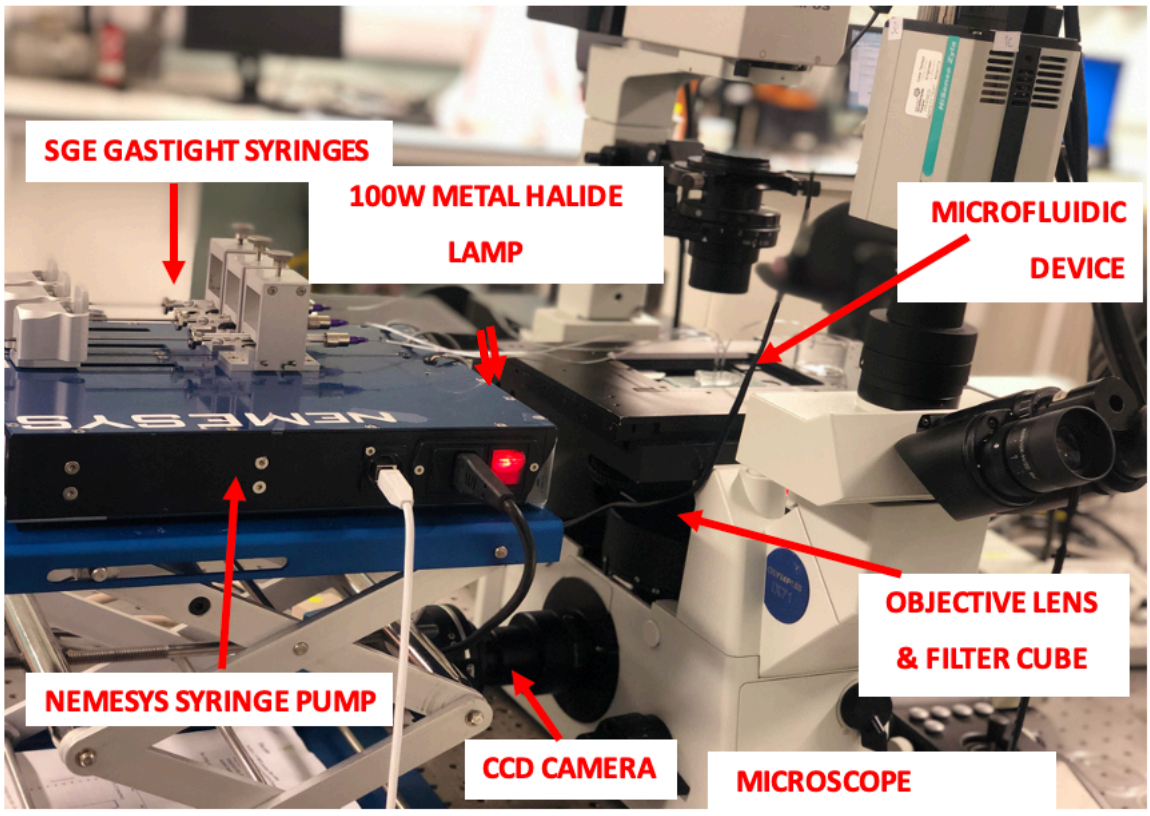

Figure 3.15: Image of microfluidic set up used for experiments.

3.3.2 Flow Visualisation

For flow characterisation, a number of experiments were carried out using streak photography in which the fluids were seeded with $\approx 1\ \mu m$ fluorescent tracer particles (FluoSpheres carboxylate- modified, $1.0\ \mu m$, Nile Red) at concentration of approximately 0.02%wt or Rhodamine B dye (Sigma-Aldrich) at a concentration of approximately 0.016%. These concentrations had no impact on the viscosity measurements of the fluids. Images were obtained using Epi-Fluorescent Microscopy with long exposure times, that strongly depend on the velocity of the fluids. This allows the camera to capture the path travelled by individual particles and therefore capture the flow patterns within the geometry.

Epi-Fluorescent Microscopy is based on the process where a fluorescent sample absorbs, and is excited by, a light source of a specific wavelength (the excitation wavelength) and emits light at a higher wavelength (the emission wavelength) (Bretschneider and Weille 2019). Epifluorescence uses a singular objective lens that allows light to pass through to excite the sample and then also detects the emitted light that is then produced by the sample. A schematic of the process is shown in Figure 3.16.

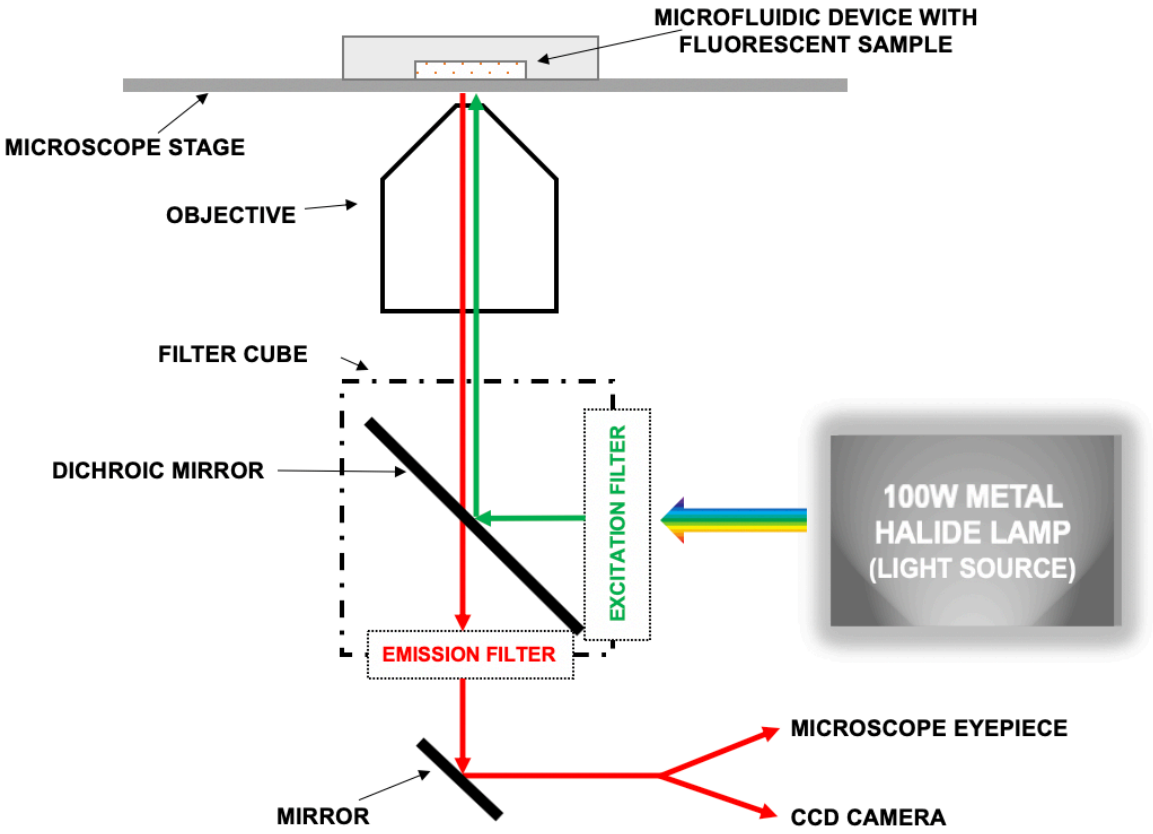

Figure 3.16: Schematic of Epi-Fluorescence Microscopy light path.

In microfluidic experiments conducted in this work fluorescent Rhodamine B dye (Sigma-Aldrich) or fluorescent tracer particles (FluoSpheres carboxylate- modified, 1.0 µm, Nile Red (Ex/Em: 535/575, cf. spectrum in Figure 3.17)) are added to the samples for visualisation purposes and the source of illumination is a 100 W metal halide lamp.

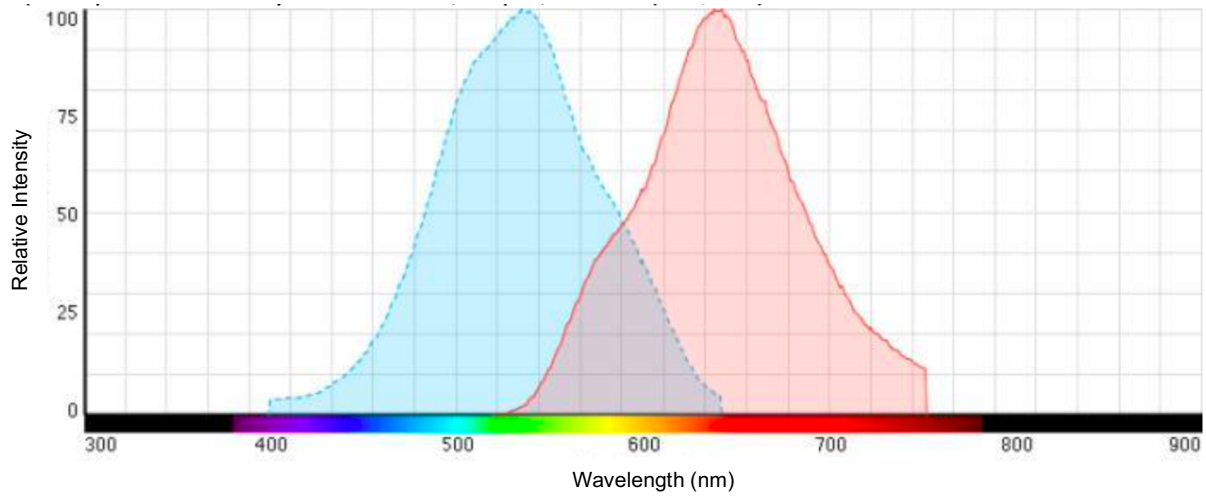

Figure 3.17: Spectrum of excitation and emission wavelengths for ≈ 1 µm fluorescent tracer particles (FluoSpheres carboxylate- modified, 1.0 µm, Nile Red).

Every fluorescent sample has specific excitation and emission wavelength, therefore an adequate filter cube has to be employed inside the microscope. For the samples used in this work the chosen filter cube was an OLYMPUS U-MWIGA3 which encompasses an excitation filter (Excitation 530 – 550 nm (see blue line in Figure 3.18)) and an emission filter (Emission 575 – 625 nm (see red line in Figure 3.18).

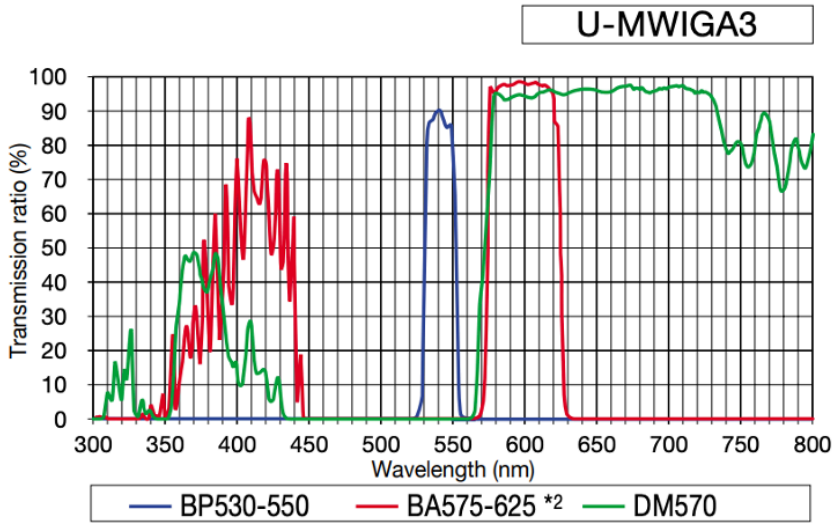

Figure 3.18: Spectrum of Transmittance vs Wavelength for the OLYMPUS U-MWIGA3 filter cube and DM570 OLYMPUS dichroic mirror (OLYMPUS).

This filter cube accepts a limited band of wavelengths from the emitting light source. After the light has passed through the excitation filter it is deflected towards the objective and thus to the sample, by a dichroic mirror with a long pass filter (DM 570 (OLYMPUS)) which allows everything of a higher wavelength to pass through, as indicated by the green line in Figure 3.16. After excitation the sample emits light at a higher wavelength which is transmitted by the dichroic mirror and passes through the emission filter (shown by the red line in Figure 3.16) to remove any additional stray light allowing samples to be viewed through the microscope eyepiece and camera.

These experiments are performed in a dark room to reduce noise and obtain the best quality of image avoiding interference from surrounding light sources.

3.4 EXPERIMENTAL UNCERTAINTIES

As a result of the physical size of these microfluidic systems, the experimental uncertainties can become quite significant. It is therefore important to quantify the errors in the experimental data. Two of the most used standards for measuring experimental uncertainties, ASME PTC 19.1 (ASME 2005) and NIST Technical note 1297 (Taylor and Kuyatt 1994) state that the total error, or uncertainty, $\in$, is comprised of two parts; the systematic error and the random error within the system.

The random error arises from unpredictable changes that occur during an experiment, for example from environmental conditions, and this error changes randomly over the course of repeated experimental runs. To quantify this random error we use a measure of the scatter of the individual measurements around the population mean (ASME 2005). The population mean, $\bar{X}$ can be calculated from the value of each individual measurement, X_j and the total number of measurements, N, as:

$$\overline{X} = \frac{\sum_{j=1}^{N} X_j}{N} \qquad (3.31)$$

The scatter of the data can then be expressed by the standard deviation, s_X:

$$s_X = \sqrt{\sum_{j=1}^{N} \frac{\left(X_j - \bar{X}\right)^2}{N-1}} \quad (3.32)$$

The final expression for the random error within the system, $s_{\bar{X}}$, can then be related to the standard deviation as shown:

$$s_{\bar{X}} = \frac{s_X}{\sqrt{N}} \quad (3.33)$$

The systematic error is in general a consistent repeated error that arises from various elements involved in obtaining experimental measurements. To reduce these errors as much as possible, instrument calibrations were frequently conducted. Each error source, k, has its own associated systematic error, $\beta_{\bar{X}_k}$. This value for each source can be found using published information or estimated using a 95% confidence level. All elemental systematic errors can then be combined into a singular estimate, $\beta_{\bar{X}}$. The total systematic standard uncertainty, $b_{\bar{X}}$, can then be expressed as:

$$b_{\bar{X}} = \frac{\beta_{\bar{X}}}{2} \quad (3.34)$$

The total error can therefore be expressed as a combination of both equation (3.33) and equation (3.34) as follows:

$$\in = 2\sqrt{\left(b_{\bar{X}}\right)^2 + \left(s_{\bar{X}}\right)^2} \quad (3.35)$$

Within this work a number of parameters are calculated to quantify the flow patterns observed inside microfluidic devices. The uncertainty of a calculated parameter can be estimated as:

$$\in_P = \sqrt{\sum_{i-1}^{n} \left(\frac{\partial P}{\partial a_i} \in_{a_i}\right)^2} \quad (3.36)$$

where $\in_P$ is the total error, or uncertainty associated with the calculated generic parameter, P is the parameter of interest, a_i is a variable used to calculate this parameter and $\in_{a_i}$ is the associated uncertainty for variable a_i.

To calculate the uncertainty associated with the average velocity and velocity ratio variables frequently used in this work, the independent parameters are namely the main geometric dimensions of the microfluidic device (W and D) and the volumetric flow rate applied by the Nemesys syringe pump (the accuracy of which is based on supplied specifications from manufacturers). To reduce these errors as much as possible, instrument calibrations were frequently conducted. The uncertainties relating to each of these independent variables are outlined in Table 3.3.

Table 3.3: Uncertainty values for measured independent parameters.

Parameter	Measurement Range	Uncertainty
Geometric Dimensions of Microfluidic Device (μm)	26-126	5%
Volumetric Flow Rate (ml/h)	0.002-1	1.2%

3.4.1 Experimental Average Velocity Uncertainties

Applying equation (3.36) the uncertainties in the average flow velocity, U within rectangular microfluidic devices of cross-sectional area width, W multiplied by the depth, D can be determined using the following process:

$$U = \frac{Q}{A} = \frac{Q}{WD} \tag{3.37}$$

$$\in_U = \sqrt{\left(\frac{\partial U}{\partial Q} \in_Q\right)^2 + \left(\frac{\partial U}{\partial W} \in_W\right)^2 + \left(\frac{\partial U}{\partial D} \in_D\right)^2} \tag{3.38}$$

$$\in_U = \sqrt{\left(\frac{1}{WD} \in_Q\right)^2 + \left(\frac{-Q}{W^2 D} \in_W\right)^2 + \left(\frac{-Q}{WD^2} \in_D\right)^2} \quad (3.39)$$

$$\frac{\in_U}{U} = \sqrt{\left(\frac{\in_Q}{Q}\right)^2 + \left(\frac{\in_W}{W}\right)^2 + \left(\frac{\in_D}{D}\right)^2} \quad (3.40)$$

The uncertainty associated with average velocity values presented in this work is therefore calculated to be approximately ± 7%.

3.4.1 Experimental Velocity Ratio Uncertainties

Applying equation (3.35), the uncertainties in the velocity ratio measurements, VR (defined in Chapter 5), can be determined as follows using the uncertainty associated with the average velocity of each fluid stream ($i = 1$ or $i = 2$):

$$VR = \frac{U_2}{U_1} \quad (3.41)$$

$$\in_{VR} = \sqrt{\left(\frac{\partial VR}{\partial U_2} \in_{U_2}\right)^2 + \left(\frac{\partial VR}{\partial U_1} \in_{U_1}\right)^2} \quad (3.42)$$

$$\in_{VR} = \sqrt{\left(\frac{1}{U_1} \in_{U_2}\right)^2 + \left(\frac{-U_2}{{U_1}^2} \in_{U_1}\right)^2} \quad (3.43)$$

$$\frac{\in_{VR}}{VR} = \sqrt{\left(\frac{\in_{U_2}}{U_2}\right)^2 + \left(\frac{\in_{U_1}}{U_1}\right)^2} \quad (3.44)$$

The uncertainty associated with velocity ratio values presented in this work is therefore calculated to be approximately ± 10%.

3.5 REFERENCES

ASME (2005). Performance Test Codes. PTC 19.1-2005, American Society of Mechnical Engineers.

Association, G. P. (1963). Physical Properties of glycerine and its solutions Glycerine Producers' Association.

Barnes, H. A. (2000). A Handbook of Elementary Rheology, Institute of Non-Newtonian Fluid Mechanics.

Barnes, H. A., Hutton, J. F. and Walters, K. (1989). An Introduction to Rheology, Elsevier.

Bashforth, F. and Adams, J. C. (1883). "An attempt to test the theories of capillary action: By comparing the theoretical and measured forms of drops of fluid, Cambridge University Press.

Berg, J. C. (2010). An introduction to interfaces & colloids : the bridge to nanoscience, Singapore ; Hackensack, NJ : World Scientific.

Berry, J. D., Neeson, M. J., Dagastine, R. R., Chan, D. Y. and Tabor, R. F. (2015). "Measurement of surface and interfacial tension using pendant drop tensiometry." J Colloid Interface Sci 454: 226-237.

Bird, R. B., Hassager, O. and Armstrong, R. C. (1977). Dynamics of polymeric liquids. Vol. 1: Fluid Mechanics, John Wiley and Sons.

Bretschneider, F. and Weille, J. d. (2019). Chapter 10 - Microscopy and Optical Methods in Electrophysiology. Introduction to Electrophysiological Methods and Instrumentation (Second Edition). F. Bretschneider and J. d. Weille, Academic Press: 285-310.

Clasen, C., Plog, J. P., Kulicke, W. M., Owens, M., Macosko, C., Scriven, L. E., Verani, M. and McKinley, G. H. (2006). "How dilute are dilute solutions in extensional flows?" Journal of Rheology 50(6): 849-881.

Doi, M. and Edwards, S. F. (1986). The Theory of Polymer Dynamics. USA, Oxford University Press Inc. New York.

Dyer, S. A. (2004). Wiley Survey of Instrumentation and Measurement, John Wiley & Sons.

Ebnesajjad, S. (2016). Introduction to Plastics. Chemical Resistance of Commodity Thermoplastics. E. Baur, K. Ruhrberg and W. Woishnis, William Andrew Publishing.

Entov, V. M. and Hinch, E. J. (1997). "Effect of a spectrum of relaxation times on the capillary thinning of a filament of elastic liquid." Journal of Non-Newtonian Fluid Mechanics 72(1): 31-53.

Galindo-Rosales, F. J., Alves, M. A. and Oliveira, M. S. N. (2012). "Microdevices for extensional rheometry of low viscosity elastic liquids: a review." Microfluidics and Nanofluidics 14(1-2): 1-19.

Grassley, W. W. (1980). "Polymer chain dimensions and the dependence of viscoelastic properties on concentration, molecular weight and solvent power." POLYMER 21: 258 - 262.

Hassouna, F., Morlat-Thérias, S., Mailhot, G. and Gardette, J. L. (2007). "Influence of water on the photodegradation of poly(ethylene oxide)." Polymer Degradation and Stability 92(11): 2042-2050.

Instruments, T. (2013). Discovery Hybrid Rheometer (DHR Series): Getting Started Guide, TA Instruments-Waters LLC.

Irgens, F. (2014). Rheology and Non-Newtonian Fluids, Springer International.

Israelachvili, J. N. (1991). Intermolecular and Surface Forces. London, Academic Press.

Kim, J. M., Wolf, F. and Baier, S. K. (2015). "Effect of varying mixing ratio of PDMS on the consistency of the soft-contact Stribeck curve for glycerol solutions." Tribology International 89: 46-53.

Liang, R. F. and Mackley, M. R. (1994). "Rheological Characterisation of the time and strain dependence for polyisobutylene solutions." Journal of Non-Newtonian Fluid Mechanics 52: 387 - 405.

Macosko, C. W. and Larson, R. G. (1994). Rheology principles, measurements and applications, New York, NY : VCH.

McDonald, J. C. and Whitesides, G. M. (2002). "Poly(dimethylsiloxane) as a material for fabricating microfluidic devices." Accounts of Chemical Research 35(7): 491-499.

McKinley, G. H., Brauner, O. and Yao, M. (2001). "Kinematics of stretching in dilute and concentrated polymer solutions." Korea-Australia Rheology Journal 13(1): 29 - 35.

Morrison, F. A. (2001). Understanding Rheology, New York : Oxford University Press.

Oliveira, M. S. N., Yeh, R. and McKinley, G. H. (2006). "Iterated stretching, extensional rheology and formation of beads-on-a-string structures in polymer solutions." Journal of Non-Newtonian Fluid Mechanics 137(1-3): 137-148.

OLYMPUS UIS2 Fluorescence mirror units technical specifications. OLYMPUS. Japan.

R. Larson, Muller, S. and Shaqfeh, E. S. G. (1994). "The effect of fluid rheology on the elastic Taylor-Couette instability." Journal of Non-Newtonian Fluid Mechanics 51: 195-225.

Rodd, L. E., Scott, T. P., Cooper-White, J. J. and McKinley, G. H. (2005). "Capillary break up rheometry of low viscosity elastic fluids." Applied Rheology 15(1): 15 - 27.

Scriven, L. E. (1988). "Physics and Applications of DIP Coating and Spin Coating." Materials Research Society Proceedings
Cambridge Univeristy Press 121.

Sdougos, H. P., Bussolari, S. R. and Dewey, C. F. (2006). "Secondary flow and turbulence in a cone-and-plate device." Journal of Fluid Mechanics 138: 379-404.

Sousa, P. C., Vega, E. J., Sousa, R. G., Montanero, J. M. and Alves, M. A. (2016). "Measurement of relaxation times in extensional flow of weakly viscoelastic polymer solutions." Rheologica Acta 56(1): 11-20.

Sousa, P. C. S. d. (2010). Entry Flow of Viscoelastic Fluids at Macro- and Micro-Scale. Doctor of Philosophy in Chemical and Biological Engineering, University of Porto.

Strivens, T. A. and Schoff, C. K. (2010). Rheometry. In Ullmann’s Encylcopedia of Industrial Chemistry, Wiley - VCH.

Taylor, B. N. and Kuyatt, C. E. (1994). Guidelines for Evaluating and Expressing the Uncertainty of NIST Measurement Results. Technical Report
, National Institute of Standards and Technology Gaithersburg.

Tirtaatmadja, V., McKinley, G. H. and Cooper-White, J. J. (2006). "Drop Formation and Breakup of Low Viscosity Elastic Fluids: Effects of Molecular Weight and Concentration." Physics of Fluids 18(4): 043101-043101-043118.

Tsao, C. W. (2016). "Polymer Microfluidics: Simple, Low-Cost Fabrication Process Bridging Academic Lab Research to Commercialized Production." Micromachines (Basel) 7(12): 225.

Waals, J. D. V. d. (1979). "The thermodynamics theory of capillarity under the hypothesis of a continuous variation of density." Journal of Statistical Physics 20: 197-244.

Xia, Y. and Whitesides, G. M. (1998). "Soft lithography " Annual Review of Materials Science 28(1): 153-184.

Yakhshi-Tafti, E., Kumar, R. and Cho, H. J. (2011). "Measurement of Surface Interfacial Tension as a Function of Temperature Using Pendant Drop Images." International Journal of Optomechatronics 5(4): 393-403.

CHAPTER 4

Stabilisation of purely elastic instabilities in cross-slot geometries

---

The content of this chapter is adapted from (Davoodi et al. 2021)

Davoodi, M., Houston, G., Downie, J., Oliveira, M. S. N. and Poole, R. J. (2021). "Stabilization of purely elastic instabilities in cross-slot geometries." Journal of Fluid Mechanics 922

In this chapter, two-phase flows of Newtonian and/or viscoelastic fluids in a ‘cross-slot’ geometry are investigated both experimentally and numerically in the creeping-flow limit. A series of microfluidic experiments – using Newtonian fluids – have been carried out in different cross-section aspect ratios to use as reference. The numerical simulations, conducted by a colleague in the research group of Professor Robert Poole at the University of Liverpool (Dr Mahdi Davoodi), rely on a Volume-of-Fluid method and make use of a log-conformation formulation in conjunction with the simplified viscoelastic Phan-Thien and Tanner model. University of Liverpool colleagues also provided analytical estimations of the thickness of each fluid layer for both two- and three-dimensional cases downstream from the central cross, once the flow has become fully developed. In addition to providing a benchmark test for the numerical solver, these analytical results also provide insight into the role of the viscosity ratio. Injecting two fluids with different elastic properties from each inlet arm is shown to be an effective approach to stabilise the purely elastic instability observed in the cross-slot geometry based on the properties of the fluid with the larger relaxation time. The results show that interfacial tension can also play an important role in the shape of the interface of the two fluids near the free-stagnation point (i.e., in the central cross). By reducing the interfacial tension, the interface of the two fluids becomes curved and this can consequently change the curvature of streamlines in this region which, in turn, can modify the purely elastic flow transitions. Thus, increasing interfacial tension is shown to have a stabilising effect on the associated steady symmetry-breaking purely elastic instability. However, at high values of the viscosity ratio, a new time-dependent purely elastic instability arises most likely due to the change in streamline curvature observed under these conditions. Even when both fluids are Newtonian, outside of the two-dimensional limit, a weak instability arises such that the fluid interface in the depth (neutral) direction no longer remains flat.

4.1 INTRODUCTION

Purely elastic instabilities, i.e., those in which the Reynolds number (Re) is vanishingly small and inertia can play no role, in viscoelastic flows occur frequently due to the nonlinear nature of the elastic stresses generated not only in simple viscometric flows but also in more complex flows with so-called 'mixed' kinematics of shear and extension. Generally, beyond a critical value of the Weissenberg number (Wi) – the ratio of elastic to viscous stresses – the 'simple' solution branch of the base state (i.e., steady and/or symmetric) in such flows bifurcates to a more complex flow either spatially or temporally. A geometry that allows the study of mixed kinematics but where elongational flow is important is the so-called 'cross-slot' geometry, which is used frequently in extensional-flow related studies (Haward et al. 2012). This geometry consists of four bisecting rectangular channels with two sets of opposing inlets and outlets. These opposing inlets and outlets produce a flow field with a free-stagnation point. At this point the velocity is zero and a finite velocity gradient in the streamwise direction appears. In principle, due to the zero velocity at this point, a fluid element is trapped for an 'infinite' time, generating a significant strain and potentially enabling 'steady-state' extensional-flow kinematics to be realised. Such an effect is a hallmark of this geometry and for this reason it is often proposed as an extensional rheometer (Haward et al. 2012). Gardner et al (1982) were the first to report a steady asymmetric flow field for viscoelastic fluids in this geometry, although the much later study carried out by Arratia et al. (2006) was the first in which this phenomenon was suitably characterised and such an asymmetric distribution of the flow field was unequivocally associated with a purely elastic instability. Interestingly, this instability has been reproduced numerically by Poole, Alves & Oliveira (2007) using the Upper Convected Maxwell (UCM) model, which is an unsatisfactory model for any steady-state extensional flow beyond a critical strain rate, and finite extensible nonlinear elastic (FENE)-type models by Rocha et al. (2009). Since then, there have been a number of experimental and numerical studies on the effects of various parameters on the onset and development of the elastic instabilities in cross-slot flows (Haward et al. 2012, Sousa et al. 2015, Cruz et al. 2016, Haward et al. 2016, Kalb et al. 2018, Sousa et al. 2018). However, so far, there is no prediction of the corresponding instability beyond the bifurcation point using linear stability for two-dimensional purely elongational flows

(Lagando and Leal 1990, Wilson 2012). One should note that, in this geometry, although a nominally purely elongational flow is observed at the stagnation point, due to the existence of re-entrant corners (Dean and Montagnon 1949, Davies and Devlin 1993, Hinch 1993, Moffatt 2006), a fluid particle may experience a complex mix of shear and extensional deformation as it flows through the domain. Recently, Davoodi, Domingues & Poole (2019) suggested the use of a cylinder at the geometric centre of the cross-slot geometry to investigate the effect on the onset of instability. This geometric modification applies a fundamental difference on the flow field as the finite value of the strain rate at the free-stagnation point in the standard geometry is replaced with zero-strain-rate pinned stagnation points at the surface of the cylinder. The findings showed that the suggested modification, although significantly changing the flow distribution in the region near the stagnation point, does not change the nature of the symmetry-breaking instability or, for small cylinders, the critical condition for onset. It was therefore concluded that the instability cannot be solely related to the extensional flow near the stagnation point but it is more likely related to streamline curvature and the high deformation rates towards the corners i.e., a classic 'curved streamlines' purely elastic instability (Shaqfeh 1996). In the work of Davoodi et al. (2019) using a combination of an analytical approach and supporting numerical simulations, it was shown that, by controlling the size of the cylinder, and consequently the curvature of streamlines, one may be able to control/delay the onset of the instability to higher Weissenberg numbers. A well-known dimensionless parameter which rationalises these types of 'curved streamline' instabilities is the M parameter introduced by McKinley, Pakdel & Öztekin (1996) (often referred to as the 'Pakdel–McKinley' criterion) which is defined as:

$$\sqrt{\frac{\lambda \tilde{U}}{\Re}\frac{\tau_{11}}{\left(\mu_0 \dot{\gamma}\right)}} \geq M \qquad (4.1)$$

where $\tilde{U}$ is a reference velocity, λ is the relaxation time, $\Re$ is the curvature of the streamline, τ_{11} is the elastic normal stress in the streamwise direction, μ_0 is the zero-shear-rate viscosity of the fluid and $\dot{\gamma}$ is the magnitude of the shear rate. This

parameter can be considered as the viscoelastic complement of the Görtler number (Görtler 1955). In equation (4.1), the first term on the right-hand side shows the ratio of a characteristic length $\lambda\tilde{U}$ over which disturbance information is convected before it decays to the streamline curvature (this term can also be referred to as the local Deborah number, showing the ratio of the relaxation time of the fluid to the time a disturbance takes to travel along a streamline). The second term on the right-hand side of equation (4.1) is added to properly scale the effect of the normal stress in the streamwise direction with a reference stress scale. This term is generally of the same order of magnitude as a local Weissenberg number, which is the destabilising term in the disturbance equation (McKinley et al. 1996). Equation (4.1) proposes that the kinematic and dynamic conditions corresponding to the curvature of the flow and the tensile elastic stress along the streamlines, respectively, can be combined into a single dimensionless criterion that must be exceeded for the onset of purely elastic instabilities. Using this approach, Haward et al. (2016) have shown that in an ideal planar elongational flow, such as that observed in the optimised-shape cross-slot extensional rheometer, the purely elastic instability may also be triggered due to strong streamline curvature close to the stagnation point.

In two-phase flow problems, the influence of the Capillary number (Ca) on the interface shape, and so on the streamline curvature, of two fluids has been studied in many different problems (e.g., (Chinyoka et al. 2005, Capobianchi et al. 2019, Zografos et al. 2020)). In such situations, across the interface of two fluids, a jump in normal forces is balanced by the curvature of the interface and the interfacial tension. As an example, in studies related to drop motion and deformation, Taylor & Acrivos (1964) have shown that by increasing Re the shape of Newtonian droplets may change from a spherical shape to an oblate shape, which is related to the nonlinear contribution of the inertial force. Such complex deformations are attributed to the presence of a non-uniform distribution of the normal forces at the interface of two fluids. Due to this non-uniform jump of the normal stress, at a constant interfacial tension, a non-uniform distribution of curvature is required to balance the applied forces (so the droplet loses its constant-curvature spherical shape). In such problems, it is well-known that, by increasing the interfacial tension, this distribution of the curvature along the interface of two fluids can be changed to retain the spherical shape of the droplet. The use of the interfacial tension as an important parameter in the evolution of a disturbance at the interface of

two fluids has been studied in many different two-phase flow instabilities (see for example (Graham 2003, Lee et al. 2011)).

For viscoelastic fluids, all previous studies in the cross-slot were restricted to a single fluid phase. In this work, a series of two-phase flow simulations were performed, supported by Newtonian experiments, and some limited three-dimensional (3D) calculations, to investigate the effect of different viscoelasticities in each inlet arm, viscosity jumps across the interface and the interfacial tension applied at the boundary of two different fluids injected from opposing inlets of the cross-slot geometry. By increasing the interfacial tension to a sufficiently large value, one may hope to influence the streamline curvature $\Re$ in the central region of the cross-slot geometry. Thus, we postulate that the interfacial tension may be used as a means to control the symmetry-breaking instability.

4.2 GEOMETRIC AND PROBLEM SET-UP CONFIGURATION

Here, two-phase flows through cross-slot geometries are considered. A schematic of the problem being studied is presented in Figure 4.1. In this study, inlets are located at the left (Fluid-1) and right (Fluid-2) side arms while outlets are located at the top and bottom arms. The width, W, of all inlet and outlet arms are the same. We consider both 2D and 3D configurations with different aspect ratios $AR = D/W$, where D is the depth of the channel, which is considered constant throughout. Two different fluids are injected at the inlets with an equal constant bulk velocity, U_B. A range of fluid pairs are considered, both miscible and immiscible (referred to throughout this work as two 'phases' for simplicity) to study the effect of viscosity ratio, $K = \mu_2/\mu_1$, with $\mu_1$and μ_2 being the total viscosity of Fluid-1 and Fluid-2, and Capillary number, Ca, on the interface and on the onset of elastic instabilities. We combine 2D and 3D numerical simulations together with analytical solutions and experiments in microfluidic devices to characterise the flow field for both Newtonian and viscoelastic fluid flows.

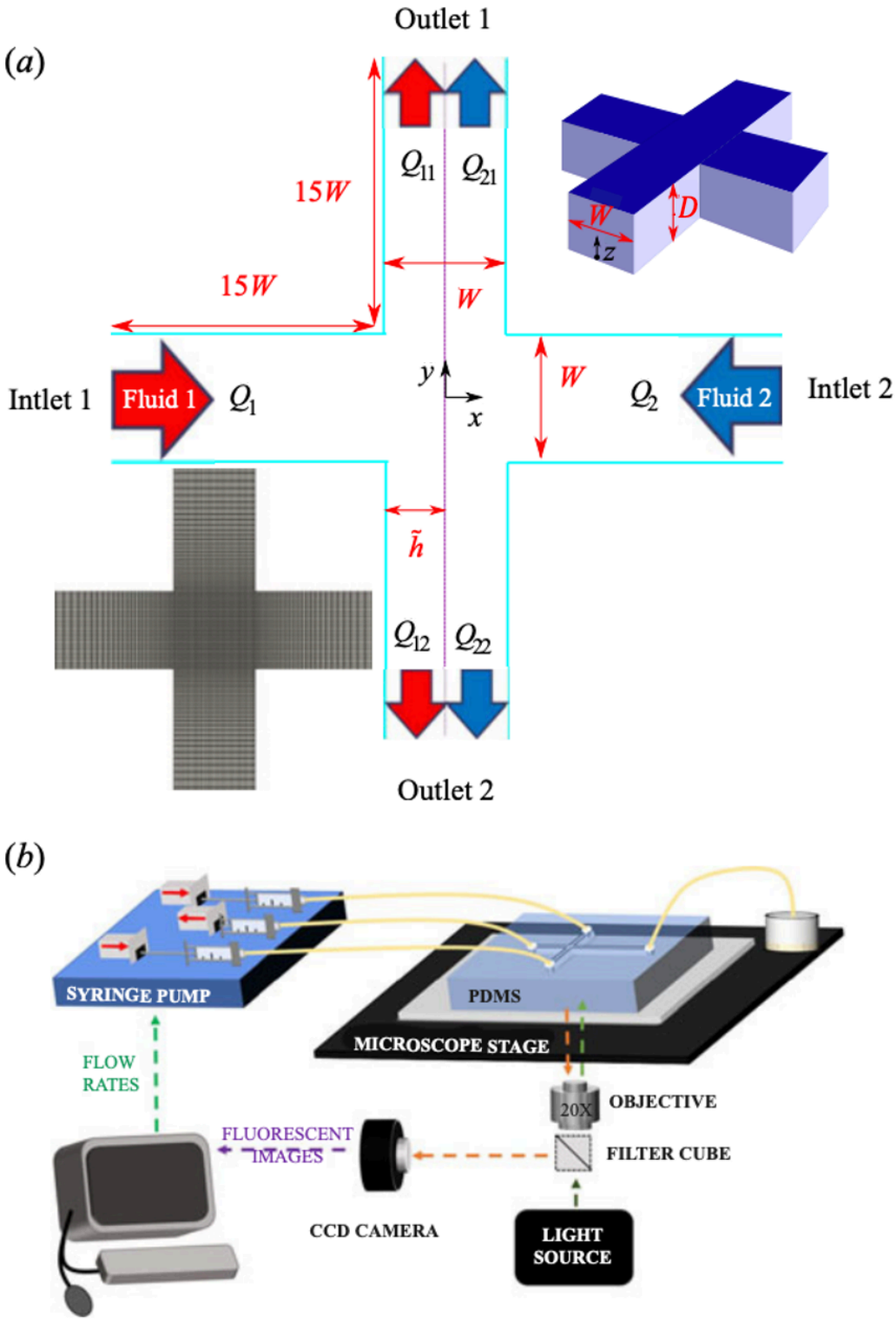

Figure 4.1: a) Schematic of the cross-slot geometry with insets highlighting the notation used in 3D (top right) and a typical 2D computational mesh (bottom left). Here, $\tilde{h}$ indicates the passage width of Fluid-1 in the outlet arms. b) Schematic illustrating the experimental microfluidic cross-slot apparatus allowing for direct observation of the (x, y) plane. Not to scale.

4.3 GOVERNING EQUATIONS AND NUMERICAL METHOD

Numerical approaches to simulate a two-phase flow field may be divided into two main categories, known as 'interface-tracking' and 'interface-capturing' methods. Amongst the interface-tracking methods, such as immersed boundary (Peskin 1982, Mittal and Iaccarino 2005), front-tracking (Tryggvason et al. 2001) and boundary integral (Peterlin 1976) methods have received considerable attention due to their accurate prediction of the shape of the interface at the boundary of the two fluids. In such methods, a moving sharp boundary is considered to track the interface of the two fluids. Tracking methods are known to be accurate for most flows but due to singularity issues in problems with morphological change, such as the ones observed in droplet breakup and coalescence (Jacqmin 1999, Yue et al. 2004, Magaletti et al. 2013), cannot be used for these types of simulations. Also, due to the presence of a moving mesh (which needs to be updated and reconstructed in every time step in the simulation), such methods are expensive with respect to their simulation computational time.

In contrast, in numerical simulations involving interface-capturing methods, the mesh could be either static (i.e., fixed grid distribution) or dynamic and the interface between two fluids is defined based on the variation of a scalar phase indicator parameter, α. The Volume-of-Fluid (VOF) and Phase-Field (PF) methods are arguably the most popular interface-capturing methods (Hirt and Nichols 1981). For VOF and PF, this scalar quantity is usually related to a volume fraction or a mass concentration. In these methods, the scalar parameter, α, varies between two limits (mostly $0 \leq \alpha \leq 1$), with α equal to the lower and upper limits being indicative of Fluid-1/Fluid-2, respectively. The interface of the two fluids is specified where α exhibits a mid-value in between these two limits (in the current case $\alpha = 0.5$). In the VOF method, in order to find the evolution of α, generally, the classic transport diffusion equation is solved, while in the PF model, this equation has an additional double-well potential term in comparison with the classic diffusion equation. In these methods, the system is dealt with as one single fluid with variable properties. By solving the transport equation for α, one can define different properties in space and time based on the regions that different fluids flow and treat the interfacial tension as a body force.

In the current work, the VOF method is used to find the variation of the α parameter in both space and time domains, the standard advection transport equation using a velocity field $\mathbf{u}$ is solved as:

$$\frac{\partial \alpha}{\partial t} + \mathbf{u}\nabla \alpha = 0, \qquad 0 \leq \alpha \leq 1. \tag{4.2}$$

For a binary fluid composed of Fluid-1 and Fluid-2, once the space/time distribution of α is known, one can define the following equations as was recommended in the viscoelastic toolbox RheoTool version 4.1 (Pimenta and Alves 2017):

$$\rho = \alpha\rho_1 + (1-\alpha)\rho_2, \tag{4.3}$$

$$\mu_s = \alpha\mu_{s,1} + (1-\alpha)\mu_{s,2}, \tag{4.4}$$

$$\boldsymbol{\tau} = \alpha\boldsymbol{\tau}_1 + (1-\alpha)\boldsymbol{\tau}_2, \tag{4.5}$$

where indices 1 and 2 indicate Fluid-1 and Fluid-2, μ_s is the solvent viscosity, ρ is the density and $\boldsymbol{\tau}$ is the viscoelastic contribution of the stress tensor. The governing equations for the motion of this fluid are conservation of mass, assuming incompressibility, and momentum:

$$\nabla \cdot \mathbf{u} = 0, \tag{4.6}$$

$$\rho\left(\frac{\partial \mathbf{u}}{\partial t} + \mathbf{u}\cdot\nabla\mathbf{u}\right) = -\nabla p + \nabla\cdot\boldsymbol{\tau} + \nabla\cdot\left(\mu_s\left(\nabla\mathbf{u} + (\nabla\mathbf{u})^{\mathrm{T}}\right)\right) + \boldsymbol{F}, \tag{4.7}$$

where p is the pressure and $\boldsymbol{F}$ is the capillary force applied at the interface of the two fluids due to the existence of the interfacial tension and is calculated as follows (Brackbill et al. 1992, Figueiredo et al. 2016):

$$\boldsymbol{F} = \sigma\kappa\boldsymbol{n}\delta_i = \sigma\kappa\nabla\alpha, \tag{4.8}$$

where σ is the surface tension coefficient, $\kappa = -\boldsymbol{\nabla} \cdot \boldsymbol{n}$ is the interface curvature, $\boldsymbol{n} = \nabla \alpha / \| \nabla \alpha \|$ is the unit vector normal to the interface (Francois et al. 2006) and δ_i is the δ-function at the interface. Here, to simulate the viscoelastic contribution of the stress tensor (i.e., $\boldsymbol{\tau}$), the simplified Phan-Thien and Tanner (sPTT) constitutive equation is employed which is derived from network theory (PhanThien and I.Tanner 1977) and is a suitable model for simulation of shear-thinning polymeric fluids (Bird et al. 1977). The extra-stress tensor using the sPTT model may be calculated as follows:

$$f_i \boldsymbol{\tau}_i + \lambda \overset{\nabla}{\boldsymbol{\tau}}_i = \mu_{p,i} \left(\nabla \mathbf{u} + \nabla \mathbf{u}^{\mathrm{T}} \right) \qquad i = \{1, 2\}, \tag{4.9}$$

where index i can be either 1 or 2 (i.e., $i = \{1, 2\}$) indicating Fluid-1 and Fluid-2. Here, the f_i function for the linear-sPTT model is defined as

$$f_i = 1 + \varepsilon_i \frac{\lambda_i}{\mu_{p,i}} Tr\left(\boldsymbol{\tau}_i \right) \qquad i = \{1, 2\}, \tag{4.10}$$

where ε is the extensibility parameter. In the limiting case of $\varepsilon = 0$ the sPTT constitutive equation reduces to the Oldroyd-B model and, if additionally, $\mu_s = 0$, the UCM model is recovered. The upper-convective derivative of the extra-stress tensor $\overset{\nabla}{\boldsymbol{\tau}}_i$, is defined as:

$$\overset{\nabla}{\boldsymbol{\tau}}_i = \frac{D}{Dt}\left(\boldsymbol{\tau}_i \right) - \left(\boldsymbol{\tau}_i \cdot \nabla \mathbf{u} + \nabla \mathbf{u}^{\mathrm{T}} \cdot \boldsymbol{\tau}_i \right) \qquad i = \{1, 2\}, \tag{4.11}$$

where the material derivative of an arbitrary matrix $\boldsymbol{A}$ is defined as $\left(D/Dt \right)(\boldsymbol{A}) = \left(\partial \boldsymbol{A} / \partial t + \mathbf{u} \cdot \nabla \boldsymbol{A} \right)$. To solve the series of equations presented in equations (4.2) – (4.11) the rheoInterFoam solver in the rheoTool package of OpenFoam is used (Pimenta and Alves 2017).

Table 4.1: Characteristics of the computational meshes. NC is number of cells, W is channel width and D is channel depth.

Mesh	**NC**	$\frac{\Delta x_{min}}{W} = \frac{\Delta y_{min}}{W}$	$\frac{\Delta z}{D}$
M21	13005	0.02	2D
M22	51005	0.01	2D
M31	663255	0.02	0.02
M32	5151505	0.01	0.02

Table 4.2: Mesh dependency study for 2D simulations using M21 with 13005 and mesh M22 with 51005 cells.

	$Ca = \infty$	$Ca = 0.5$	$Ca = 0.1$	$Ca = 0.05$	$Ca = 0.03$
Wi_{cr} – M21	0.5109	0.5235	0.5806	0.6604	0.7684
Wi_{cr} – M22	0.5086	0.5195	0.5769	0.6563	0.7622

A zero gradient boundary condition for the stress and velocity components is applied at the outlets to simulate fully developed conditions. At the walls, values of the stress components are calculated using an extrapolation method, as suggested by Pimenta and Alves (2017) and no slip is assumed for the velocities. For the phase indicator parameter, α, constant values of 1 and 0 are used at the left and right inlet arms and a zero gradient at the outlet and walls (cf. Figure 4.1). The flow domain has been divided into 5 smaller sub-domain blocks (four inlet/outlet arms and one central block). Most simulations were carried out using a mesh similar in density to that of Cruz et al. (2016) (Table 4.1). Additionally, some limited 3D simulations are also carried out to study the effect of the K parameter and Ca on the interface shape and location. The effect of mesh refinement on the numerical simulations is presented in Table 4.2 and Figure 4.8 for 2D and 3D cases, respectively. In Table 4.2, the effect on the critical

Weissenberg number for two different uniform meshes are shown for different Capillary numbers. The total number of cells for the M21 and M22 meshes are 13005 and 51005, respectively and the error between these two calculated critical Weissenberg numbers is less than 1%. Similarly, two different meshes, consisting of 663255 and 5151505 cells, have been used to study the effect of mesh on the 'dimple size' – discussed later in Section 4.7– of 3D geometries and the error was calculated to also be smaller than 1%. These results give us sufficient confidence to continue the study with the smaller of the meshes in both 2D and 3D cases.

4.4 NON-DIMENSIONALISATION

In this analysis, to better characterise the flow field and the important parameters playing a role in this problem, the following dimensionless parameters are adopted:

$$\left.\begin{aligned} & x^* = \frac{x}{W},\ y^* = \frac{y}{W},\ z^* = \frac{z}{D},\ AR = \frac{D}{W},\ \mathbf{u}^* = \frac{\mathbf{u}}{U_B},\ \boldsymbol{\tau}^* = \frac{\boldsymbol{\tau}}{\mu_1 U_B / W},\ p^* = \frac{p}{\mu_1 U_B / W}, \\ & Re_i = \frac{\rho_i U_B W}{\mu_i},\ Wi = \frac{\lambda U_B}{W},\ Ca = \frac{\mu_1 U_B}{\sigma},\ K = \frac{\mu_2}{\mu_1},\ AP = \frac{Q_{i1} - Q_{i2}}{Q_i}, \end{aligned}\right\} \quad (4.12)$$

where index i can be either 1 or 2 (i.e., $i = \{1, 2\}$) indicating properties of Fluid-1 and Fluid-2 respectively, x, y, z are the variables related to the Cartesian coordinate system, W is the width and D is the depth of the channel, AR is the cross-section aspect ratio, $\mathbf{u}$ is the velocity vector, U_B is the imposed bulk velocity at the inlets, $\boldsymbol{\tau}$ is the extra-stress tensor, p is the pressure, Re_i is the Reynolds number in each inlet stream and was set to a value of 10^{-3} for all simulations in order to model creeping flow, Wi_i is the Weissenberg number defined for each phase, β_i is the solvent-to-total viscosity ratio of each of the two phases and μ_i is the total viscosity of each of the phases (i.e., $\mu_i = \mu_{i,s} + \mu_{i,p}$), Ca is the Capillary number defined based on the properties of Fluid-1, K is the ratio of total viscosity of Fluid-2 to Fluid-1 (and so CaK is the Capillary number based on Fluid-2), Q_i is the imposed flow rate at the inlets (i.e. in the two-dimensional problem $Q_i = WU_B$), $Q_{i1}$and Q_{i2} are defined in Figure 4.1 and AP is the asymmetry parameter used in the simulations to quantify the magnitude of

asymmetry in the flow (before the onset of any symmetry-breaking instability $Q_{i1} = Q_{i2}$ so $AP = 0$, but once the symmetry of the flow is broken $Q_{i1} \neq Q_{i2}$ and AP exhibits a non-zero value). A previous study conducted by Wilson & Rallison (1997) has shown that a non-zero value of the normal-stress jump at the interface of viscoelastic fluids may trigger an instability in three-layer planar flows. In this work, to concentrate on two key effects we study the effect of either varying the elasticity of each fluid stream (but in the limit of negligible interfacial tension) or keeping the elasticity fixed, but interfacial tension can be varied. The values of $\beta_1 = \beta_2 = 1/9$ and the extensibility parameter of two fluids $\varepsilon_1 = \varepsilon_2 = 0.02$ are held fixed to reduce the parameter space.

4.5 EXPERIMENTAL

Experiments in 3D microfluidic planar channels were carried out to visualise the Newtonian flow field for comparison with the numerical results and to study the effect of aspect ratio. A schematic diagram of the experimental rig is shown in Figure 4.1. The experimental microchannels were made from polydimethylsiloxane (Sylgard 184, Dow Corning) and were fabricated using a SU-8 mould by standard soft-lithography techniques. Three different cross-slot microfluidic devices with varying aspect ratios ($AR = D/W$) were used: AR = 0.83 (with $W = 109 \pm 2\ \mu m$ and $D = 91 \pm 1\ \mu m$), AR = 0.28 (with $W = 96 \pm 2\ \mu m$ and $D = 26 \pm 1\ \mu m$) and AR = 0.22 (with $W = 125 \pm 2\ \mu m$ and $D = 26 \pm 1\ \mu m$). To study the effect of viscosity ratio, deionised water and a variety of glycerol/water solutions were prepared with viscosities ranging from 6.47 mPa s to 300 mPa s (cf. Table 4.3).

Table 4.3: Characterisation of different fluids used in the experiment.

Fluid	Density (kg/m^3)	Viscosity (Pa s)	Viscosity Ratio, K
Deionised Water	998	1.00x10^{-3}	1
22.8 wt% Glycerol solution	1047	1.97x10^{-3}	1.97
41.9 wt% Glycerol solution	1100	4.15x10^{-3}	4.15
50.9 wt% Glycerol solution	1172	6.41x10^{-3}	6.41
61.6 wt% Glycerol solution	1154	1.22x10^{-2}	12.0
74.3 wt% Glycerol solution	1195	3.36x10^{-2}	33.6
80.1 wt% Glycerol solution	1209	6.90x10^{-2}	60.90
84.2 wt% Glycerol solution	1222	1.01x10^{-1}	101
HPF10	1908	6.70x10^{-3}	6.7
91.8 wt% Glycerol solution	1240	3.00x10^{-1}	44.8*

*Reference fluid for all cases is water, except for the 91.8 wt% glycerol and water solution, for which the viscosity ratio is reported relative to HPF10.

In addition, for the experiments on the effect of interfacial tension, perfluorodecalin (Sigma Aldrich, μ = 6.7 mPa s) was used together with the most viscous glycerol/water solution tested (μ = 300 mPa s). The interfacial tension between these two fluids was measured to be 35.03 ± 0.04 mN m^{-1} at 293.2 K. The fluids were characterised in steady shear on a DHR-2 hybrid rotational rheometer (TA Instruments) with a cone-plate geometry (60 mm diameter, 1° cone angle) at a temperature of 293.2 K. The surface tension and interfacial tension measurements were carried out with a drop shape analyser (model DSA25, Kruss) using the pendant-drop method, in which the shape of the pendant drop was fit using the Young–Laplace equation:

$$\Delta p = \sigma\left(\frac{1}{R_1} + \frac{1}{R_2}\right), \qquad (4.13)$$

where Δp is the pressure difference across the interface and R_1 and R_2 are the principal radii of curvature of the interface. A high-precision syringe pump with independent modules (neMESYS, Cetoni GmbH) was used for precise fluid control, imposing flow rates in the range $Q \leq 2.5$ ml h^{-1}, yielding a maximum Reynolds number $Re \leq 3.0$ (based on the less viscous fluid properties as reference). SGE^{TM} gastight syringes of appropriate volumes were used to ensure that the syringe pump pulsation-free minimum dosing rate was exceeded. The flow was illuminated with a 100W metal halide lamp and visualised using an inverted microscope (Olympus IX71), equipped with a 20X objective lens, a CCD camera (Olympus XM10) and an adequate filter cube (Olympus U-MWIGA3). For flow visualisation Rhodamine-B (Sigma-Aldrich) was added to one of the inlet streams. In addition, a number of experiments were also carried out using streak photography in which the fluids were seeded with 1 μm fluorescent tracer particles (FluoSpheres carboxylate-modified, Nile Red (Ex/Em: 535/575nm)) at concentration of approximately 0.02%wt. Long exposure photography was used to capture the flow patterns at the centre plane of the microchannel $(z = D/2)$.

4.6 ANALYTICAL SOLUTIONS FOR TWO-PHASE FLOW OF FULLY DEVELOPED NEWTONIAN FLUIDS IN A CHANNEL AND RECTANGULAR DUCTS

It is well known that in the limit of no inertia or surface tension, channel flows of Newtonian fluids with a viscosity stratification are potentially linearly unstable (Yih 1967), nevertheless, in this section, exact analytical solutions for the pressure driven, creeping two-phase fully developed flow of Newtonian fluids in a 1D channel between two infinite parallel plates (Figure 4.2a) and rectangular cross-sections (Figure 4.2b) are derived. These solutions will then provide a partial benchmark solution for the nonlinear simulations in the cross-slot geometry (i.e., in the outlet arms sufficiently far downstream of the cross-slot where the flow becomes ‘fully developed’). Dimensionless formulation and all variables refer to the normalised variables as defined in equation (4.12). To avoid Yih-type instability, the numerical simulations

include interfacial tension (Hooper and Boyd 1983, Barmak et al. 2016). A schematic of the problem and the employed coordinate system is shown in Figure 4.2.

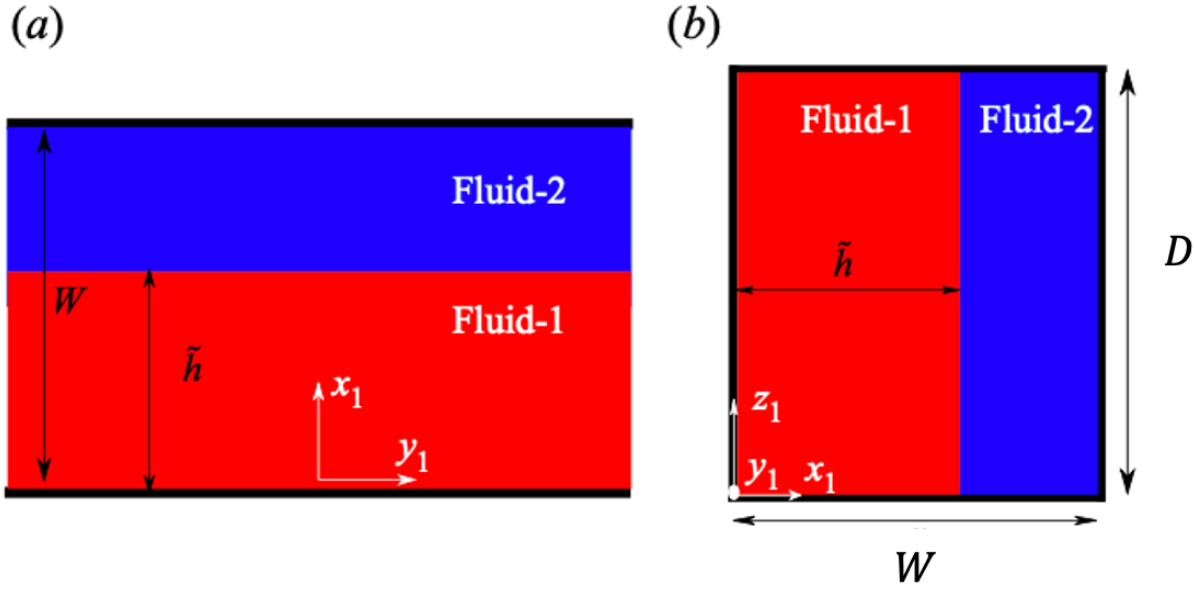

Figure 4.2: Schematic of a) the 1D channel geometry (flow is left to right) and b) the 1D rectangular duct geometry (flow is into page) and the employed coordinate system. Not to scale. Note choice of coordinate system to match that of 'outlet' arms in cross-slot.

In the limit of no inertia, or fully developed flow, the Navier–Stokes equation in dimensionless form for Fluid-1 and Fluid-2 can be written as:

$$\nabla^2 U_i^* = G^*, \qquad i = 1, \tag{4.14}$$

$$K\nabla^2 U_i^* = G^*, \qquad i = 2, \tag{4.15}$$

where U_i^* is the dimensionless velocity in the y-direction with respect to the reference bulk velocity (i.e. $U_i^* = U_i/U_B$) and G^* is the dimensionless pressure gradient defined as $G^* = \left(\partial p/\partial y\right) \Big/ \left(\mu_i U_B/W^2\right)$. Note that, to obtain a rectilinear 1D flow distribution, the pressure drop in both phases must be equal, otherwise it will lead to a pressure gradient in the lateral direction of the flow resulting in a secondary motion. Solutions to equations (4.13) and (4.14) for 1D channel flows may be presented as follows:

$$U_{1,2D}{}^{*} = \frac{1}{2} G^{*}\left(x_1{}^{*}\right)^2 + C_1 x_1{}^{*} + C_2, \tag{4.16}$$

$$U_{2,2D}{}^{*} = \frac{1}{2} \frac{G^{*}}{K}\left(x_1{}^{*}\right)^2 + C_3 x_1{}^{*} + C_4, \tag{4.17}$$

and similarly for rectangular 2D ducts as:

$$U_{1,2D}{}^{*} = \sum_{n=1}^{n=\infty}\left(A_1 \cosh\left(\frac{n\pi x_1{}^{*}}{AR}\right) + A_2 \sinh\left(\frac{n\pi x_1{}^{*}}{AR} x_1{}^{*}\right) + \frac{2G^{*}\left(1-(-1)^{n}\right)}{n^3\pi^3}\right)\sin\left(n\pi z_1{}^{*}\right), \tag{4.18}$$

$$U_{2,2D}{}^{*} = \sum_{n=1}^{n=\infty}\left(A_3 \cosh\left(\frac{n\pi x_1{}^{*}}{AR}\right) + A_4 \sinh\left(\frac{n\pi x_1{}^{*}}{AR} x_1{}^{*}\right) + \frac{2G^{*}\left(1-(-1)^{n}\right)}{Kn^3\pi^3}\right)\sin\left(n\pi z_1{}^{*}\right), \tag{4.19}$$

where $x_1{}^{*}$ and $z_1{}^{*}$ are the dimensionless variables in the rectangular coordinate system (i.e., $x^{*} = x/W$ and $z^{*} = z/D$). Equations (4.16) – (4.19) should be solved subject to continuity of tangential velocity and shear stress at the interface i.e., $x^{*} = \tilde{h}/W = h^{*}$ as

$$U_1{}^{*}\Big|_{x_1{}^{*}=h^{*}} = U_2{}^{*}\Big|_{x_1{}^{*}=h^{*}}, \tag{4.20}$$

$$\left.\frac{dU_1{}^{*}}{dx_1{}^{*}}\right|_{x_1{}^{*}=h^{*}} = K\left.\frac{dU_2{}^{*}}{dx_1{}^{*}}\right|_{x_1{}^{*}=h^{*}}, \tag{4.21}$$

and the no-slip boundary condition at the walls. For 1D channel flows, solving these equations with respect to the previously mentioned boundary condition leads to

$$\left.\begin{aligned} C_1 = C_3 &= \frac{3\left(K(h^*)^2 - (h^*)^2 + 1\right)}{(h^*)^2\left(K(h^*)^2 - (h^*)^2 - 2h^* + 3\right)}, \\ C_2 = 0, \quad C_4 &= \frac{3\left(Kh^* - K - h^* + 1\right)}{(h^*)^2\left(K(h^*)^2 - (h^*)^2 - 2h^* + 3\right)}, \end{aligned}\right\} \tag{4.22}$$

and for 2D rectangular channels, assuming a flat interface (i.e., $Ca = 0$), leads to

$$A_1 = 2(-1+(-1)^n)\left(\cosh\left(\frac{1}{AR}n\pi\right)(K-1)\cosh\left(\frac{1}{AR}n\pi\right)^2 - (K-1)\left(\sinh\left(\frac{1}{AR}n\pi h^*\right)\sinh\left(\frac{1}{AR}n\pi\right) + \cosh\left(\frac{1}{AR}n\pi\right)\right)\cosh\left(\frac{1}{AR}n\pi h^*\right) + \sinh\left(\frac{1}{AR}n\pi\right)(K-1)\sinh\left(\frac{1}{AR}n\pi h^*\right) + \cosh\left(\frac{1}{AR}n\pi\right) - 1\right) G^* \Big/ \left(\pi^3\left(\sinh\left(\frac{1}{AR}n\pi\right)(K-1)\cosh\left(\frac{1}{AR}n\pi h^*\right)^2 - \sinh\left(\frac{1}{AR}n\pi h^*\right)\cosh\left(\frac{1}{AR}n\pi\right)(K-1)\cosh\left(\frac{1}{AR}n\pi h^*\right) - K\sinh\left(\frac{1}{AR}n\pi\right)\right)n^3\right), \tag{4.23}$$

$$A_2 = 2G^*(-1+(-1)^n)/(n^3\pi^3), \tag{4.24}$$

$$A_3 = 2\left((K-1)\cosh\left(\frac{1}{AR}n\pi h^*\right)^2 - \cosh\left(\frac{1}{AR}n\pi\right)(K-1)\cosh\left(\frac{1}{AR}n\pi h^*\right) + K\left(\cosh\left(\frac{1}{AR}n\pi\right) - 1\right)\right)(-1+(-1)^n) G^* \Big/ \left(\pi^3\left(\sinh\left(\frac{1}{AR}n\pi\right)(K-1)\cosh\left(\frac{1}{AR}n\pi h^*\right)^2 - \sinh\left(\frac{1}{AR}n\pi h^*\right)\cosh\left(\frac{1}{AR}n\pi\right)(K-1)\cosh\left(\frac{1}{AR}n\pi h^*\right) - K\sinh\left(\frac{1}{AR}n\pi\right)\right)n^3K\right), \tag{4.25}$$

$$A_4 = -2(-1+(-1)^n)\left((K-1)\left(\sinh\left(\frac{1}{AR}n\pi h^*\right)\sinh\left(\frac{1}{AR}n\pi\right)\right)\cosh\left(\frac{1}{AR}n\pi h^*\right) + K\sinh\left(\frac{1}{AR}n\pi\right)\right) G^* \Big/ \left(\pi^3\left(\sinh\left(\frac{1}{AR}n\pi\right)(K-1)\cosh\left(\frac{1}{AR}n\pi h^*\right)^2 - \sinh\left(\frac{1}{AR}n\pi h^*\right)\cosh\left(\frac{1}{AR}n\pi\right)(K-1)\cosh\left(\frac{1}{AR}n\pi h^*\right) - K\sinh\left(\frac{1}{AR}n\pi\right)\right)n^3K\right), \tag{4.26}$$

One should note that, along with the unknown constants ($C_1 - C_4$ and $A_1 - A_4$ in 1D and 2D problems, respectively), values of G^* and h^* are also unknown but they can be calculated by setting the flow rate of each fluid to be equal. In the 1D problem we consider the flow rate in each phase to be equal to $U_B W/2$ (or in dimensionless form equal to 0.5). Using the flow rate constraint for Fluid-1, one can calculate the unknown pressure gradient G^* for the 1D problem as

$$G^* = \frac{6\left(Kh^* - h^* + 1\right)}{(h^*)^2\left(K(h^*)^2 - (h^*)^2 - 2h^* + 3\right)}, \tag{4.27}$$

which is equal in both fluids. Setting the flow rate to the value of 0.5 for Fluid-2, leads to the following constraint for the variable h^*:

$$\frac{0.5 + (0.5 - 0.5K^2)(h^*)^4 + (4K - 2)(h^*)^3 + (3 - 6K)(h^*)^2 + (2K - 2)h^*}{(h^*)^2\left(K(h^*)^2 - (h^*)^2 - 2h^* + 3\right)} = 0. \tag{4.28}$$

For the 1D problem, the unknown value of h^* can be obtained, now, by solving equation (4.28) numerically. In this work, a bisection method has been used to solve this (Chapra and Canale 2010). A similar approach can be used to calculate the unknown values of G^* and h^* in the 2D problem, which, due to the series form of the problem and large size of the equations, are not presented here.

4.7 RESULTS AND DISCUSSION

In this section, results obtained using the analytical solutions, numerical simulations and some supporting experiments for two-phase flows of both Newtonian and viscoelastic fluids in the cross-slot geometry are presented.

4.7.1 Newtonian fluids

To better understand the effect of the various parameters playing a role in this problem, a discussion on the location and shape of the interface of two Newtonian fluids in the fully developed section of the outlet arms is first carried out. This discussion will then be used to qualitatively investigate the effect of these parameters on the important kinematics of the flow field near the corners of the cross-slot geometry, which are known to be regions driving the instability for the viscoelastic case (Davoodi et al. 2019). Similar to the idea used by Davoodi et al. (2018) for normalisation of the aspect ratio, here, a modified form of the viscosity ratio parameter is defined as:

$$K^* = \frac{K}{K+1}. \qquad (4.29)$$

Using this definition, when the viscosity ratio K changes from zero to infinity, the modified form of the viscosity ratio K^* varies from zero to one, respectively. For the 1D problem, using equation (4.28), one can say that, by changing the viscosity ratio parameter, the term $h^*(1-h^*)$ should show two roots at K^* = 0 and K^* = 1. So, in the limits of $K \to 0$ and $K \to \infty$, the h^* parameter tends toward one and zero, respectively. Similarly, for K = 1 (K^* = 0.5) (i.e., fluids in each phase have identical properties), one can easily show analytically that h^* = 0.5.

Knowing that experiments are necessarily carried out in finite cross-section aspect ratio domains, in Figure 4.3 we analyse the variation of the position of the boundary between the two fluids, represented here via the use of $h^*(1-h^*)$ plotted against the normalised viscosity ratio parameter K^* using both 2D and 3D numerical solutions for four different aspect ratios (the corresponding analytical solutions are simply one-dimensional and two-dimensional as there is no variation in the flow direction due to the fully developed assumption). The analytical results are shown to be in good agreement with the experimental and numerical results. Note that at $Ca = \infty$, i.e., when interfacial tension is zero, due to the jump of normal forces at the interface the flow may be unstable (Yih 1967) and one might need to use large interfacial tension to

avoid such instability (Hooper and Boyd 1983, Barmak et al. 2016). Considering the fact that it is impossible to obtain Ca = 0, i.e., interfacial tension equal to infinity, the numerical results for $0 < K^* < 0.5$ presented in Figure 4.3 were carried out at a high value of the interfacial tension (Ca = 0.005) and the $h^*(1 - h^*)$ parameter is calculated downstream of the central cross such that the flow is fully developed. A series of complimentary simulations with $Ca = \infty$, were also carried out for $0.5 < K^* < 1$. As was also previously reported initially by Yih (1967), the numerical simulations suggest that, in the absence of interfacial tension, the flow may be unstable and the interface in the neutral direction is no longer flat (Figure 4.4). In these cases, the value of h^* obtained numerically and experimentally is taken at the central plane z^* = 0.5. Knowing that this instability is observed due to the nonlinear nature of the convection terms in the Navier–Stokes equation, one may expect that, by reducing the Reynolds number, the size of the disturbance along the interface should reduce and eventually, at Re = 0, the flow, and consequently the interface of the two fluids, should obtain a steady-state form. Interestingly, in both the numerical simulations and experimental procedure, the location of the interface of the two fluids is shown to be quasi-static, in agreement with the results of Bonhomme et al. (2011) using similar systems (water and glycerol solutions), which is related to the very small value of the Reynolds number ($Re \approx 10^{-3}$) in these cases (Yih 1967). Thus, it should be recognised that, outside of the 2D simulations, the experiments and numerical simulations (with high Ca) may not be truly steady state, although, as the interface remains essentially constant in time, we will treat them as so.

For all aspect ratios, the effect of the normalised viscosity ratio parameter is exactly symmetric about K^* = 0.5 (i.e., K = 1), highlighting the inherent symmetry in the problem. From the results presented in Figure 4.3, it is clear that by increasing the viscosity of one of the two fluids, considering that the pressure drop should be equal in both phases, to retain a rectilinear flow, the average velocity of the more viscous fluid reduces, and so the area required to satisfy the constant flow rate constraint increases. The analytical and experimental results suggest that this effect is magnified as the aspect ratio is reduced.

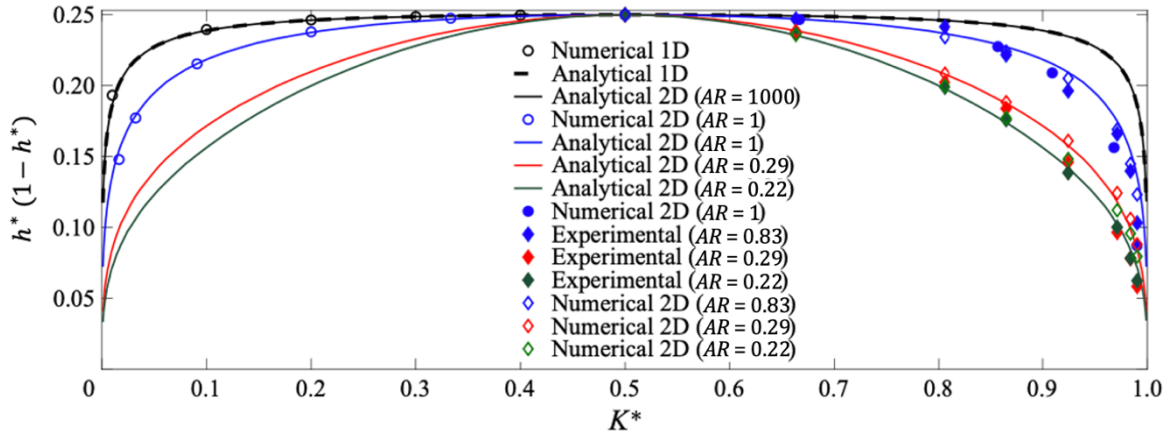

Figure 4.3: Variation of the height of the interface between two fluids with viscosity ratio for Newtonian fluids. The values of the numerical simulations presented in the ranges $0 < K^* < 0.5$ and $0.5 < K^* < 1$ are taken in the outlet arms for $y^* = 5W$ with Ca = 0.005 and Ca = ∞, respectively.

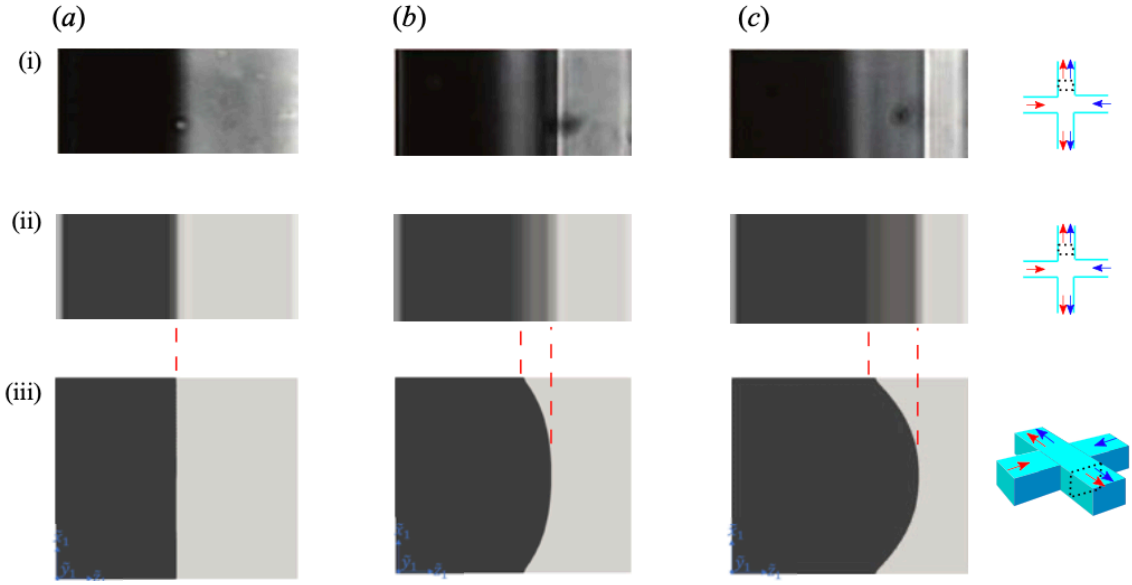

Figure 4.4: Visualisation of the interface between two Newtonian fluids in the fully developed region of the outlet arm with $Ca \rightarrow \infty$ and viscosity ratios a) $K = 1$, b) $K = 0.16$, c) $K = 0.03$ (where the fluid shown in dark grey is the most viscous one) using AR = 0.83 i) in the experiment and (ii–iii) in numerical simulations. Figures i) and ii) are presented in (x, y) plane centred at $z^* = 0$ for $1.5 < y^* < 2$ while (iii) show a cross-sectional view of the channel ((x, z) plane) at $y^* = 1$.

Figure 4.4i shows the interface of two fluids in the fully developed region of the outlet arm ($1 < y^* < 1.4$) observed in experiments. As also shown in Figure 4.3, if the viscosity

of the two fluids is identical (i.e., K = 1 or K^* = 0.5), the interface is located at the mid-distance between the two walls, as the K parameter exhibits a non-unity value the more viscous fluid moves the interface such that the average velocity decreases in this phase and increases for the less viscous phase. By changing K, one can clearly see the appearance of a 'shadow' region at the interface. The presence of this shadow region suggests that, when K exhibits a non-unity value, the interface location is varying along the depth of the cross-section. It should be noted that, in the experiments of this work, Re is low and the Péclet number (Pe), i.e., the relative importance of advection to diffusion, is large (in excess of 1000), suggesting that, here, the two miscible fluids flow side by side without mixing (Petitjeans and Maxworthy 1996, d'Olce et al. 2009, Bonhomme et al. 2011). To investigate this shape of the interface in more detail, a series of 3D numerical simulations for aspect ratio AR = 0.83 with different values of K was simulated (Figure 4.4ii,iii) in the limit of Ca = ∞ (by setting the interfacial tension equal to zero). Note that, to portray the 'shadow' influence of the interface in the numerical simulations, the opacity of the two fluids is reduced to 50 % while the opacity of the interface (i.e., the iso-contour with α = 0.5) is kept at 100%.

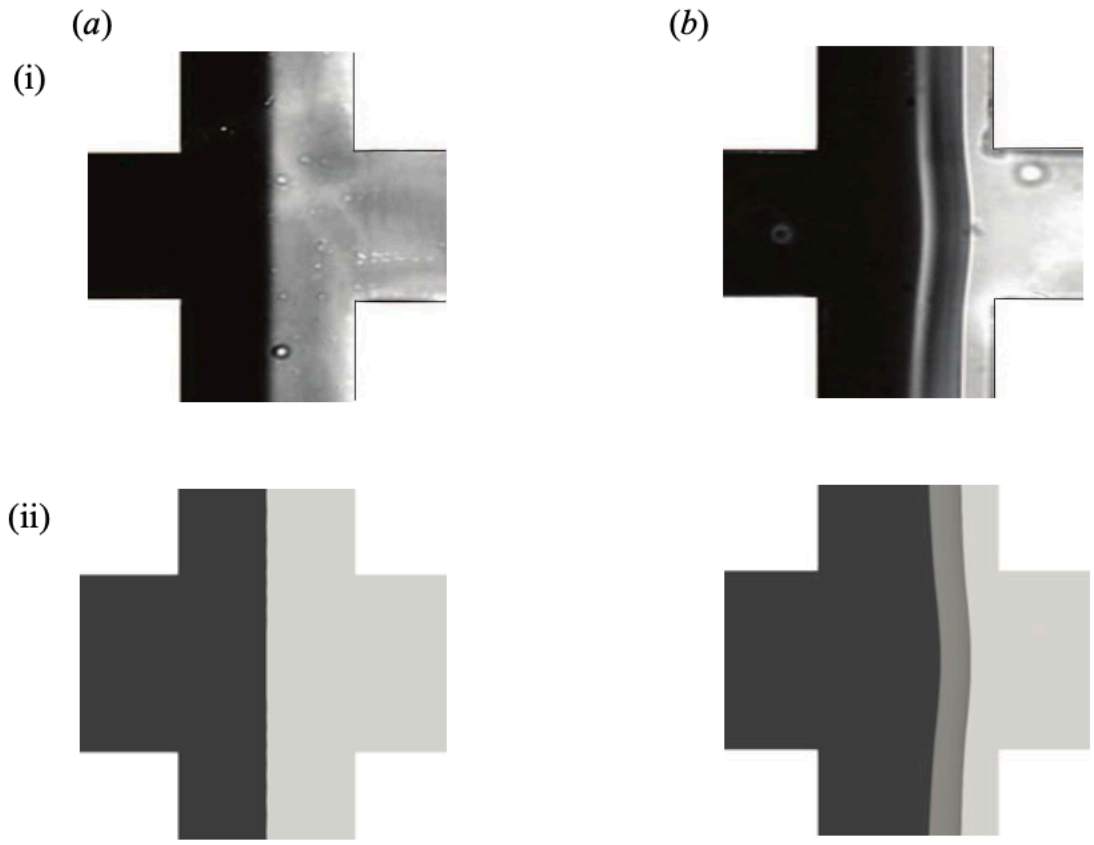

Figure 4.5: Effect of viscosity ratio with Ca = ∞ and a) K = *1*, b) K = *0.03* for AR = *0.83* in i) the experiment and ii) in numerical simulations, where the most viscous fluid (Fluid-1) is on the left-hand side.

In Figure 4.5, results related to the effect of the viscosity ratio parameter K on the central region of the cross-slot geometry are presented. As can be seen, by increasing the viscosity of Fluid-1 (the fluid injected from the 'left' inlet), the interface of the two fluids shifts towards 'the right' and a 'dimple' starts to grow near the stagnation point. The mechanism responsible for the shift of the interface of the two fluids is identical to the one previously discussed in the fully developed regions of the outlet arms. By increasing the viscosity of Fluid-1, the pressure gradient required to ensure a constant average flow velocity is increased, so the fluid requires more space to satisfy the constant flow rate constraint. As is well known, in two-phase flow problems, a jump of normal forces appears at the interface of the two fluids that is balanced by the effect of interfacial tension as follows (Rybczynski 1911, Taylor and Acrivos 1964):

$$\tau_{1,xx} - \tau_{2,xx} - p_1 + p_2 = \sigma \frac{1}{\mathfrak{R}}, \qquad (4.30)$$

where in the Newtonian problem $\tau_{i,xx} = 2\mu_i \left(\partial U_{i,x} \big/ \partial x \right)$. One can show that, at the stagnation point, because $\partial U^* \big/ \partial x^* = \partial U_{1,x}{}^* \big/ \partial x^* = \partial U_{2,x}{}^* \big/ \partial x^* = const$, if $\mu_2 < \mu_1$ then $\tau_{2,xx} < \tau_{1,xx}$, that can potentially lead to the presence of a positive curvature at the interface. In the inlet arms, a higher pressure is required to flow the fluid with higher viscosity and consequently a pressure difference at the two inlet arms appears. Due to this reasoning, by increasing the viscosity of Fluid-1, one may expect a jump of the normal force at the interface of the two fluids leading to the appearance of a dimple with a positive curvature at the interface of the two fluids (i.e., the left-hand side terms in equation (4.30) find a positive value that balances with the interfacial stress and interfacial tension-curvature of interface product, on the right-hand side). From equation (4.30), one can realise that, by increasing the interfacial tension, to balance a constant jump in the normal force, a smaller curvature is required.

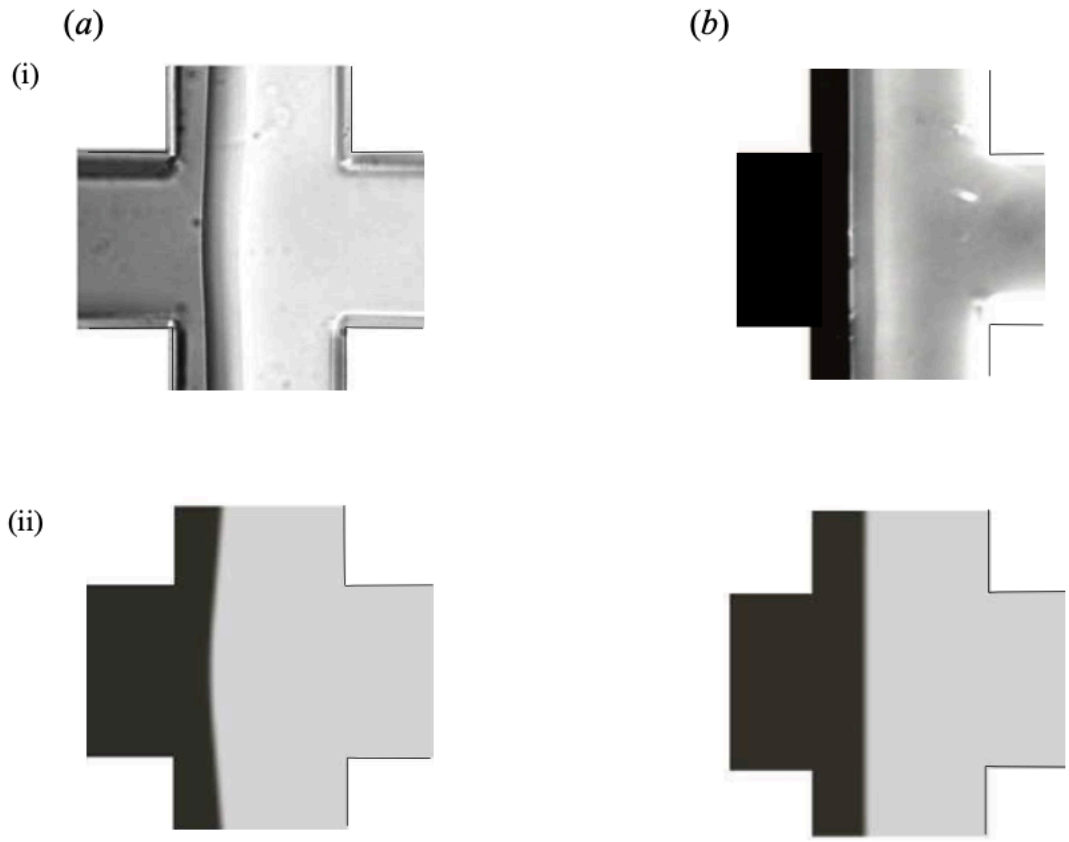

Figure 4.6: Effect of interfacial tension for K = 44.78 with (a) Ca = 5.90 × 10^{-1}, (b) Ca = 7.08 × 10^{-4} for i) AR = 0.83 in the experiment and ii) 2D numerical simulations. In the experiments, the oil is injected through inlet-1 and the aqueous solution through inlet-2.

As shown in Figure 4.6, by increasing the interfacial tension (i.e., reducing Ca) the curvature appearing at the interface of the two fluids reduces and eventually leads to a flat interface below a critical value of Ca (see Figure 4.6b). Further experiments, using geometries with different aspect ratios, shown in Figure 4.7, reveal that the size of this dimple d_h (defined in Figure 4.7b) is also a function of the aspect ratio. As the aspect ratio parameter is reduced, the influence of the shear stress at the walls and consequently on the pressure gradient at the inlet arms becomes more important leading to a more pronounced curvature at the interface of the two fluids. A more quantitative investigation on the effect of aspect ratio and viscosity ratio parameter on the dimple size is presented in Figure 4.8 using experimental results and 3D numerical simulation.

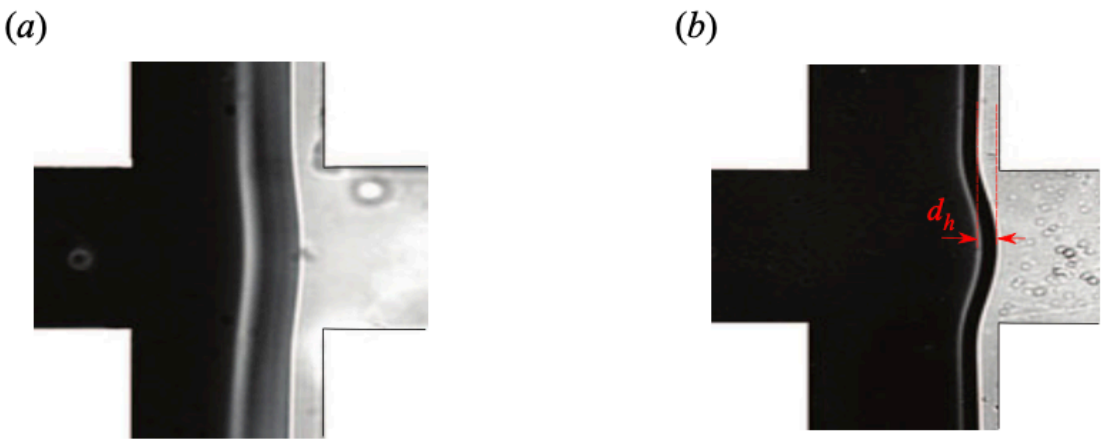

Figure 4.7: Effect of aspect ratio for K = 0.03 with (a) AR = 0.83, (b) AR = 0.22 including definition of dimple size d_h. The most viscous fluid (Fluid-1) is on the left-hand side.

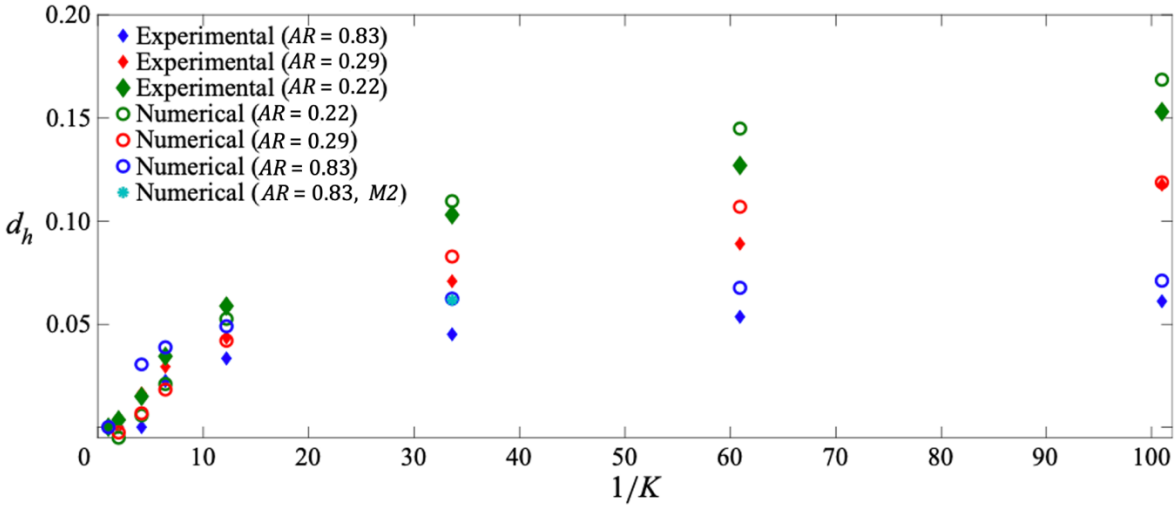

Figure 4.8: Variation of the normalised dimple size (normalised by the channel width) with the viscosity ratio for different aspect ratios. Dimple size d_h is defined in Figure 4.7.

Figure 4.9 shows the effect of the viscosity ratio on the flow patterns, showing good qualitative agreement between the numerical simulation (where the streamlines are superimposed on contour plots of the magnitude of the non-dimensional velocity gradient) and the experimental results. As also shown in Figure 4.3, by increasing the viscosity of Fluid-1, the h^* parameter increases leading to a reduction in the associated area which Fluid-2 requires to pass in the outlet arms. To satisfy the constant flow rate

constraint in the outlet arms, the mean value of velocity in Fluid-2 increases which also leads to a higher shear rate near the corners of the cross-slot geometry.

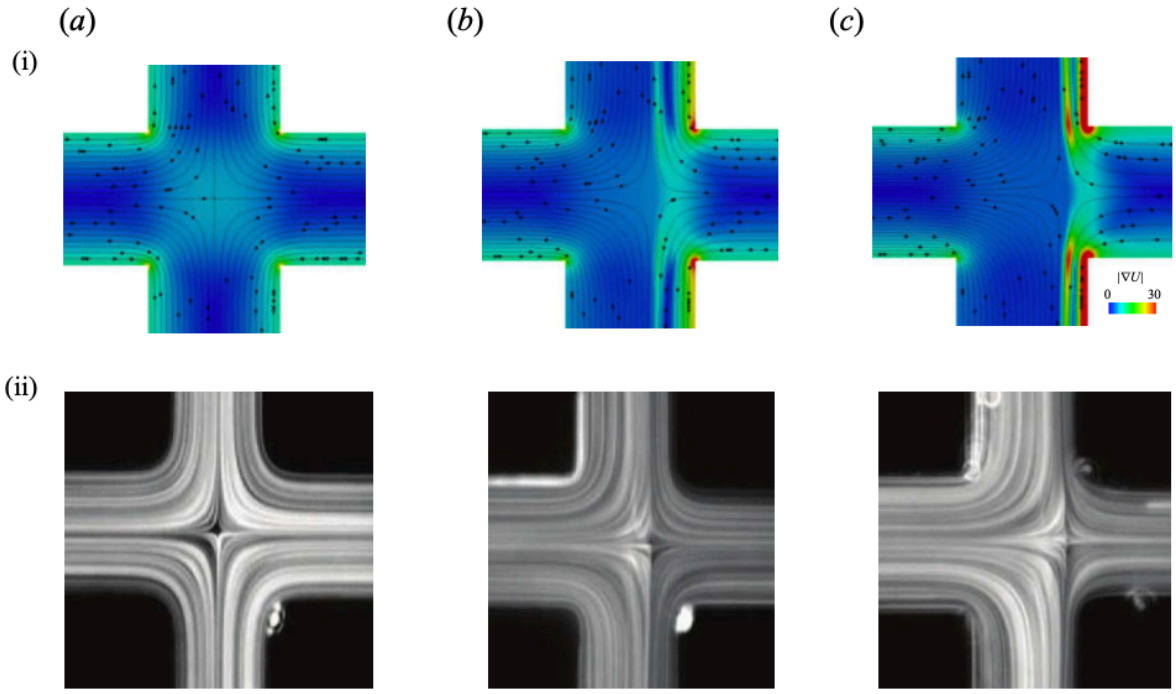

Figure 4.9: Streamlines obtained using i) numerical method superimposed on the magnitude of the non-dimensional velocity gradient with AR = 0.83 and $Ca = \infty$ and ii) experimental results with AR = 0.83 for a) K = 1, b) K = 0.16, c) K = 0.03, where the most viscous fluid enters through inlet-1 (on the left-hand side).

4.7.2 Effect of elasticity on the symmetry-breaking instability

In Figure 4.10 and Figure 4.11 the effects of the elasticity on the symmetry-breaking instability for $Ca = \infty$ is illustrated. In Figure 4.10, 2D simulation results, corresponding to cases in which the fluids in the inlet arms have the same elastic properties, are presented. It is shown that, beyond a critical value of the Weissenberg number, even in the absence of any significant inertia, elasticity can break the symmetry of the flow field leading to a steady-state purely elastic instability, as seen in previous works with 2D cross-slot flows with a single viscoelastic fluid (e.g., (Poole et al. 2007)). Imposing a zero value of interfacial tension (i.e., σ = 0), the body force applied on the interface is set to zero (the $\boldsymbol{F}$ term in equation (4.7)). In this case, by setting the rheological

properties of the two fluids to be equal, one can expect the conservation of momentum (equation (4.7) for the two-phase flow problem) to reduce to its equivalent equation in a single-phase problem. In Figure 4.11a, a comparison between the results obtained using the rheoFoam and rheoInterFoam solvers for cases with $Wi_1 = Wi_2$ is presented with red diamonds and circles, respectively, showing both good qualitative and quantitative agreement. The rheoFoam solver is a single-phase flow solver and rheoInterFoam is a two-phase flow solver implemented in the rheoTool package in OpenFOAM (Pimenta and Alves 2017). Both solvers predict a supercritical growth of the asymmetry parameter AP near the critical value of the Weissenberg number Wi_{cr} = 0.511, which is in good agreement with previously reported studies for the same model and parameters (Cruz et al. 2016). The present results give us confidence in the correct implementation of the viscoelastic constitutive equation in the two-phase flow solver.

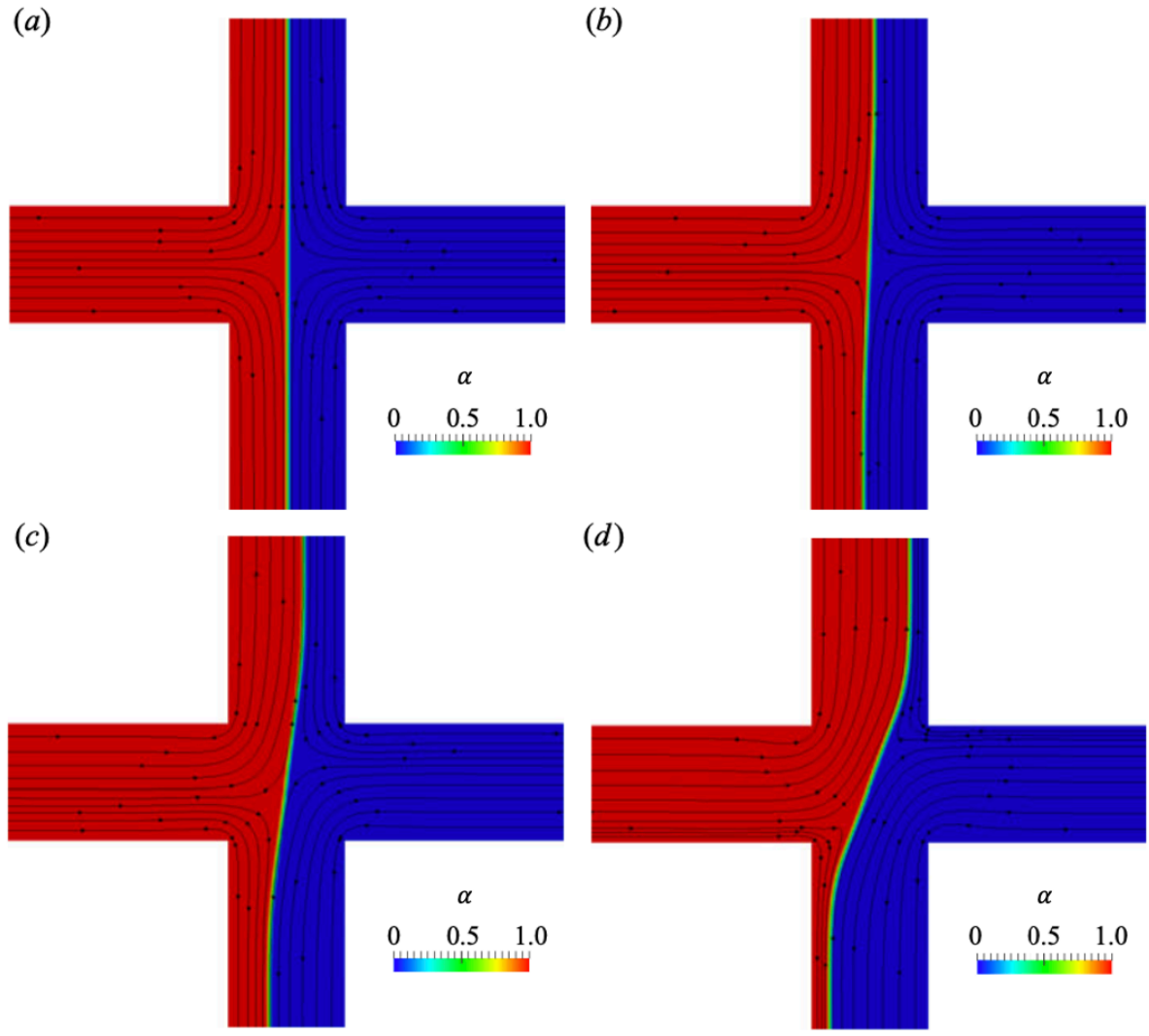

Figure 4.10: Effect of viscoelasticity on the 2D steady symmetry-breaking instability of two fluids with K = 1, Ca = ∞ for a) Wi_i = 0.4, b) Wi_i = 0.515, c) Wi_i = 0.55, d) Wi_i = 1,and $i = \{1, 2\}$.

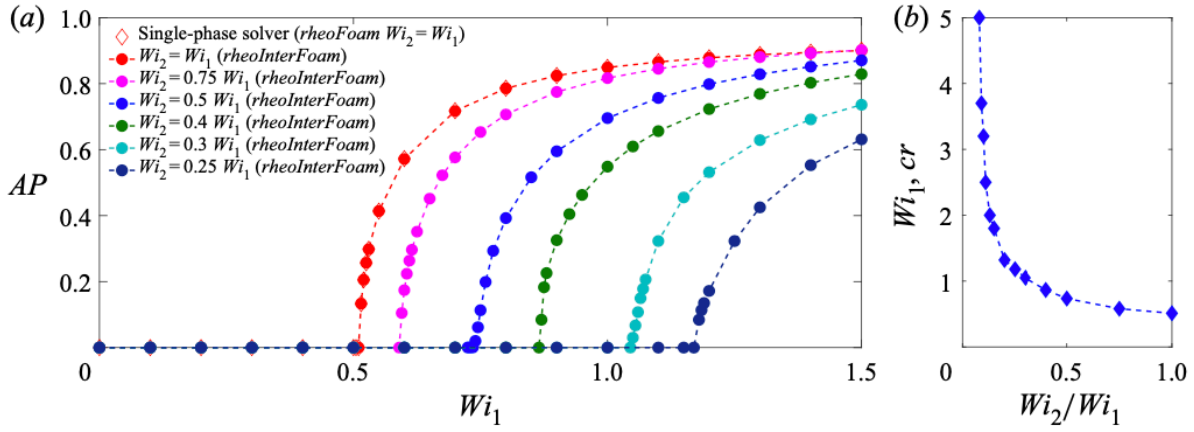

Figure 4.11: a) The stability diagram for symmetry-breaking instability and b) the variation of critical Weissenberg number with the ratio of Weissenberg numbers for two-phase flow problems with $Ca = \infty$ and K = 1.

To investigate the effect of different viscoelastic properties of each fluid in this two-phase flow problem, in Figure 4.11a, the ratio of the relaxation times of each fluid injected in the inlet arms are varied. As can be seen, in agreement with the single-phase results, the instabilities in all cases exhibit supercritical growth beyond the critical Weissenberg number: this is a well-known signature of the symmetry-breaking purely elastic instability in cross-slot geometries for single-phase fluids.

Numerical results show that, when a fluid with a lower relaxation time is injected from one inlet (here, inlet-2), the critical condition based on the properties of the more elastic fluid (i.e., inlet-1) is shifted to a higher value of Weissenberg number. As such, injection of a less elastic fluid in one arm is seen to be stabilising overall in the sense that the more elastic arm remains steady and symmetric at values of the Weissenberg number well beyond which it would when flowing as a single-phase fluid.

The variation of this critical Weissenberg number vs the ratio of inlet arm Weissenberg numbers is presented in Figure 4.11b. We can see that, for small differences between the elasticities of the two inlets, $0.75 < Wi_2/Wi_1 < 1$, an average Weissenberg number (i.e., $0.5(Wi_1 + Wi_2)$) exhibits an approximately constant critical value but, for greater differences, the stabilisation effect becomes significantly more pronounced. In fact, in the limit that a Newtonian fluid is injected from one of the inlets, no symmetry-breaking instability was observed for the range of Weissenberg number investigated

in this work (tested up to $Wi_1 \approx 5$). As we have already stated, one should note that, once the elasticity of the two fluids is different, the presence of a jump in normal stresses across the interface means the flow becomes potentially unstable leading to a time-dependent instability of the type previously reported by Wilson & Rallison (1997). However, for the values of parameters shown here, we do not observe an instability of this type. We note Figure 4.11b suggests that, in the limit that the elasticity of one of the inlets goes to zero (i.e., Newtonian), the critical Weissenberg for the other inlet stream becomes singular and the flow should be stable. However, it is likely that, in this limit, other, possibly time-dependent instabilities, will arise – such as those observed by Wilson & Rallison (1997) – and therefore very careful studies of this region are suggested. Indeed, Dr Davoodi's preliminary simulations in this region do suggest that a new time-dependent instability arises which is possibly subcritical and very sensitive to initial conditions, time step and mesh.

In recent work using a modified form of the cross-slot with a cylinder placed at the geometric centre, Davoodi et al (2019), have shown that the symmetry-breaking instability observed in the 'standard' cross-slot geometry for single-phase fluids is more than likely related to streamline curvature and the high deformation rates as the flow rounds the corner of the geometry. In addition, they were able to show that the so-called Pakdel–McKinley (McKinley et al. 1996) criterion (the 'M' parameter given in equation (4.1)) can be used successfully to predict the scaling of this instability (for example how the diameter of the cylinder used changes the critical flow rate).

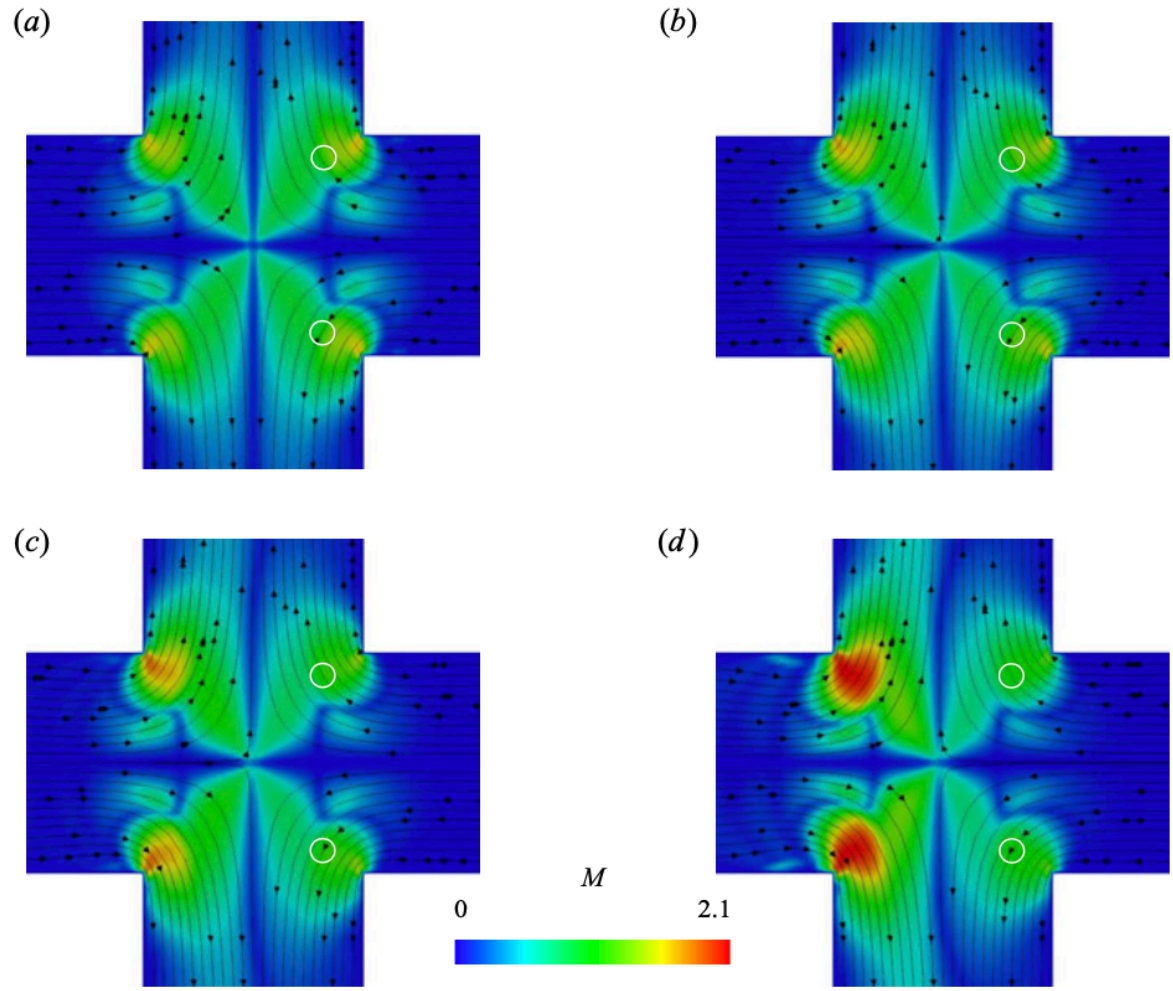

Figure 4.12: The local distribution of the M parameter before the onset of the instability at a) Wi_1 = 0.51, b) Wi_1 = 0.58, c) Wi_1 = 0.735 and d) Wi_1 = 1.18 for a) Wi_2/Wi_1 = 1, b) Wi_2/Wi_1= 0.75, c) Wi_2/Wi_1= 0.5 and d) Wi_2/Wi_1 = 0.25 with $Ca = \infty$ and K = 1. The white circles indicate the location where M reaches a critical value of ≈ 1 in Fluid-2.

In Figure 4.12 the local distribution of the Pakdel–McKinley M parameter is shown just prior to instability onset at Wi_1 = 0.51, 0.58, 0.735 and 1.18 for Wi_2/Wi_1 = 1, 0.75, 0.5 and 0.25 respectively. As can be seen, the location of the maximum M value appears at the corners of the more elastic fluid stream (the left-hand inlet in all cases) with the maximum value not appearing to be a constant but depending on the ratio of Wi_2/Wi_1. In fact, as the Pakdel–McKinley parameter is singular for flow around a sharp corner (as discussed in Appendix A), simply looking at the maximum value of M in the cross-slot domain when a sharp corner is present is unhelpful. Instead, we probed the differences between these contour distributions near critical conditions to identify

critical regions in the flow outside of the domain of influence of the singularity from the corner. In doing so, we identified a repeating pattern where the M value reaches a critical value of ≈ 1 in each case just immediately prior to instability onset. This location is highlighted by the white circles in each panel in Figure 4.12 and is consistent with regions in the flow which were associated with the instability in Poole et al. (Poole et al. 2007). It appears that instability occurs only once a critical value of M is exceeded in this region in both inlet streams. Thus, in combination with the singularity induced by the sharp corner, simply looking at the maximum value of M in the whole cross-slot domain does not predict instability onset.

4.7.3 Effect of interfacial tension on the symmetry-breaking instability

As is well known, the interfacial tension acts along a surface which suggests that, by increasing the interfacial tension, the interface of two fluids should become flatter (as was also discussed in the Newtonian creeping-flow problem). In Figure 4.13, this stabilising effect of the interfacial tension on the flow of viscoelastic fluids in a cross-slot is illustrated.

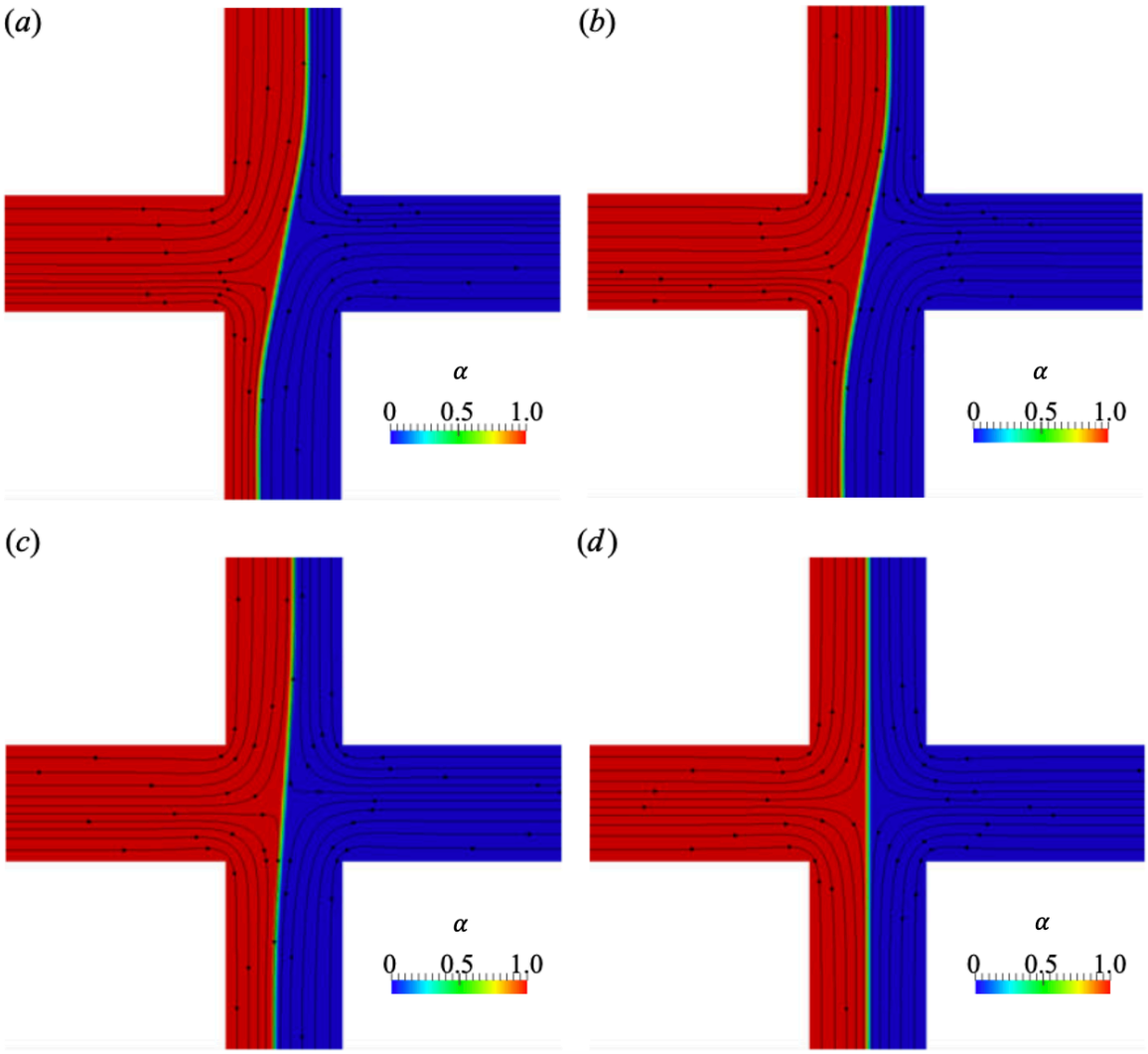

Figure 4.13: Effect of interfacial tension on the symmetry-breaking instability of two fluids for a) Ca = ∞, b) Ca = 1, c) Ca = 0.1, (d) Ca = 0.05, with Wi_i = 0.6, $i = \{1, 2\}$ and K = 1.

The results suggest that at fixed values of $Wi_1 = Wi_2$, once the instability is triggered, by increasing the interfacial tension (i.e., reducing Ca) the interface of the two fluids becomes flatter, having a stabilising effect. The variation of the AP parameter with Wi_i, $i = 1, 2$, is plotted in Figure 4.14, showing that the fundamental supercritical nature of this instability is unchanged as is also observed in the single-phase case (Figure 4.11).

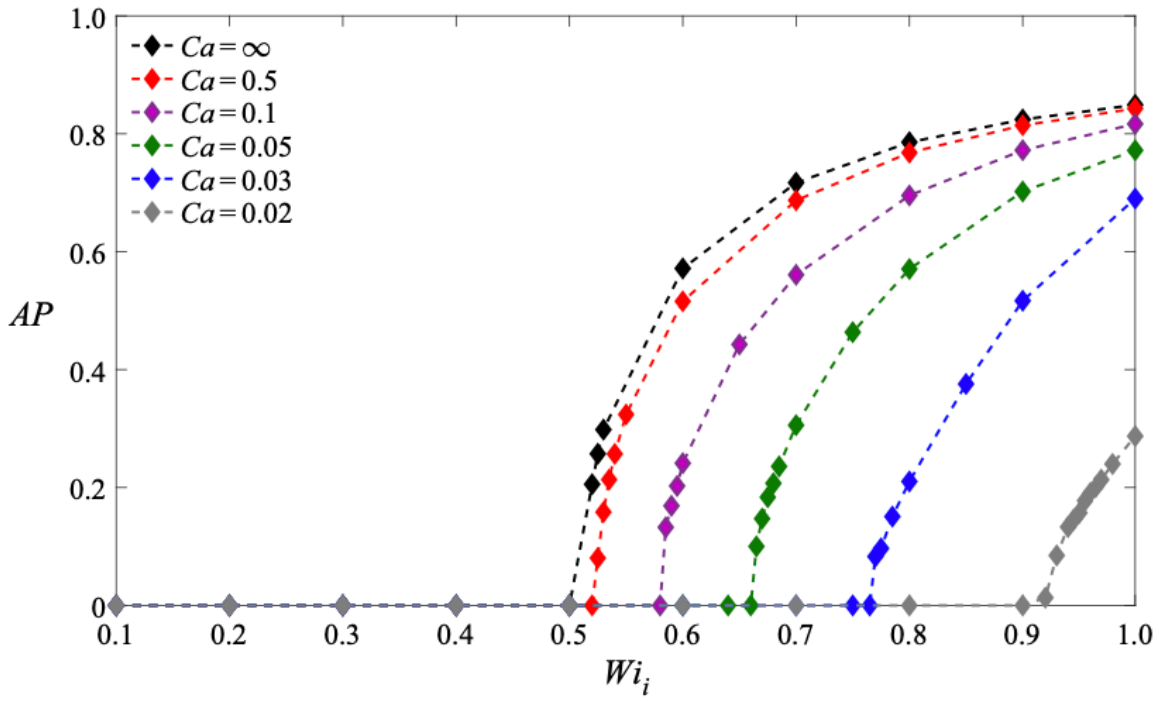

Figure 4.14: Effect of Wi_i with $i = \{1, 2\}$ on the steady symmetry-breaking instability for K = 1 and different Capillary numbers.

In a single-phase flow problem in the cross-slot geometry the curvature parameter can be estimated using the width of the channel as $1/\Re = 1/(aW)$ in equation (4.1) where a is an unknown constant which scales this reference length. In the two-phase problem, due to the presence of the normal-stress jump in equation (4.30), an additional curvature modification appears with a contribution from the interfacial tension. Assuming a constant jump of the normal stress $\tilde{b}$ at the interface of the two fluids (i.e., considering the left-hand side of equation (4.30) to be equal to a constant $\tilde{b}$), the radius of the interfacial curvature can be scaled as $\Re = \sigma/\tilde{b}$. Strictly speaking, the normal-stress jump at the interface is a weak function of the Capillary number. Here, for the sake of an approximate scaling analysis, the stress jump is assumed to be a constant in order to make progress. Later, a comparison between the results predicted using this assumption and the results in the 2D numerical simulations will be carried out to show that the jump of normal stress at the interface of two fluids is only a weak function of Ca and this assumption is therefore a valid approximation in this analysis.

An initial analysis suggests that neither $\sigma/\tilde{b}$ nor aW provides a good approximation of the characteristic curvature of the streamlines in the two-phase cross-slot flow problem and in fact this characteristic length scale is influenced by both of these parameters. Introducing the modifying effect of the interfacial tension on the curvature radius of the flow using a linear combination, the reference curvature may be estimated as:

$$\frac{1}{\mathfrak{R}} = \frac{1}{aW + \sigma/\tilde{b}}. \qquad (4.31)$$

Assuming the modification applied to the streamline curvature due to the interfacial tension is small (i.e., $aW \gg \sigma/\tilde{b}$), using a Taylor expansion equation (4.31) can be rewritten as:

$$\frac{1}{\mathfrak{R}} = \frac{1}{aW} - \frac{\sigma.}{\tilde{b}a^2W^2}. \qquad (4.32)$$

Here, a and $\tilde{b}$ are undetermined constants. Assuming a steady-state purely shear flow for an Oldroyd-B fluid (which the sPTT model approaches in the $\varepsilon \rightarrow 0$ limit), one may scale the normal-stress component in equation (4.1) as

$$\tau_{11} = 2\lambda\mu_p\dot{\gamma}^2. \qquad (4.33)$$

Here, using $\tilde{U}_b$ and $\mathfrak{R}$ as reference scales for the velocity field and the length, respectively, the reference shear rate may be expressed as $\dot{\gamma} = \tilde{U}_b/\mathfrak{R}$. Substitution of these estimates into the dimensionless M criterion (equation (4.1)), results in the following condition for the onset criterion of a purely elastic instability in the two-phase cross-slot flow problem:

$$M_c = \sqrt{\frac{\lambda\tilde{U}_b}{W}\left(a' - \frac{b'}{Ca}\right)2(1-\beta)\frac{\lambda\tilde{U}_b}{W}\left(a' - \frac{b'}{Ca}\right)}, \qquad (4.34)$$

Where $a' = 1/a$, $b' = \tilde{\eta}_t U_B / \tilde{b} a^2 W$ and M_c are unknown constants. However, factoring out the quantity $\left(\lambda \tilde{U}_b / W\right)^2$ and, after some rearrangement, the equation can be simplified to:

$$\frac{1}{Wi_{cr}} = \bar{a} - \frac{\bar{b}}{Ca}, \qquad (4.35)$$

where $\bar{a} = \left(a' \sqrt{2(1-\beta)}\right) / M_c$ and $\bar{b} = \left(b' \sqrt{2(1-\beta)}\right) / M_c$ are unknown constants.

Figure 4.15 shows good agreement between the fit obtained based on equation (4.35) and the results of 2D numerical simulations. This simple correlation allows the prediction of the onset of a purely elastic instability in the two-phase cross-slot flow as a function of the Capillary number and captures the stabilising effect of interfacial tension.

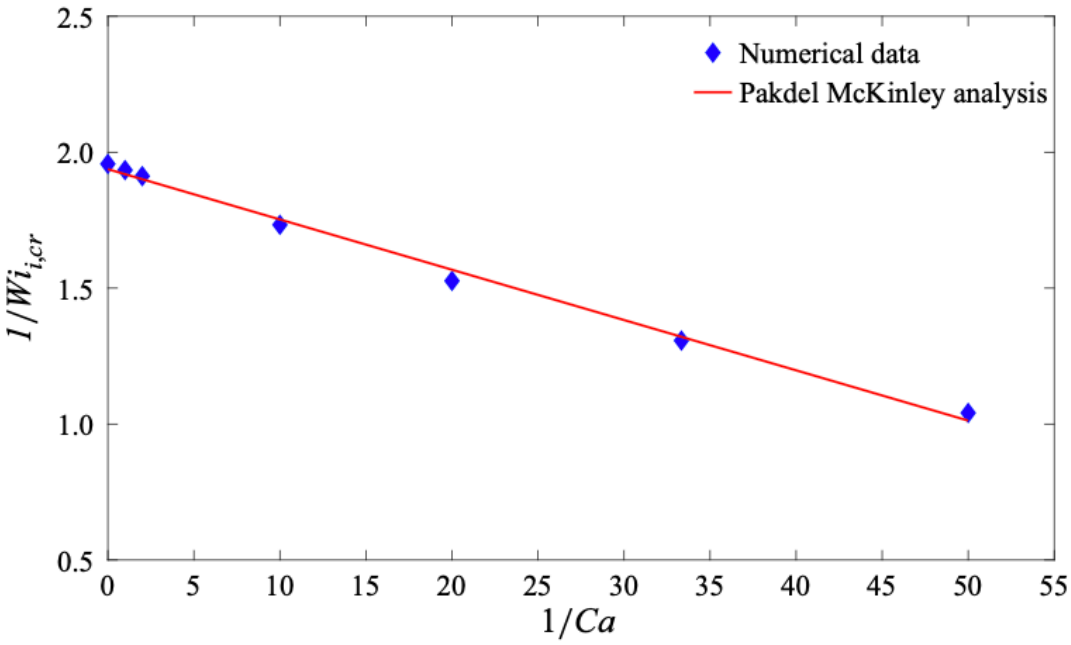

Figure 4.15: Variation of critical values of Weissenberg number against Capillary number for K = 1. Analytical fit $1/Wi_{i,cr} = (0.0185/Ca) + 1.938$ shown by solid line for $i = \{1, 2\}$.

The effect of the total viscosity ratio parameter K is briefly depicted in Figure 4.16 – Figure 4.18. As shown in Figure 4.16, reducing the K parameter pushes the interface

of the two fluids towards the 'right', in agreement with the Newtonian results having an initial stabilising effect. However, the simulations show that a further reduction of K below a critical value triggers a time-dependent instability (cf. Figure 4.17). There are a number of plausible mechanisms which could drive this instability: an increase in the shear rate of Fluid-2 near the corner (i.e., an increase in the local value of the Weissenberg number in this region), the stratification of viscosity (Yih 1967), a jump of elastic normal stresses across the interface (Wilson and Rallison 1997) or a combination of these.

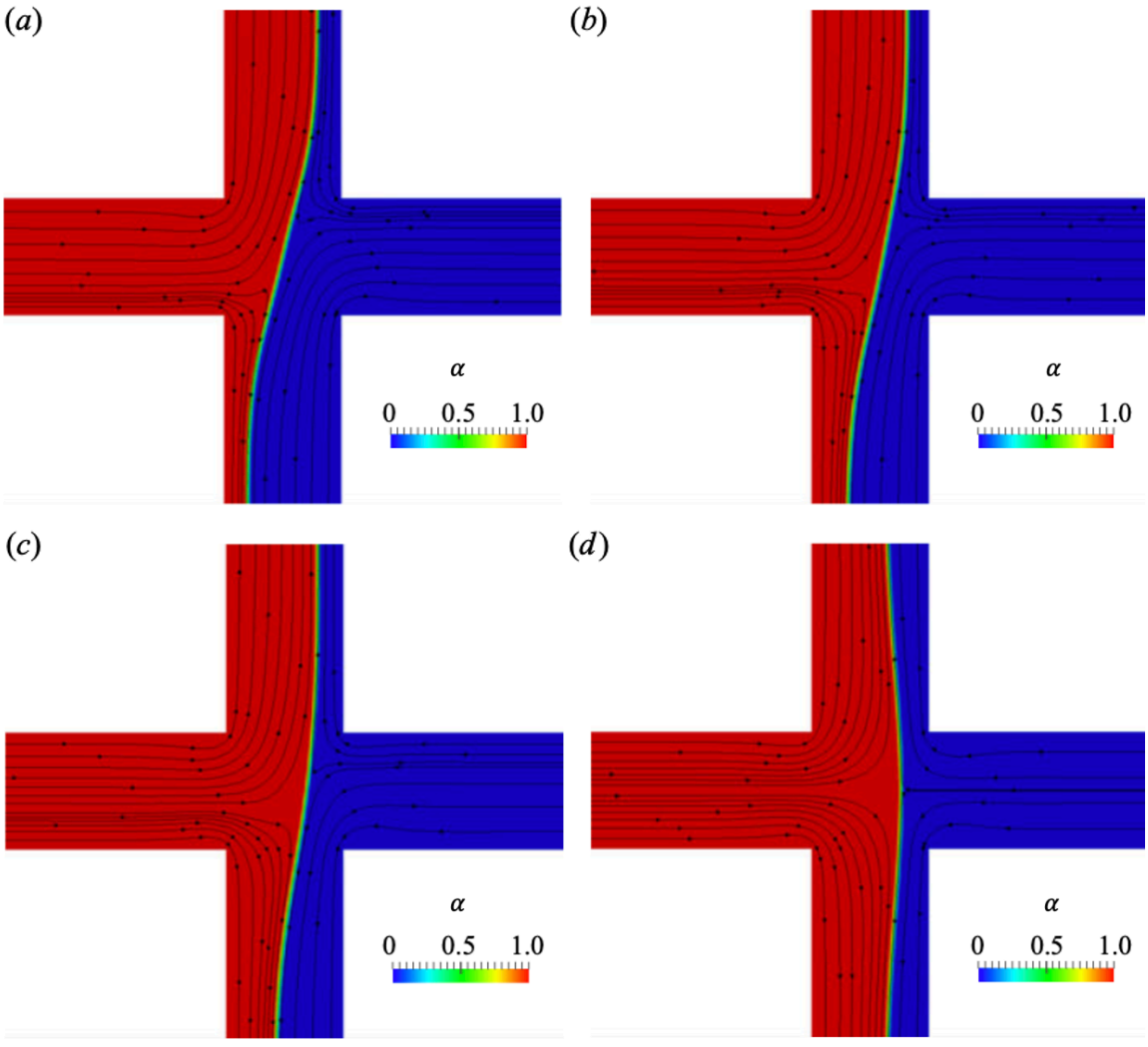

Figure 4.16: Effect of the viscosity ratio parameter on the symmetry-breaking instability of two fluids for a) K = 1, b) K = 0.25, c) K = 0.5, d) K = 0.1, with Wi_i = 1, $i = \{1, 2\}$ and Ca = 0.005.

The results presented in Figure 4.17 show the time-dependent nature of this instability at two different instances in time. By computing the variation of the root-mean-square ($r.m.s.$) of the asymmetry parameter (i.e., $AP_{r.m.s.}$) with the Weissenberg number, such as those shown in Figure 4.18 , we quantify this instability for both increasing and decreasing Weissenberg number ramps. It can be seen that a hysteresis exists at the critical conditions for the instability between the two ramps considered. The $AP_{r.m.s.}$ parameter is defined as follows:

$$AP_{r.m.s} = \sum_{n=1}^{n=N} \sqrt{\frac{\left(\langle AP \rangle - AP_n \right)^2}{N}}, \qquad (4.36)$$

where AP_n is the value of asymmetry parameter at time t and $\langle AP \rangle$ indicates an average of the asymmetry parameter in the defined period of interest from n = 1 to $n = N$.

Here, the critical Weissenberg number for the decreasing ramp is found to be 0.745 while for the increasing ramp it is 0.815. As is well known, the level of hysteresis observed in such instabilities depends on the level of noise and therefore on many factors including the numerical solver, numerical method and mesh. Therefore, aside from demonstrating that this new instability is clearly sub-critical we do not probe this further here.

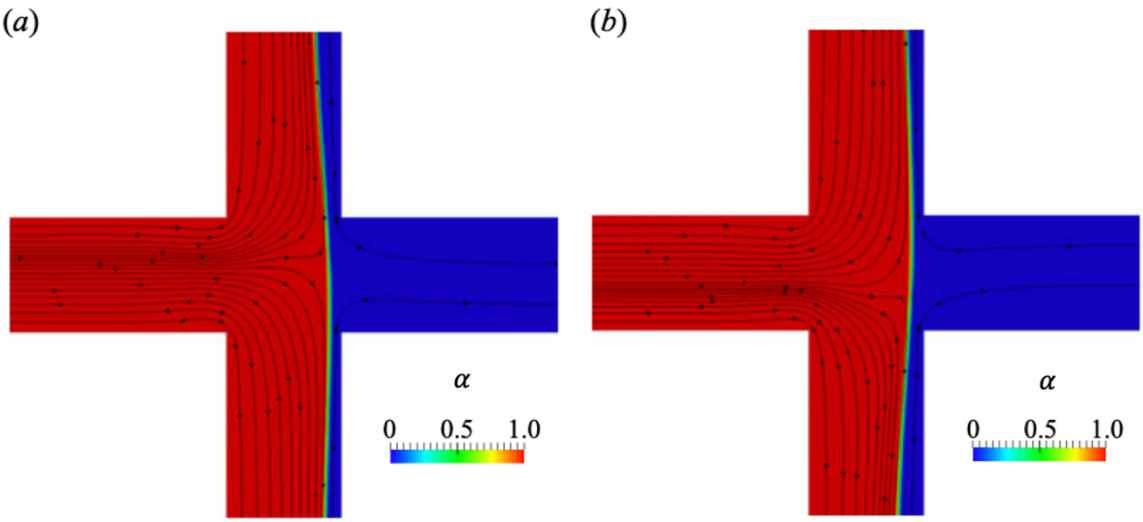

Figure 4.17: Onset of the new time-dependent symmetry-breaking instability in two different time instances for K = 0.001, Wi_i = 1, $i = \{1, 2\}$and Ca = 0.005.

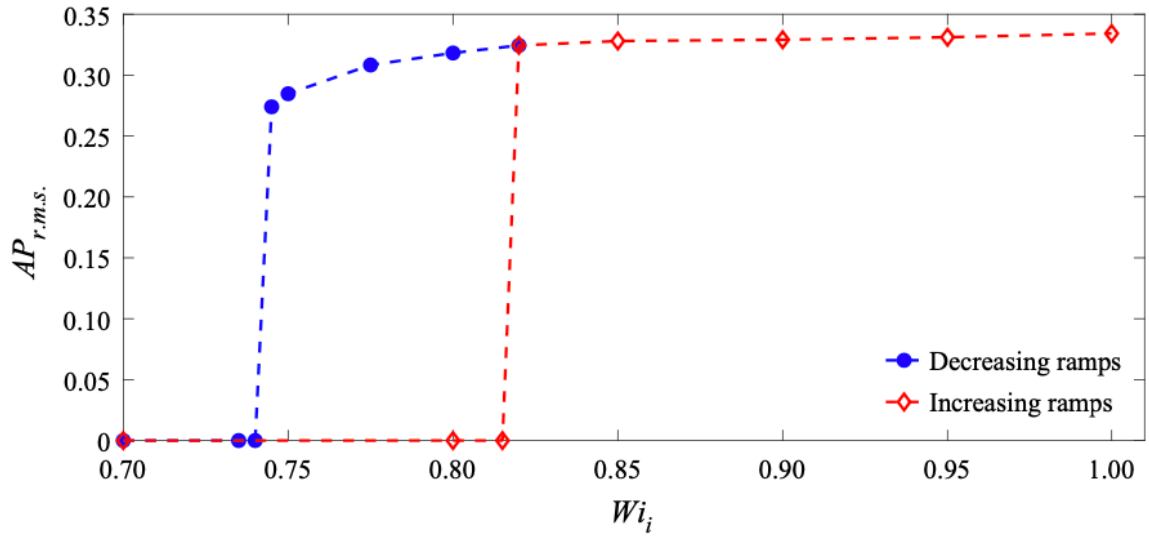

Figure 4.18: The variation of $r.m.s.$ of the asymmetry parameter for the time-dependent symmetry-breaking instability with K = 0.001 and Ca = 0.005 using an increasing Wi_i ramp (open) and decreasing ramp (closed symbols) for $i = \{1, 2\}$.

4.8 CONCLUSIONS

In this chapter, a series of numerical simulations and experiments were carried out to investigate the effects of two-phase flows of Newtonian and/or viscoelastic fluids on the flow characteristics and onset of a well-known purely elastic instability in the cross-slot geometry. Simulations for creeping Newtonian flows, with significant interfacial tension (Ca = 0.005), suggest that, by reducing K, the interface of the two fluids is displaced to a new location. It is worth mentioning that the effect of the viscosity ratio on the location of the interface of two fluids in microfluidic devices has been previously studied and used in rheometry for the measurement of the shear viscosity (Guillot et al. 2006, Gachelin et al. 2013). To study the effect of this phenomenon, an analytical solution for the creeping fully developed flow of two fluids with a flat interface in between two infinite parallel plates (1D channel flow) was obtained and compared with experimental results in the fully developed regions of the outlet channels of the cross-slot. Results have shown that, by increasing the viscosity of one of the fluids, the pressure drop changes and so the average velocity of the fluid with higher viscosity reduces. To satisfy a constant flow rate constraint in both fluids the area required for the higher viscosity fluid to flow needs to increase resulting in a relocation of the interface. The mechanism behind the relocation of the interface in the fully developed region downstream of the cross-slot is similar to the one discussed analytically in a planar channel. Using both numerical simulations and experimental results it is also shown that, when K exhibits a non-unitary value, a ‘dimple’ appears at the interface of the two fluids in the central region of the cross-slot stagnation point, which is related to the jump of the viscous normal stresses at the interface of the two fluids. The results suggest the size of this dimple is a function of the channel aspect ratio and interfacial tension, with the interface becoming flatter as interfacial tension is increased. This change in the shape of the interface is related to a balance between interfacial stress and the jump of the viscous normal stress.

For the viscoelastic simulations, injecting two fluids with different elastic properties from each inlet arm is shown to have a significant stabilising effect on the purely elastic instability, based on the properties of the fluid with the larger relaxation time. The results also show that the Pakdel–McKinley criterion needs to obtain large values on

both sides of the cross-slot before instability will occur. This result suggests a simple method that could be used experimentally to delay the onset of this symmetry-breaking instability practically. Also, for the cases where both fluids have similar viscoelastic properties, at a constant Capillary number, by increasing the Weissenberg number beyond a critical value such that a purely elastic instability arises, the flow distribution and consequently the interface of the two fluids becomes asymmetric yet remains steady in most cases. Once the instability is triggered, by reducing the Capillary number (i.e., increasing the interfacial tension) at a constant Weissenberg number the interface of the two fluids becomes flatter and eventually regains symmetry. Finally, the modification of the interfacial stress on the streamline curvature is introduced in the onset criterion for instability using the so-called Pakdel–McKinley criterion (equation (4.1)). An approximate analytical expression was obtained that can be successfully used to predict how the critical Weissenberg number scales with the Capillary number. Excellent qualitative agreement is found between this approximation analysis and the full nonlinear simulations. Finally, at high interfacial tension (i.e., low Ca) a new time-dependent viscoelastic instability is shown to occur.

4.9 REFERENCES

Arratia, P. E., Thomas, C. C., Diorio, J. D. and Gollub, J. P. (2006). "Elastic Instabilities of Polymer Solutions in Extensional Flows ".

Barmak, I., Gelfgat, A., Vitoshkin, H., Ullmann, A. and Brauner, N. (2016). "Stability of stratified two-phase flows in horizontal channels." Physics of Fluids 28(4): 044101.

Bird, R. B., Hassager, O. and Armstrong, R. C. (1977). Dynamics of polymeric liquids. Vol. 1: Fluid Mechanics, John Wiley and Sons.

Bonhomme, O., Morozov, A., Leng, J. and Colin, A. (2011). "Elastic instability in stratified core annular flow." Phys Rev E Stat Nonlin Soft Matter Phys 83(6): 065301-065301.

Brackbill, J. U., Kothe, D. B. and Zemach, C. (1992). "A continuum method for modeling surface tension." Journal of computational physics 100(2): 335-354.

Capobianchi, P., Pinho, F. T., Lappa, M. and Oliveira, M. S. N. (2019). "Thermocapillary motion of a Newtonian drop in a dilute viscoelastic fluid." Journal of Non-Newtonian Fluid Mechanics 270: 8-22.

Chapra, S. C. and Canale, R. P. (2010). Numerical methods for engineers, Boston: McGraw-Hill Higher Education.

Chinyoka, T., Renardy, Y. Y., Renardy, M. and Khismatullin, D. B. (2005). "Two-dimensional study of drop deformation under simple shear for Oldroyd-B liquids." Journal of Non-Newtonian Fluid Mechanics 130(1): 45-56.

Cruz, F. A., Poole, R. J., Afonso, A. M., Pinho, F. T., Oliveira, P. J. and Alves, M. A. (2016). "Influence of channel aspect ratio on the onset of purely-elastic flow instabilities in three-dimensional planar cross-slots." Journal of Non-Newtonian Fluid Mechanics 227: 65-79.

d'Olce, M., Martin, J., Rakotomalala, N., Salin, D. and Talon, L. (2009). "Convective/absolute instability in miscible core-annular flow. Part 1: Experiments." Journal of Fluid Mechanics 618: 305-322.

Davies, A. R. and Devlin, J. (1993). "On corner flows of Oldroyd-B fluids." Journal of Non-Newtonian Fluid Mechanics 50(2-3): 173-191.

Davoodi, M., Domingues, A. F. and Poole, R. J. (2019). "Control of a purely elastic symmetry-breaking flow instability in cross-slot geometries." Journal of Fluid Mechanics 881: 1123-1157.

Davoodi, M., Houston, G., Downie, J., Oliveira, M. S. N. and Poole, R. J. (2021). "Stabilization of purely elastic instabilities in cross-slot geometries." Journal of Fluid Mechanics 922: A12.

Davoodi, M., Lerouge, S., Norouzi, M. and Poole, R. J. (2018). "Secondary flows due to finite aspect ratio in inertialess viscoelastic Taylor–Couette flow." Journal of Fluid Mechanics 857: 823-850.

Dean, W. R. and Montagnon, P. E. (1949). "On the steady motion of viscous liquid in a corner." Mathematical Proceedings of the Cambridge Philosophical Society 45(3): 389-394.

Figueiredo, R. A., Oishi, C. M., Afonso, A. M., Tasso, I. V. M. and Cuminato, J. A. (2016). "A two-phase solver for complex fluids: Studies of the Weissenberg effect." International Journal of Multiphase Flow 84: 98-115.

Francois, M. M., Cummins, S. J., Dendy, E. D., Kothe, D. B., Sicilian, J. M. and Williams, M. W. (2006). "A balanced-force algorithm for continuous and sharp interfacial surface tension models within a volume tracking framework." Journal of Computational Physics 213(1): 141-173.

Gachelin, J., Mino, G., Berthet, H., Lindner, A., Rousselet, A. and Clement, E. (2013). "Non-Newtonian viscosity of Escherichia coli suspensions." Phys Rev Lett 110(26): 268103.

Gardner, K., Pike, E. R., Miles, M. J., Keller, A. and Tanaka, K. (1982). "Photon-correlation velocimetry of polystyrene solutions in extensional flow fields." Polymer 23(10): 1435-1442.

Görtler, H. (1955). " Dreidimensionale Instabilität der ebenen Staupunktströmung gegenüber wirbelartigen Störungen." In: Görtler, H., Tollmien, W. (eds) 50 Jahre Grenzschichtforschung. Vieweg+Teubner Verlag, Wiesbaden.: 304-314.

Graham, M. D. (2003). "Interfacial hoop stress and instability of viscoelastic free surface flows." Physics of Fluids 15(6): 1702-1710.

Guillot, P., Panizza, P., Salmon, J.-B., Joanicot, M. and Colin, A. (2006). "Viscosimeter on a Microfluidic Chip." Langmuir 22: 6438-6445.

Haward, S. J., McKinley, G. H. and Shen, A. Q. (2016). "Elastic instabilities in planar elongational flow of monodisperse polymer solutions." Sci Rep 6: 33029.

Haward, S. J., Ober, T. J., Oliveira, M. S. N., Alves, M. A. and McKinley, G. H. (2012). "Extensional rheology and elastic instabilities of a wormlike micellar solution in a microfluidic cross-slot device." Soft Matter 8(2): 536-555.

Haward, S. J., Oliveira, M. S., Alves, M. A. and McKinley, G. H. (2012). "Optimized cross-slot flow geometry for microfluidic extensional rheometry." Phys Rev Lett 109(12): 128301.

Hinch, E. J. (1993). "The flow of an Oldroyd fluid around a sharp corner." Journal of Non-Newtonian Fluid Mechanics 50(2-3): 161-171.

Hirt, C. W. and Nichols, B. D. (1981). "Volume of fluid (VOF) method for the dynamics of free boundaries." Journal of computational physics 39(1): 201-225.

Hooper, A. P. and Boyd, W. G. C. (1983). "Shear-flow instability at the interface between two viscous fluids." Journal of Fluid Mechanics 128: 507-528.

Jacqmin, D. (1999). "Calculation of two-phase Navier–Stokes flows using phase-field modeling." Journal of computational physics 155(1): 96-127.

Kalb, A., Villasmil-Urdaneta, L. A. and Cromer, M. (2018). "Elastic instability and secondary flow in cross-slot flow of wormlike micellar solutions." Journal of Non-Newtonian Fluid Mechanics 262: 79-91.

Lagando, R. R. and Leal, L. G. (1990). "Visualization of three-dimensional flow in a four-roll mill." Experiments in Fluids 9(1-2): 25-32.

Lee, H. G., Kim, K. and Kim, J. (2011). "On the long time simulation of the Rayleigh-Taylor instability." International Journal for Numerical Methods in Engineering 85(13): 1633-1647.

Magaletti, F., Picano, F., Chinappi, M., Marino, L. and Casciola, C. M. (2013). "The sharp-interface limit of the Cahn–Hilliard/Navier–Stokes model for binary fluids." Journal of Fluid Mechanics 714: 95-126.

McKinley, G. H., Pakdel, P. and Oztekin, A. (1996). "Rheological and geometric scaling of purely elastic flow instabilities." Journal of Non-Newtonian Fluid Mechanics 67: 19 - 47.

Mittal, R. and Iaccarino, G. (2005). "Immersed boundary methods." Annual review of fluid mechanics 37(1): 239-261.

Moffatt, H. K. (2006). "Viscous and resistive eddies near a sharp corner." Journal of Fluid Mechanics 18(1): 1-18.

Peskin, C. S. (1982). "The fluid dynamics of heart valves- experimental, theoretical, and computational methods." Annual review of fluid mechanics, 14(1): 235-259.

Peterlin, A. (1976). "Optical effects in flow." Annual review of fluid mechanics 8(1): 35-55.

Petitjeans, P. and Maxworthy, T. (1996). "Miscible displacements in capillary tubes. Part 1. Experiments." Journal of Fluid Mechanics 326: 37-56.

PhanThien, N. and I.Tanner, R. (1977). "A new constitutive equation derived from network theory." Journal of Non-Newtonian Fluid Mechanics 2(4): 353-365.

Pimenta, F. and Alves, M. A. (2017). "Stabilization of an open-source finite-volume solver for viscoelastic fluid flows." Journal of Non-Newtonian Fluid Mechanics 239: 85-104.

Poole, R. J., Alves, M. A. and Oliveira, P. J. (2007). "Purely elastic flow asymmetries." Phys Rev Lett 99(16): 164503.

Rocha, G. N., Poole, R. J., Alves, M. A. and Oliveira, P. J. (2009). "On extensibility effects in the cross-slot flow birfurcation." Journal of Non-Newtonian Fluid Mechanics 156: 58-69.

Rybczynski, W. (1911). "Uber die fortschreitende bewegung einer flussigen kugel in einem zahen medium." Akad. Umiej. 1: 40-46.

Shaqfeh, E. S. G. (1996). "Purely elastic instabilities in viscometric flows." Annual Reviews Fluid Mechanics 160: 122-139.

Sousa, P. C., Pinho, F. T. and Alves, M. A. (2018). "Purely-elastic flow instabilities and elastic turbulence in microfluidic cross-slot devices." Soft Matter 14(8): 1344-1354.

Sousa, P. C., Pinho, F. T., Oliveira, M. S. and Alves, M. A. (2015). "Purely elastic flow instabilities in microscale cross-slot devices." Soft Matter 11(45): 8856-8862.

Taylor, T. D. and Acrivos, A. (1964). "On the deformation and drag of a falling viscous drop at low Reynolds number." Journal of Fluid Mechanics 18(3): 466-476.

Tryggvason, G., Bunner, B., Esmaeeli, A., Juric, D., Al-Rawahi, N., Tauber, W., Han, J., Nas, S. and Jan, Y. J. (2001). "A Front-Tracking Method for the Computations of Multiphase Flow." Journal of Computational Physics 169(2): 708-759.

Wilson, H. J. (2012). "Open mathematical problems regarding non-Newtonian fluids." Nonlinearity 25(3): R45-R51.

Wilson, H. J. and Rallison, J. M. (1997). "Short wave instability of co-extruded elastic liquids with matched viscosities." Journal of Non-Newtonian Fluid Mechanics 72: 237-251.

Yih, C.-S. (1967). "Instability due to viscosity stratification." Journal of Fluid Mechanics 27(2): 337-352.

Yue, P., Feng, J. J., Liu, C. and Shen, J. I. E. (2004). "A diffuse-interface method for simulating two-phase flows of complex fluids." Journal of Fluid Mechanics 515: 293-317.

Zografos, K., Afonso, A. M., Poole, R. J. and Oliveira, M. S. N. (2020). "A viscoelastic two-phase solver using a phase-field approach." Journal of Non-Newtonian Fluid Mechanics 284.

CHAPTER 5

Flow focusing with miscible fluids in microfluidic devices

The content of this chapter is adapted from (Houston et al. 2023)

Houston, G., Capobianchi, P. and Oliveira, M. S. N. (2023). "Flow focusing with miscible fluids in microfluidic devices." Physics of Fluids 1 35 (5): 052015.

In this chapter, a series of experiments and numerical simulations performed using a Volume-of-Fluid approach were carried out to investigate the flow of miscible viscous fluid systems through microfluidic flow focusing devices with one central inlet stream (with 'Fluid 1') and two lateral inlet streams (with 'Fluid 2'). The numerical simulations were set up by a colleague at the University of Strathclyde, Dr Paolo Capobianchi. The combined effect of the fluid viscosity ratio and the inlet velocity ratio on the characteristics of the central focused outlet stream was assessed in microfluidic channels with different aspect ratios. An analytical expression for the one-dimensional case, relating the width of the central focused stream in the outlet channel with the velocity ratio and the viscosity ratio, was also derived from first principles. The analytical results are in excellent agreement with the two-dimensional numerical results, and the expression is also able to represent well the experimental findings for the configuration with an aspect ratio of 0.84. The width of the central focused outlet stream at the centre plane is seen to decrease with both the velocity ratio and the viscosity ratio. The results of the three-dimensional numerical simulations and experimental measurements are in good agreement, producing further insight into the curved interface known to exist when high viscosity contrasts are present in parallel flow systems. It was observed that the interface curvature across the depth of the channel cross-section is strongly dependent on the ratio of inlet viscosities and microchannel aspect ratio, highlighting the 3D nature of the flow, in which confinement plays a significant role.

5.1 INTRODUCTION

Hydrodynamic flow focusing at the microscale has been adopted in a number of practical applications that require bringing multiple fluids into contact, such as microfluidic mixing (Knight et al. 1998, Nguyen and Huang 2005), droplet formation (Cubaud et al. 2005, Guerrero et al. 2020, Li et al. 2021), cell analysis (Ateya et al. 2008) and in the microfabrication of fibres, known as microfluidic spinning (Lan et al. 2009, Daniele et al. 2015). Microfluidic spinning has sparked interest over the past few decades with the ability to fabricate fibres of diverse shapes and sizes without the requirement for complex machinery (Jun et al. 2014). Improving the level of control and manipulation of fluids within these devices is key for the production of well defined, predictable, tuneable fibres according to their specific purpose (Lee et al. 2006, Ateya et al. 2008, Kong et al. 2023).

Typical flow focusing devices consist of a cross shaped microchannel with three fluid inlets (a central inlet stream with Fluid 1 and two lateral streams with Fluid 2 as shown in Figure 5.1) and a longer outlet channel, in which a central focused stream is produced. Different design configurations, in which lateral streams confine and shape a central fluid stream, have been used depending on the application. These include simple configurations with lateral perpendicular (cf. Figure 5.1c) or angled inlets (cf. Figure 5.1b) relative to the central inlet stream (Cubaud and Mason 2008, Oliveira et al. 2012), or more complex configurations with additional geometrical features, where e.g., an orifice smaller than the channel width aids controlling the size of the central fluid stream (cf. Figure 5.1a) (Anna et al. 2003, Garstecki et al. 2005, Ward et al. 2005, (Anna et al. 2003, Garstecki et al. 2005, Ward et al. 2005, Guerrero et al. 2020, Li et al. 2021). By changing the flow rate of Fluid 2 relative to Fluid 1 (cf. Figure 5.1c), the portion of the cross-section of the outlet channel occupied by Fluid 1 varies, and the size and shape of the central fluid stream in the outlet channel (referred throughout this work as the central focused stream) can thus be modified (Lee et al. 2006, Oliveira et al. 2011, Golden et al. 2012) . Throughout this work we will refer to the ratio between the inlet velocities (or flow rates - equivalent only if the cross-sectional areas of all inlets are the same as is the case in the present work) as the velocity ratio, $VR = U_2/U_1$, as defined in Figure 5.1c.

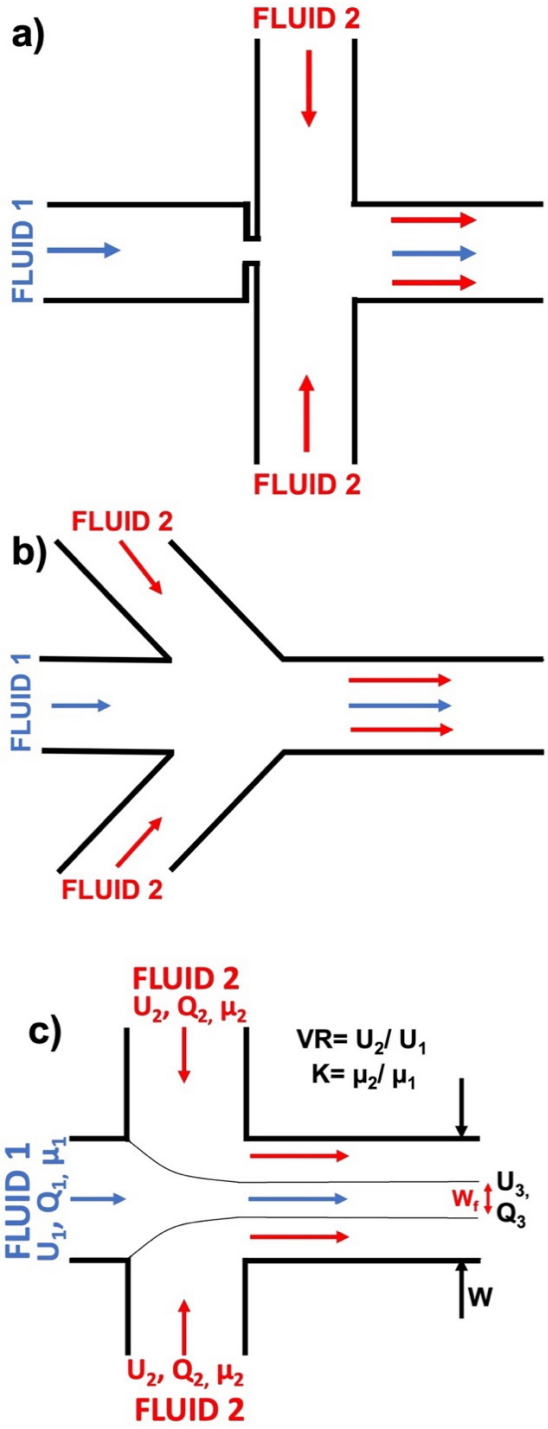

Figure 5.1: Examples of various flow focusing configurations used for bringing fluid streams into contact: a) where an orifice at the centre of the geometry is used to aid control of the shape of the outlet central focused stream; b) with angled lateral inlet streams, and c) with perpendicular lateral inlet streams. The latter configuration is used in this work and important variables are identified in the schematic, where μ_i, Q_i and U_i indicate the viscosity, flow rate

and velocity of each of the fluid streams, respectively. The subscripts $i = 1$ and $i = 2$ refer to the fluid in the central and lateral inlets, respectively, and $i = 3$ refers to the outlet.

The flow of different Newtonian fluid pairs, both miscible and immiscible, have been considered experimentally and numerically within microfluidic flow focusing devices (Knight et al. 1998, Lee et al. 2006, Hu and Cubaud 2016, Cubaud et al. 2021), highlighting the various parameters that affect the shape and size of the produced central focused stream. An early study by Knight et al (1998), showed that within channels of rectangular cross-section (with aspect ratio defined as $AR = D/W$, where D refers to the depth of the channel), when using the same fluid in all inlets (arguably the most common case considered in the literature), the produced central focused stream at the outlet also exhibits an approximately rectangular cross-section. This central focused stream is known to have a width that depends on the ratio of the inlet velocities, with this width decreasing significantly as $VR > 1$ (Knight et al. 1998, Lee et al. 2001, Lee et al. 2006, Oliveira et al. 2012). The ratio of viscosities of the inlet fluids ($K = \mu_2/\mu_1$) is another parameter that plays a crucial role in the formation and characteristics of the central focused fluid stream in microfluidic flow focusing devices. It is important to distinguish the different flow patterns that can be observed depending on the arrangement and characteristics of the fluids. For both miscible and immiscible fluid pairs, when the fluid in the central stream (of viscosity μ_1) is significantly more viscous than the fluid in the laterally injected streams (of viscosity μ_2), so that the ratio between the viscosities is smaller than 0.06, a cylindrical thread is formed (Cubaud and Mason 2012). This is usually referred to as a “lubricated viscous thread” or “core-annular flow” (Cubaud et al. 2012, Cubaud and Mason 2012, Cubaud 2020, Cubaud et al. 2021). Under these flow conditions the thread diameter has been found to be independent of the viscosity ratio, provided the abovementioned conditions are met (Cubaud and Mason 2006, Cubaud 2020). In contrast, when the central fluid is less viscous than the laterally injected fluid streams i.e., $K > 1$, fluid stratification occurs where each fluid, occupies a layer that spans the whole depth of the outlet channel from the top to the bottom channel walls. This yields an interfacial curvature between streams across the channel cross-section (Cubaud and Mason 2008, Cubaud and Mason 2012), with larger portions of the regions of high shear being occupied by the lower viscosity fluid (see Figure 5.2, where an example of the cross-sectional shape

of the central focused stream in the outlet channel obtained in numerical simulations of this work is shown).

Figure 5.2: Example of the cross-sectional shape of the central focused stream in the outlet channel obtained in numerical simulations of this work for viscosity ratio $K > 1$ ($VR = 1, K = 9.56$) and $AR = 0.84$, where Fluid 1 is shown in grey and Fluid 2 is shown in black.

There have been a number of correlations proposed in previous research works to quantify the size of the central outlet focused stream, W_f, which have shown good agreement with experimental results under certain specific circumstances. In microfluidic devices (such as those considered in this work), the microchannels are typically planar with constant depth throughout, and a summary of proposed correlations for such channels is compiled in Table 5.1. The list in Table 5.1 is not exhaustive, but strives to provide relevant information about the fluid systems used and conditions under which each correlation applies.

Table 5.1: Summary of previous studies, proposed correlations for estimating the size of the Newtonian fluid focused stream, and conditions under which they apply. For variable definitions see Figure 5.1.

Reference	Analytical Expression	Fluid Information	Experimental (Exp)/Numerical (Num)	Channel Cross-Section
(Knight et al. 1998)	$\frac{W_f}{W} = B^* \frac{(1 + 2a_c - 2a_c\psi)}{(1 + 2a_c b_c \psi)}$ *where a_c and b_c reflect geometrical parameters, B^* is a constant of order 1 dependent on channel geometry and ψ is the ratio of inlet pressures* $= {}^{p_2}/_{p_1}$.	Viscosity-matching streams ($K = 1$)	Exp	**Rectangular:** Channel with changing Aspect Ratio: Side and outlet channels $AR = 1$ Central inlet channel tapers down to a nozzle of $AR = 5$
(Wu and Nguyen 2005)	$\frac{W_f}{W} = \frac{1}{1 + 2\,(VR)\,K} = [1 + 2\,(VR)\,K]^{-1}$	**Newtonian Miscible Fluids:** Small variation in viscosity ratios ($1/1.8 \leq K \leq 1.8$)	Exp/2D Num/ Analytical (Hele-Shaw Limit)	**Rectangular (Exp):** $AR = 0.06$
(Cubaud and Mason 2006)	$W_f \approx \left(\frac{1}{2\,VR}\right)^{0.6}$	**Newtonian Miscible Fluids**: Viscous fluid is fully surrounded by a less viscous fluid. Lubricated viscous thread. Low Viscosity Ratios ($0.001 < K < 0.06$)	Exp	**Square**: $AR = 1$
(Lee et al. 2006)	$\frac{W_f}{W} = \frac{Q_1}{\bar{v}_*(Q_1 + 2Q_2)} = \bar{v}_*\,(1 + 2\,VR)$ $U_* = \frac{U_f}{U_3} = \frac{1 - \left({}^{192D}/_{\pi^5 W_f}\right) \sum_{n=0}^{\infty} \frac{1}{(2n+1)^5} \frac{sinh[(2n+1)\,\pi W_f\,/2D]}{cosh[(2n+1)\,\pi W/2D]}}{1 - \left({}^{192D}/_{\pi^5 W}\right) \sum_{n=0}^{\infty} \frac{tanh[(2n+1)\,\pi W/2D]}{(2n+1)^5}}$ *where U_f and U_3 represent the average velocities in the focused stream and outlet channel respectively.*	**Newtonian Miscible Fluids:** Viscosity-matching streams ($K = 1$)	Exp/ Analytical	**Rectangular:** $0.05 < AR < 1.78$
(Cubaud and Mason 2008)	$\frac{W_f}{W} \approx \left(\frac{Q_1}{2Q_2}\right)^{1/2} = \left(\frac{1}{2\,VR}\right)^{1/2}$	**Newtonian Immiscible Fluids**: Viscous fluid is fully surrounded by a less viscous fluid. Lubricated viscous thread. Low Viscosity Ratios ($0.0007 \leq K \leq 0.04$)	Exp	**Square:** $AR = 1$

(Cubaud and Mason 2008, Cubaud and Mason 2012)	$\frac{W_f}{W} \approx [1 + 2\,(VR)\,K]^{-1}$	**Newtonian Miscible:** High viscosity fluid surrounded by less viscous fluid: low viscosity ratios ($K = 0.002, 0.008, 0.016$) Low viscosity fluid surrounded by more viscous fluid: range of viscosity ratios ($K = 1.7, 6.3, 83, 625$)	Exp	**Rectangular:** $AR = 0.05$
(Cubaud et al. 2012, Cubaud and Mason 2012)	$\frac{W_f}{W} \approx \left[1 + 2\,(VR)\,K^{1/2}\right]^{-1}$	**Newtonian Miscible Fluids**: Low viscosity fluid surrounded by more viscous fluid. Large Viscosity Ratios ($K > 10$)	Exp	**Square**: $AR = 1$
(Hu and Cubaud 2016)	$\frac{W_f}{W} \approx \frac{1}{1 + 0.67\,(2\,VR)^{2/3}(K)^{1/2}}$ $\left(for\ \frac{W_f}{W} > 10^{-2}\right)$	**Newtonian Miscible Fluids:** Low viscosity fluid surrounded by more viscous fluid. Large viscosity contrasts ($100 \leq K \leq 10000$)	Exp	**Square**: $AR = 1$
(Cubaud 2020)	$\frac{W_f}{W} \approx \left(\frac{1/2VR}{2 + (1/2VR)}\right)^{1/2}$ Small flow rate ratios: $\frac{W_f}{W} \approx \left(\frac{1}{VR}\right)^{1/2}$	**Newtonian Miscible and Partially Miscible Fluids**: Viscous fluid fully surrounded by less viscous fluid. Lubricated viscous thread. Low Viscosity Ratios ($K \leq 0.1$)	Exp	**Square**: $AR = 1$

As illustrated in Table 5.1, past research focuses mainly on conditions of either high viscosity ratios, low viscosity ratios or cases where the viscosity ratio is equal to 1. Studies that cover a range of intermediate viscosity ratios, where differences have a large impact on the development of the central fluid focused stream, are limited and are thus considered in the present work.

Specifically, we report experimental and numerical simulations of miscible Newtonian fluid flows in microfluidic flow focusing devices to study in detail the combined effect of the viscosity ratio (for a range of intermediate K: $1 \leq K \leq 15.07$), the velocity ratio ($1 < VR < 20$) and geometrical aspect ratio on the characteristics of the central focused stream in the outlet channel. Such conditions have been selected to enable the investigation of flows where we observe the formation of a continuous central fluid stream, which remains in contact with the top and bottom channel walls. Additionally, using these ranges we are able to provide further insight into the curved interface that has been observed along the depth of the cross-section when high viscosity contrasts are present in parallel flow systems (Knight et al. 1998, Cubaud and Mason 2008, Cubaud et al. 2012, Cubaud and Mason 2012), and show how the interface curvature changes as the viscosity ratio is varied from unity. We also present a 2D analytical expression derived from first principles for scaling the findings.

5.2 EXPERIMENTAL METHODOLOGY

The flow focusing configuration considered here is composed of four identical planar orthogonal channels (cf. Figure 5.3a) with two opposing lateral streams that shape a third central inlet stream. The reference fluid (Fluid 1), which is characterised by a dynamic viscosity μ_1, is inserted into the central inlet channel with a volumetric flow rate Q_1. Two additional fluid streams (Fluid 2, with a dynamic viscosity μ_2), are symmetrically injected into each of the lateral fluid inlets with a volumetric flow rate Q_2. The flow rates of the two opposing lateral streams are always kept equal to each other ensuring symmetric inlet flow conditions. In this case, the total flow rate in the outlet flow stream can be calculated as: $Q_3 = Q_1 + 2Q_2$. The corresponding average velocity in each of the streams can be calculated as $U_i = \frac{Q_i}{D_i W_i}$, where i represents either the core, lateral or outlet fluid streams ($i = 1, 2$ or 3, respectively). It is worth noting that in this type of device, the extensional rate can be varied by varying, for instance, the ratio between the flow rates in the lateral inlet streams and the central inlet stream (Oliveira et al. 2007, Sousa et al. 2009).

All microchannels were fabricated using polydimethylsiloxane (PDMS; Sylgard 184, Dow Corning) with a SU-8 mould using standard soft-lithography techniques. Subsequently, the microchannels were bonded to a PDMS coated glass slide to ensure that all surfaces had similar characteristics. A schematic diagram of the microfluidic geometry and the experimental set up are shown in Figure 5.3. The microfluidic flow focusing devices used exhibit a rectangular cross section of width, $W = 109 \pm 2\mu$m and a uniform depth, $D = 92 \pm 1\mu$m, which results in an aspect ratio, defined as the ratio of the channel depth to the channel width ($AR = D/W$) that is constant throughout the device and equal to 0.84. To analyse the effect of the channel aspect ratio, an additional geometry having width $W = 125 \pm 2\mu$m and depth $D = 27 \pm 1\mu$m (aspect ratio of $AR = 0.22$) was also used.

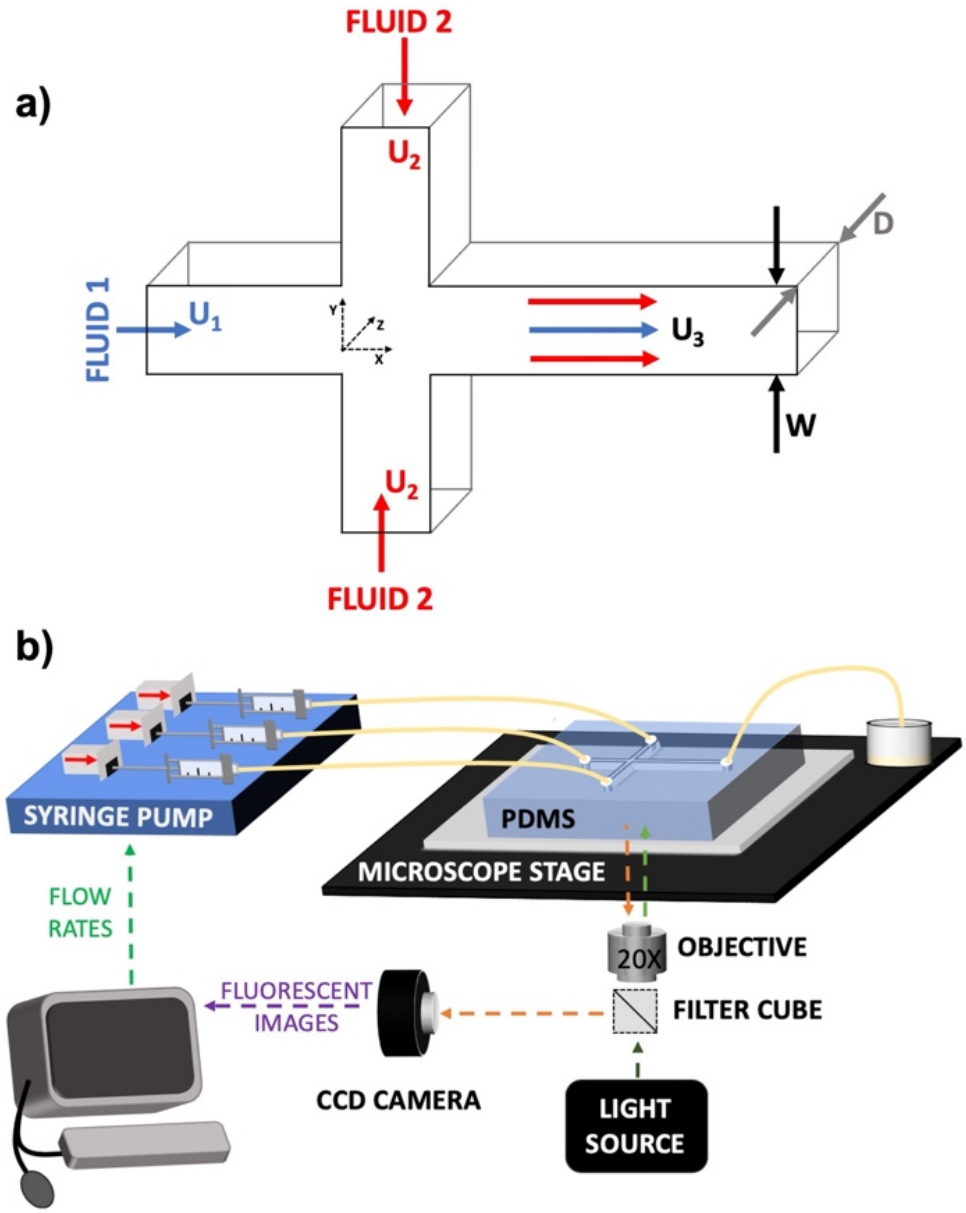

Figure 5.3: Schematic of a) 3D microfluidic flow focusing device used in this work showing relevant variables and coordinate system, and b) experimental flow visualisation set up.

To study the effect of viscosity ratio, aqueous solutions of glycerol of varying concentrations were prepared. The solutions were then divided into three samples for flow visualisation purposes: sample (A), in which Rhodamine-B dye (Sigma-Aldrich) at a concentration of approximately 0.016% was added; sample (B), in which fluorescent tracer particles with nominal diameter of 1 μm (FluoSpheres carboxylate-modified, Nile Red (Ex/Em: 535/575)) were added at concentration of approximately

0.02%wt; and sample (C) which was left as the original solution. A summary of the composition and properties of these fluids is given in Table 5.2, with GLY52 being used as the reference fluid. The density of the solutions was measured using pycnometry and the viscosity was characterised in steady shear on a DHR-2 hybrid rotational rheometer (TA Instruments) with a cone-plate geometry (60mm diameter, 1° cone angle) at a temperature of 20°C.

Table 5.2: Characteristics of the fluids used in the experimental work including fluid composition and physical properties (density and viscosity) at 20°C.

Fluid ID	Composition	Density (kg/m^3)	Viscosity (Pa s)	Viscosity Ratio (K)*
Water	Deionised Water	1000	$1.00x10^{-3}$	0.15
GLY52	***51.7 wt% Glycerol**	**1172**	**$6.81x10^{-3}$**	**1**
GLY61	61.4 wt% Glycerol	1181	$1.20x10^{-2}$	1.76
GLY71	71.2 wt% Glycerol	1190	$2.55x10^{-2}$	3.74
GLY76	75.6 wt% Glycerol	1195	$3.84x10^{-2}$	5.64
GLY81	80.5 wt% Glycerol	1209	$6.51x10^{-2}$	9.56
GLY84	84.4 wt% Glycerol	1222	$1.03x10^{-1}$	15.07

*Viscosity ratio calculated relative to GLY52 used as reference fluid.

The fluids were injected into the three geometry inlets simultaneously at controlled flowrates using a high-precision syringe pump with independent modules (neMESYS, Cetoni GmbH). SGE™ gastight glass syringes were connected to the microchannel using Tygon tubing, and the geometry outlet was left open to the atmosphere. The flow was illuminated with a 100W metal halide lamp and visualised using an inverted microscope (Olympus IX71). The microscope was equipped with a 20X objective lens (numerical aperture NA = 0.4) and an adequate filter cube (Olympus U-MWIGA3). The images were acquired at the centre plane of the microchannel ($z = D/2$), unless stated otherwise, using a CCD camera (Olympus XM10) and the exposure time was adjusted according to the flow conditions.

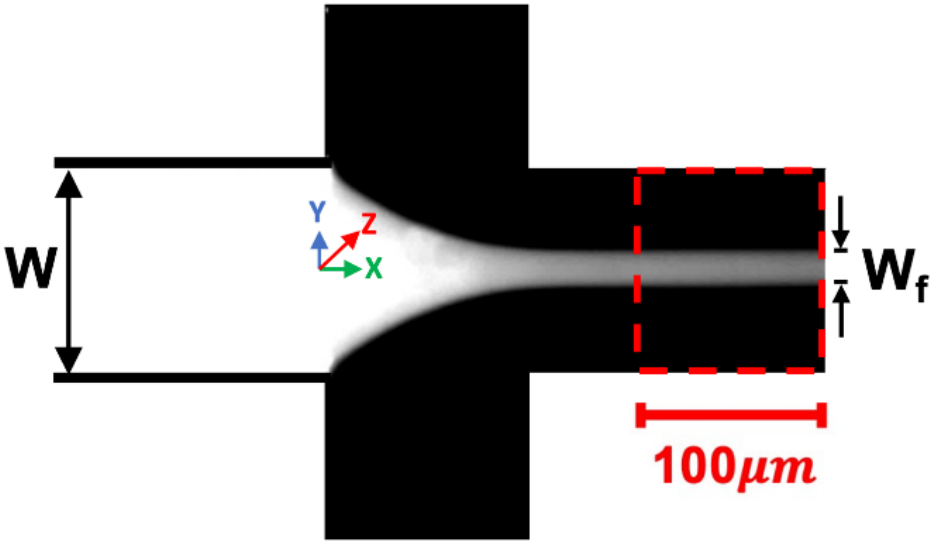

Figure 5.4: Example of a microscope image obtained with the central fluid stream dyed with Rhodamine-B and undyed lateral streams, highlighting the region over which the measurement of the outlet central focused stream width was performed (the reported value of W_f being an average across the highlighted region).

Image analysis was used to assess the impact of viscosity ratio, velocity ratio and aspect ratio of the device on the shape and size of the generated central fluid focused stream. The width of the central focused stream in the outlet channel at the centre plane, W_f, was measured using the image processing software ImageJ in the region of the bounding rectangle indicated by the red box in Figure 5.4. The bounding measurement rectangle spanned ~100 μm along the *x*-direction in the region of $1.7 \leq x/W \leq 2.7$ where the newly formed central focused stream exhibited an approximately constant shape. An average value for the focused stream width over this length was then determined. Defining the exact boundaries for these experimental measurements is not straightforward due to a small gradient in the interface region between the two fluids as illustrated by the gradual variation of grayscale intensity profile shown in Figure 5.5. For consistency, the mid-point was considered for the measurements presented in this work (a normalised gray scale value of 0.5).

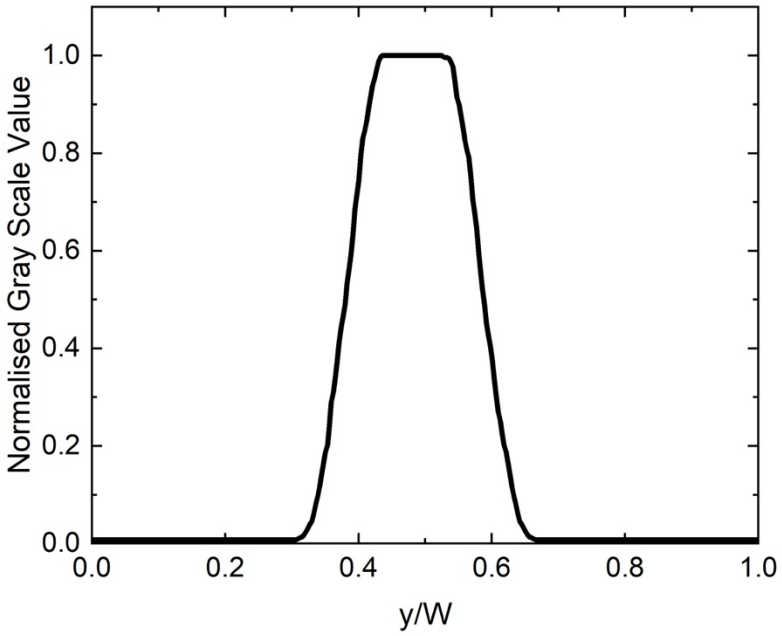

Figure 5.5: Normalised grayscale profile along the width of the outlet channel at location $x/W = 2.5$ (within the experimental measurement region) for $AR = 0.84$, $K = 1$ and $VR = 1$. The profile highlights the variation of grayscale intensity in the regions of the interface between the undyed outer fluid and the central focused fluid stream dyed with Rhodamine-B.

For all 3D simulations, measurements were taken at a location in the downstream channel, corresponding to $x/W = 2.5$. This location lies within the experimental measuring window to ensure comparable results. This measurement location is also comparable to that used in the work of Cubaud et al (2008) ensuring the flow is fully developed in the outlet stream without being too far downstream thus avoiding significant diffusion effects, as witnessed by Wu et al (2005).

5.3 DIMENSIONLESS PARAMETERS

Dimensionless parameters of interest for the flow under consideration include the Reynolds number, Re, the viscosity ratio, $K = \mu_2/\mu_1$, and the velocity ratio, $VR = U_2/U_1$, which in this case is equal to the flow rate ratio Q_2/Q_1, given the incompressibility constraint and to the fact that the inlet channels have the same cross-

sectional area. Given the significant role played by the velocity ratio on the characteristics of the central outlet stream, the effect of this parameter was systematically investigated throughout this work. To this end, the central flow rate was maintained constant throughout the whole set of experiments, while the flow rate of the lateral streams was systematically increased. When the fluid is the same in all inlet streams ($K = 1$), for low values of VR (i.e., for $VR < 1$) the central stream encompasses a large portion of the outlet channel, leaving only a thin region for the flow of the outer fluid streams (Hu and Cubaud 2016). In this work, however, we focus on larger values of VR (i.e., $VR \geq 1$), for which, as we shall see, a relatively narrow central focused stream is observed. Inertial effects are not important since the Reynolds numbers considered here are small ($0.01 < Re < 0.5$).

5.4 NUMERICAL METHOD

In addition to experiments, a set of selected three-dimensional simulations were carried out using a Volume-of-Fluid (VOF) method using the opensource computational toolbox OpenFOAM. In such an approach, the interface between the fluids is described through the adoption of a volume fraction phase, α. This represents the volume average of one fluid (arbitrarily defined between two possible choices) with respect to the total fluid encapsulated in one computational cell. Thus, this function takes values $0 < \alpha < 1$ at the interface, while the values 0 and 1 characterise the two bulk phases away from the interface. Such quantity is then evolved numerically in space and time through an advection equation of the type reported below (albeit particular modifications required to avoid excessive smearing of the interface introduced in the implementation of the method in OpenFOAM e.g., see Capobianchi et al. 2017 for more details):

$$\frac{\partial \alpha}{\partial t} + \nabla \cdot (\alpha \mathbf{u}) = 0. \qquad (5.1)$$

Finally, since miscible fluids are under consideration, capillary forces are not taken into account, and the ‘one-fluid’ formulation of the momentum equation reads (gravity is not accounted for due to the small length scale and similar density of the two fluids):

$$\rho\left[\frac{\partial \mathbf{u}}{\partial t}+(\mathbf{u}\cdot\nabla)\mathbf{u}\right]=-\nabla p+\nabla\cdot(2\mu S), \qquad (5.2)$$

where $S=\frac{1}{2}\left(\nabla\mathbf{u}+(\nabla\mathbf{u})^{\mathrm{T}}\right)$ is the rate-of-strain tensor. In such an approach, variables such as velocity and pressure, are defined continuously throughout the whole domain, while the fluid properties are continuous functions of the volume fraction:

$$\rho=\alpha\rho_1+(1-\alpha)\rho_2, \qquad \mu=\alpha\mu_1+(1-\alpha)\mu_2. \qquad (5.3)$$

The problem was discretised numerically using the boundary conditions shown in Table 5.3 and a structured mesh consisting of approximately 3×10^5 identical cubic cells and an adaptive octree mesh refinement approach has been applied at the region of the interface (only for the 3D cases), where larger resolution was deemed necessary. The thickness of the central stream undergoes substantial variations depending on the flow conditions considered (i.e., velocity ratio and/or viscosity ratio), hence the level of refinement adopted was selected on the basis of this constraint. In other terms, since the density of the unrefined mesh was always the same, the dimension of the cells to be employed at the interface was necessarily different for different flow conditions across the whole region of the flow parameter explored to have a sufficiently high resolution.

Table 5.3: Boundary conditions used in numerical simulations in the flow focusing device utilising numbered channel notation from Figure 5.3a.

Flow Parameter	**Boundary**		
	Channel 1(inlet)	**Channel 2 (inlet)**	**Channel 3 (outlet)**
Velocity, U	Fixed Value	Fixed Value	Zero-Gradient
Pressure, P	Zero-Gradient	Zero-Gradient	Fixed Value
Volume Fraction, α	Zero-Gradient	Zero-Gradient	Zero-Gradient

5.5 ANALYTICAL SOLUTION FOR THE ONE-DIMENSIONAL PROBLEM

In this section, an exact solution for the 1D creeping flow, obtained assuming absence of confinement in the spanwise z-direction, is derived by taking advantage of the symmetry of the flow established at a sufficient distance downstream of the cross junction. Owing to these hypotheses, the problem can be simplified to that of a pressure-driven, creeping flow between 2 parallel plates (cf. Figure 5.6) in which the interface between the fluids is perfectly flat. A schematic of the problem highlighting the coordinate system adopted, and the equivalent symmetric counterpart of the flow is shown in Figure 5.6.

The problem under consideration is governed by the steady-state Navier-Stokes equations for incompressible creeping flows for the two fluids considered:

$$0 = -\frac{\partial p}{\partial x} + \mu_1 \frac{\partial^2}{\partial y^2}\left(u_{1,x}\right), \tag{5.4}$$

$$0 = -\frac{\partial p}{\partial x} + \mu_2 \frac{\partial^2}{\partial y^2}\left(u_{2,x}\right), \tag{5.5}$$

where $u_{1,x}$ and $u_{2,x}$ are the x-component of the velocities of Fluid 1 and Fluid 2, respectively. The origin of the y-axis is taken at the centreline (dashed line in Figure 5.6). The central stream is characterised by a half height $h = {W_f}/{2}$, while $H = {W}/{2}$ represents the extension of the semi portion of the domain from the centreline to the wall as shown in Figure 5.6.

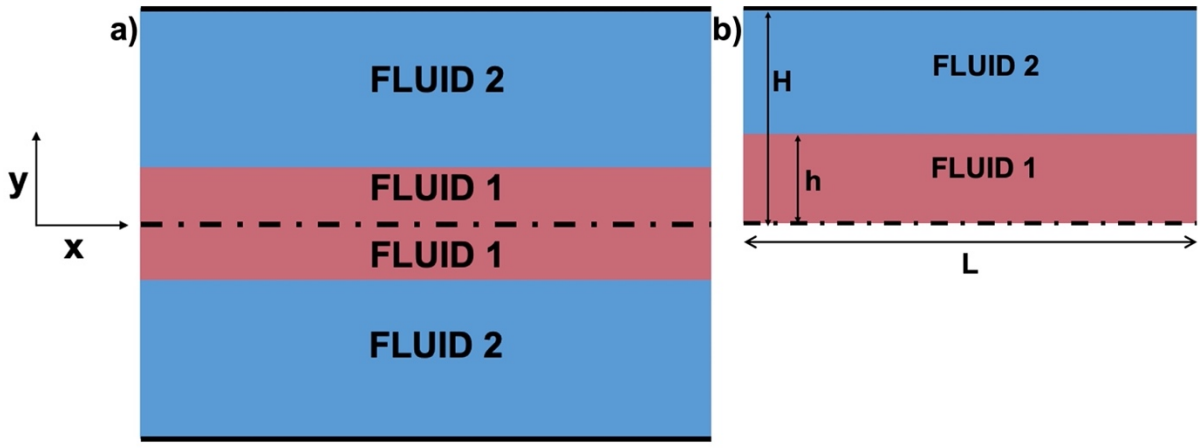

Figure 5.6: Schematic of a) the full 1D geometry used to replicate the outlet channel of the flow focusing device highlighting the region of symmetry and the employed coordinate system, b) the 1D geometry used to derive the 1D analytical expression considering the symmetry of the flow.

The general solutions of equations (5.4) and (5.5) are:

$$u_{1,x} = \frac{Gy^2}{2\mu_1} + \overline{A}y + \overline{B}, \qquad u_{2,x} = \frac{Gy^2}{2\mu_2} + \overline{C}y + \overline{D}, \tag{5.6}$$

where G is the applied constant pressure gradient defined as $G = \Delta p/L$, L is the length of the domain in the *x*-direction and $\overline{A}$, $\overline{B}$, $\overline{C}$ and $\overline{D}$ are yet to be determined constants of integration. Given the geometrical constraints of the flow and its boundary conditions, the y-component of the velocity is null everywhere, i.e., $u_{1,y} = u_{2,y} \equiv 0$. At the fluid interface ($y = h$), continuity of the velocity and of the shear stress is imposed, while at the upper wall ($y = H$), we impose the no-slip boundary condition, i.e.,

$$u_{1,x}\Big|_{y=h} = u_{2,x}\Big|_{y=h} \tag{5.7}$$

$$\mu_1 \frac{\partial u_{1,x}}{\partial y}\bigg|_{y=h} = \mu_2 \frac{\partial u_{2,x}}{\partial y}\bigg|_{y=h} \tag{5.8}$$

$$u_{2,x}\Big|_{y=H}=0. \tag{5.9}$$

By substituting these boundary conditions into equation (5.6) we found the following expressions for each constant: $\overline{A}=0,\ \overline{B}=\dfrac{-G\left(H^2\mu_1-h^2\mu_1+h^2\mu_2\right)}{2\mu_1\mu_2}$, $\overline{C}=0,$ $\overline{D}=-\dfrac{GH^2}{2\mu_2}$, which allows determining $u_{1,x}$ and $u_{2,x}$ as:

$$u_{1,x}=-\frac{G\left(\left(H^2-h^2\right)\mu_1+\mu_2\left(h^2-y^2\right)\right)}{2\mu_1\mu_2}, \qquad u_{2,x}=-\frac{G\left(H^2-y^2\right)}{2\mu_2}, \tag{5.10}$$

The average velocities of each fluid stream (i.e., $u_{1,x}$ and $u_{2,x}$) can then be calculated as follows:

$$U_{1,x}=\frac{1}{h}\int_0^h u_{1,x}dy=-\frac{\left(\left(H^2-h^2\right)\mu_1+\dfrac{2h^3\mu_2}{3}\right)G}{2\mu_1\mu_2}, \tag{5.11}$$

$$U_{2,x}=\frac{1}{(H-h)}\int_h^H u_{2,x}dy=-\frac{(2H+h)\,G(H-h)}{6\mu_2}. \tag{5.12}$$

Substituting the following variables for the dimensionless focused stream width, $W_f^*=h/H$ and the viscosity ratio, $K=\mu_2/\mu_1$ into the previous equations, we obtain the following expression for the velocity ratio:

$$VR\equiv\frac{U_{2,x}}{U_{1,x}}=\frac{\left(W_f{}^*+2\right)\left(W_f{}^*-1\right)^2}{(4K-6)\,W_f{}^{*3}+6W_f{}^*}. \tag{5.13}$$

For a desired value of the velocity ratio and viscosity ratio, it is therefore possible to determine the dimensionless thickness W_f^* which satisfies equation (5.13).

5.6 ANALYTICAL SOLUTION AND NUMERICAL RESULTS FOR THE 2D PROBLEM

The dimensionless width of the central focused stream (normalised using the channel width) in the fully developed region of the outlet channel of the flow focusing device obtained in the 2D flow numerical simulations is compared with the analytical solution derived in Section 5.5. A strong effect of the velocity ratio (especially for low VR values) on the width of the central focused stream is observed as seen in previous work (Wu and Nguyen 2005, Oliveira et al. 2012), with the width decreasing as VR is increased. The viscosity ratio is also seen to impact the size of the focused stream for $VR = 1$, however this effect is not as significant for higher values of K over the ranges considered. There is excellent quantitative agreement between the 2D numerical and analytical results for a range of VR (Figure 5.7a) and K values (Figure 5.7b) with a maximum relative error of 7%. It is worth noting that the relative errors are smaller for lower values of VR and K. The analytical solution also shows that for higher values of VR, the effect of K becomes less significant (for $VR = 5$ e.g., as shown in Figure 5.7b, the relative difference between the normalised width for $K = 1$ and $K = 15$ is $\lesssim 3\%$).

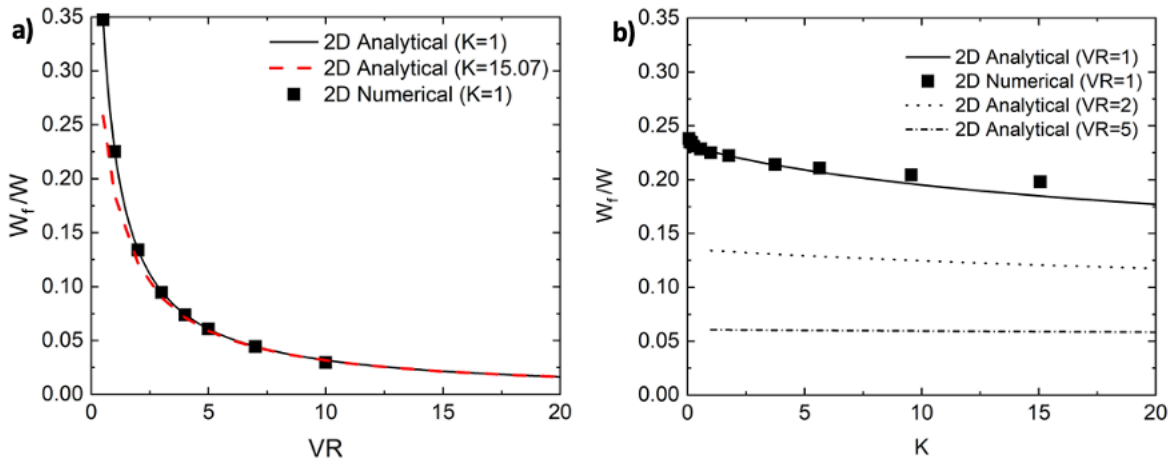

Figure 5.7: Comparison of analytical solution and 2D numerical simulations (at $x/W = 2.5$) showing a) Impact of velocity ratio for $K = 1$ b) Impact of viscosity ratio for $VR = 1$, $VR = 2$ and $VR = 5$.

Good agreement between the 2D numerical and analytical results can also be observed in terms of velocity distribution in the cross-section of the outlet channel (normalised using the maximum velocity at the centreline ($y/W = 0.5$) for each case) for a range of K values and $VR = 1$ (Figure 5.8). When $K = 1$ (Figure 5.8a), the velocity profile exhibits a symmetric parabolic shape across the width of the cross-section as expected. As K is increased beyond unity (Figure 5.8b-d), the velocity profile appears 'cusped' at the interface; a circumstance that is dictated by the stress condition given in equation (5.8). In fact, while stresses are continuous at the interface, the derivative of the velocity must be necessarily discontinuous when the viscosity of the two fluids are not matched. Therefore, as the viscosity of the lateral streams increases, the strain rate tensor experiences increasingly larger jumps across the interface causing the increase in the velocity of the central stream to satisfy the incompressibility requirements (this behaviour is further discussed in Section 5.7.2), becoming more pronounced as K increases, in agreement with previous research (Wu and Nguyen 2005). For increasingly larger viscosity ratios, both Figure 5.7 and Figure 5.8 show that the agreement becomes less accurate, which can be attributed to the numerical approach which considers the two fluids as a single entity characterised by generally different material properties, such as the viscosity, as appropriate in this context. Discontinuities in properties across the interface are linearised by means of equation (5.3). This, in turn, inevitably introduces inaccuracies in the numerical solution which become less reliable for increasingly large viscosity ratios: an issue, which could be partially mitigated by the adoption of larger mesh resolutions.

The mesh requirement conditions for the numerical work has been justified by the close correspondance to the analytical solutions (shown in Figure 5.7 and 5.8) and because a developed flow condition is used for flow measurements which is independent of upstream conditions.

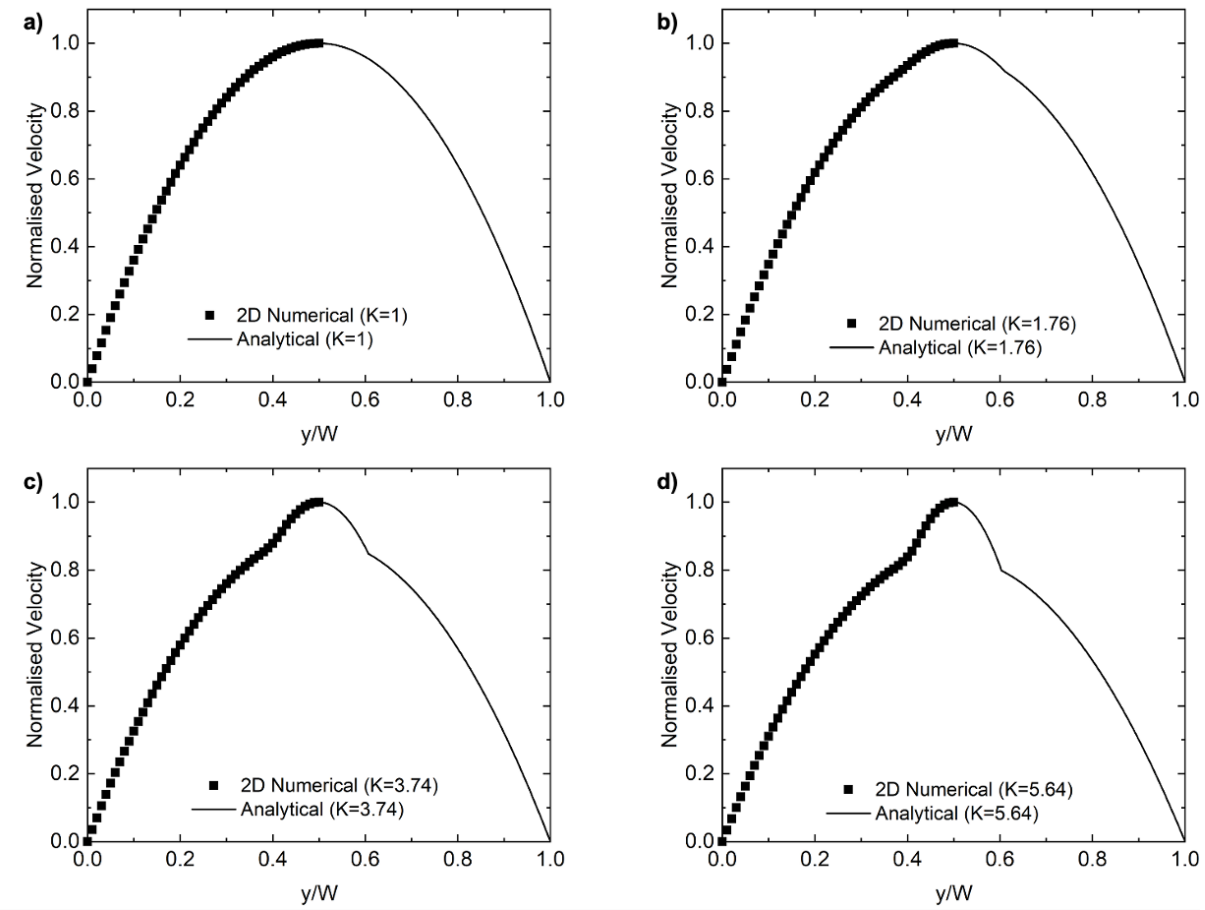

Figure 5.8: Comparison of analytical solution and 2D numerical simulations (at $x/W = 2.5$) showing the impact of viscosity ratio when $VR = 1$ on the normalised velocity profile (normalised using the maximum velocity at the centreline ($y/W = 0.5$) for each case) in the y-direction for a) $K = 1$ b) $K = 1.76$ c) $K = 3.74$ and d) $K = 5.64$.

5.7 RESULTS AND DISCUSSION

In this work, a series of experiments supported by 3D numerical simulations were conducted to investigate the influence of various parameters on the characteristics (shape and width) of the central focused outlet fluid stream. As anticipated, we focus on those conditions where inertia can be assumed negligible, and the flow is always steady and symmetric about the x-axis (Lee et al. 2006). We also neglect molecular diffusion as in most cases the Peclet number (defined as $Pe = {U_3 W}/{D_c}$, where D_c is the diffusion coefficient for each fluid pair, as detailed by Petitjeans and Maxworthy (1996)

is large ($Pe > 10^3$)) suggesting the two miscible fluids flow side by side without mixing (Petitjeans and Maxworthy 1996, d'Olce et al. 2009). When interfacial tension is relatively low or miscible fluids are considered, the flow may experience an instability referred to as viscosity stratification (Yih 1967). To avoid such instabilities, previous researchers have reported that high values of interfacial tension can be used (Hooper and Boyd 2006) or, as this instability is said to be of inertial origin, low Reynolds number flows (Bonhomme et al. 2011). It is possible that the system may not be truly steady state; however, since for all cases considered here, the Reynolds number was always below unity and no visible instabilities were identified, in agreement with the results of Bonhomme et al. (2011), the system will be treated as being stable throughout this work (as done previously in Davoodi et al. 2021).

5.7.1 Effect of Velocity Ratio

To assess the impact of the velocity ratio, experiments were conducted considering viscosity matching streams (i.e., considering $K = 1$), in which the velocity ratio, VR, was adjusted from $VR = 1$ up to the maximum value of $VR = 20$. Simulations for some selected cases were also performed for comparison. Typical flow patterns encountered for the base case geometry ($AR = 0.84$) can be observed in Figure 5.9.

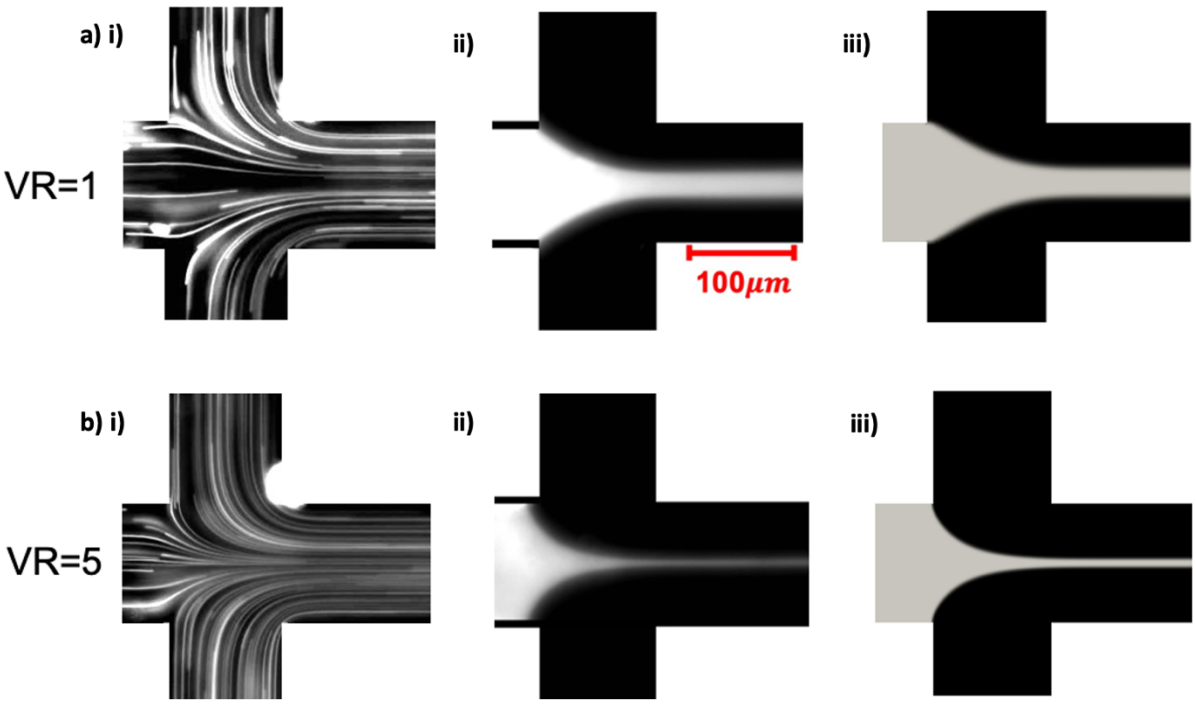

Figure 5.9: Flow patterns observed in the flow focusing geometry with $AR = 0.84$ and $Q_1 = 0.02$ ml/h, with matching fluid in all inlets ($K = 1$) and different velocity ratios a) $VR = 1$, b) $VR = 5$. i-ii) Experimental images obtained by adding i) fluorescent tracer particles to all inlet streams to show the pathlines and ii) Rhodamine-B dye to the central fluid inlet only. iii) 3D numerical simulations, where Fluid 1 is shown in gray and Fluid 2 is shown in black.

For the cases shown in Figure 5.9, a converging flow region is present at the centre of the flow focusing device, producing a centralised straight focused stream downstream of the central region that extends along the outlet of the microchannel. In agreement with previous works for $K = 1$ (e.g., Lee et al. 2006), the width of the central focused stream decreases as the velocity ratio is increased, and its cross-sectional area is approximately rectangular (Knight et al. 1998). For all VR tested here ($1 < VR < 20$), the separating streamlines in the central region of the device where the three inlet fluids meet display a concave shape (as seen in the experimental flow patterns of Figure 5.9ai and bi, and in the numerical results shown in Figure 5.10) as expected when $VR > K^{-3/4}/2$ (Hu and Cubaud 2016). The streamlines in the converging region near the centre of the geometry (cf. Figure 5.9) exhibit a near hyperbolic shape characteristic of extensional flows (Oliveira et al. 2007). Increasing

VR to higher values, increases the curvature of the streamlines and reduces the width of the central outlet focused stream (Nguyen and Huang 2005, Oliveira et al. 2012). Under these conditions the viscous stresses from the lateral fluid streams dominate how the central fluid profile is formed. Similar experimental observations are discussed in the work of Lee et al (2006) where the range of $0.1 \leq VR \leq 8$ was studied for $K = 1$.

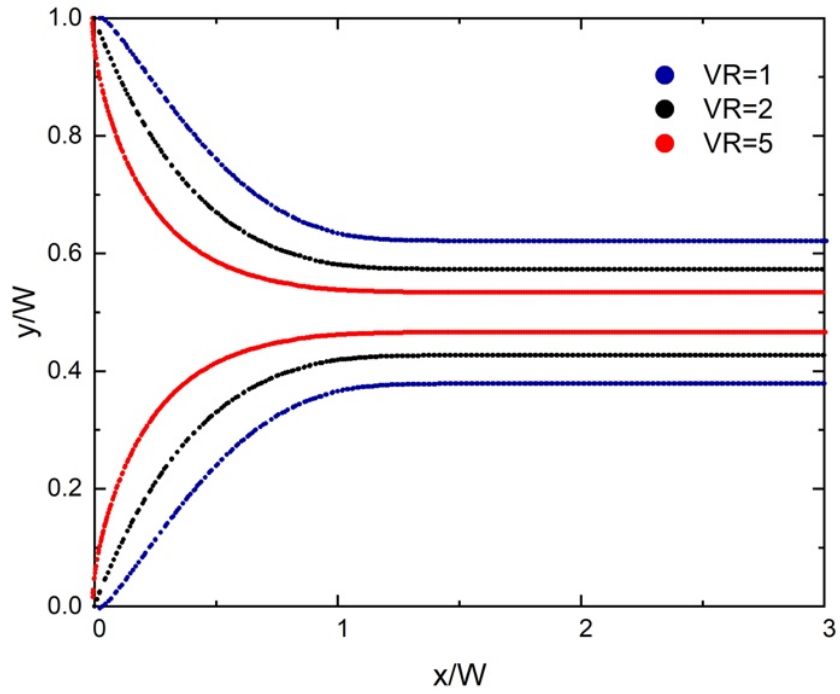

Figure 5.10: Outline of the separating streamlines observed from numerical simulations at the centre plane with increasing velocity ratio within the flow focusing geometry of $AR = 0.84$, for $K = 1$.

The size of the central focused stream developed in the outlet channel is quantified in Figure 5.11, where the central focused stream thickness measured experimentally at the centre plane is normalised using the channel width. In this figure, results predicted by the simulations and by the analytical solution (Equation (5.13)) are also included.

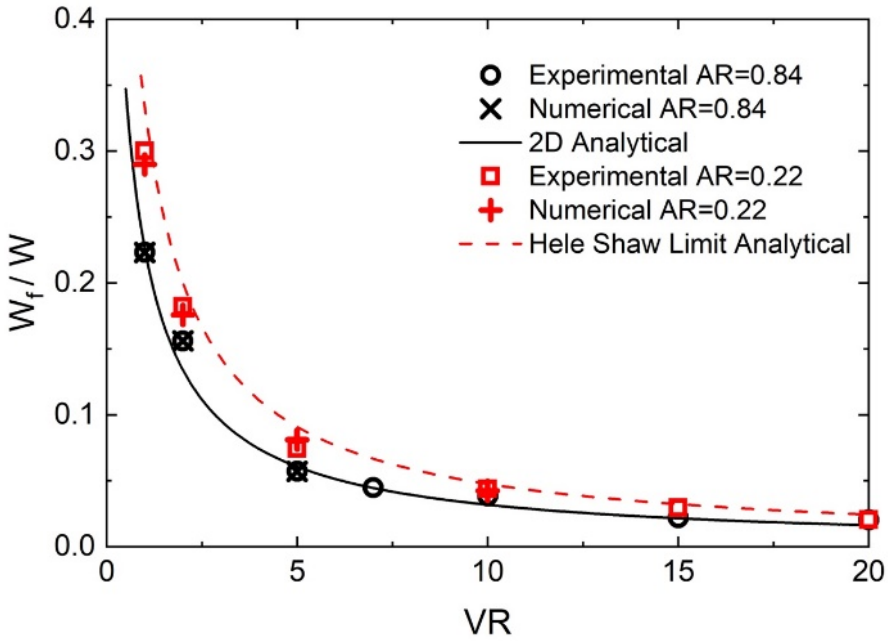

Figure 5.11: Experimental measurements and 3D numerical simulation results of the normalised width of the central focused outlet stream at the centre plane of the flow focusing geometries of $AR = 0.84$ and $AR = 0.22$ with increasing velocity ratio for $K = 1$. Comparison of the results with the derived 2D analytical solution (Equation (5.13)) and Hele-Shaw solution $\frac{W_f}{W} = [1 + 2\,(VR)K]^{-1}$ (Wu and Nguyen 2005) are also shown.

The experimental and 3D numerical results show an excellent agreement. The two-dimensional analytical solution also captures well the experimental and numerical results in the channel with $AR = 0.84$, showing the ability of the two-dimensional analytical solution to capture reasonably well the dynamics of the focused stream in these particular conditions. In addition to the base case of $AR = 0.84$, we also show in the figure the case of $AR = 0.22$. Again, there is an excellent agreement between experimental measurements and 3D numerical simulations. However, as expected in this case, deviations from the analytical solution are observed, which can be attributed to the fact that, as the microchannel becomes shallower, the 2D approximation becomes less accurate and the experimental values are better captured by the analytical solution proposed by Wu and Nguyen (Wu and Nguyen, 2005) in the Hele-Shaw limit.

5.7.2 Effect of Viscosity Ratio

The effect of the viscosity ratio, K, was analysed experimentally by increasing the glycerol concentration in the two lateral inlet streams, while maintaining the same reference fluid in the central inlet stream. Numerical simulations were also performed for comparison and to provide additional insight that would be challenging to obtain experimentally (e.g., the detailed shape of the interface along the depth direction). As shown qualitatively in Figure 5.12, for $VR = 1$, the viscosity ratio is seen to have a small effect on streamline curvature in the central region of the device where the inlet streams meet (particularly for low values of K), and strongly impacts the shape/curvature of the interface along the depth of the microchannel cross-section, i.e., along the z-direction.

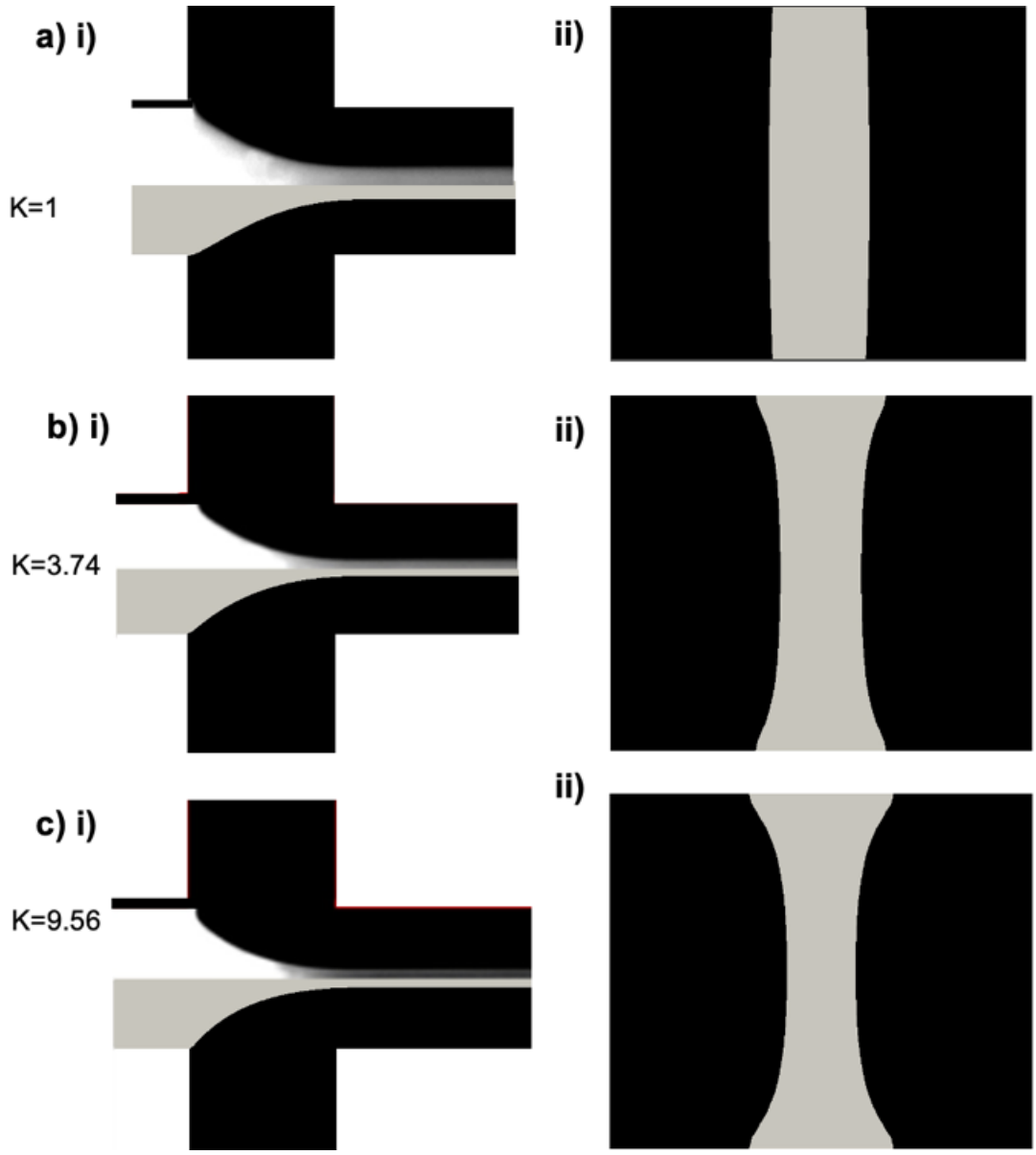

Figure 5.12: Qualitative flow patterns observed in the flow focusing geometry with $AR = 0.84$, for $VR = 1$ and three viscosity ratios a) $K = 1$, b) $K = 3.74$, and c) $K = 9.56$: i) comparison of experimental (top half) and 3D numerical simulation (bottom half) at the $z = D/2$ centre plane, showing the focusing of the central stream ; ii) 3D numerical simulations showing the filament cross-section in the y-z plane at $x/W = 2.5$, where Fluid 1 is shown in grey and Fluid 2 is shown in black.

Similarly to the effect of velocity ratio, the normalised central focused stream width at the $z = D/2$ centre plane was found to decrease in size as the viscosities of the lateral fluids increased relative to the viscosity of Fluid 1. Good agreement was found

between the dimensionless focused stream size obtained in the experiments and in 3D numerical simulations for $AR = 0.84$. (cf. Figure 5.13).

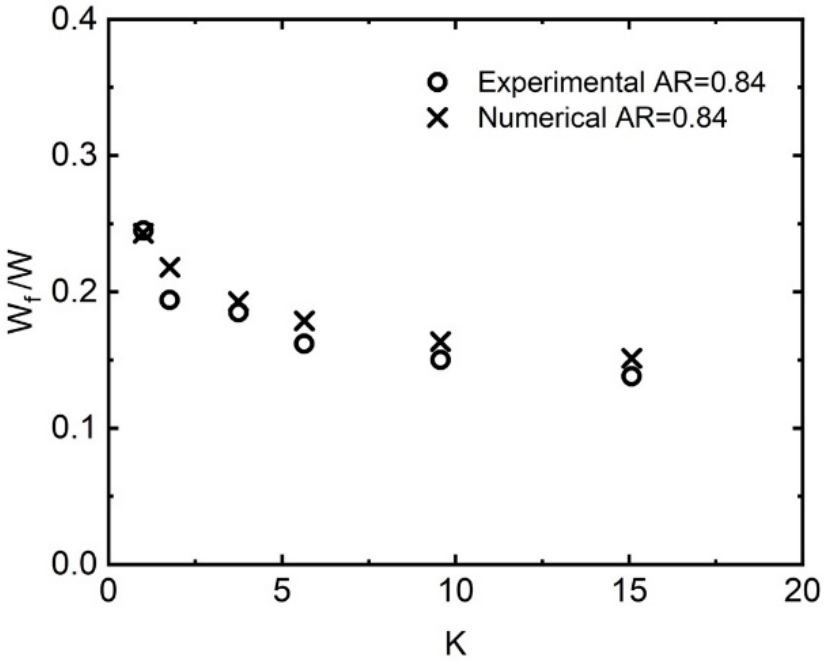

Figure 5.13: Impact of viscosity ratio on the normalised width of the central focused outlet stream at the $z = D/2$ centre plane for $VR = 1$. Comparison of experimental and 3D numerical simulations for $AR = 0.84$.

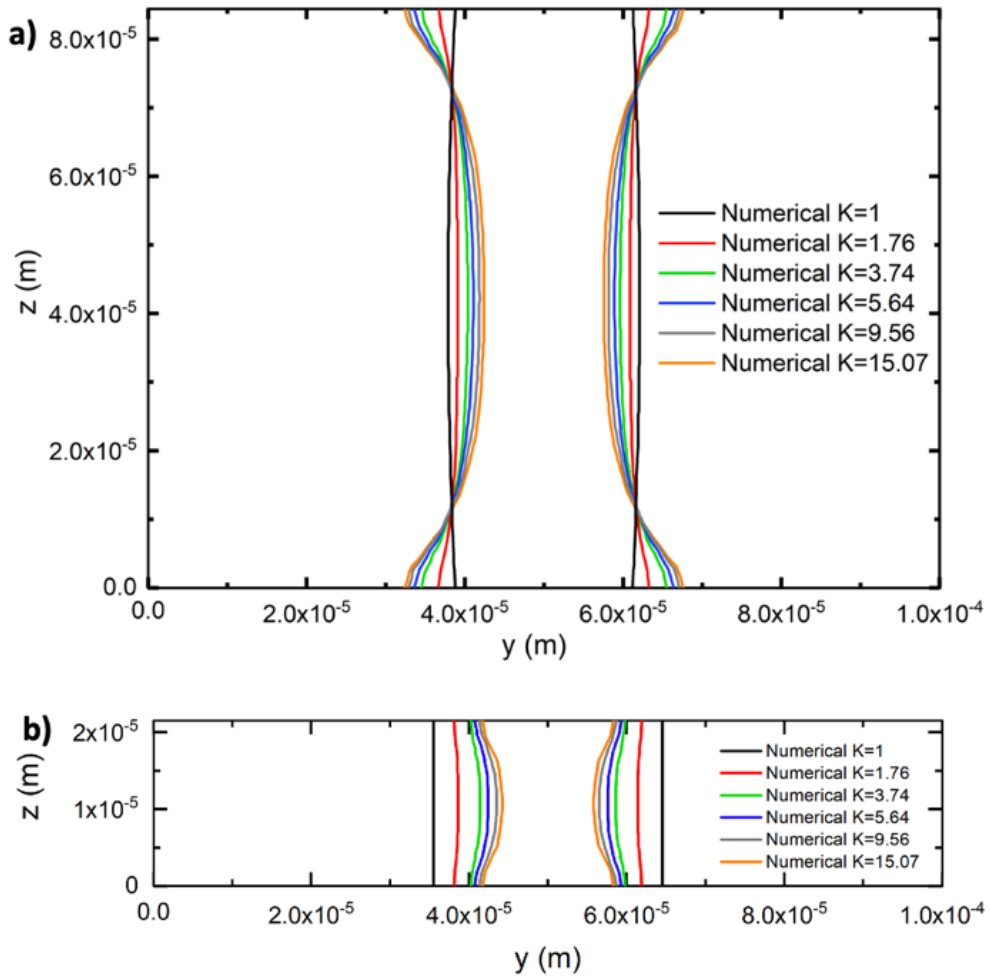

Figure 5.14: Variation of the cross-sectional shape of the central focused stream with viscosity ratio for $VR = 1$. Comparison of the profile of the interface along the channel depth with increasing K obtained using 3D numerical simulations with a) $AR = 0.84$, and b) $AR = 0.22$.

When the two fluids have the same viscosity ($K = 1$), the central focused stream in the outlet channel exhibits an approximately rectangular cross-section (cf. Figure 5.12aii), as also reported in the work of Knight et al (1998). When $K > 1$, the interface location varies along the depth of the cross-section (Figure 5.12bii and cii), showing a concave shape, where the central focused stream width is larger at the walls than at the centre plane of the microchannel ($z = D/2$), where experimental measurements of the central focused stream size are typically taken in this work. Similar effects have also been observed in other type of geometries, such as the microfluidic cross-slot (Davoodi et al. 2021) and in the T-channels (Guillot et al. 2006); as well as in flow

focusing configurations similar to those considered here (Guillot et al. 2006, Cubaud and Mason 2012, Hu and Cubaud 2016), however these studies have not shown how the shape changes with the ratio of inlet viscosities. For parallel flows, when large viscosity ratios are considered, the less viscous fluids are known to migrate towards the regions of high shear near the channel walls while the more viscous fluids move to the regions of low shear (Joseph et al. 1984). This interfacial curvature is therefore deemed to be a "self-lubricating" aspect of the flow (Cubaud and Mason 2008).

Figure 5.14 shows the shape of the central focused stream cross-section obtained numerically for a wide range of values of K for $AR = 0.84$ (Figure 5.14a) and $AR = 0.22$ (Figure 5.14b). It can be observed that as K increases beyond unity, the shape of the focused stream interface moves away from the case of a nearly straight interface seen when all fluid streams have the same viscosity. The difference between the central focused stream width at the channel walls and the minimum width at the centre plane of the microchannel becomes larger as the lateral streams become more viscous than the central stream.

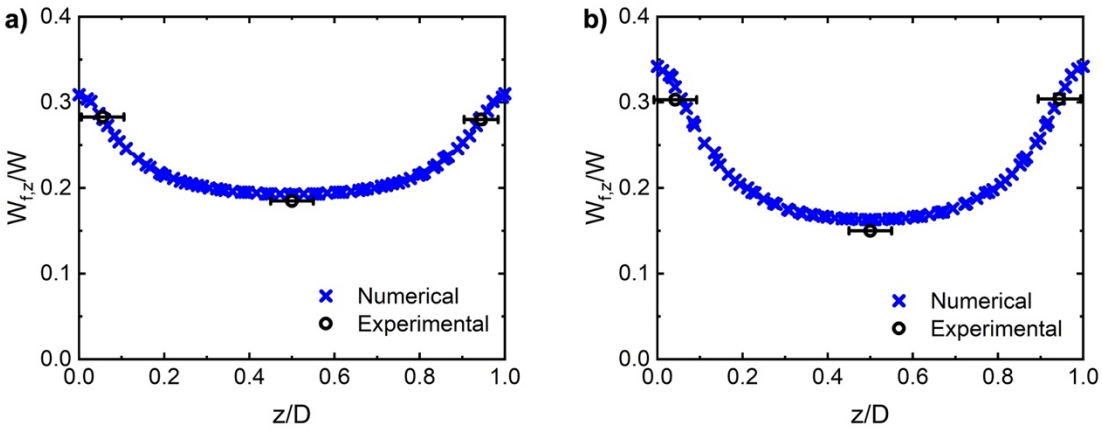

Figure 5.15: Comparison of the normalised width of the central focused outlet stream along the z-direction obtained in the 3D numerical simulations and in the experiments with $AR = 0.84$ for a) $K = 3.74$, and b) $K = 9.56$. $W_{f,z}$ represents the central focused stream width at a particular z position $(0 < z/D < 1)$ and horizontal error bars indicate the experimental depth of field estimated for the optical set-up used in this work.

Figure 5.15a and b show a quantitative comparison between experimental and numerical results of the width of the central focused stream along the depth of the channel for two viscosity ratios ($K = 3.74$ and $K = 9.56$). Although experimental measurements could not be taken accurately over the full length of the channel, measurements could be performed in three specific locations: close to each of the channel walls and the centre of the cross-section (i.e., for $z = D/2$). Good agreement was found between experiments and numerical simulations for all viscosity ratios studied, showing the good accuracy of the numerical framework (only a selection of results is displayed here for the sake of conciseness, further examples can be found in the Appendix B).

Contours of the shear component of the rate-of-strain tensor, S_{xy}, and its magnitude, $S = \sqrt{S{:}S}$, taken for a cross-section in the y-z plane at $x/W = 2.5$ (location in the outlet channel away from the junction), and normalised with a reference quantity (U_3/W where U_3 and W are defined in Section 5.2), are shown in Figure 5.16 for three different values of the viscosity ratio: $K = 1, 3.74, 9.56$. Lines showing the location of the interface are superimposed on each image. Not surprisingly, for $K = 1$, S is distributed almost symmetrically, since the two fluids have the same viscosity, thus corresponding to the stress field obtained in a single fluid configuration. Nevertheless, with reference to Figure 5.16a, due to the fact that the cross-section is characterised by an aspect ratio different from unity ($AR = 0.84$), stresses generated at the walls propagate over different lengths along the two coordinate directions resulting in a slightly curved interface. As the viscosity of the lateral channels' fluid is increased ($K > 1$), in addition to the geometrical constraint mentioned above, the stress field is also influenced by the presence of the interface, where the stresses experience a discontinuity since here $(S_n)_1/(S_n)_2 = K$, where $S_n = S_{xy}n_y + S_{xz}n_z$ is the projection of the traction in the direction of the motion, i.e., tangent to the interface having normal $\boldsymbol{n}$ (where the interface is roughly normal to the y-axis, $(S_{xy})_1/(S_{xy})_2 \approx K$). This constraint impacts the velocity field, resulting in an increment of the velocity within the central stream (Fluid 1) as previously displayed in Figure 5.8, which, in turn, results in a contraction of the central stream to satisfy the incompressibility requirements. Analogous considerations apply to the case for $AR = 0.22$ (Figure 5.16b), where only the contours for the shear component S_{xy} are shown. In this case, it can be observed

that for $K = 1$ the interface is almost straight, reflecting the fact that the stresses generated at the walls have a negligible impact on it due to the larger relative distance over which these are produced compared to the case $AR = 0.84$. For the case $AR = 0.22$, shear stresses next to the interface are vanishingly small, while, on the contrary, for the corresponding $AR = 0.84$ situation these are non-negligible in the region of the interface.

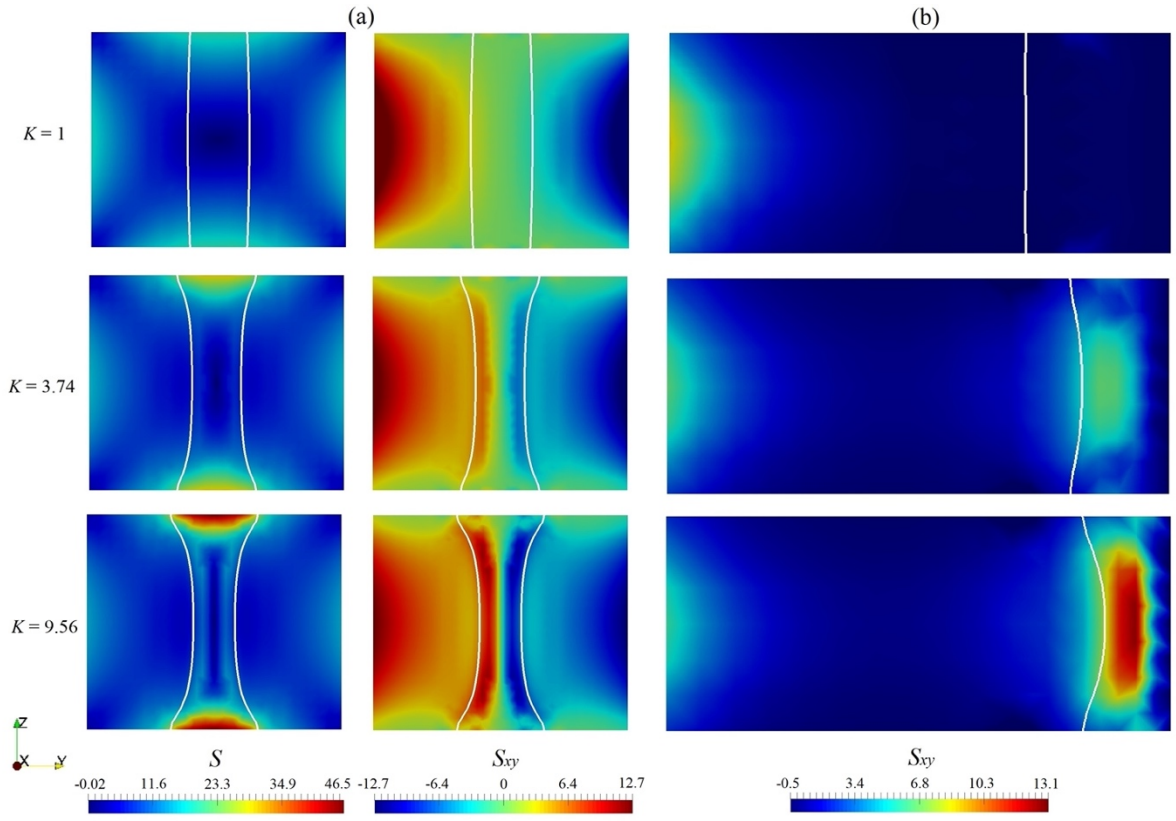

Figure 5.16: a) Contours of the magnitude of the rate-of-strain tensor, S, and its shear component, S_{xy}, observed in the y-z plane in the flow focusing geometry with $AR = 0.84$ and $VR = 1$ and three viscosity ratios $K = 1, 3.74, 9.56$ for full channel depth ($0 < z/D < 1$) at location $x/W = 2.5$. b) Contours for the S_{xy} component for the case $AR = 0.22$ (only half of the domain is shown) for the same conditions in (a). Solid white lines showing the location of the interface are superimposed in each image.

The shape of the central focused stream was further investigated numerically by varying the viscosity ratio within a channel of aspect ratio 0.22 (Figure 5.17).

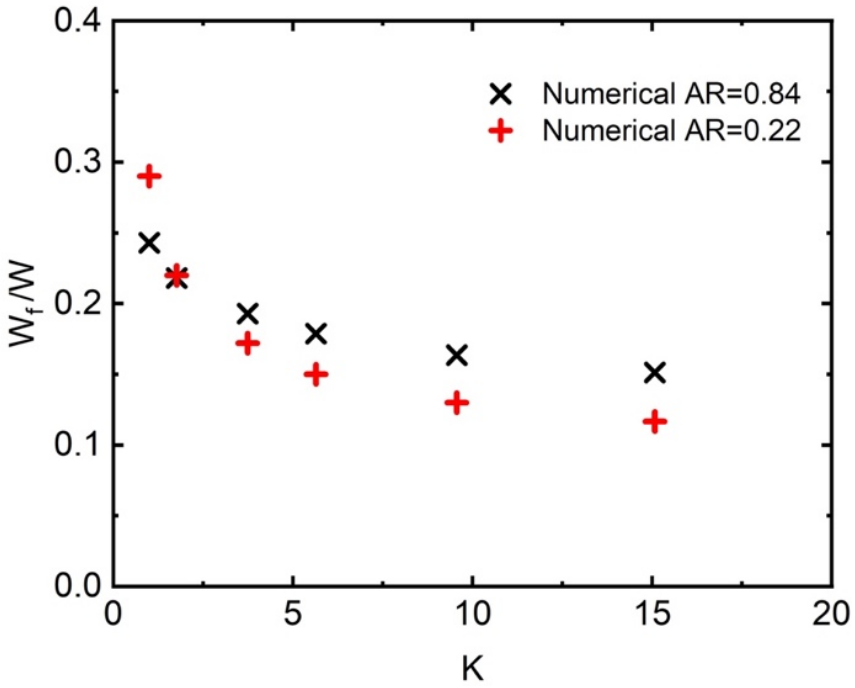

Figure 5.17: Impact of viscosity ratio on the central focused outlet stream in flow focusing geometries at the centre plane $(z = D/2)$ for $VR = 1$. Comparison of the normalised width of the focused stream for increasing values of K obtained from 3D numerical simulations for $AR = 0.84$ and $AR = 0.22$.

As the channel aspect ratio is reduced to $AR = 0.22$, similar trends to those obtained for the case $AR = 0.84$ are observed for increasing values of K with regards to the decreasing dimensionless filament width at the centre plane (cf. Figure 5.17) and changing interfacial shape across the channel cross-section (cf. Figure 5.14b). However, if we consider the average width ($\overline{W}_f$) of the central outlet stream along the whole depth of the channel (cf. Figure 5.18), we can see that for the aspect ratio of 0.84 the average width varies only slightly with K (similarly to the 2D analytical solution) however, as expected, for the aspect ratio of 0.22, the average value varies significantly with K, highlighting that confinement plays a significant role in the development of 3D viscous effects.

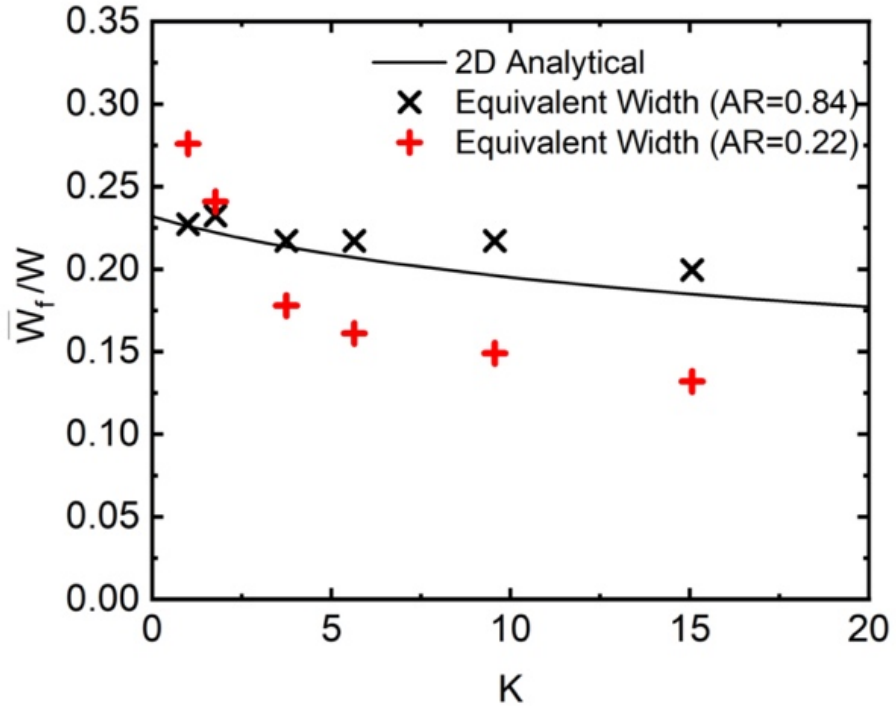

Figure 5.18: Impact of viscosity ratio on the central focused outlet stream for $VR = 1$ comparing the normalised width obtained via the 2D analytical solution with the normalised width averaged along the cross-section obtained in the simulations for $AR = 0.84$ and $AR = 0.22$.

5.8 CONCLUSIONS

In this work, a series of experiments and numerical simulations were carried out considering a microfluidic flow focusing device to investigate the impact of flow parameters influencing the characteristics of the produced central focused stream. Hydrodynamic focusing was induced using three fluid inlets (two lateral streams and a central stream of miscible Newtonian fluids). Specifically, we investigated the effect of the viscosity ratio, K, considering a relatively wide range of conditions ($1 \leq K \leq 15.07$), while simultaneously considering the combined effect of different velocity ratios ($1 < VR < 20$) and aspect ratio on the characteristics of the outlet central focused stream. An increase of the velocity ratio brings about a reduction of the width of the

central focused stream at the centre plane ($z = D/2$) and enhances the curvature of the separation streamlines in agreement with previous work (Nguyen and Huang 2005, Oliveira et al. 2012). Under these conditions the viscous stresses from the lateral fluid streams dominate how the central fluid profile is formed.

A two-dimensional analytical expression has also been derived, which is in agreement with 2D numerical results and provides a good estimate of the findings for the configuration with aspect ratio $AR = 0.84$. As the microchannel becomes shallower, i.e., D becomes progressively smaller than W, the two-dimensional analytical solution provides less accurate estimations, and the experimental values are better captured by the analytical solution proposed by Wu and Nguyen (Wu and Nguyen, 2005) in the Hele-Shaw limit. The results obtained provide further insight into the curved interface along the channel depth that has been observed in previous research when high viscosity contrasts are present in parallel flow systems (Knight et al. 1998, Cubaud and Mason 2008, Cubaud et al. 2012, Cubaud and Mason 2012). The numerical results confirm that a jump in stresses at the interface between the two fluids influences the concave shape of the interface along the depth of the channel cross-section. It was observed that the curved shape across the depth of the channel cross-section (i.e., along the z-direction) is strongly dependent on the viscosity ratio and aspect ratio, highlighting that confinement also plays an important role in the development of three-dimensional viscous effects.

5.9 REFERENCES

Anna, S. L., Bontoux, N. and Stone, H. A. (2003). "Formation of dispersions using “flow focusing” in microchannels." Applied Physics Letters 82(3): 364-366.

Ateya, D. A., Erickson, J. S., Howell, P. B., Jr., Hilliard, L. R., Golden, J. P. and Ligler, F. S. (2008). "The good, the bad, and the tiny: a review of microflow cytometry." Anal Bioanal Chem 391(5): 1485-1498.

Bonhomme, O., Morozov, A., Leng, J. and Colin, A. (2011). "Elastic instability in stratified core annular flow." Phys Rev E Stat Nonlin Soft Matter Phys 83(6 Pt 2): 065301.

Capobianchi, P., Lappa, M. and Oliveira, M. S. N. (2017). "Walls and domain shape effects on the thermal Marangoni migration of three-dimensional droplets." Physics of Fluids 29(11): 112102.

Cubaud, T. (2020). "Swelling of Diffusive Fluid Threads in Microchannels." Phys Rev Lett 125(17): 174502.

Cubaud, T., Conry, B., Hu, X. and Dinh, T. (2021). "Diffusive and capillary instabilities of viscous fluid threads in microchannels." Physical Review Fluids 6(9): 094202.

Cubaud, T., Jose, B. M., Darvishi, S. and Sun, R. (2012). "Droplet breakup and viscosity-stratified flows in microchannels." International Journal of Multiphase Flow 39: 29-36.

Cubaud, T. and Mason, T. G. (2006). "Folding of viscous threads in diverging microchannels." Phys Rev Lett 96(11): 114501.

Cubaud, T. and Mason, T. G. (2008). "Capillary threads and viscous droplets in square microchannels." Physics of Fluids 20(5): 053302-053302-11.

Cubaud, T. and Mason, T. G. (2008). "Formation of miscible fluid microstructures by hydrodynamic focusing in plane geometries." Phys Rev E Stat Nonlin Soft Matter Phys 78(5 Pt 2): 056308.

Cubaud, T. and Mason, T. G. (2012). "Interacting viscous instabilities in microfluidic systems." Soft Matter 8(41): 1573-1582.

Cubaud, T., Tatineni, M., Zhong, X. and Ho, C. M. (2005). "Bubble dispenser in microfluidic devices." Phys Rev E Stat Nonlin Soft Matter Phys 72(3 Pt 2): 037302..

d'Olce, M., Martin, J., Rakotomalala, N., Salin, D. and Talon, L. (2009). "Convective/absolute instability in miscible core-annular flow. Part 1: Experiments." Journal of Fluid Mechanics 618: 305-322.

Daniele, M. A., Boyd, D. A., Adams, A. A. and Ligler, F. S. (2015). "Microfluidic strategies for design and assembly of microfibers and nanofibers with tissue engineering and regenerative medicine applications." Adv Healthc Mater 4(1): 11-28.

Davoodi, M., Houston, G., Downie, J., Oliveira, M. S. N. and Poole, R. J. (2021). "Stabilization of purely elastic instabilities in cross-slot geometries." Journal of Fluid Mechanics 922: A12..

Garstecki, P., Stone, H. A. and Whitesides, G. M. (2005). "Mechanism for flow-rate controlled breakup in confined geometries: a route to monodisperse emulsions." Phys Rev Lett 94(16): 164501.

Golden, J. P., Justin, G. A., Nasir, M. and Ligler, F. S. (2012). "Hydrodynamic focusing--a versatile tool." Anal Bioanal Chem 402(1): 325-335.

Guerrero, J., Chang, Y. W., Fragkopoulos, A. A. and Fernandez-Nieves, A. (2020). "Capillary-Based Microfluidics-Coflow, Flow-Focusing, Electro-Coflow, Drops, Jets, and Instabilities." Small 16(9): e1904344.

Guillot, P., Panizza, P., Salmon, J.-B., Joanicot, M. and Colin, A. (2006). "Viscosimeter on a Microfluidic Chip." Langmuir 22: 6438-6445.

Hooper, A. P. and Boyd, W. G. C. (2006). "Shear-flow instability at the interface between two viscous fluids." Journal of Fluid Mechanics 128(-1): 507-528.

Houston, G., Capobianchi, P. and Oliveira, M. S. N. (2023). "Flow focusing with miscible fluids in microfluidic devices." Physics of Fluids 1 35 (5): 052015.

Hu, X. and Cubaud, T. (2016). "Inertial destabilization of highly viscous microfluidic stratifications." Physical Review Fluids 1(4): 044101..

Joseph, D. D., Nguyen, K. and Beavers, G. S. (1984). "Non-uniqueness and stability of configuration of flow of immiscible fluids with different viscosities." Journal of Fluid Mechanics 141: 319-345.

Jun, Y., Kang, E., Chae, S. and Lee, S. H. (2014). "Microfluidic spinning of micro- and nano-scale fibers for tissue engineering." Lab Chip 14(13): 2145-2160.

Knight, J. B., Vishwanath, A., Brody, J. P. and Austin, R. H. (1998). "Hydrodynamic Focusing on a Silicon Chip: Mixing Nanoliters in Microseconds." Physical Review Letters 80(17): 3863-3866.

Kong, B., Liu, R., Guo, J., Lu, L., Zhou, Q. and Zhao, Y. (2023). "Tailoring micro/nano-fibers for biomedical applications." Bioact Mater 19: 328-347.

Lan, W., Li, S., Lu, Y., Xu, J. and Luo, G. (2009). "Controllable preparation of microscale tubes with multiphase co-laminar flow in a double co-axial microdevice." Lab Chip 9(22): 3282-3288.

Lee, G.-B., Chang, C.-C., Huang, S.-B. and Yang, R.-J. (2006). "The hydrodynamic focusing effect inside rectangular microchannels." Journal of Micromechanics and Microengineering 16(5): 1024-1032.

Lee, G.-B., Hung, C.-I., Ke, B.-J., Huang, G.-R., Hwei, B.-H. and Lai, H.-F. (2001). "Hydrodynamic Focusing for a Micromachined Flow Cytometer." Journal of Fluids Engineering 123(3): 672-679.

Li, H., Qiao, D., Ren, F., Li, H., Zhu, W., Zhao, D. and Wang, M. (2021). "Computational fluid dynamics analysis of droplet generation in microfluidic multi-cell coupled systems." Physics of Fluids 33(10): 103313.

Nguyen, N. T. and Huang, X. (2005). "Mixing in microchannels based on hydrodynamic focusing and time-interleaved segmentation: modelling and experiment." Lab Chip 5(11): 1320-1326.

Oliveira, M., Pinho, F. T. and Alves, M. A. (2011). Extensional Flow of Newtonian and Boger Fluids Through a Flow Focusing Microdevice. 3rd Micro and Nano Flows Conference. Thessaloniki, Greece.

Oliveira, M. S. N., Alves, M. A., Pinho, F. T. and McKinley, G. H. (2007). "Viscous flow through microfabricated hyperbolic contractions." Experiments in Fluids 43(2-3): 437-451.

Oliveira, M. S. N., Pinho, F. T. and Alves, M. A. (2012). "Divergent streamlines and free vortices in Newtonian fluid flows in microfluidic flow-focusing devices." Journal of Fluid Mechanics 711: 171-191.

Petitjeans, P. and Maxworthy, T. (1996). "Miscible displacements in capillary tubes. Part 1. Experiments." Journal of Fluid Mechanics 326: 37-56.

Sousa, P. C., Coelho, P. M., Oliveira, M. S. N. and Alves, M. A. (2009). "Three-dimensional flow of Newtonian and Boger fluids in square–square contractions." Journal of Non-Newtonian Fluid Mechanics 160(2-3): 122-139.

Ward, T., Faivre, M., Abkarian, M. and Stone, H. A. (2005). "Microfluidic flow focusing: drop size and scaling in pressure versus flow-rate-driven pumping." Electrophoresis 26(19): 3716-3724.

Wu, Z. and Nguyen, N.-T. (2005). "Hydrodynamic focusing in microchannels under consideration of diffusive dispersion: theories and experiments." Sensors and Actuators B: Chemical 107(2): 965-974.

Yih, C.-S. (1967). "Instability due to viscosity stratification." Journal of Fluid Mechanics 27(2): 337-352.

CHAPTER 6

Flow Focusing Device with Viscoelastic Fluids

Microfluidic flow focusing devices operate by having two opposing lateral streams that shape a third central inlet stream, producing a converging region with a strong extensional flow near the centre of the geometry. Purely elastic flow instabilities have been observed in past research in viscoelastic fluid flows within this type of device (Oliveira et al. 2009, Oliveira et al. 2011, Ballesta and Alves 2017), with distinct flow regimes that depend on both the Weissenberg number (Wi) and the ratio of the inlet velocities (VR). Typically, at low Wi, the flow remains steady and symmetric about the geometry centreline. As the Wi is increased beyond a critical value, while maintaining a low VR, the flow transitions directly to a time-dependent flow (Oliveira et al. 2009, Oliveira et al. 2011). For moderate to high VR, two transitions were reported when Wi was increased: a first transition to steady asymmetric flow and a second at higher Wi to time-dependent flow (Oliveira et al. 2009). The study of these instabilities have been limited usually to single-fluid flows. They have been shown to arise even in the absence of inertia and are associated to high streamline curvature and large normal stress as described by the Pakdel-McKinley criterion (McKinley et al. 1996). Here we begin by providing further insight into the impact of geometrical effects, (channel aspect ratio defined as the ratio between the channel depth and channel width ($AR = D/W$)) in single phase flow using 3D microfluidic flow focusing channels produced by soft-lithography along with fluorescence microscopy for flow visualisation. More importantly, we experimentally demonstrate the impact of different fluid streams by introducing a Newtonian fluid alongside a dilute viscoelastic fluid. For these experiments, two multiple fluid flow configurations were studied in addition to the reference single-fluid case: one configuration where the central inlet stream is Newtonian (N) and the fluid in the lateral streams is viscoelastic (VE), and vice versa. The observed flow instabilities were of a similar nature to that of the single-fluid case. Interestingly findings show no significant change in the critical Wi for the transition to steady asymmetric flow for the various configurations, but, placing the Newtonian fluid in the lateral streams delayed the transition to time-dependent flow, suggesting that these elastic instabilities cannot be solely related to the extensional flow.

6.1 INTRODUCTION

Purely elastic instabilities that arise in the presence of strong elastic stresses, in the absence of inertia, have been found not only in simple viscometric flows (Shaqfeh 1996), but also in a variety of other complex viscoelastic flow configurations including shear dominated, extension dominated and those of mixed kinematics (Oliveira et al. 2012, Poole 2019). Using microfluidics, the role of elasticity can be heightened to levels far beyond those typical at the equivalent macroscale, due to the small length-scales involved, in which surface effects are enhanced. This enables the generation of low Reynolds number flows with high deformation rates (Oliveira et al. 2009). These flow conditions produce strong viscoelastic flow effects even for dilute polymer solutions.

The underlying mechanism has been shown to be related to a combination of the elastic first normal–stress differences generated in the flowing fluid and the centrifugal forces that act on the curved streamlines in accordance with the Pakdel – McKinley criterion (McKinley et al. 1996, Pakdel and McKinley 1996, Poole et al. 2013). As outlined in Chapter 2, McKinley et al. (1996) introduced a dimensionless parameter, M, that provides a critical condition that must be exceeded for the onset of such purely elastic instabilities (McKinley et al. 1996):

$$\sqrt{\frac{\lambda \tilde{U}}{\Re}\frac{\tau_{11}}{\left(\mu_0 \dot{\gamma}\right)}} \geq M \qquad (6.1)$$

where λ and μ_0 are the relaxation time and zero-shear rate viscosity of the polymeric fluid respectively, $\tilde{U}$ and τ_{11} are the characteristic fluid velocity and first normal elastic stress in the streamwise direction respectively, $\Re$ is the characteristic radii of curvature of the streamlines and $\dot{\gamma}$ is the magnitude of the shear rate.

Most early studies focused on understanding these instabilities under shear-dominated flow conditions (McKinley et al. 1996, Shaqfeh 1996), however, despite the

early mention of elastic instability phenomena in extensional dominated flow (Giesekus 1968, Boger 1987), the bulk of the work in extensional dominated flows is more recent (as reviewed in Haward et al. (2016)) taking advantage of the conditions provided by microfluidics. It is therefore important to increase the knowledge of the conditions under which these purely elastic instabilities arise in extensional flow configurations to improve and ultimately benefit various industrial applications including inkjet printing, fiber-spinning, extrusion and more (Haward et al. 2016).

Extensionally dominated microfluidic cross-shaped devices have been used in the past to study the onset of instabilities, in either a cross-slot or flow focusing configuration, due to the combined effects of their strong elongational flows and the small length scales (Oliveira et al. 2009, Ballesta and Alves 2017). The flow focusing set up operates by having two opposing lateral streams that shape a third inlet, central, stream. The work of Oliveira et al (2011) details the extensional behaviour of the flow in the converging region of this device which, at the microscale can significantly deform the underlying microstructure of complex fluids. As a result, these flow focusing devices are often used for bringing different streams, often involving multiple fluids, into contact to promote mixing (Knight et al. 1998, Nguyen and Huang 2005) or for droplet generation (Anna et al. 2003, Garstecki et al. 2005). An interesting characteristic of this geometry is that, unlike abrupt and smooth contractions which exhibit an extensional flow along the centreline and are also known to trigger flow induced elastic instabilities (Sousa et al. 2009, Liu et al. 2020), we can adjust the Hencky strain by varying the velocities of the lateral streams without changing the size or shape of the device (Ballesta and Alves 2017).

As outlined in Chapter 2, the type of instability that is of interest to this work is the supercritical flow induced elastic instabilities found in previous research (Poole et al. 2007) however these works are generally limited to single-phase flows. Early numerical and experimental investigations in the flow focusing device (Oliveira et al. 2009, Oliveira et al. 2011) have studied the onset of these flow induced elastic instabilities and reported distinct transitions: one in which the flow becomes asymmetric, but remains steady; and another which involves the onset of time-dependent flow. The time-dependent instabilities have been found to eventually lead on to chaotic flow, often referred to as elastic turbulence, with the avenue to this

transition being strongly dependent on both the Hencky strain and Weissenberg number of the flow (Ballesta and Alves 2017). Using micro-PIV (Particle Image Velocimetry), Ballesta and Alves (2017) determined three distinct time-dependent regimes that occur with increasing Wi prior to the flow reaching chaotic conditions: one at low values of Hencky strain, where the flow is unsteady with periodic oscillations (named 'symmetric periodic flow'); a second at higher values of Hencky strain, where the flow is unsteady with asymmetric periodic oscillations (named 'asymmetric periodic flow') and a third transition at higher values of Wi and Hencky strain where the flow is unsteady with only short bursts of periodic oscillations (named 'semiperiodic flow'). Chaotic flow can then be described as having nonperiodic oscillations shown as large fluctuations in the velocity field (Ballesta and Alves 2017).

Past research has suggested that an important factor for the development of viscoelastic instabilities within the flow focusing device is the strong extensional flows that occur at the centre of the geometry (Oliveira et al. 2009, Ballesta and Alves 2017). Similar instabilities have been found to arise in the cross-slot configuration (Rocha et al. 2009, Sousa et al. 2015) where recent developments, previously discussed in Chapter 4, have found that these elastic instabilities cannot be solely related to the extensional flow effects and instead are more likely related to streamline curvature and the high deformation rates near the re-entrant corners (Davoodi et al. 2019, Davoodi et al. 2021). It is clear that the prospect of this has not yet been studied within the flow focussing device opening a research avenue for the work of this chapter.

Geometric parameters, such as the channel aspect ratio, AR, defined in this work as the ratio between the depth and width of the microchannel ($AR = D/W$) have been shown to strongly influence the appearance of these elastic instabilities and also the modes of transition in the extensional cross-slot microfluidic device (Sousa et al. 2015, Cruz et al. 2016). Similar trends between experimental and numerical investigations within the microfluidic cross-slot have separated geometries into two distinct categories: high aspect ratios, generally $AR > 1$ (where channel walls have little or no influence), with two distinct elastic instability transitions, and low aspect ratios where only one transition to time-dependent flow is visualised (Sousa et al. 2015, Cruz et al. 2016). As a result, the bounding channel walls have been said to have a stabilising effect on the elastic instabilities that occur supressing the steady flow asymmetries

and delaying the time-dependent onset to higher Weissenberg number flows (Sousa et al. 2015).

To date there is a limited understanding of the geometrical effects, in particular of the channel aspect ratio, on the elastic instabilities that arise within the flow focusing configuration (Ballesta and Alves 2017). In the work of Oliveira et al (2009), it was found that decreasing the width ratio (defined as the ratio between the width of the lateral side streams and the central inlet stream) in the flow focusing device resulted in the development of larger asymmetries, and had a non-monotonic effect on the critical onset conditions. Increasing our knowledge of the geometrical effects will enhance our ability to control these complex flows and thus characterise the critical onset conditions of these supercritical elastic instabilities within the flow focusing device.

Motivated by the aforementioned single-fluid studies (Oliveira et al. 2009, Oliveira et al. 2011, Ballesta and Alves 2017) this work investigates experimentally the effects of Weissenberg number, velocity ratio and channel aspect ratio on the onset of the flow induced purely elastic instabilities observed in the microfluidic flow focusing device. This will serve as a reference case and provide a better understanding of the conditions that characterise the onset of these instabilities, required to ultimately control and improve a number of industrial applications (Haward et al. 2016, Ballesta and Alves 2017) e.g., emulsions (Poole et al. 2012) and enhanced oil recovery applications (Datta et al. 2013, Clarke et al. 2015, Browne et al. 2020). As previously mentioned, to the author's knowledge investigations of elastic instabilities of this nature within the flow focusing device, under low Reynolds number conditions, have been limited to single-fluid flows (Oliveira et al. 2009, Oliveira et al. 2011). In this work, we therefore also aim to determine the impact when multiple fluid streams are involved, in particular, when Newtonian fluid streams are introduced to the system alongside the viscoelastic fluid. This work will provide an insight into the underlying mechanisms behind these flow induced elastic instabilities within the flow focusing device.

6.2 MATERIALS AND METHODS

6.2.1 Fluid Preparation and Characterisation

In this chapter, Boger viscoelastic (notation 'VE' often used throughout this work) fluid streams of polyethylene oxide (PEO), supplied by Sigma Aldrich, with nominal molecular weight $M_w = 8\text{x}10^6$ g mol^{-1} at a concentration of 280ppm (w/w), were used in a Newtonian solvent (60:40 water/glycerol mixture). These Boger viscoelastic fluids were prepared using the process outlined in Chapter 3 and used to isolate elastic effects from effects of variable shear rate-dependent viscosity.

The overlap concentration, c^*, of PEO is ≈ 350ppm (Rodd et al. 2005) and thus the prepared solution can be considered a dilute PEO solution (Bird et al. 1977, Casanellas et al. 2016). The intrinsic viscosity $[\eta]$ of these PEO solutions was found to be $2.21\text{x}10^3$ cm^3/g (Tirtaatmadja et al. 2006).

In Section 6.3.2 of this chapter, Newtonian fluids (notation 'N' often used throughout this work) are used alongside the viscoelastic fluid. For these cases, the Newtonian fluid (51.6% glycerol solution) was created to ensure the shear viscosity was comparable to that of the dilute viscoelastic fluid. All prepared solutions were seeded with fluorescent tracer particles (FluoSpheres® carboxylate- modified, 1.0 μm, Nile Red (Ex/Em: 535/575)) at concentration of ~0.02%wt for flow visualisation purposes.

A summary of the composition and properties of the fluids used in this chapter is given in Table 6.1. The density of the solutions was measured using pycnometry and the viscosity was characterised in steady shear on a DHR-2 hybrid rotational rheometer (TA Instruments) with a cone-plate geometry (60 mm diameter, 1° cone angle) at a temperature of 20°C.The relaxation time was determined using a Capillary Breakup Extensional Rheometer (HAAKE™ CaBER™).

Table 6.1: Characteristics of the fluids used in the experimental work including fluid composition and physical properties (density and viscosity) at 20 °C.

Fluid ID	Composition	Density (kg/m^3)	Viscosity (Pa s)	Relaxation Time (ms)
Viscoelastic (VE)	PEO (M_w8 x10^6), 280ppm (w/w), in Water/ Glycerol (60/40)	1146	6.30x10^{-3} (+/- 0.0007)	52.37
Newtonian (N)	Water/Glycerol (48.4/51.6)	1172	6.81x10^{-3}	-

The steady shear rheology data for the viscoelastic fluid described in Table 6.1 can be found in Figure 6.1, where the viscosity is shown to exhibit an almost constant value for all shear rates, and thus can be considered a Boger-like fluid.

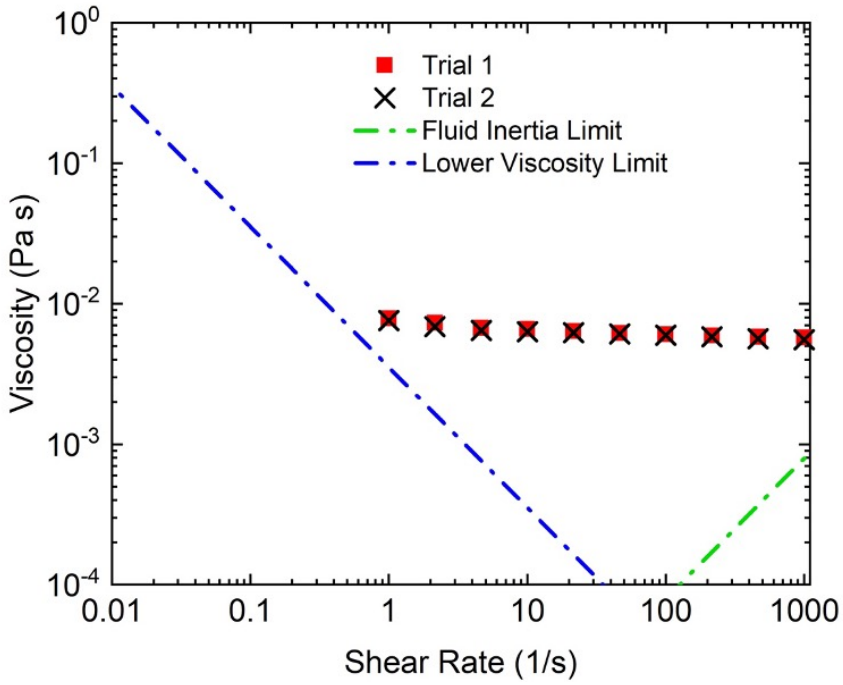

Figure 6.1: Shear rheology flow curves (DHR-2 Rotational Rheometer) for the solution of PEO (M_w 8x10^6) at a concentration of 280ppm in a 60/40 solution of water and glycerol (cf. Table 6.1). Measurement limits outlined in equations (3.13) and (3.14) are shown as dashed lines.

6.2.2 Microfluidic Geometry and Experimental Set-Up

The flow focusing configuration considered here is composed of four identical planar orthogonal channels (cf. Figure 5.1a) with two opposing lateral streams and a perpendicular third central inlet stream, as was previously described in the work of Chapter 5. The experimental microchannels were made from polydimethylsiloxane (Sylgard 184, Dow Corning) and were fabricated using a SU-8 mould by standard soft-lithography techniques. Three different microfluidic devices with varying aspect ratios ($AR = D/W$) were used: $AR = 0.84$ (with $W = 109 \pm 2\ \mu m$ and $D = 92 \pm 1\ \mu m$), $AR = 0.28$ (with $W = 96 \pm 2\ \mu m$ and $D = 26 \pm 1\ \mu m$) and $AR = 0.22$ (with $W = 125 \pm 2\ \mu m$ and $D = 26 \pm 1\ \mu m$). A schematic diagram of the microfluidic geometry and the experimental set up can be visualised in Figure 5.3.

The experimental visualisation procedure outlined in Chapter 5 was adopted for the work of this chapter. In this case the inverted microscope (Olympus IX71) was equipped with either a 20X objective lens (numerical aperture NA = 0.4) or a 10X objective lens (numerical aperture NA = 0.25) and an adequate filter cube (Olympus U-MWIGA3, Excitation Filter BP530-550). The images were acquired at the centre plane of the microchannel ($z = D/2$) using a CCD camera (Olympus XM10). Streak imaging was employed to obtain images using long exposure times which were set according to the velocity of the fluids. This allows the camera to capture the path travelled by individual particles and therefore capture the flow patterns within the geometry.

6.2.3 Relevant Dimensionless Numbers

The dimensionless parameters of interest for the flow under consideration are the Reynolds number, $Re = \rho_i U_i W/\mu_i$ (defined relative to a particular fluid stream, i), the velocity ratio, $VR = U_2/U_1$, which in this case is equal to the flow rate ratio Q_2/Q_1, given the incompressibility constraint and to the fact that the inlet channels have the same cross-sectional area, and the Weissenberg number, Wi (defined below). In previous work detailed in Chapter 5 of this thesis, an increase of the velocity ratio parameter is shown to reduce the width of the central fluid filament (Nguyen and Huang 2005,

Oliveira et al. 2012) but also enhance the curvature of the streamlines which, when polymer solutions are involved, is known to be a factor that encourages the onset of elastic instabilities in accordance with the “Pakdel - McKinley criterion (McKinley et al. 1996, Pakdel and McKinley 1996). The velocity ratio is therefore a parameter that will be used extensively to study the elastic instability onsets in this chapter.

When calculating the Weissenberg number, previously detailed in Section 2.1.2 by equation (2.3), the approach of Ballesta and Alves was adopted (2017). The strain rate for this flow configuration is estimated as:

$$\dot{\varepsilon}_{FF} = \frac{\left(U_3 - U_1 \right)}{W} \tag{6.2}$$

and the Weissenberg number is defined as:

$$Wi = \lambda \frac{\left(U_3 - U_1 \right)}{W} \tag{6.3}$$

6.2.4 Image Analysis Techniques

To quantify the degree of asymmetry of the flow patterns within the flow focusing device an asymmetry parameter, χ, was introduced:

$$|\chi| = \frac{\left| W_{2L} - W_{2R} \right|}{W_{2L} + W_{2R}}, \tag{6.4}$$

where W_{2L} and W_{2R} represent the widths that each of the lateral fluid streams occupy within the central channel at $x = 0$ as shown in Figure 6.2. This expression yields a value of $\chi = 0$ when fluid from both lateral streams occupy the same portion of the central inlet channel ($W_{2L} = W_{2R}$) i.e., the flow is symmetric about the x-axis. A value of $\chi = 1$ is approached in the limit if one of the lateral fluid streams were to fully occupy

the central inlet channel ($W_{2L} \gg W_{2R}$) i.e., fully asymmetric. Similarly, $\chi = -1$ is approached when $W_{2R} \gg W_{2L}$. Measurements were conducted at the same location for each case [$x = 0$ at the centre plane ($z = D/2$)] using the image processing software ImageJ.

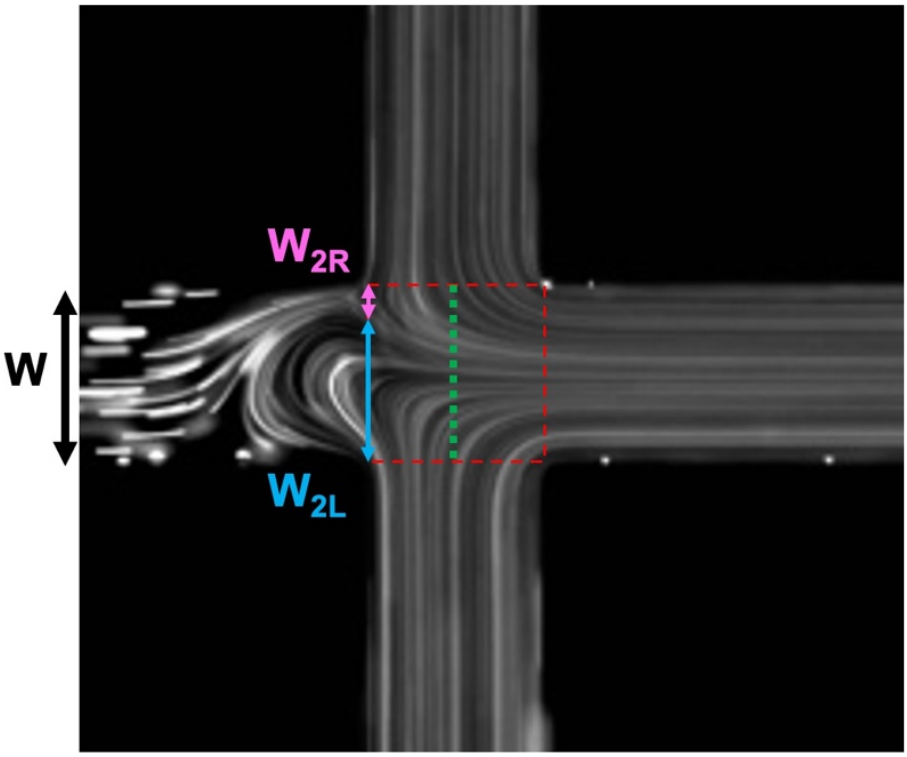

Figure 6.2: An experimental image exemplifying asymmetric flow within the flow focusing microfluidic device highlighting the variables used to determine the asymmetry parameter. The measurements were carried out at $x = 0$ with additional checks carried out at $x = 0.5W$ (green line).

Additional measurement checks were conducted in the centre of the geometry cross-section ($x = 0.5W$), indicated by the green dotted line in Figure 6.2. It was found that although the asymmetry parameter is different in magnitude at the two locations, it exhibits the same trends in both cases in terms of the various effects studies. The measurements were therefore carried out at the position of $x = 0$, where the asymmetries were most visible and easier to quantify.

6.3 RESULTS AND DISCUSSIONS

6.3.1 Part 1: Viscoelastic Instabilities in Single-Fluid Systems

Prior to testing polymer solutions in the flow focusing device, the flow field was confirmed to be highly symmetric and stable over a wide range of Reynolds numbers ($4.5\text{x}10^{-2}$ – 9) and velocity ratios (1 – 40) using a Newtonian fluid (deionised water) as discussed in Chapter 5 and shown again in Figure 6.3 for the readers' convenience. The experimental images of Figure 6.3 obtained at a velocity ratio of 25 highlight the symmetry of the flow about the x-axis and the streamline curvature. The Reynolds number stated throughout this chapter (Re_3) uses the average velocity in the outlet stream of the device (U_3) as reference. The flow conditions tested in the Newtonian experiments covered a range of Reynolds number larger than those used for the polymeric fluid flows discussed in this chapter. This stability can also be visualised in the work of Chapter 5, where, for all experimental parameters studied, the flow remained steady and symmetric relative to $y = 0$.

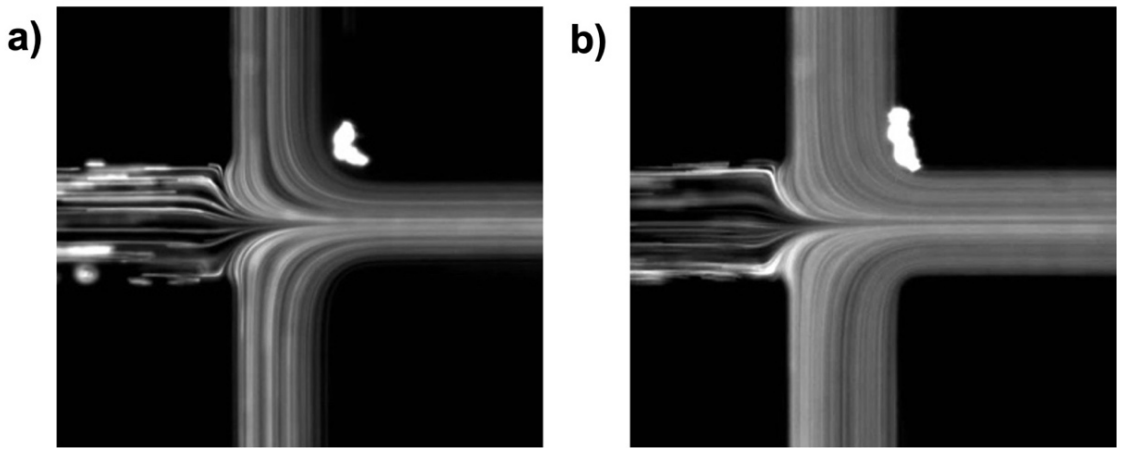

Figure 6.3: Flow patterns in the flow focusing device (at $z = D/2$ using a single Newtonian fluid (deionised water) at $VR = 25$ for different inlet flow conditions a) Re_3= $7.69\text{x}10^{-1}$ b) Re_3= 4.92 to highlight the symmetric flow obtained for Newtonian fluid flows over the range of Re covered in this chapter.

When viscoelastic fluids are used, more complex flow patterns arise with the onset of flow induced elastic instabilities. In this section these complex flow patterns are visualised for a range of Weissenberg number, while maintaining low inertia, and analysed to assess how they are affected by various experimental parameters such as velocity ratio (Section 6.3.1.1) and channel aspect ratio (Section 6.3.1.2). For all experimental work carried out in this chapter, downstream of the intersection, a straight focused central stream was visualised in most of the outlet channel, which is common behaviour at low flow rates (Bonhomme et al. 2011).

Using geometries that involve sharp inlet corners, previous researchers have observed the development of large lip vortices in the inlet channels (at the reentrant corners of the flow focusing device) when Weissenberg numbers were increased (Ballesta and Alves 2017). In this work, these vortices were never found to arise for the range of Reynolds number and Weissenberg number used. As mentioned in Chapter 3, due to the adopted fabrication methods, the experimental microfluidic geometry corners are not fully sharp, instead a minimal radii of curvature exists. The effects of this however, are not explored in this work.

6.3.1.1 Effect of Velocity Ratio and Weissenberg Number

When using Newtonian fluids within the flow focusing device, it is shown in Chapter 5 that as the velocity ratio (VR) is increased it not only reduces the width of the central focused stream (Nguyen and Huang 2005, Oliveira et al. 2012) but also enhances the curvature of the separating streamlines in the central region of the geometry, as previously shown in Figure 5.10. When a polymeric viscoelastic fluid is introduced a combination of this enhanced curvature and the tensile elastic stress acting along the streamlines, according to the definition of Pakdel - McKinley criterion (equation (6.1)), can potentially provide suitable conditions to trigger purely elastic instabilities.

Figure 6.4 illustrates the effect of the Weissenberg number, for a constant velocity ratio of 25, where a high curvature of the separating streamlines already exists.

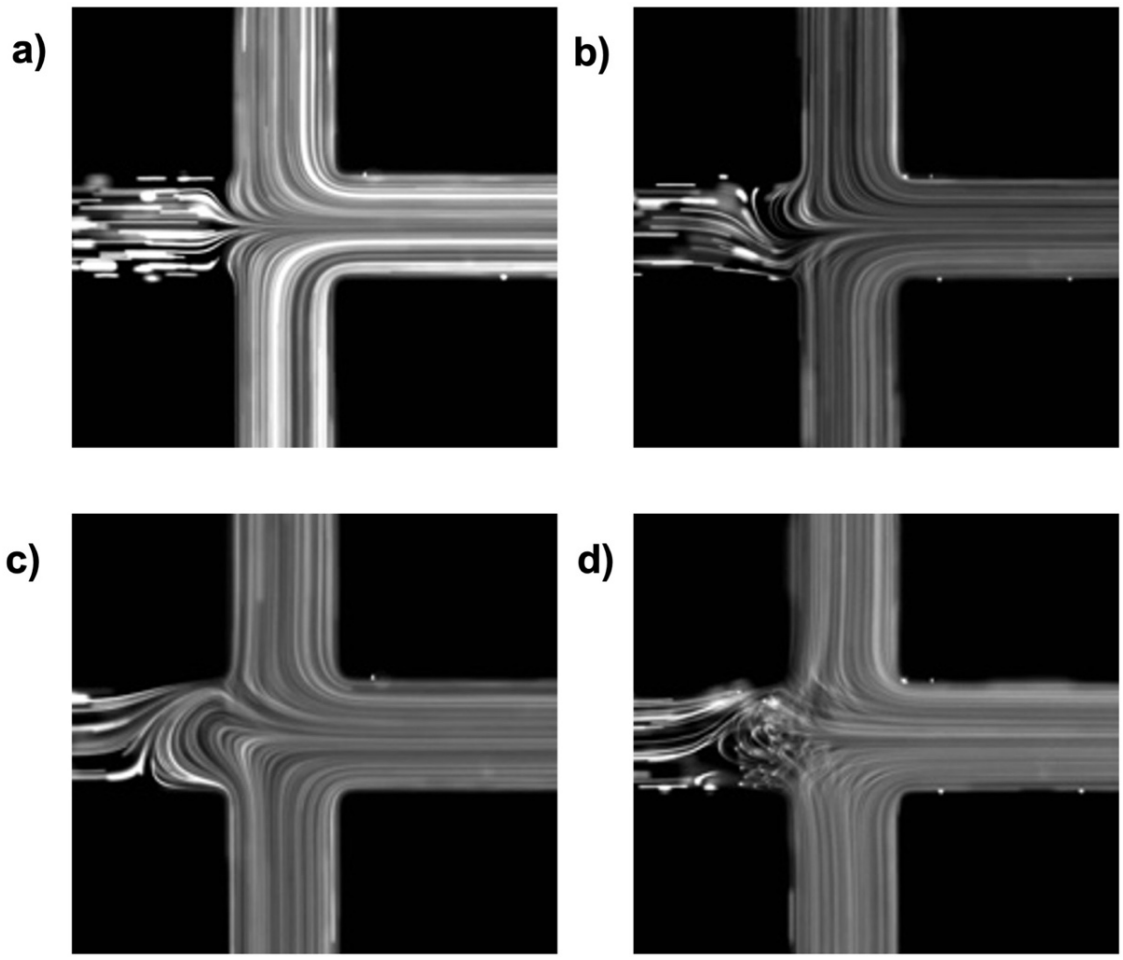

Figure 6.4: Flow patterns for $VR = 25$ with increasing values of Wi in the flow focusing device ($AR = 0.84$) using the same viscoelastic solution (PEO 280ppm in 60:40 water/glycerol solution) in all inlet streams a) $Wi = 1.32$ b) $Wi = 2.64$ c) $Wi = 3.31$ d) $Wi = 5.29$. For all cases $Re < 0.2$.

The results are in qualitative agreement with those of Oliveira et al (2009) demonstrating that at low values of the Weissenberg number the flow is symmetric relative to $y = 0$ (cf. Figure 6.4). Above the critical Weissenberg number, the onset of a steady (and bistable, i.e., the system has two possible stable solutions, one being the mirror image of the other with respect to $y = 0$ as in the work of Oliveira et al. (2009)) asymmetric flow regime is observed, with the degree of asymmetry increasing with Weissenberg number (Figure 6.4b - c). Beyond a second critical Weissenberg number time-dependent flow is visible with crossing streamlines (cf. Figure 6.4d).

It is important to note that it is not possible to pinpoint the exact value of the critical Weissenberg number for each transition in this work however, it can be determined within a small interval based on the flow map presented in Figure 6.5. For $VR = 25$, the first transition to steady asymmetric flow is shown to lie between $1.58 < Wi < 1.98$ and therefore, from this point onwards a value that lies within this range ($Wi_c \cong 1.59$) calculated using the supercritical bifurcation data curve fit outlined in equation (6.5) (cf. Figure 6.6) will be used. The second transition from steady asymmetric to time-dependent flow is found to lie between $4.62 < Wi < 4.76$. For presentation purposes the average between these two points will be used to denote the critical point for the second transition with a value of $Wi_c \cong 4.69$.

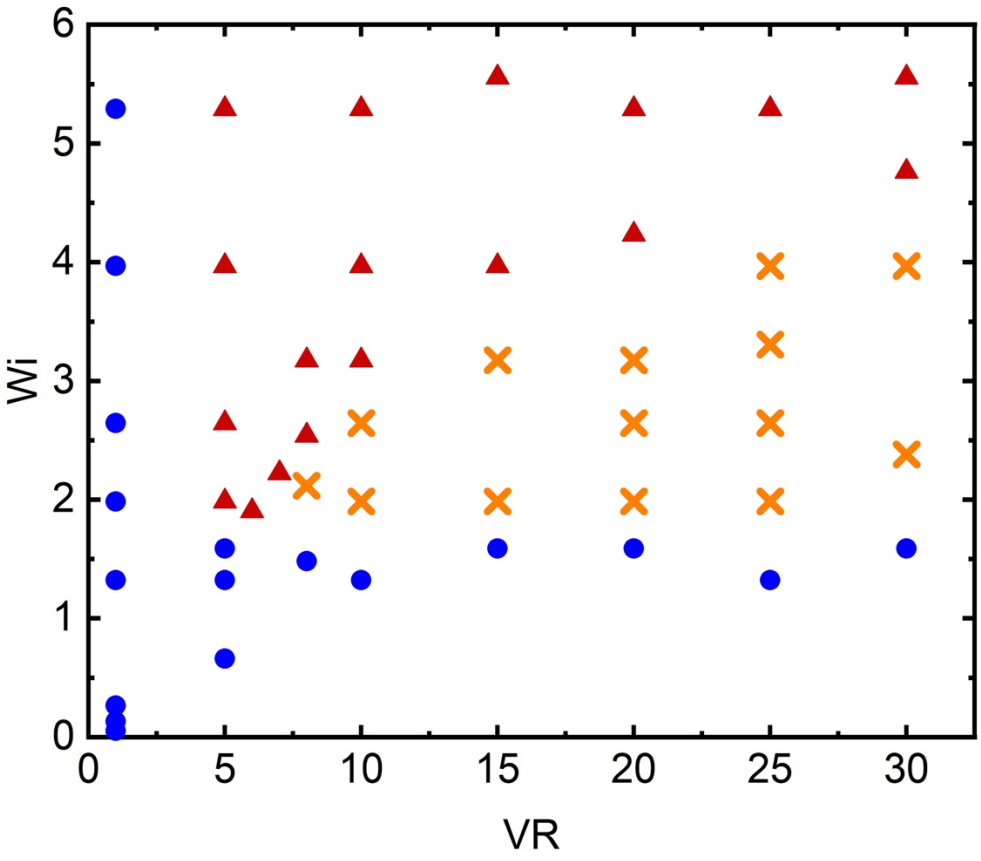

Figure 6.5: Flow classification map in the $Wi - VR$ domain for single-phase Boger fluid (PEO 280ppm in 60:40 water/glycerol solution) flow within the flow focusing device of $AR = 0.84$. Blue circles indicate the symmetric flow regime, orange crosses indicate the asymmetric flow regime and red triangles indicate the time-dependent flow regime.

Flow behaviours for various values of Wi and VR (up to a maximum VR of 30) are illustrated in the flow classification map of Figure 6.5. For low velocity ratios, $5 \leq VR < 8$, only one transition from steady symmetric flow to time-dependent flow was observed. For this range of VR the flow was never seen to exhibit steady asymmetric behaviour. It is believed that the normal stresses within the flow are not sufficiently high to trigger this intermediate instability (Oliveira et al. 2009). For moderate to high velocity ratios, $VR \geq 8$, two transitions were observed for increasing Wi as described previously: a first transition to steady asymmetric flow and a second transition from steady asymmetric to time-dependent flow at higher Wi. The critical Wi for the time-dependent transition is shown to increase with increasing Hencky Strain, defined as $\varepsilon_{H_{FF}} = \ln\left(U_3 / U_1\right)$. These results agree with those of Oliveira et al (2009) however, are contrasting with those obtained experimentally by Ballesta and Alves (2017) who found that above a critical value of the Hencky strain ($\cong 2$) the critical Wi for the time-dependent flow transition decreased with further increases in Hencky strain. This may be due to geometric differences, where, in their case, the width of the lateral inlet channels was double that of the central inlet channel, or due to the fact that all fluids used in the work of Ballesta and Alves (2017) had a slight degree of shear thinning. For high velocity ratios, $VR \geq 20$, the critical Wi for each instability transition is approximately constant as also previously observed by Oliveira et al (2009).

To evaluate the degree of flow asymmetry under steady flow conditions, the measuring technique described in Section 6.2.4 was adopted using the asymmetry parameter, χ, defined in equation (6.4). To reiterate, the asymmetry parameter has a value of 0 when the flow is steady and symmetric about the x-axis and would exhibit the highest value of 1 when fluid from one of the lateral streams occupies the full channel width. The data just above the critical point to steady asymmetric flow was fitted using equation (6.5) (Xi and Graham 2009) highlighting the typical supercritical bifurcation observed for flow of a single viscoelastic Boger fluid in the flow focusing device:

$$F_{sb} = a_1 \sqrt{Wi - Wi_c} \tag{6.5}$$

where Wi_c represents the critical Weissenberg number of the first steady asymmetric instability and a_1 represents the magnitude of the asymmetry.

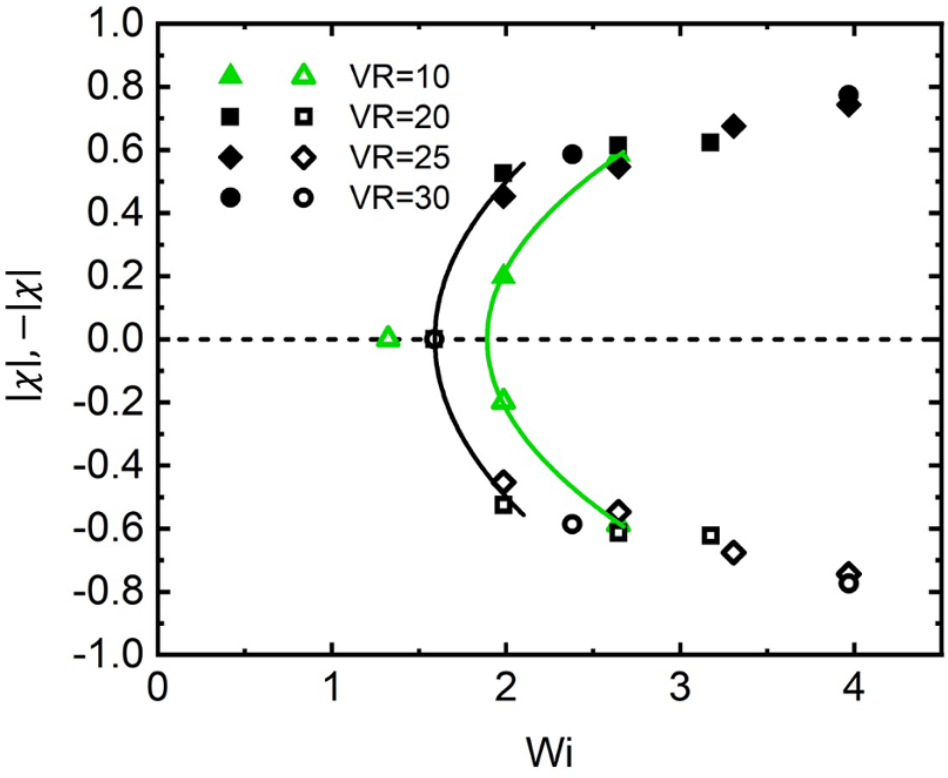

Figure 6.6: Supercritical bifurcation diagram for asymmetric flow patterns within the flow focusing device using single-phase viscoelastic fluid flow (PEO 280ppm in 60:40 water/glycerol solution) showing the effect of Wi on the degree of asymmetry for high and low VR. Solid lines represent the fit (equation (6.5)). Low velocity ratio ($VR = 10$) data is shown in green and high velocity ratios ($VR \geq 20$) are shown in black, in particular, black squares indicate $VR = 20$, black diamonds indicate $VR = 25$ and black circles indicate $VR = 30$. Solid symbols represent $|\chi|$ and hollow symbols represent $-|\chi|$ highlighting the bistable nature of this instability.

It can be confirmed that the critical Wi for the first transition to asymmetric flow occurs at lower values when higher velocity ratios are used. The bifurcation data curve for the lower velocity ratio ($VR = 10$) has an equation of $0.67\sqrt{Wi - 1.89}$. Interestingly, the data for high velocity ratios fall onto a single bifurcation data fit curve with an equation

of $0.78\sqrt{Wi-1.59}$. As such, from this point onwards only high velocity ratio data points will be shown for asymmetry parameter measurements.

The findings of Figure 6.6 alongside those from the flow classification map (Figure 6.5) where it was found that for high velocity ratios the critical Wi is approximately constant, highlights that the development of the asymmetries are no longer highly dependent on the velocity ratio. This effect can be visualised in Figure 6.7, for a constant Weissenberg number, $Wi = 2.65$, within the steady asymmetric flow regime. For high velocity ratios (cf. Figure 6.7b-d), the size of the asymmetry is shown to remain approximately constant, with Figure 6.7c highlighting the bistable nature of the instability (i.e., the large asymmetry has swapped side). However, for the smaller velocity ratio (cf. Figure 6.7a) it is clear that the defined asymmetry is smaller.

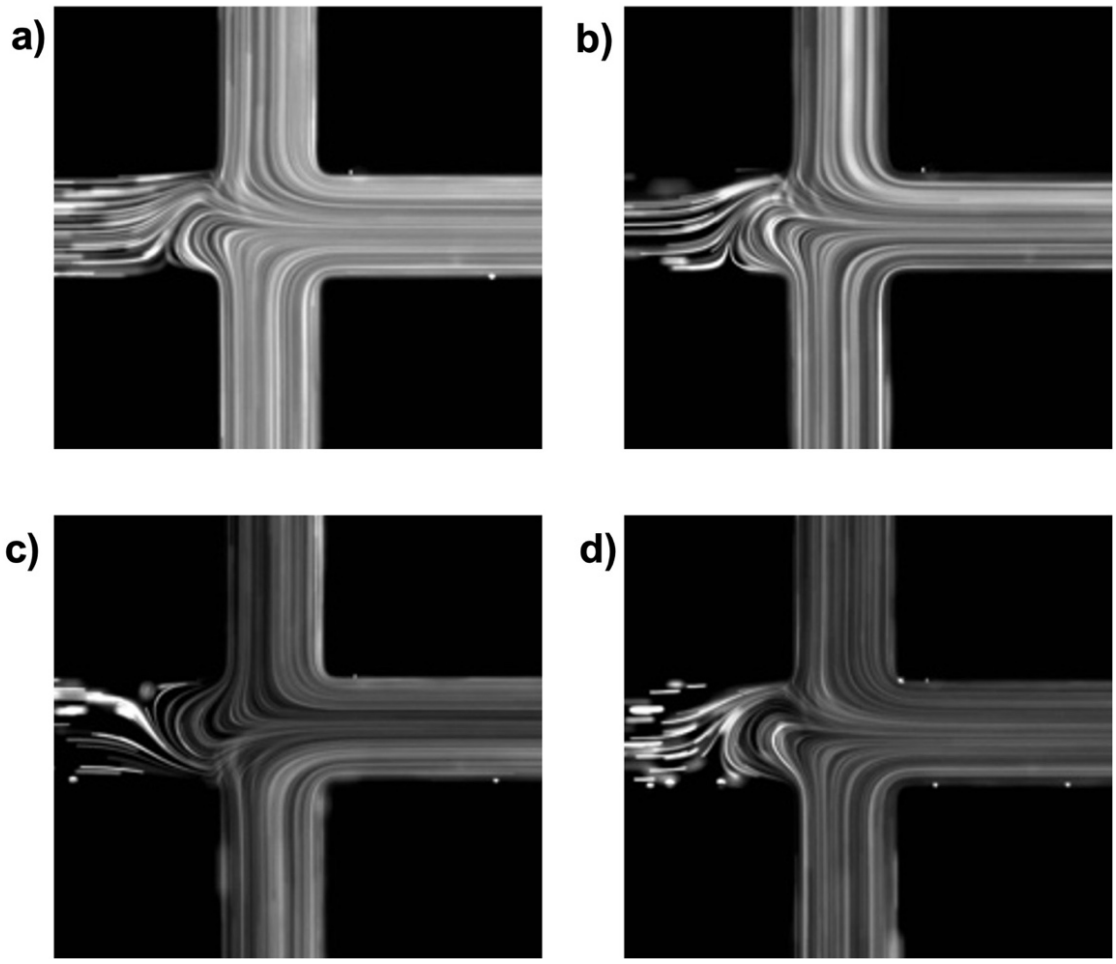

Figure 6.7: Flow patterns for $Wi = 2.65$ with increasing values of VR in the flow focusing device using single-phase viscoelastic solution (PEO 280ppm in 60:40 water/glycerol solution) a) $VR = 10$ b) $VR = 20$ c) $VR = 25$ d) $VR = 30$ showing that for high velocity ratios the size of the asymmetry is shown to remain approximately constant while for the $VR = 10$ case the asymmetry is visibly smaller. For all cases $Re < 0.2$.

6.3.1.2 Effect of Channel Aspect Ratio

To study the effect of channel aspect ratio, in this section three different microfluidic devices with varying aspect ratios ($AR = 0.84,\ AR = 0.28$ and $AR = 0.22$) were used. The single-phase viscoelastic flow case for an aspect ratio of 0.84 was discussed in great detail in the previous section of this chapter and will be used as the reference case for comparison. Figure 6.8 illustrates the effect of the Weissenberg number (Wi) for each of the microfluidic geometries at a constant velocity ratio of 20.

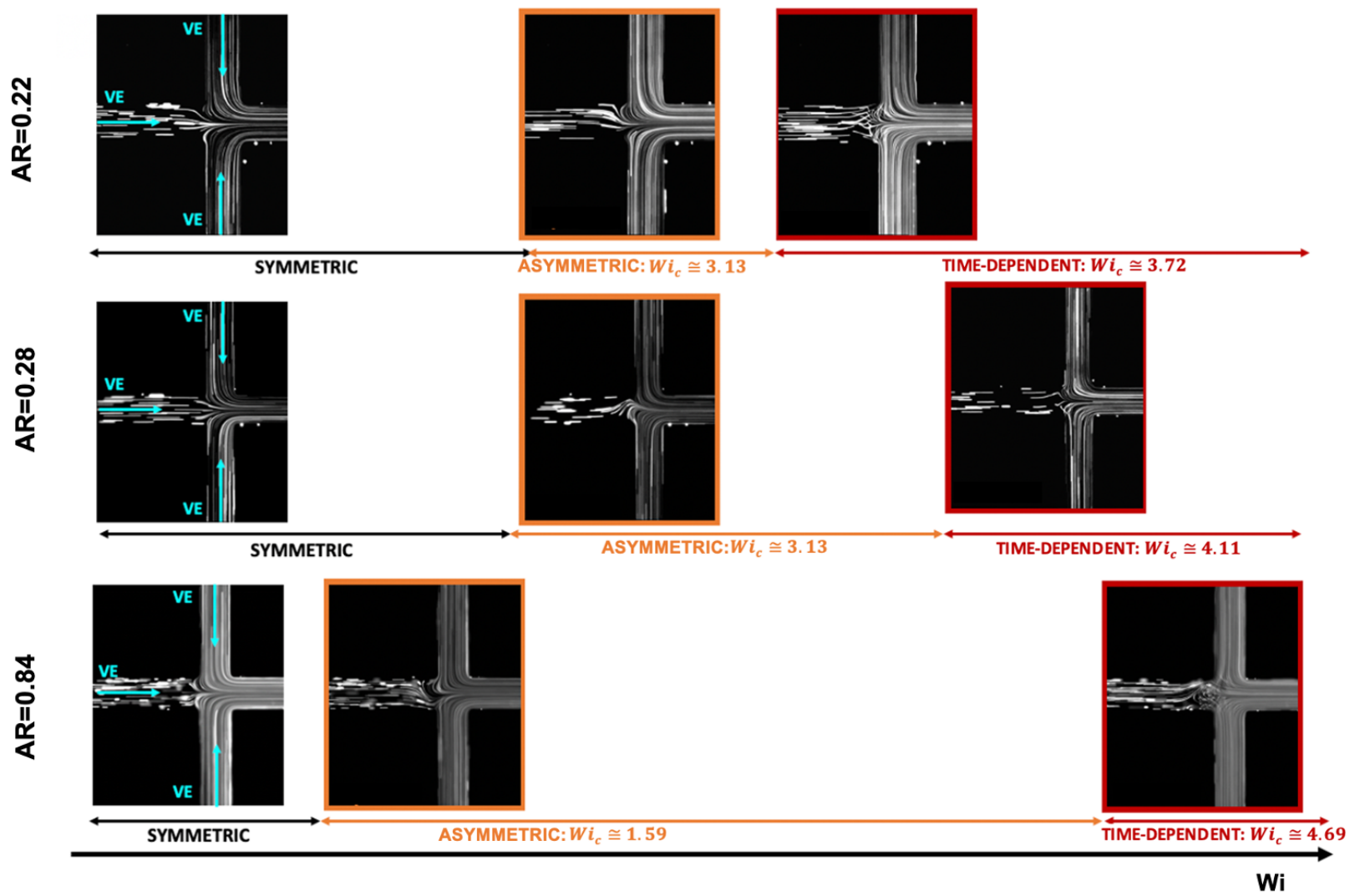

Figure 6.8: Experimental images showing the impact of Wi on the flow patterns observed for single-phase flow of PEO (M_w8 x10^6), 280ppm (w/w), in Water/ Glycerol (60/40) in the flow focusing device for different geometry aspect ratios show at $VR = 20$. Steady asymmetric flow is indicated by the orange highlighted images and time-dependent flow is indicated by the red highlighted images.

While similar trends to those outlined in the previous section were observed for all aspect ratios studied as the velocity ratio is varied i.e., no steady asymmetric flow was observed for low VR, e.g., $VR \leq 5$, while for higher VR, e.g., $VR = 20$, (shown in Figure 6.8) the flow is seen to exhibit two transitions in all microfluidic geometries studied: the first from steady symmetric flow to steady asymmetric flow (indicated by the orange highlighted images in Figure 6.8) and a second from steady asymmetric flow to time-dependent flow (indicated by the red highlighted images in Figure 6.8).

For such VR (e.g., $VR = 20$), reducing the aspect ratio of the microchannel resulted in the steady asymmetries occurring at a higher critical Weissenberg number (i.e., reducing the aspect ratio from 0.84 to 0.28 the first critical Weissenberg number increased from 1.59 to 3.13), in line with previous observations in the cross-slot configuration (Sousa et al. 2015, Cruz et al. 2016). The opposite effect can be observed for the second transition, where reducing the aspect ratio of the microchannel resulted in the time-dependent flow regime occurring at a lower critical Weissenberg number, agreeing with other work conducted by previous researchers Cruz et al within the cross-slot device (2016). These effects can also be seen in the map of flow behaviour in the $\mathcal{H} - Wi$ parameter space, where $\mathcal{H} = {AR}/{(AR + 1)}$ (defined as in Sousa et al. (2015)) shown in Figure 6.9.

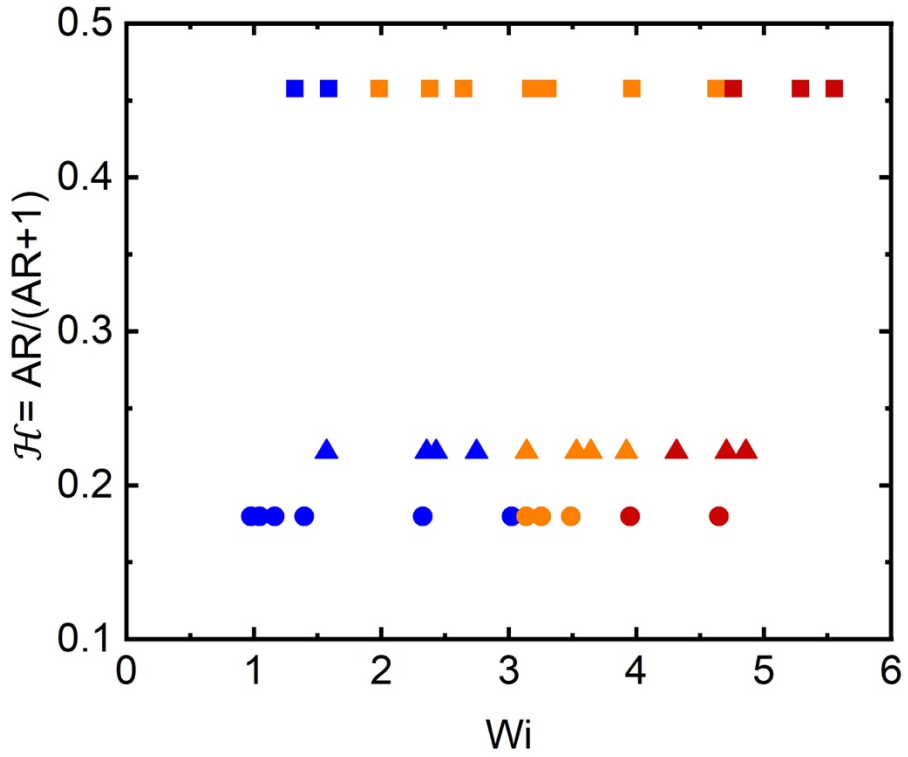

Figure 6.9: Flow map in $\mathcal{H} - Wi$ parameter space at $VR = 20$ for single-phase viscoelastic fluid flow in the flow focusing devices of varying channel aspect ratios and Weissenberg number. Blue symbols indicate the symmetric flow regime, orange symbols indicate the asymmetric flow regime and red symbols indicate the time-dependent flow regime.

Despite the similarities in the trends and types of instabilities that occur, clear differences can be identified when geometric changes are introduced (cf. Figure 6.9). Adopting the same approach as previous researchers Sousa et al (2015), a high value of, $\mathcal{H} = 1$, represents 2D flow and lower values represent decreasing channel depths. A value of $\mathcal{H} = 0.5$ corresponds to a square microchannel with an aspect ratio of 1. A value of $\mathcal{H} = 0.46$ corresponds to the reference microchannel with an aspect ratio of 0.84. Reducing the $\mathcal{H}$ value is shown to result in an increase in the first critical transition point and a decrease in the second critical transition point, and consequently a decrease in the size of the steady asymmetric flow region. The increase in the first critical Weissenberg number is in agreement with trends found for the cross-slot configuration (Sousa et al. 2015).

However, for the flows of the viscoelastic Boger fluid studied here it was found that the second transition time-dependent flow appears at gradually smaller Wi as the aspect

ratio is decreased ($\mathcal{H}$ decreases), showing the same behaviour as numerical simulations using the UCM model in research conducted by Cruz et al within the cross-slot device (2016), but in contrast with the experiments of Sousa et al (2015) in the cross-slot configuration where the opposite effects were found. This difference is thought to be due to the use of shear thinning fluids in the work of Sousa et al (2015), where the viscosity decreases with the shear rate unlike the case for the work presented here where Boger fluids of approximately constant viscosity are used. Decreasing the channel aspect ratio increases the influence of the channel walls and enhances the shear effects within the flow because of the top and bottom channel walls. These increasing shear rates and bounding walls within the flow focusing configuration make it difficult to achieve a stable asymmetric flow that can be easily obtained for high aspect ratio channels.

Results suggest that for 2D Boger-like fluid flows this area of steady asymmetric flow would be maximised and, on the other hand, for a very shallow channel (Hele-Shaw approximation) there could infact be no region of steady asymmetry at all, agreeing with results found in other extensional configurations like the cross-slot (Cruz et al. 2016).

To quantify the effect of aspect ratio in the degree of flow asymmetry, the asymmetry parameter was again utilised. The bifurcation plots can be viewed in Figure 6.10.

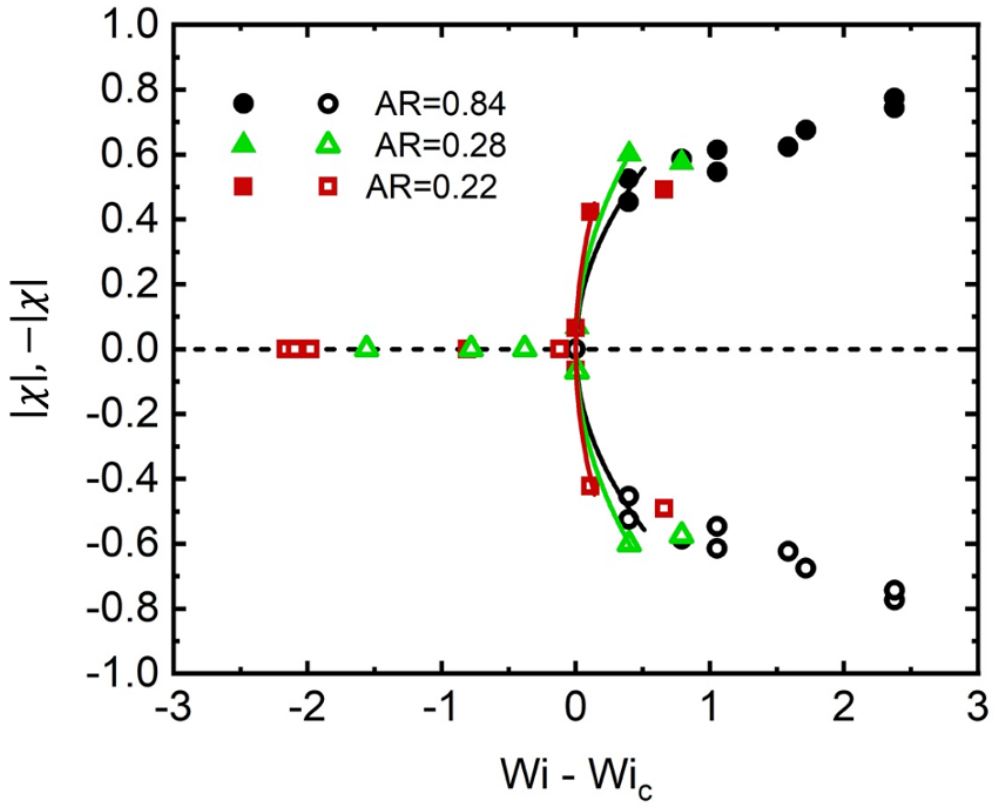

Figure 6.10: Effect of Wi on the degree of asymmetry for asymmetric flow patterns within the flow focusing device using single-phase viscoelastic fluid flow (PEO 280ppm in 60:40 water/glycerol solution): for $AR = 0.84$ at $VR \geq 20$, and $AR = 0.28$ and $AR = 0.22$ at $VR = 20$. Solid lines represent the fit to the supercritical bifurcation equation (equation (6.5)). Black data represents the case of $AR = 0.84$, green data represents the case of $AR = 0.28$ and red data represents the case of $AR = 0.22$. Solid symbols represent $|\chi|$ and hollow symbols represent $-|\chi|$ highlighting the bistable nature of this instability.

As previously discussed, the critical Weissenberg number for the transition to steady asymmetric flow was found to increase with decreasing channel aspect ratio. From Figure 6.10 it can be also observed, by looking at the solid lines that represent the fit to the supercritical bifurcation equation (equation (6.5)), that the size of the asymmetries may increase slightly with decreasing channel aspect ratio. As the channel aspect ratio is decreased, it appears that the data fit solid line has a slightly less pronounced curved shape however, further quantification techniques would be required to accurately assess this impact. These findings would be similar to those of Oliveira et al (2009) where an increase in the width of central channel relative to the

lateral side channels caused an increase in the size of the produced asymmetries within the flow focusing device. This highlights that at high velocity ratios, although the size of the asymmetries is independent of velocity ratio, the size is dependent on the geometry of the microfluidic device, in particular the channel aspect ratio.

6.3.2 Viscoelastic Instabilities – Multiple Fluid Systems

In this section, the impact on the flow patterns and the onset of elastic instabilities that arise when multiple fluid streams are involved is studied, in particular when Newtonian fluid (N) streams are introduced alongside a viscoelastic fluid (VE). In all cases, the channel of aspect ratio $AR = 0.84$ was used. In addition to the single-phase flow system discussed in the previous section, where the polymer solution occupied all inlet streams, which is used here as a reference case (named 'CASE A'), in this section, two additional inlet configurations were considered as shown schematically in Figure 6.11 to analyse the impact of multiple fluid systems. In one of the configurations, the Newtonian fluid is inserted in the central fluid stream and the polymeric fluid flows in the lateral/ side streams only (N1VE2, named 'CASE B') where the polymeric fluid is mostly subjected to shear dominated flow near the re-entrant corners where high streamline curvature is observed. As the viscoelastic fluid flows through the curvature of the system, the polymers will still experience a degree of extension. In the other case (VE1N2, named 'CASE C') the Newtonian fluid is inserted into the lateral side streams and the polymeric fluid flows in the central region experiencing strong elongational effects near the centreline region.

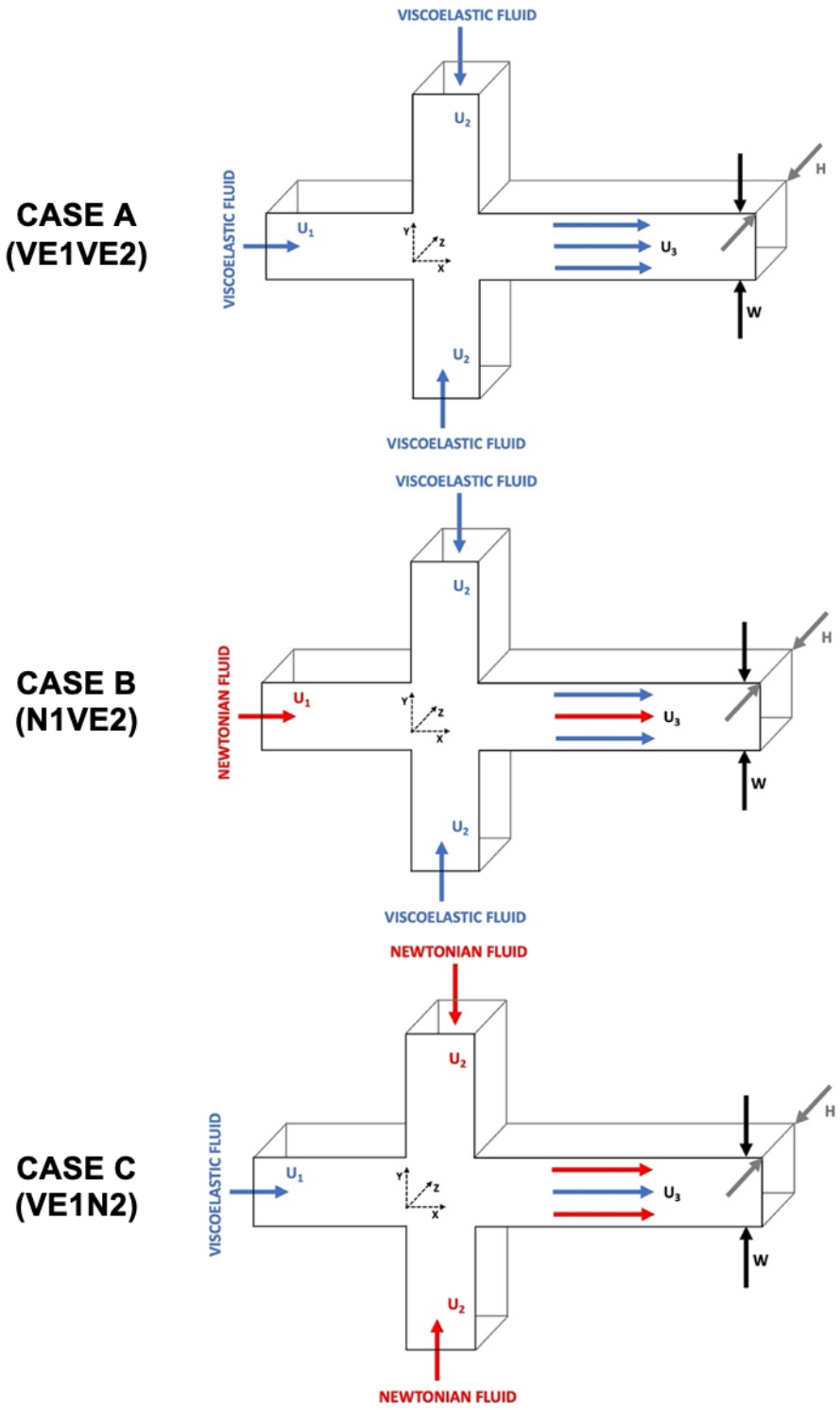

Figure 6.11: Experimental flow configurations for flows of multiple fluids in the flow focusing device. CASE A – The reference single-phase flow system where polymer solution occupied all inlet streams. CASE B - Newtonian fluid is inserted through the central inlet channel and the polymeric fluid through two lateral/ side channels CASE C - Newtonian fluid is inserted into the two lateral inlet channels and the polymeric fluid flows in through the central channel.

It is important to note that although miscible fluids are used within these experiments, viscosity stratification is excluded as the origin of the instabilities observed (Yih 1967, Bonhomme et al. 2011). As shown in chapter 5, when Newtonian miscible solutions of water and glycerol are used, unstable interfaces are never visualised and this form of instability is considered not to impact the flow patterns under the flow conditions used in this work, in agreement with previous researchers (Bonhomme et al. 2011). For all experimental work carried out, after the region of instability, straight jets were visualised throughout the full outlet of the channel which is common behaviour at low flow rates (Bonhomme et al. 2011).

The viscoelastic fluids used in this work are Boger-like fluids which exhibit a constant viscosity (cf. Figure 6.1). Newtonian fluids of comparable shear viscosities were used to reduce any effects due to viscosity differences between the fluids instead, for these cases a jump in elasticity will be present across the interface (fluid properties outlined in Table 6.1).

Figure 6.12 illustrates the effect of the Weissenberg number (Wi) for each of the configurations at a constant velocity ratio of 25, which exhibits a high Hencky Strain, $\varepsilon_{H_{FF}} = 3.93$, and a pronounced converging region of the central stream.

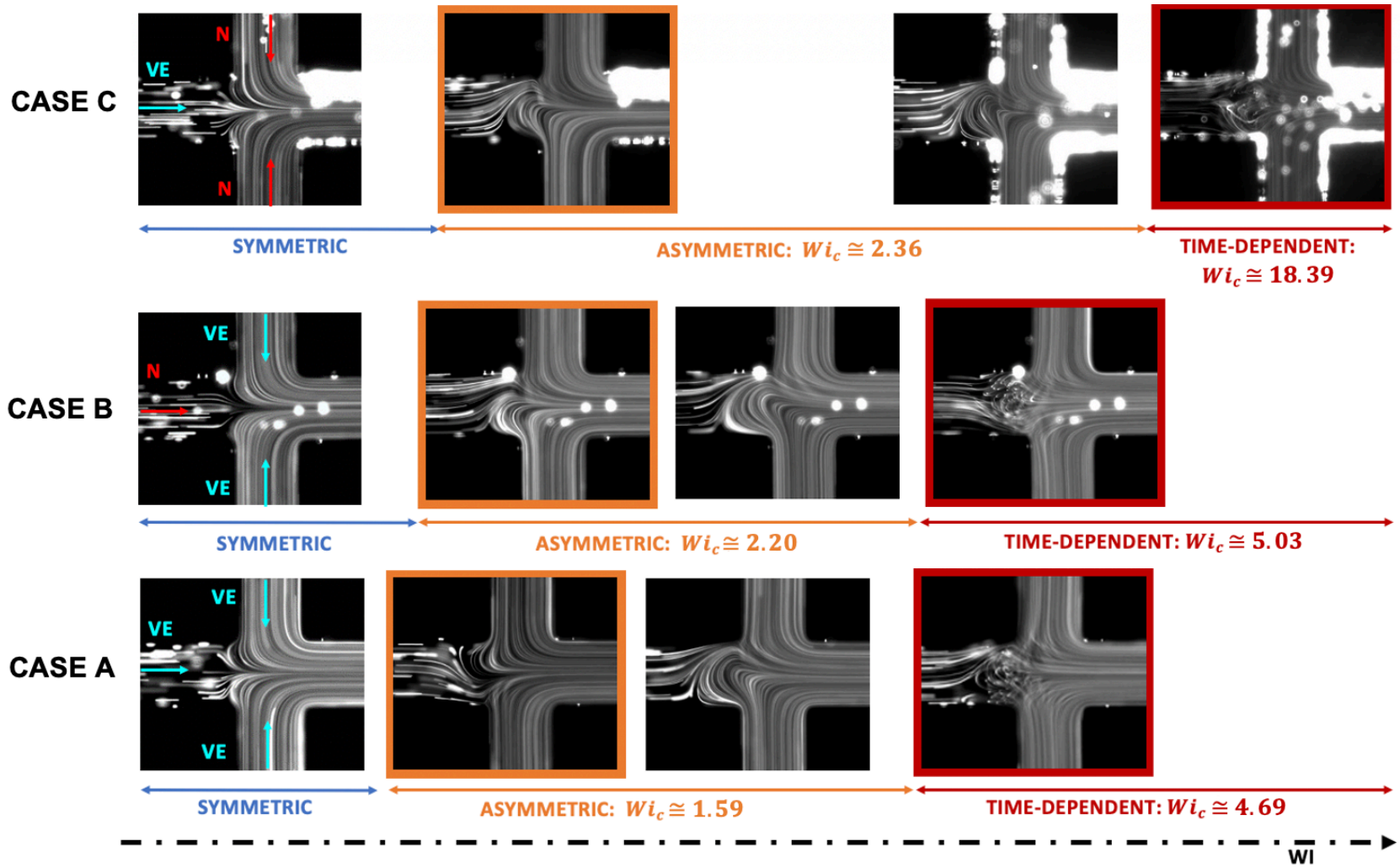

Figure 6.12: Experimental images showing the impact of Wi on the flow patterns observed for the three fluid configurations at $VR = 25$ using viscoelastic solution (VE) of PEO (M_w8 x10^6), 280ppm (w/w), in Water/ Glycerol (60/40) and Newtonian solution (N) of Water/ Glycerol (48.4/51.6). The first transition from steady symmetric flow to steady asymmetric flow is indicated by the orange highlighted images and the second transition to time-dependent flow is indicated by the red highlighted images.

The experimental images shown here compare the three flow configurations at a constant velocity ratio of 25, above which, the critical conditions for transitions are known to remain approximately constant (Oliveira et al. 2009). Elastic instabilities are found to arise in all cases with two transitions: the first from steady symmetric flow to steady asymmetric flow (indicated by the orange highlighted images in Figure 6.12) and a second from steady asymmetric flow to time-dependent flow (indicated by the red highlighted images in Figure 6.12). Interestingly, the most similar case to that of the single-phase flow system is that when the Newtonian fluid is placed in the central inlet stream (CASE B). In this case, the polymeric viscoelastic fluid (VE) only occupies the lateral inlet streams where they are subjected to a shear-dominated flow. If extension was the dominating feature required for the onset of these elastic instabilities, it would be expected that the onset of the instabilities be delayed in the case of this configuration.

In CASE C of Figure 6.12, where the Newtonian fluids are in the lateral streams, differences can be observed in transition points in comparison to the single-phase flow system. The effect on the critical Weissenberg number for the first transition is only small, however it can be observed that the transition to time-dependent flow occurs at a substantially larger Weissenberg number. Remember that in this case the polymeric fluid is flowing in the central fluid stream where it is subjected to strong elongational effects.

This effect can also be visualised in the $Wi - VR$ flow maps of Figure 6.13. Here, the effects at lower velocity ratios can also be appreciated.

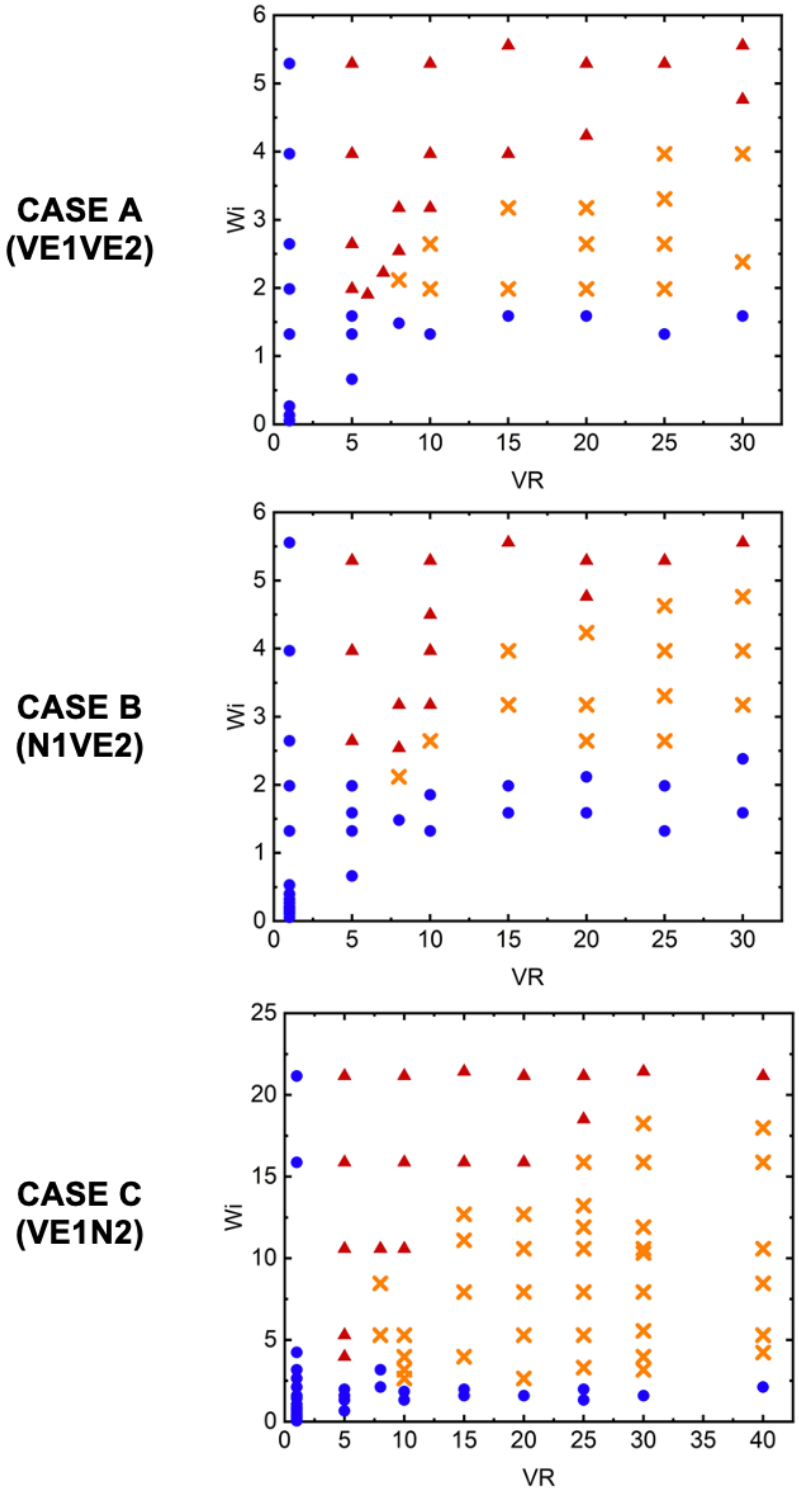

Figure 6.13: Flow classification maps in the $Wi - VR$ domain in the flow focusing device of $AR = 0.84$ for multiple fluid flow configurations; CASE A, CASE B and CASE C. Fluids used are a viscoelastic solution (VE) of PEO (M_w8 x10^6), 280ppm (w/w), in Water/ Glycerol (60/40) and a Newtonian solution (N) of similar shear viscosity. Blue circles indicate the symmetric flow regime, orange crosses indicate the asymmetric flow regime and red triangles indicate the time-dependent flow regime.

From Figure 6.13, it can be observed that all cases show similar trends in relation to the types of elastic instabilities, and thus the transitions, that occur as those discussed in Section 6.3.1.1 for low and high velocity ratios. However, despite similar trends in all three flow configurations clear differences can also be observed when looking at the flow maps (cf. Figure 6.13) which further highlight the points discussed above in relation to Figure 6.12. Replacing the lateral streams with Newtonian fluids (CASE C) largely increases the size of the steady asymmetric region (indicated by the orange crosses in Figure 6.13) and delays the onset of both instabilities (albeit the delay being more significant for the second transition to time-dependent flow).

To analyse the effect of each configuration on the degree of flow asymmetry, the asymmetry parameter was utilised. The bifurcation data curves and fits can be viewed in Figure 6.14 and Table 6.2. It is important to reiterate that the section where the expression is fitted mimics that typical of a supercritical bifurcation and only high velocity ratio measurement points are shown (i.e., $VR \geq 20$).

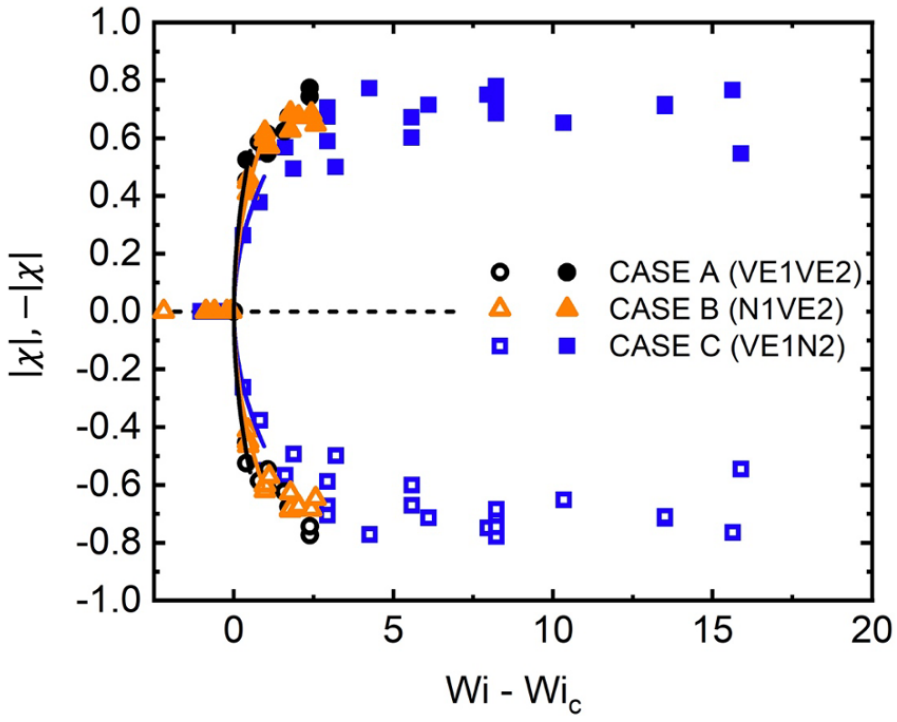

Figure 6.14: Bifurcation diagram for asymmetric flow patterns within the flow focusing device using multiple fluids. Effect of $Wi - Wi_c$ on the degree of asymmetry for $AR = 0.84$ at $VR \geq 20$. Solid lines represent the data fit (equation (6.5)). Black data represents the case of single-phase flow, orange data represents the case with the Newtonian fluid in the central stream and viscoelastic fluid in the lateral side streams and blue data represents the case with the Newtonian fluid in the lateral side streams and the viscoelastic fluid in the central stream. Solid symbols represent $|\chi|$ and hollow symbols represent $-|\chi|$ highlighting the bistable nature of this instability.

Table 6.2: Parameters of bifurcation data curves fitted to experimental measurements for multiple fluid flow configurations.

FLOW SYSTEM	SUPERCRITICAL BIRFURCATION DATA FIT
Single-Phase Flow	$0.78\sqrt{Wi - 1.59}$
Newtonian Central Stream & Viscoelastic Lateral Streams	$0.63\sqrt{Wi - 2.2}$
Newtonian Lateral Streams & Viscoelastic Central Stream	$0.5\sqrt{Wi - 2.36}$

The critical Weissenberg number at which the transition to steady asymmetric flow occurs is found to be slightly lower for the single-phase flow configuration suggesting that this onset of the purely elastic flow instabilities could infact be due to a combination of both extension and shear effects within this flow system. This can be discussed further by looking at the approximate magnitude of the asymmetries in Table 6.2, represented by parameter a_1 in equation (6.5). The magnitude does not change substantially between the different cases however, the magnitude appears to be larger for the single-phase flow system than for the other two cases. Again, as previously mentioned, this method is not entirely accurate to investigate this impact and to assess this more thoroughly other quantification methods would be required, such as numerical simulations as in the work of Oliveira et al. (2009).

When comparing both multiple fluid flow configurations the largest asymmetries (closest in size to the single-phase reference case) arise for CASE B, when the polymer fluids occupy the lateral inlet streams, while smaller asymmetries arise for CASE C, when the polymer fluids are in central inlet stream only. The results suggest that the elastic instabilities within the flow focusing device are not solely related to the extensional flow effects within this set up and the shear region where there is a high streamline curvature is important. Such observations are in line with previous work in the cross-slot geometry (Davoodi et al. 2021).

6.4 CONCLUSIONS

In this chapter single and multifluid flows involving a viscoelastic Boger fluid through a microfluidic flow focusing geometry under creeping-flow conditions was investigated experimentally to gain an understanding of the critical features for the onset of flow induced elastic instabilities in this geometry.

The general trends of the flow induced elastic instabilities observed in the flow focusing geometry agree with previous findings (Oliveira et al. 2009) where at low values of the Weissenberg number the flow is symmetric relative to the centreline i.e., the x-axis.

Above a first critical Weissenberg number, the onset of a steady and bistable asymmetric flow regime with the degree of asymmetry increasing with Weissenberg number for moderate to high VR $(8 \leq VR < 30)$ is observed. Beyond a second critical Weissenberg number the onset of a time-dependent flow regime is observed. For $VR = 1$, the flow remains steady and symmetric about the x-axis over the full range of Wi studied in this chapter. For low velocity ratios, $5 \leq VR < 8$, only one transition from steady symmetric flow to time-dependent flow was observed above a critical Weissenberg number and for moderate to high velocity ratios, $8 < VR < 30$, two transitions were observed for increasing Wi.

The critical Weissenberg number for the transition to steady asymmetric flow and the size of the flow asymmetries was found to increase with decreasing channel aspect ratio. Additionally, the range of Weissenberg number for which the asymmetric flow regime region is observed was found to decrease as the aspect ratio of the flow focusing device is decreased. Reducing the channel aspect ratio increases the influence of the channel walls and enhances the shear effects within the flow making it difficult to achieve a stable asymmetric flow that can be easily obtained for high aspect ratio channels.

All of the single-fluid work included in this chapter has used Boger fluids, where the viscosity is constant, however it would also be interesting to study the effects of shear thinning and how this affects such transitions. Some preliminary work has been carried out on this and is summarised in Appendix C.

In the second part of this chapter, presented results show the impact of introducing multiple fluid streams on the onset of the purely elastic flow instabilities. In addition to the single-fluid configuration, two other configurations using miscible fluids, where a Newtonian fluid (N) is introduced alongside the viscoelastic solution (VE) with the aim of understanding the impact of an elasticity jump and critical regions of extensional flow. The observed flow instabilities were of a similar nature to that of the single-fluid case. Interestingly these findings show no significant change in the critical Wi for the transition to steady asymmetric flow for the various configurations, but placing the Newtonian fluid in the lateral streams delayed the transition to time-dependent flow

quite significantly. The size of the asymmetries were found to be the largest for the single-fluid case, with the closest similarity observed for the shear dominated case. These results suggest that these elastic instabilities cannot be solely related to the extensional flow, which is in agreement with recent work in the cross-slot geometry (Davoodi et al. 2021).

6.5 REFERENCES

Anna, S. L., Bontoux, N. and Stone, H. A. (2003). "Formation of dispersions using “flow focusing” in microchannels." Applied Physics Letters 82(3): 364-366.

Ballesta, P. and Alves, M. A. (2017). "Purely elastic instabilities in a microfluidic flow focusing device." Physical Review Fluids 2(5): 053301.

Bird, R. B., Hassager, O. and Armstrong, R. C. (1977). Dynamics of polymeric liquids. Vol. 1: Fluid Mechanics, John Wiley and Sons.

Boger, D. V. (1987). "Viscoelastic flows through contractions." Annual Review of Fluid Mechanics 19: 157-182.

Bonhomme, O., Morozov, A., Leng, J. and Colin, A. (2011). "Elastic instability in stratified core annular flow." Phys Rev E Stat Nonlin Soft Matter Phys 83(6 Pt 2): 065301.

Browne, C. A., Shih, A. and Datta, S. S. (2020). "Pore-Scale Flow Characterization of Polymer Solutions in Microfluidic Porous Media." Small 16(9): e1903944.

Casanellas, L., Alves, M. A., Poole, R. J., Lerouge, S. and Lindner, A. (2016). "The stabilizing effect of shear thinning on the onset of purely elastic instabilities in serpentine microflows." Soft Matter 12(29): 6167-6175.

Clarke, A., Howe, A. M., Mitchell, J., Staniland, J., Hawkes, L. and Leeper, K. (2015). "Mechanism of anomalously increased oil displacement with aqueous viscoelastic polymer solutions." Soft Matter 11(18): 3536-3541.

Cruz, F. A., Poole, R. J., Afonso, A. M., Pinho, F. T., Oliveira, P. J. and Alves, M. A. (2016). "Influence of channel aspect ratio on the onset of purely-elastic flow instabilities in three-dimensional planar cross-slots." Journal of Non-Newtonian Fluid Mechanics 227: 65-79.

Datta, S. S., Chiang, H., Ramakrishnan, T. S. and Weitz, D. A. (2013). "Spatial fluctuations of fluid velocities in flow through a three-dimensional porous medium." Phys Rev Lett 111(6): 064501.

Davoodi, M., Domingues, A. F. and Poole, R. J. (2019). "Control of a purely elastic symmetry-breaking flow instability in cross-slot geometries." Journal of Fluid Mechanics 881: 1123-1157.

Davoodi, M., Houston, G., Downie, J., Oliveira, M. S. N. and Poole, R. J. (2021). "Stabilization of purely elastic instabilities in cross-slot geometries." Journal of Fluid Mechanics 922: A12.

Garstecki, P., Ganan-Calvo, A. M. and Whitesides, G. M. (2005). "Formation of bubbles and droplets in microfluidic systems." Bulletin of the Polish Academy of Sciences Technical Sciences 53(4).

Giesekus, H. (1968). "Nicht-lineare Effekte beim Strömen viskoelastischer Flussigkeiten durch Schlitz- und Lochdüsen." Rheol. Acta 7: 127-138.

Haward, S. J., McKinley, G. H. and Shen, A. Q. (2016). "Elastic instabilities in planar elongational flow of monodisperse polymer solutions." Sci Rep 6: 33029.

Knight, J. B., Vishwanath, A., Brody, J. P. and Austin, R. H. (1998). "Hydrodynamic Focusing on a Silicon Chip: Mixing Nanoliters in Microseconds." Physical Review Letters 80(17): 3863-3866.

McKinley, G. H., Pakdel, P. and Oztekin, A. (1996). "Rheological and geometric scaling of purely elastic flow instabilities." Journal of Non-Newtonian Fluid Mechanics 67: 19 – 47..

Nguyen, N. T. and Huang, X. (2005). "Mixing in microchannels based on hydrodynamic focusing and time-interleaved segmentation: modelling and experiment." Lab Chip 5(11): 1320-1326.

Oliveira, M., Pinho, F. T. and Alves, M. A. (2011). Extensional Flow of Newtonian and Boger Fluids Through a Flow Focusing Microdevice. 3rd Micro and Nano Flows Conference. Thessaloniki, Greece.

Oliveira, M. S. N., Pinho, F. T. and Alves, M. A. (2012). "Divergent streamlines and free vortices in Newtonian fluid flows in microfluidic flow-focusing devices." Journal of Fluid Mechanics 711: 171-191.

Oliveira, M. S. N., Pinho, F. T., Poole, R. J., Oliveira, P. J. and Alves, M. A. (2009). "Purely elastic flow asymmetries in flow-focusing devices." Journal of Non-Newtonian Fluid Mechanics 160(1): 31-39.

Pakdel, P. and McKinley, G. H. (1996). "Elastic Instability and Curved Streamlines." Physical Review Fluids 77(12): 2459-2462.

Poole, R. J., Alves, M. A. and Oliveira, P. J. (2007). "Purely elastic flow asymmetries." Phys Rev Lett 99(16): 164503.

Poole, R. J., Budhiraja, B., Cain, A. R. and Scott, P. A. (2012). "Emulsification using elastic turbulence." Journal of Non-Newtonian Fluid Mechanics 177-178: 15-18.

Poole, R. J., Lindner, A. and Alves, M. A. (2013). "Viscoelastic secondary flows in serpentine channels." Journal of Non-Newtonian Fluid Mechanics 201: 10-16.

Rocha, G. N., Poole, R. J., Alves, M. A. and Oliveira, P. J. (2009). "On extensibility effects in the cross-slot flow birfurcation." Journal of Non-Newtonian Fluid Mechanics 156: 58-69.

Rodd, L. E., Scott, T. P., Boger, D. V., Cooper-White, J. J. and McKinley, G. H. (2005). "The inertio-elastic planar entry flow of low-viscosity elastic fluids in micro-fabricated geometries." Journal of Non-Newtonian Fluid Mechanics 129(1): 1-22.

Shaqfeh, E. S. G. (1996). "Purely elastic instabilities in viscometric flows." Annual Reviews Fluid Mechanics 160: 122-139.

Sousa, P. C., Coelho, P. M., Oliveira, M. S. N. and Alves, M. A. (2009). "Three-dimensional flow of Newtonian and Boger fluids in square–square contractions." Journal of Non-Newtonian Fluid Mechanics 160(2-3): 122-139.

Sousa, P. C., Pinho, F. T., Oliveira, M. S. and Alves, M. A. (2015). "Purely elastic flow instabilities in microscale cross-slot devices." Soft Matter 11(45): 8856-8862.

Tirtaatmadja, V., McKinley, G. H. and Cooper-White, J. J. (2006). "Drop Formation and Breakup of Low Viscosity Elastic Fluids: Effects of Molecular Weight and Concentration." Physics of Fluids 18(4): 043101-043101-18.

Xi, L. I. and Graham, M. D. (2009). "A mechanism for oscillatory instability in viscoelastic cross-slot flow." Journal of Fluid Mechanics 622: 145-165.

Yanan Liu, Konstantinos Zografos, Joana Fidalgo, Charles Duchêne, Clément Quintard, Thierry Darnige, Vasco Filipe, Sylvain Huille, Olivia du Roure, Monica S. N. Oliveira and Lindner, A. (2020). "Optimised hyperbolic microchannels for the mechanical characterisation of bio-particles." Soft Matter 16(43): 9844-9856.

Yih, C.-S. (1967). "Instability due to viscosity stratification." Journal of Fluid Mechanics 27(2): 337-352.

CHAPTER 7

Conclusions & Future Work

In this thesis, two different microfluidic device configurations (namely the cross-slot (Chapter 4) and the flow focusing device (Chapter 5 and Chapter 6)) were utilised to investigate extensionally dominated flows. Using either a single or multiple fluid system involving Newtonian and/or viscoelastic (polymeric) fluids, this thesis investigated, and thus provides new insight on, the effects of geometrical and operational parameters as well as fluid properties on flow behaviour, and specifically, on the onset conditions of the well-known flow induced elastic instabilities. The hope is that this new knowledge can ultimately be utilised to control these instabilities, either to enhance or prevent them depending on a particular application.

This chapter will summarise the main conclusions, discussing the achievements and limitations of the work, aswell as suggestions for future work.

7.1 MICROFLUIDIC CROSS-SLOT DEVICE

In this thesis, an investigation was carried out for two-phase flows of Newtonian and/or viscoelastic fluids in the microfluidic cross-slot device (discussed in Chapter 4). A series of Newtonian microfluidic experiments in channels of different geometric aspect ratios supported numerical simulations. The aim of this work was to investigate the effect of elasticity and viscosity differences between the two inlet fluids, and the effects of interfacial tension on the position and shape of the interface between the two fluids, and the impact this has on the onset of the purely elastic instabilities that arise.

For Newtonian fluids, results show that, when the viscosity of one of the fluids is increased, the pressure drop changes and so there is a reduction in the average velocity of the fluid with higher viscosity. To satisfy a constant flow rate constraint in both fluids, the area required for the higher viscosity fluid to flow increases resulting in a relocation of the interface. When there is a viscosity difference between the two inlet fluids, a 'dimple' is shown to appear in the central region of the cross-slot stagnation point, at the interface of the two fluids. This feature is related to the jump of the viscous normal stresses at the interface of the two fluids. Investigations show that the size of this 'dimple' depends on both the geometric channel aspect ratio, with a more pronounced curvature of the dimple appearing as the aspect ratio is reduced from $AR = 0.83$ to $AR = 0.22$, and interfacial tension, with the interface becoming flatter as interfacial tension is increased (i.e., the Capillary number is reduced from $Ca = 5.90\text{x}10^{-1}$ to $Ca = 7.08\text{x}10^{-4}$).

For viscoelastic fluids, the results suggest that when the viscoelasticity (i.e., the relaxation time) of one of the inlet fluids is decreased relative to the other, an overall stabilising effect occurs, where the critical onset condition for the symmetry breaking instability, based on the properties of the more elastic fluid, is shifted to a higher value of Weissenberg number. The results also indicate, for the case where the viscoelastic properties of the two inlet fluids are the same, that once an instability is triggered, the flow can be stabilised by increasing the interfacial tension or the viscosity difference between the two inlet fluids.

An approximate analytical expression has also been proposed to predict how the critical Weissenberg number scales with the Capillary number and it has been successfully applied for the range $0.02 \leq Ca \leq 1$.

7.2 MICROFLUIDIC FLOW FOCUSING DEVICE

To date, studies in the extensional flow focusing geometry, involving complex viscoelastic fluids, tend to be the most common for single-phase flow systems, leaving a limited fundamental understanding of what happens in multiple fluid systems. As a result, the aim of this part of the thesis was to initially understand the impact of geometric and operational flow parameters on the flow of multiple Newtonian fluids in this flow configuration, acting as a baseline to understanding the fundamentals involved in these flows, before progressing onto investigations using complex viscoelastic fluids and the impact of parameters on the onset of elastic instabilities.

For Newtonian fluids, a series of microfluidic experiments and three-dimensional numerical simulations were carried out to investigate the impact of flow parameters (inlet velocity ratio, inlet viscosity ratio and geometrical aspect ratio) on the shape and size of the produced central focused stream. In Chapter 5, it was shown that an increase in either the velocity or viscosity of the fluid in the lateral inlet streams relative to the central inlet stream, resulted in a decrease of the width of the central focused stream at the centre plane ($z = D/2$). Results were also complimented with the development of a two-dimensional analytical expression, which is in agreement with 2D numerical results. Increasing the velocity of these lateral streams also enhanced the curvature of the separation streamlines in agreement with previous work (Nguyen and Huang 2005, Oliveira et al. 2012).

When high viscosity contrasts are present in parallel flow systems, a curved interface along the channel depth is known to occur (Knight et al. 1998, Cubaud and Mason 2008, Cubaud et al. 2012, Cubaud and Mason 2012). This thesis provided further insight into this curved interface, confirming that a jump in stresses at the interface

between the two fluids influences the concave shape of the interface along the depth of the channel cross-section. Results show that the channel aspect ratio and differences in fluid viscosity between the lateral and central fluid inlet streams highly influence this curved shape, highlighting that confinement plays an important role in the development of three-dimensional viscous effects.

When viscoelastic fluids are used in this flow configuration, purely elastic flow instabilities are known to arise with distinct flow regimes that depend on both the Weissenberg number (Wi) and the ratio of the inlet velocities (VR) (Oliveira et al. 2009, Oliveira et al. 2011, Ballesta and Alves 2017). In this thesis, the impact of an elasticity jump between fluid streams within this extensional flow system was assessed to ultimately determine the critical features for the onset of flow induced elastic instabilities in this geometry i.e., the dependence on the Weissenberg number, the velocity ratio, the channel aspect ratio and regions of extensional flow.

The general trends of the flow induced elastic instabilities visualised in the flow focusing geometry agree with previous findings (Oliveira et al. 2009). Results of this thesis show that decreasing the channel aspect ratio from $AR = 0.84$ to $AR = 0.22$ causes an increase in the critical Weissenberg number for the first flow transition (to steady asymmetric flow) from $Wi = 1.59$ to $Wi = 3.13$ and the size of the flow asymmetries, but a decrease in the range of Weissenberg number for which asymmetric flow is visible.

Introducing a Newtonian fluid alongside the non-Newtonian viscoelastic fluid, allowed the impact of elasticity jumps and critical regions of extensional flow to be investigated. In this thesis, two multiple fluid flow configurations were introduced to compare with the single-fluid case: one where the Newtonian fluid occupied the central fluid inlet stream and the viscoelastic fluid occupied the lateral inlet streams, and vice versa. The observed flow instabilities in both cases were of a similar nature to that of the single-fluid case. Interestingly no significant change in the critical Wi for the transition to steady asymmetric flow was observed for the various configurations. However, placing the Newtonian fluid in the lateral streams delayed the transition to time-

dependent flow quite significantly from $Wi \cong 4.69$ for the single-fluid case to $Wi \cong 18.39$. The largest asymmetries were visualised for the single-fluid case, with the closest similarity observed for the shear dominated case. These results suggest that these elastic instabilities cannot be solely related to the extensional flow within this set up and the shear region where there is a high streamline curvature is important, which is in agreement with recent work in the cross-slot geometry (Davoodi et al. 2019, Davoodi et al. 2021).

7.3 FINAL REMARKS & FUTURE WORK

The findings of this thesis suggest that flow induced elastic instabilities in extensional flow devices where multiple fluids are involved depend on a number of critical flow parameters, relating to the geometrical parameters of the microfluidic geometries, the fluids that are used and the configuration of those fluids. This work can assist in a range of future studies to investigate the behaviour of Newtonian and complex viscoelastic fluids in multiple fluid flow systems.

The systematic study using two phase flows of viscoelastic fluids in the cross-slot device was only investigated using numerical simulations in this thesis. This is because in experimental work it is more challenging to alter, and thus analyse the effect of, one singular fluid property (for example the relaxation time) without changing other properties simultaneously. This work could be expanded to introduce Newtonian fluids (both miscible and immiscible) alongside a viscoelastic fluid. For this work, it would be recommended to initially keep the ratio of inlet viscosities equal to visualise the impact of an elasticity jump, before introducing interfacial tension and viscosity jumps across the interface. It would be interesting to see if flow induced elastic instabilities still occur in these cases or if a fully viscoelastic flow system would be required in this flow configuration.

The multiple fluid work in the flow focusing device opens a number of exciting opportunities for future work both experimentally and numerically. Numerical simulations involving complex multiphase flows is still an ongoing challenge within this

research field. As a result, the work included in this thesis within the flow focusing device is limited only to experimental flow visualisation however, it would be very beneficial to study these flows numerically to provide an insight of the stresses involved in each of these flow configurations, and how these impact when the flow instabilities arise.

This thesis addresses the impact on the purely elastic instabilities that arise when an elasticity jump exists however, this was restricted to two limiting cases, one in which there is no jump, for systems involving a single fluid only, and the case where the elasticity jump has an infinite value for a system involving a Newtonian and Viscoelastic fluid. It would be interesting to explore this further for an intermediate range of elasticity jumps to determine the impact this has on the elastic instabilities however, due to the experimental challenge of being unable to adjust only one fluid property without altering others, this may require a numerical investigation to guide experimentation. Subsequent work that would be worth doing both experimentally and numerically, would be to study the effect of Capillary number by changing the interfacial tension (using an immiscible Newtonian fluid) and also miscible Newtonian fluids of higher viscosities to observe how these differences influence the flow induced elastic instabilities that arise.

Experimental work has allowed critical conditions for elastic instability transitions to be identified in both single and multiple-fluid flows within the flow focusing device. However, to progress to higher values of Weissenberg number, where it is known that a number of other flow regimes exist on the path to elastic turbulence from the work of Ballesta and Alves (2017) and as shown in Appendix C, other experimental methods are required to quantify the velocity field, such as Micro-Particle Image Velocimetry (μPIV), the pressure drops and the stresses (birefringence) of these flows. This would provide a more thorough understanding of these multiple-fluid flows in the flow focusing device and ultimately lead to having more control when elastic instabilities occur.

All of the work conducted in the flow focusing device to observe elastic instabilities has used Boger fluids, where the viscosity remains approximately constant. This allows for

separation of elasticity effects however, preliminary work shown in Appendix C has started looking at effects of shear thinning, highlighting another interesting avenue for future work.

Ultimately, with the combination of experimental and numerical results, this work has highlighted the effects of various geometrical parameters, flow parameters and fluid properties, providing new insight into the onset of elastic instabilities within extensional flow devices. This knowledge can be exploited to design experiments to be able to enhance or delay the onset of elastic instabilities in future work involving complex fluids where, for example, if someone wanted to avoid or delay instabilities in extensional devices they would need to use low aspect ratios and low values of Weissenberg number or, introduce an interfacial tension to the flow system. On the other hand, if someone wanted to maximise the range of Weissenberg number over which the steady asymmetric flow regime occurred within a flow focusing configuration, they could move to higher values of aspect ratio, use high values of velocity ratio and/or introduce a second Newtonian fluid to the lateral inlet streams.

7.4 REFERENCES

Ballesta, P. and Alves, M. A. (2017). "Purely elastic instabilities in a microfluidic flow focusing device." Physical Review Fluids 2(5): 053301.

Cubaud, T., Jose, B. M., Darvishi, S. and Sun, R. (2012). "Droplet breakup and viscosity-stratified flows in microchannels." International Journal of Multiphase Flow 39: 29-36.

Cubaud, T. and Mason, T. G. (2008). "Formation of miscible fluid microstructures by hydrodynamic focusing in plane geometries." Phys Rev E Stat Nonlin Soft Matter Phys 78(5): 056308.

Cubaud, T. and Mason, T. G. (2012). "Interacting viscous instabilities in microfluidic systems." Soft Matter 8(41): 10573–10582.

Davoodi, M., Domingues, A. F. and Poole, R. J. (2019). "Control of a purely elastic symmetry-breaking flow instability in cross-slot geometries." Journal of Fluid Mechanics 881: 1123-1157.

Davoodi, M., Houston, G., Downie, J., Oliveira, M. S. N. and Poole, R. J. (2021). "Stabilization of purely elastic instabilities in cross-slot geometries." Journal of Fluid Mechanics 922: A12.

Knight, J. B., Vishwanath, A., Brody, J. P. and Austin, R. H. (1998). "Hydrodynamic Focusing on a Silicon Chip: Mixing Nanoliters in Microseconds." Physical Review Letters 80(17): 3863-3866.

Nguyen, N. T. and Huang, X. (2005). "Mixing in microchannels based on hydrodynamic focusing and time-interleaved segmentation: modelling and experiment." Lab Chip 5(11): 1320-1326.

Oliveira, M., Pinho, F. T. and Alves, M. A. (2011). Extensional Flow of Newtonian and Boger Fluids Through a Flow Focusing Microdevice. 3rd Micro and Nano Flows Conference. Thessaloniki, Greece: 1-6.

Oliveira, M. S. N., Pinho, F. T. and Alves, M. A. (2012). "Divergent streamlines and free vortices in Newtonian fluid flows in microfluidic flow-focusing devices." Journal of Fluid Mechanics 711: 171-191.

Oliveira, M. S. N., Pinho, F. T., Poole, R. J., Oliveira, P. J. and Alves, M. A. (2009). "Purely elastic flow asymmetries in flow-focusing devices." Journal of Non-Newtonian Fluid Mechanics 160(1): 31-39.

APPENDICES

8.1 APPENDIX A- Additional information for Chapter 4.

Following the classic asymptotic analysis carried out by Hinch (1993) for the flow of an Oldroyd-B fluid around a re-entrant corner, one can show that, close to the corners of a cross-slot geometry, the velocity vanishes like $r^{5/9}$ and so the shear rate is singular like $r^{-4/9}$, τ_{11} is singular like $r^{-2/3}$and $1/\Re$ is singular like r^{-1} (simply because u_x and u_y scale in the same manner). Note that an analytical solution for the stream function is presented in Hinch (1993) so, alternatively, one can calculate the curvature of the streamlines using the formulation presented in Cruz et al. (2016) to obtain the same result. Including all these scaling estimates in equation (4.1), M^2 should be singular like $r^{-2/3}$.

Alternatively, if the second term in equation (4.1), is estimated simply as τ_{11}/τ_{12}, as these stresses scale in the same way as you approach the corner, M^2 will scale in this case as $|u|/\Re$, which again gives a singular behaviour like $r^{-4/9}$. One thing that should be noted here is that the study of Hinch (1993) is based on the assumption that the flow flows round the corner and stays attached (while, in reality, at higher rates the flow field can also develop a so-called lip vortex). Thus, this analysis cannot strictly be used while outside the so-called 'elastic core'. Note that in all the numerical simulations and, particularly the results presented in Figure 4.12, a no-slip boundary condition for the velocity field at the wall is applied (so the velocity has an exact value of zero here), but the stress value at the wall is always extrapolated from the nearby cell and, therefore, has a necessarily finite value. As a consequence, M is always zero at the wall once this extrapolation approach is used, and in fact the maximum value of M always occurs in the first computational cell away from the corner and not exactly at the corner itself. In such situations, as the mesh is continuously refined, one would notice that M will exhibit larger and larger values here so the maximum value of the M is always mesh dependent (i.e., M is singular at the corners for any non-zero value of the Weissenberg number).

8.2 APPENDIX B – Additional information for Chapter 5.

Further examples relating to Figure 5.15a and b can be found below showing a quantitative comparison between experimental and numerical results of the width of the central focused stream along the depth of the channel for two viscosity ratios ($K = 5.64$ and $K = 15.07$). For both cases $W_{f,z}$ represents the filament width at a particular z position $(0 < z/D < 1)$ and horizontal error bars indicate the experimental depth of field estimated for the optical set-up used in this work.

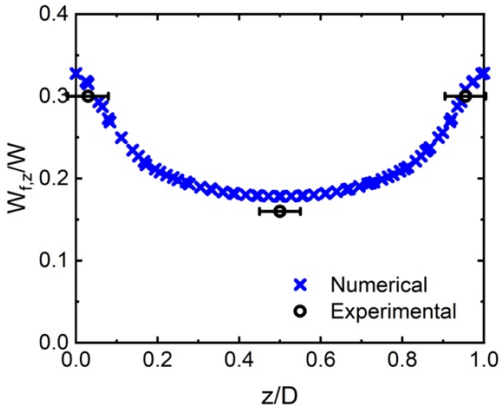

Figure B.1: Comparison of the normalised width of the central focused outlet stream along the z-direction obtained in the 3D numerical simulations and in the experiments with $AR = 0.84$ for $K = 5.64$.

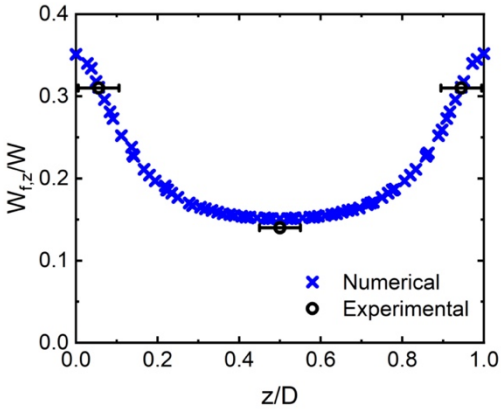

Figure B.2: Comparison of the normalised width of the central focused outlet stream along the z-direction obtained in the 3D numerical simulations and in the experiments with $AR = 0.84$ for $K = 15.07$.

8.3 APPENDIX C- Effect of Shear Thinning

8.3.1 Introduction

The work shown in this appendix follows on from the work of Chapter 6 and summarises preliminary work that has been conducted to investigate the effects of shear thinning fluid properties on the development of elastic instabilities in microfluidic flow focusing devices.

Research conducted in a variety of microfluidic devices, both extensional and shear dominated, have found that shear thinning fluid properties have a stabilising effect on the elastic instabilities that arise in these flow systems (Sousa et al. 2015, Casanellas et al. 2016). In shear dominated serpentine microchannels, the stabilising effect of shear thinning has been highlighted by the delayed onset of the time-dependent instabilities to higher values of Weissenberg number (Casanellas et al. 2016). In cross-slot configurations with low aspect ratios by increasing the degree of shear thinning Sousa et al. (2015) were able to observe the steady asymmetric regime which was absent in the case of Boger fluid flows, delaying the transition to unsteady flow to higher Weissenberg numbers. Similarly, recent investigations in the flow of polymeric solutions around microfluidic cylinders (a flow of mixed kinematics) have also highlighted the importance and requirement of shear thinning for the development of steady asymmetric flow (Haward et al. 2020).

Ballesta and Alves (2017) studied elastic instabilities that arise using viscoelastic fluids with shear thinning properties in the extensional flow focusing device however, their work focuses on the path to elastic turbulence. Their work observed various distinct time-dependent regimes that occur with increasing Weissenberg Number (Wi) and Hencky strain ($\varepsilon_{H_{FF}}$) prior to the flow reaching chaotic conditions. To the author's knowledge, to date, there is a limited understanding of how the level of shear thinning effects these instabilities, and thus the transitions, that arise within this extensional flow focusing device.

8.3.2 Materials and Methods

8.3.2.1 Fluid Preparation and Characterisation

Different viscoelastic polyethylene oxide (PEO) solutions with different levels of shear thinning were used in the work presented in this Appendix. The PEO was supplied by Sigma Aldrich, with nominal molecular weight $M_w = 8\text{x}10^6$g mol^{-1} and these aqueous solutions with different concentrations $(1000 \leq c \leq 3000)$ were prepared. The overlap concentration of PEO is $c^* \approx$ 350ppm (Rodd et al. 2005) and as the prepared solutions all have a concentration above this value, they can be no longer be considered dilute (Casanellas et al. 2016). All prepared solutions were seeded with fluorescent tracer particles (FluoSpheres® carboxylate- modified, 1.0μm, Nile Red (Ex/Em: 535/575)) at concentration of ~0.02%wt for flow visualisation purposes.

A summary of the composition and properties of the fluids used in this appendix is given in Table C.1. The density of the solutions was measured using pycnometry and the viscosity was characterised in steady shear on a DHR-2 hybrid rotational rheometer (TA Instruments) with a cone-plate geometry (60 mm diameter, 1° cone angle) at a temperature of 20°C.The relaxation time was determined using a Capillary Breakup Extensional Rheometer (HAAKE™ CaBER™). As can be seen in Figure C.1 all fluids exhibit shear thinning characteristics, with the more concentrated solution showing a higher zero-shear viscosity and higher level of shear-thinning as expected (Bird et al. 1977).

Table C.1: Characteristics of the fluids used in the experimental work including fluid composition and physical properties (density, CaBER relaxation time and zero-shear viscosity) at 20 °C.

Fluid ID	Composition	Density (kg/m^3)	Zero-shear Viscosity (Pa s)	Relaxation Time (ms)
PEO1000	PEO (M_w8 x10^6), 1000ppm (w/w) in Water	1042	7.04x10^{-3}	50.6
PEO2000	PEO (M_w8 x10^6), 2000ppm (w/w) in Water	1042	2.66x10^{-2}	68.1
PEO3000	PEO (M_w8 x10^6), 3000ppm (w/w) in Water	1042	9.70x10^{-2}	81.3

The shear rheology data (DHR-2 Rotational Rheometer) for the viscoelastic fluids described in Table 6.1 can be found in Figure C.1. In all cases the viscosity is shown to decrease with an increasing shear rate, and thus the fluids can be considered shear thinning.

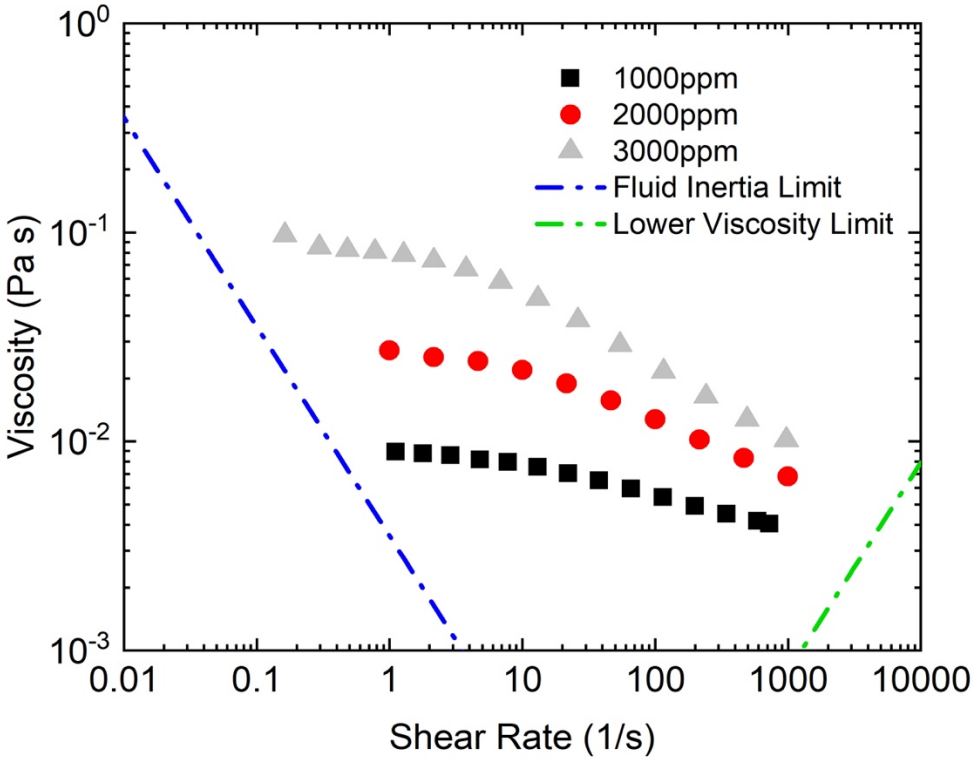

Figure C.1: Steady shear rheology data (DHR-2 Rotational Rheometer) for the viscoelastic fluids described in Table C.1. Rheometer limits outlined in equations (3.13) and (3.14) are shown. Black squares represent data for 1000ppm fluid, red circles represent data for 2000ppm fluid and grey triangles represent data for 3000ppm fluid.

8.3.2.2 Microfluidic Geometry and Experimental Set-Up

A schematic diagram of the microfluidic flow focusing geometry and the experimental set up can be visualised in Figure 5.1. The flow focusing device used in this study has a rectangular cross section of width $W = 109 \pm 2$ μm and a uniform depth $D = 92 \pm 1$ μm resulting in an aspect ratio equal to 0.84, as previously discussed in Chapter 5. The experimental microchannel was made from polydimethylsiloxane (Sylgard 184, Dow Corning) and was fabricated using a SU-8 mould by standard soft-lithography techniques.

The experimental procedure outlined in Chapter 5 and Chapter 6 was adopted for this work. In cases discussed here the inverted microscope (Olympus IX71) was equipped with a 10X objective lens (numerical aperture NA = 0.3) and an adequate filter cube (Olympus U-MWIGA3, Excitation Filter BP530-550). As previously, the images were acquired using streak imaging at the centre plane of the microchannel ($z = D/2$) using a CCD camera (Olympus XM10).

8.3.3 Effect of Shear Thinning

Figure C.2 shows preliminary flow classification maps illustrating the effect of the Weissenberg number and velocity ratio for the. three viscoelastic fluids with different levels of shear thinning.

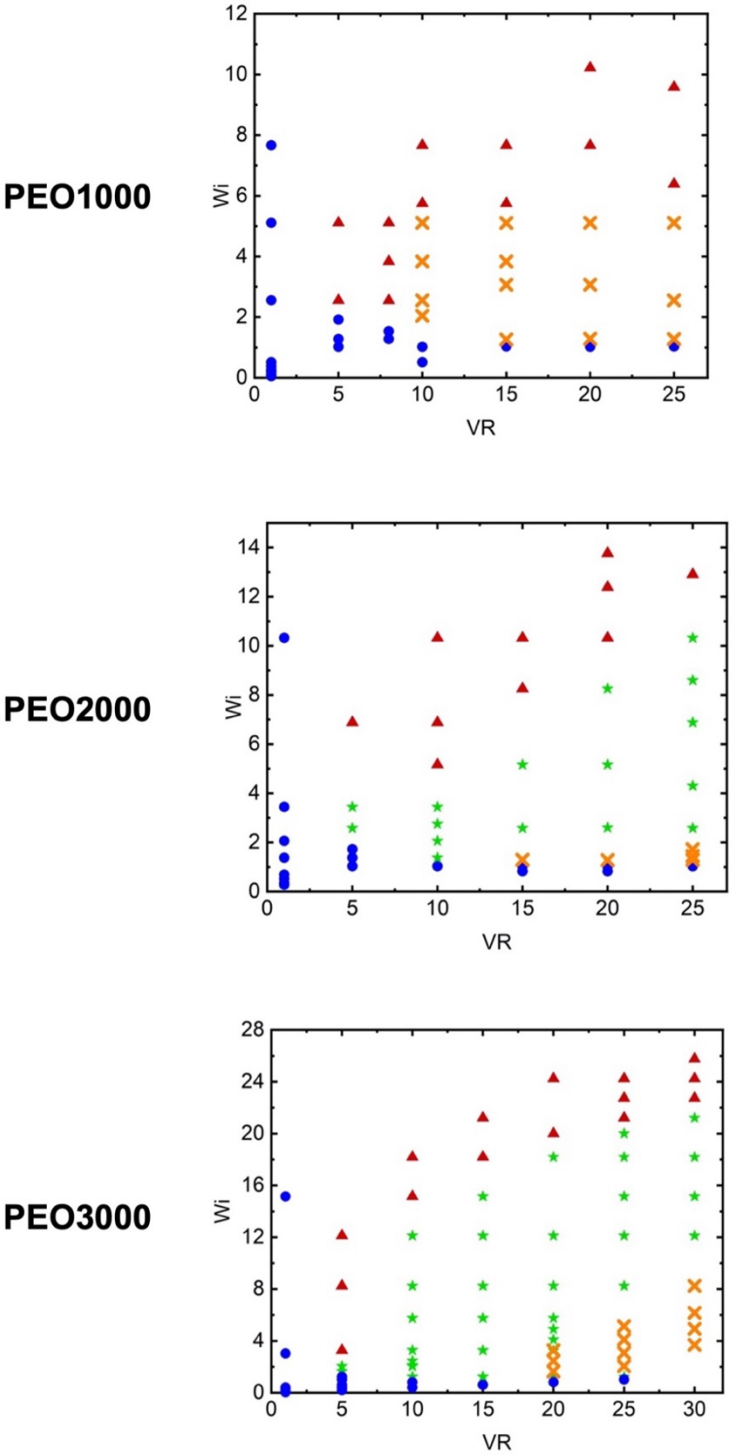

Figure C.2: Flow classification map in the $Wi - VR$ domain for single-phase viscoelastic fluid flow within the flow focusing device of AR = 0.84 for three shear thinning solutions (PEO1000, PEO2000 and PEO3000). Blue circles indicate symmetric flow regime, orange crosses indicate steady asymmetric flow regime, red triangles indicate the time-dependent flow regime, akin to that seen with Boger fluids and green stars represent the extra flow regime.

For low levels of shear thinning, as in the case of the 1000ppm solution, the flow patterns, and thus instability transitions, are similar to those observed when using the Boger-like fluid (see Figure 6.5). For low velocity ratios, $VR < 10$, only one transition from steady symmetric flow to time-dependent flow was observed. For moderate to high velocity ratios, $VR \geq 10$ $\left(\varepsilon_{H\ FF} \geq 3\right)$, two transitions were observed for increasing Wi: a first transition to steady asymmetric flow at $Wi = 1.15$ and a second transition from steady asymmetric to time-dependent flow at $Wi = 5.45$. Although not directly comparable to the single-phase Boger fluid work in Chapter 6 (due to the differences in composition of the Newtonian solvent and the fact that the solutions used here are no longer dilute), here the first transition occurs at a lower critical Weissenberg number than in the case of the Boger fluid ($Wi_c = 1.59$ for the Boger fluid), while the second transition to time-dependent flow occurs at a higher critical Wi ($Wi_c = 4.69$ for the Boger fluid).

As the degree of shear thinning is increased (i.e., for fluids 2000ppm and 3000ppm), it was evident from the flow patterns that more than just three flow regimes were present. It appears that other flow regimes exist between the steady asymmetric flow regime and the fully time-dependent flow regime, identified in Figure C.2 as blue circles and red triangles respectively. It is thought that these regimes could be similar to those discussed in the work of Ballesta and Alves (2017) where, at low values of Hencky strain the flow is unsteady with periodic oscillations (named ‘symmetric periodic flow’); as the Hencky strain is increased the flow transitions to an unsteady regime with asymmetric periodic oscillations (named ‘asymmetric periodic flow’) and as the Wi and Hencky strain are increased further a third regime occurs where the flow is unsteady with only short bursts of periodic oscillations (named ‘semiperiodic flow’). However, using only these qualitative flow visualisations it is not possible to accurately differentiate between these flow regimes to determine if this is truly the case, and as a result these are all combined into a singular flow regime termed “other” in Figure C.2.

From these visualisations it also appears that the transition to time-dependent flow (red triangles in Figure C.2) may be delayed to higher values of Wi which would show a stabilising effect of shear thinning. To fully understand the impact of shear thinning fluid properties on the elastic instabilities that arise within the flow focusing device it is clear that quantitative techniques are required. This could involve numerical simulations or experimental methods such as Micro-particle Image Velocimetry (μPIV).

8.4 Appendix References

Ballesta, P. and Alves, M. A. (2017). "Purely elastic instabilities in a microfluidic flow focusing device." Physical Review Fluids 2(5): 053301.

Bird, R. B., Hassager, O. and Armstrong, R. C. (1977). Dynamics of polymeric liquids. Vol. 1: Fluid Mechanics, John Wiley and Sons.

Casanellas, L., Alves, M. A., Poole, R. J., Lerouge, S. and Lindner, A. (2016). "The stabilizing effect of shear thinning on the onset of purely elastic instabilities in serpentine microflows." Soft Matter 12(29): 6167-6175.

Cruz, F. A., Poole, R. J., Afonso, A. M., Pinho, F. T., Oliveira, P. J. and Alves, M. A. (2016). "Influence of channel aspect ratio on the onset of purely-elastic flow instabilities in three-dimensional planar cross-slots." Journal of Non-Newtonian Fluid Mechanics 227: 65-79.

Haward, S. J., Hopkins, C. C. and Shen, A. Q. (2020). "Asymmetric flow of polymer solutions around microfluidic cylinders: Interaction between shear-thinning and viscoelasticity." Journal of Non-Newtonian Fluid Mechanics 278: 104250.

Hinch, E. J. (1993). "The flow of an Oldroyd fluid around a sharp corner." Journal of Non-Newtonian Fluid Mechanics 50(2-3): 161-171.

Rodd, L. E., Scott, T. P., Boger, D. V., Cooper-White, J. J. and McKinley, G. H. (2005). "The inertio-elastic planar entry flow of low-viscosity elastic fluids in micro-fabricated geometries." Journal of Non-Newtonian Fluid Mechanics 129(1): 1-22.

Sousa, P. C., Pinho, F. T., Oliveira, M. S. and Alves, M. A. (2015). "Purely elastic flow instabilities in microscale cross-slot devices." Soft Matter 11(45): 8856-8862.